



# Generation 1.5 High Speed Civil Transport (HSCT) Exhaust Nozzle Program

E.B. Thayer, E.J. Gamble, A.R. Guthrie, and D.F. Kehret  
United Technologies Corporation, Pratt & Whitney Aircraft, East Hartford, Connecticut

T.J. Barber and G.J. Hendricks  
United Technologies Research Center, East Hartford, Connecticut

K.S. Nagaraja and J.E. Minardi  
Rohini International, Cleveland, Ohio

## The NASA STI Program Office . . . in Profile

Since its founding, NASA has been dedicated to the advancement of aeronautics and space science. The NASA Scientific and Technical Information (STI) Program Office plays a key part in helping NASA maintain this important role.

The NASA STI Program Office is operated by Langley Research Center, the Lead Center for NASA's scientific and technical information. The NASA STI Program Office provides access to the NASA STI Database, the largest collection of aeronautical and space science STI in the world. The Program Office is also NASA's institutional mechanism for disseminating the results of its research and development activities. These results are published by NASA in the NASA STI Report Series, which includes the following report types:

- **TECHNICAL PUBLICATION.** Reports of completed research or a major significant phase of research that present the results of NASA programs and include extensive data or theoretical analysis. Includes compilations of significant scientific and technical data and information deemed to be of continuing reference value. NASA's counterpart of peer-reviewed formal professional papers but has less stringent limitations on manuscript length and extent of graphic presentations.
- **TECHNICAL MEMORANDUM.** Scientific and technical findings that are preliminary or of specialized interest, e.g., quick release reports, working papers, and bibliographies that contain minimal annotation. Does not contain extensive analysis.
- **CONTRACTOR REPORT.** Scientific and technical findings by NASA-sponsored contractors and grantees.

- **CONFERENCE PUBLICATION.** Collected papers from scientific and technical conferences, symposia, seminars, or other meetings sponsored or cosponsored by NASA.
- **SPECIAL PUBLICATION.** Scientific, technical, or historical information from NASA programs, projects, and missions, often concerned with subjects having substantial public interest.
- **TECHNICAL TRANSLATION.** English-language translations of foreign scientific and technical material pertinent to NASA's mission.

Specialized services that complement the STI Program Office's diverse offerings include creating custom thesauri, building customized databases, organizing and publishing research results . . . even providing videos.

For more information about the NASA STI Program Office, see the following:

- Access the NASA STI Program Home Page at <http://www.sti.nasa.gov>
- E-mail your question via the Internet to [help@sti.nasa.gov](mailto:help@sti.nasa.gov)
- Fax your question to the NASA Access Help Desk at 301-621-0134
- Telephone the NASA Access Help Desk at 301-621-0390
- Write to:  
NASA Access Help Desk  
NASA Center for Aerospace Information  
7121 Standard Drive  
Hanover, MD 21076



# Generation 1.5 High Speed Civil Transport (HSCT) Exhaust Nozzle Program

E.B. Thayer, E.J. Gamble, A.R. Guthrie, and D.F. Kehret  
United Technologies Corporation, Pratt & Whitney Aircraft, East Hartford,  
Connecticut

T.J. Barber and G.J. Hendricks  
United Technologies Research Center, East Hartford, Connecticut

K.S. Nagaraja and J.E. Minardi  
Rohini International, Cleveland, Ohio

Prepared under Contract NAS3-26618

National Aeronautics and  
Space Administration

Glenn Research Center

## Document History

This research was originally published internally as HSR028 in May 1996.

Note that at the time of research, the NASA Lewis Research Center was undergoing a name change to the NASA John H. Glenn Research Center at Lewis Field. Both names may appear in this report.

Available from

NASA Center for Aerospace Information  
7121 Standard Drive  
Hanover, MD 21076

National Technical Information Service  
5285 Port Royal Road  
Springfield, VA 22100

Available electronically at <http://gltrs.grc.nasa.gov>



# CONTENTS

<i>Section</i>	<i>Page</i>
1. SUMMARY .....	1
2. INTRODUCTION .....	2
2.1 Background.....	2
3. MIXER/EJECTOR MODEL TESTS .....	5
3.1 Background.....	5
3.2 Test Facility Description .....	5
3.3 Hardware .....	6
3.4 Test Matrix .....	6
3.5 Instrumentation .....	7
3.6 Test Procedure .....	7
3.7 Discussion of Results.....	8
3.7.1 Discussion of Performance and Pumping .....	9
3.7.2 Discussion of Static Pressures/Mode Shift .....	47
3.7.3 Discussion of Schlieren Photography .....	64
3.8 Conclusions .....	64
3.9 Recommendations .....	65
4. HIGH-SPEED MODEL TESTS.....	93
4.1 Test Apparatus and Method.....	93
4.1.1 Two-Dimensional/Convergent-Divergent (2-D/C-D) Nozzle .....	93
4.1.2 Two-Dimensional (2-D) Plug Nozzle .....	102
4.1.3 Single Expansion Ramp Nozzle (SERN) .....	102
4.2 Facility Description .....	110
4.3 Test Data Validation .....	110
4.4 Results and Discussion .....	111
4.4.1 2-D/C-D Nozzle .....	111
4.5 2-D Plug Nozzle .....	112
4.5.1 2-D Plug Nozzle Flap Angle .....	121
4.5.2 Plug Nozzle Flap Length .....	121
4.6 SERN .....	121
4.6.1 SERN Ramp Contour Effects .....	121
4.6.2 SERN Flap Angle and Length Effects .....	121
4.7 CONCLUSIONS .....	121
4.7.1 2-D/C-D Nozzle Performance Summary .....	121
4.7.2 2-D Plug Performance Summary .....	122
4.7.3 SERN Performance Summary .....	122

5.	COMPUTATIONAL FLUID DYNAMICS .....	130
5.1	Geometry .....	130
5.2	Grid Generation .....	131
5.2.1	Background .....	131
5.2.2	Grid Generation .....	131
5.3	Design Point .....	132
5.4	Flow Field Solver .....	132
5.4.1	NASTAR Navier-Stokes Analysis .....	132
5.5	Flow Field Analysis-Isolated Nacelle.....	133
5.5.1	Experimental Data .....	133
5.5.2	Isolated Nacelle Analysis .....	133
5.5.3	Operating Mode 1 — Normal Shock at Ejector Exit Plane .....	134
5.5.4	Operating Mode 2 — Shock-Free Ejector Duct .....	134
5.5.5	Convergence History .....	134
5.5.6	Analysis of Installation Effects .....	135
5.6	Conclusions — Flowfield Observations.....	136
6.	HEAT TRANSFER STUDIES.....	148
6.1	Design Assumptions .....	148
6.2	Analytic Results.....	148
6.3	Conclusions and Recommendations .....	150
7.	THROAT AUGMENTATION STUDIES .....	162
7.1	Secondary Throat Ejector .....	163
7.2	Nozzle Performance Using Fanno and Rayleigh Lines.....	164
7.2.1	Unchoked Flow .....	164
7.2.2	Choked flow (Fixed Fanno Line at Exit) .....	164
7.3	Ejector Performance Using Fanno and Rayleigh Lines.....	165
7.3.1	Unchoked Flow .....	165
7.3.2	Choked flow: Fixed Fanno Line at Exit .....	165
7.4	Typical Ejector Results.....	166
7.5	Secondary Exit Area Study.....	166
7.6	Inlet Lip Ejectors .....	166
7.7	Conclusions and Recommendations.....	167
7.7.1	Conclusions .....	167
7.7.2	Recommendations .....	167

## FIGURES

<i>Figure</i>	<i>Page</i>
1. Typical 2-D/C-D Mixer/Ejector Shown at Takeoff and Supersonic Cruise Positions.....	3
2. Boeing Nozzle Test Facility .....	11
3. Nozzle Assembly .....	12
4. Nozzle Installation .....	12
5. HSCT Generation 1.5 Mixer Summary .....	13
6. HSCT Generation 1.5 Test Matrix .....	14
7. Mixer/Ejector Rig for Generation 1.5 Performance Tests .....	15
8. Mixer for Generation 1.5 Performance Tests.....	15
9. Geometric Definition for Aerodynamically Shaped Mixers .....	16
10. Mixer Instrumentation Locations .....	16
11. Mixer Instrumentation — Static Pressure Taps .....	17
12. Mixer Total Pressure Probe Locations .....	19
13. Ejector Shroud and Sidewall Static Pressure Taps .....	20
14. Ejector Shroud Static Pressure Taps .....	20
15. Comparison of Corrected Performance and Entrainment Effects of Primary Total Temperature at SNPR = 1.0 for Baseline Configuration .....	21
16. Comparison of Corrected Performance and Entrainment Effects of SAR at SNPR = 1.0 and $T_{t_p} = 700^\circ\text{F}$ .....	22
17. Comparison of Corrected Entrainment Effects of SAR at NPR = 3.5 and $T_{t_p} = 700^\circ\text{F}$ .....	23
18. Mixer-Only Nozzle Performance Effects of Mixer Lobe Height (SAR), $T_{t_p} = 700^\circ\text{F}$ .....	23
19. Comparison of Corrected Performance and Entrainment Effects of MAR at SNPR = 1.0, Mixer L/D = 1.0, and $T_{t_p} = 700^\circ\text{F}$ .....	24
20. Comparison of Corrected Performance and Entrainment Effects of MAR at SNPR = 1.0, Mixer L/D = 0.6 and $T_{t_p} = 700^\circ\text{F}$ .....	25
21. Comparison of Corrected Performance and Entrainment Effects of CER at SNPR = 1.0 and $T_{t_p} = 700^\circ\text{F}$ .....	26
22. Comparison of Corrected Performance and Entrainment Effects of CER at NPR = 3.5 and $T_{t_p} = 700^\circ\text{F}$ .....	27
23. Comparison of Corrected Performance and Entrainment Effects of CER at NPR = 4.5 and $T_{t_p} = 700^\circ\text{F}$ .....	28
24. Mixer-Only Nozzle Performance Effects of CER at $T_{t_p} = 700^\circ\text{F}$ .....	29

25.	Comparison of Corrected Performance and Entrainment Effects of Penetration at SNPR = 1.0, SAR = 3.0.....	30
26.	Comparison of Corrected Performance and Entrainment Effects of Penetration at SNPR = 1.0, SAR = 3.4, and $T_{tp} = 700^{\circ}\text{F}$ .....	31
27.	Mixer-Only Nozzle Performance Effects of Mixer Lobe Height (Penetration), $T_{tp} = 700^{\circ}\text{F}$ .....	32
28.	Comparison of Corrected Performance and Entrainment Effects of Mixer L/D at SNPR = 1.0 and $T_{tp} = 700^{\circ}\text{F}$ .....	33
29.	Mixer-Only Nozzle Performance Effects of Mixer L/D at $T_{tp} = 700^{\circ}\text{F}$ .....	34
30.	Comparison of Corrected Performance and Entrainment Effects of Shroud L/D at SNPR = 1.0 and $T_{tp} = 700^{\circ}\text{F}$ .....	35
31.	Comparison of Corrected Performance and Entrainment Effects of Lobe Count at SNPR = 1.0, SAR = 3.0, and $T_{tp} = 700^{\circ}\text{F}$ .....	36
32.	Mixer-Only Nozzle Performance Effects of Mixer Lobe Count at $T_{tp} = 700^{\circ}\text{F}$ .....	37
33.	Comparison of Corrected Performance and Entrainment Effects of Chute Shaping at SNPR = 0.9 and $T_{tp} = 70^{\circ}\text{F}$ .....	38
34.	Comparison of Corrected Performance and Entrainment Effects of Chute Shaping at SNPR = 1.0 and $T_{tp} = 70^{\circ}\text{F}$ .....	39
35.	Comparison of Corrected Performance and Entrainment Effects of SNPR for SAR = 2.2 and $T_{tp} = 700^{\circ}\text{F}$ .....	40
36.	Comparison of Corrected Performance and Entrainment Effects of SNPR for SAR = 2.6 and $T_{tp} = 700^{\circ}\text{F}$ .....	41
37.	Comparison of Corrected Performance and Entrainment Effects of SNPR for SAR = 3.0 and $T_{tp} = 700^{\circ}\text{F}$ .....	42
38.	Comparison of Corrected Performance and Entrainment Effects of SNPR for SAR = 3.4 and $T_{tp} = 700^{\circ}\text{F}$ .....	43
39.	Pin Supports Used for Mixers 12, 14, and 15.....	44
40.	Comparison of Corrected Performance and Entrainment Effects of Support Pins in Mixer 12 Secondary Chutes for SNPR = 1.0 and $T_{tp} = 70^{\circ}\text{F}$ .....	45
41.	Comparison of Boeing and Fluidyne Data — Baseline Configuration Performance and Flow Coefficient for SNPR = 1.0 and $T_{tp} = 700^{\circ}\text{F}$ .....	46
42.	Flow Coefficient Data for Mixers with Stiffening Pins in Secondary Chutes Recorded in Fluidyne's Channel 14.....	47
43.	Mixer External and Shroud Internal Static Pressures — Effect of MAR Using Long Mixer.....	49
44.	Mixer External and Shroud Internal Static Pressures — Effect of MAR Using Short Mixer.....	51
45.	Effect of MAR on Mode Shift Pressure Ratio.....	53

46.	Mixer External and Shroud Internal Static Pressures — Effect of Penetration .....	54
47.	Mixer External and Shroud Internal Static Pressures — Effect of Axial Versus Nonaxial Mixer Exit Flow .....	56
48.	Mixer External and Shroud Internal Static Pressures — Effect of SAR.....	57
49.	Mode Shift Trends.....	59
50.	Mixer External and Shroud Internal Static Pressures — Effect of Mixing Duct Length.....	60
51.	Effect of Primary Total Temperature on Mode Shift Pressure Ratio.....	61
52.	Mixer External and Shroud Internal Static Pressures — Effect of Temperature .....	62
53.	View Shown in Typical Schlieren Photograph .....	65
54.	Schlieren Photography Showing NPR Effects.....	66
55.	Schlieren Photography Showing SNPR Effects.....	67
56.	Schlieren Photography Showing MAR Effects.....	69
57.	Schlieren Photography Showing Penetration Effects .....	71
58.	Schlieren Photography Showing SAR Effects.....	73
59.	Schlieren Photography Showing Temperature Effects .....	75
60.	Exit Velocity and Static Pressure Versus ASAR .....	86
61.	Exit Velocity and Static Pressure Versus ASAR .....	87
62.	Exit Velocity and Static Pressure Versus ASAR .....	88
63.	Exit Velocity and Static Pressure Versus ASAR .....	89
64.	Exit Velocity and Static Pressure Versus ASAR .....	90
65.	Exit Velocity and Static Pressure Versus ASAR .....	91
66.	Typical 2-D/C-D Mixer/Ejector Shown at Takeoff and Supersonic Cruise Positions.....	94
67.	2-D/C-D Model Configuration Geometry Variations .....	95
68.	2-D/C-D Nozzle — Short, Straight Flap Configuration ( $L_f = 10$ in.).....	96
69.	2-D/C-D Nozzle — Medium, Straight Flap Configuration ( $L_f = 14$ in.).....	96
70.	2-D/C-D Nozzle — Long Straight Flap Configuration ( $L_f = 18$ in.).....	97
71.	2-D/C-D Nozzle — Long Straight Flap with Splitter Configuration ( $L_f = 18$ in., $A_e/A_j = 3.5$ ).....	97
72.	2-D/C-D Nozzle — Rough Flap ( $L_f = 18$ in., Roughness B).....	98
73.	2-D/C-D Nozzle — Rough Flap ( $L_f = 18$ in., Roughness C).....	98
74.	2-D/C-D Nozzle — Isentropic Flap ( $L_f = 10$ in.).....	99
75.	2-D/C-D Nozzle — Two-Piece Flap ( $L_f = 10$ in.) .....	99
76.	2-D/C-D Divergent Flap Pressure Tap Instrumentation .....	100

77.	2-D/C-D Convergent Flap Pressure Tap Instrumentation.....	101
78.	2-D FLADE Plug Nozzle .....	103
79.	2-D Plug Model Configuration Geometry Variations.....	104
80.	2-D Plug Nozzle — 5-Degree Isentropic Plug (Baseline) .....	105
81.	2-D Plug Nozzle — 10-Degree Isentropic Plug.....	105
82.	2-D Plug Nozzle — 15-Degree Wedge.....	106
83.	2-D FLADE SERN with an Isentropic Expansion Ramp .....	106
84.	SERN Model Configuration Geometry Variations .....	107
85.	SERN with a 5-Degree Isentropic Ramp .....	108
86.	SERN with a 7.5-Degree Isentropic Ramp .....	108
87.	SERN with a 10-Degree Isentropic Ramp .....	109
88.	SERN with Flex Ramp.....	109
89.	CE-22 Test Facility .....	113
90.	2-D/C-D Nozzle Model Mounted in CE-22 Test Facility.....	113
91.	Peak Performance of 2-D/C-D Nozzles .....	114
92.	Comparison of 2-D/C-D Nozzle Flap Contour Centerline Pressure Distributions ( $L_f = 10$ in., $A_e/A_j = 3.5$ , NPR = 27.5).....	114
93.	Effect of 2-D/C-D Nozzle Flap Contour on Axial Performance ( $L_f = 10$ in., $A_e/A_j = 3.5$ ).....	115
94.	Comparison of Separation Due to Different Flap Contours for the 2-D/C-D Nozzle ( $L_f = 10$ in., $A_e/A_j = 3.5$ ).....	116
95.	Effect of 2-D/C-D Nozzle Flap Length on Performance (Straight Flap, $A_e/A_j = 3.5$ ) .....	117
96.	Effect of 2-D/C-D Nozzle Flap Lengths on Centerline Flap Pressure Distributions (Straight Flap, $A_e/A_j = 3.5$ , NPR = 27.5).....	117
97.	Effect of Splitter on Performance of the 2-D/C-D Nozzle (Straight Flap, $L_f = 18$ in., $A_e/A_j = 3.5$ ).....	118
98.	Effect of 2-D/C-D Nozzle Flap Surface Roughness on Peak Performance (Straight Flap, $L_f = 18$ in.) .....	118
99.	Peak Performance of the 2-D Plug Nozzle .....	119
100.	Effect of Plug Contour ( $L_f = 4.958$ , Flap Angle = 0 Degrees).....	120
101.	Effect of 2-D Plug Nozzle Cowl Angle Variations on Performance (5-Degree Isentropic Plug Contour, $L_f = 4.958$ in.) .....	123
102.	Effect of 2-D Plug Nozzle Flap Length and Cowl Angle Variations on Performance (5-Degree Isentropic Plug).....	123
103.	Effect of 2-D Plug Nozzle Flap Length and Cowl Angle Variations on Performance (10-Degree Isentropic Plug).....	124

104.	Effect of 2-D Plug Nozzle Flap Length and Cowl Angle Variations on Performance (15-Degree Isentropic Plug) .....	124
105.	Peak Performance of SERN .....	125
106.	Effect of SERN Ramp Contour on the Performance ( $L_f = 7.379$ in., Flap Angle = 0 Degrees).....	125
107.	Effect of SERN Flap Angle on the Performance ( $L_f = 7.379$ in., 10-Degree Isentropic Ramp) .....	126
108.	Effect of SERN Flap Length on the Performance (Flap Angle = 0 Degrees, 10-Degree Isentropic Ramp) .....	126
109.	Schematic of HSCT with Installed Nacelles .....	136
110.	Schematic of HSCT Heat Test — 13.5 Percent Semispan Model .....	137
111.	Schematic Cutaway of GEAC 2-D Mixer/Ejector Nozzle.....	137
112.	Cross-Sectional Cuts through Mixer Nozzle.....	138
113.	2-D Cross-Sectional Grids .....	138
114.	Crest and Trough Plane Axial Grids .....	139
115.	Upper Surface Streamlines on Boeing Reference H Wing .....	139
116.	Ejector Mode Switch as seen in Isolated HAM Ejector Wall Pressures.....	140
117.	NASTAR Calculated Mode Switch (As Seen in Ejector Surface Static Pressures) .....	140
118.	NASTAR Ejector Flap Temperatures .....	141
119.	Total Temperature Evolution in Ejector Duct.....	141
120.	Shock Parameter Contours in Primary Plane .....	142
121.	Shock Parameter Illustrates Overexpanded Chute Flow .....	142
122.	Shock Parameter Contours in Primary Flow Plane.....	143
123.	Calculated Ejector Wall Static Pressure Convergence History .....	143
124.	Boundary Layer Profile Comparisons.....	144
125.	Profile Development into Ejector Inlet for Uninstalled Case .....	144
126.	Effect of Inlet Boundary Layer Profile on Flow into Ejector .....	145
127.	Computed Effect of Inlet Boundary Layer Profile on Ejector Wall Static Pressure Loading .....	145
128.	Isometric View of Typical Mixer/Ejector Nozzle in Takeoff Mode.....	151
129.	Ejector P&W HSR II Mixer/Ejector Nozzle Thermal Analysis Locations — Nozzle Shown in Supercruise Mode .....	152
130.	Ejector P&W HSR II Mixer/Ejector Nozzle Thermal Design Features .....	152
131.	Ejector Cross-Section for Transition Section, Convergent Flap and Ejector Sidewall by Primary-Nozzle Throat.....	153
132.	Ejector Cross-Section for Forward Divergent Flap/Mixer Chute .....	153
133.	Ejector Transition Section — Bare Metal .....	154
134.	Ejector Transition Section — 0.02-in. Thick Thermal Barrier Coating .....	154

135.	Ejector Transition Section — 0.10-in. Thick Nexel 440 Fiber Insulation .....	155
136.	Ejector Convergent Flap — Bare Metal.....	155
137.	Ejector Convergent Flap — 0.02-in. Thick Thermal Barrier Coating (TBC).....	156
138.	Ejector Convergent Flap — 0.10-in. Thick Nexel 440 Fiber Insulation.....	156
139.	Ejector Forward Divergent Flap — Metal Liner.....	157
140.	Ejector Stowable Mixer — Bare Metal.....	157
141.	Ejector Stowable Mixer — 0.02-in. Thick Thermal Barrier Coating (TBC).....	158
142.	Ejector Stowable Mixer — 0.10-in. Thick Nexel 440 Fiber Insulation.....	158
143.	Ejector Sidewall at Primary Nozzle Throat — Bare Metal.....	159
144.	Ejector Sidewall at Primary Nozzle Throat — 0.02-in. Thick Thermal Barrier Coating (TBC).....	159
145.	Ejector Sidewall at Primary Nozzle Throat — 0.10-in. Thick Nexel 440 Fiber.....	160
146.	Typical Ejector Design with Converging Secondary Nozzle .....	168
147.	Ejector Design with Converging-Diverging Secondary Nozzle .....	168
148.	T-s Diagram for Air With Fanno Lines, Raleigh Lines, and Lines of Constant Pressure for Nozzle Flow with an Exit Mach Number of 1.5 .....	169
149.	Normalized Impulse Function — $\Phi$ Versus Area Ratio ( $A_{\text{exit}}/A^*$ ) for $\gamma = 1.4$ .....	169
150.	T-s Diagram for Air With Lines of Constant Pressure (a Fanno Line for $\beta = 0.569$ and Two Associated Rayleigh Lines that can Yield $\beta = 0.569$ ).....	170
151.	T-s Diagram for Air With Lines of Constant Pressure (a Fanno Line for $\beta = 0.8$ and Two Associated Rayleigh Lines that can Yield $\beta = 0.8$ ).....	170
152.	$P_m/P_{os}$ Versus $M_s$ — $Pr = 3$ ; $Tr = 3$ ; $M_p = 1.0$ , and $A_{\text{exit}}/A_p^* = 3.136$ .....	171
153.	$\Phi$ Versus $M_s$ — $Pr = 3$ ; $Tr = 3$ ; $M_p = 1.0$ , and $A/A_p^* = 3.136$ .....	171
154.	Thrust Augmentation Versus Back Pressure (Subsonic Mixed Flow) or Transition Pressure (Supersonic Mixed Flow) .....	172
155.	Performance Versus $M_p$ Showing the Effect of Removing Chutes .....	172
156.	Flow at the Inlet of an Ejector.....	173



## TABLES

<i>Table</i>		<i>Page</i>
1.	Gen 1.5 Aero Mixing and Performance Model Test – List of All Geometric Variables .....	80
2.	Gen 1.5 Aero Mixing and Performance Tests — High Priority Variables .....	81
3.	HEAT Test Analysis Matrix .....	134
4.	Boundary Layer Profile Effect Study .....	135



## 1. SUMMARY

The objective of this program was to conduct an experimental and analytical evaluation of low noise exhaust nozzles suitable for future High-Speed Civil Transport (HSCT) aircraft. The experimental portion of the program involved parametric subscale performance model tests of mixer/ejector nozzles in the takeoff mode, and high-speed tests of mixer/ejectors converted to two-dimensional convergent-divergent (2-D/C-D), plug, and single expansion ramp nozzles (SERN) in the cruise mode. Mixer/ejector results show measured static thrust coefficients at secondary flow entrainment levels of 70 percent of primary flow. The baseline geometry demonstrated gross thrust performance levels (normalized by the ideal thrust of the primary flow) of approximately 1.04 for secondary pressures near ambient and nozzle pressure ratio (NPR) of 3.5. However, variations in secondary supply pressure showed that thrust coefficients are very sensitive to ejector inlet losses. By using a 16-lobe mixer, this performance could be expected to go as high as 1.055 since the 16-lobe mixer has been shown to provide a thrust benefit of 1.5 percent over the baseline 20-lobe mixer. For the design point of NPR = 3.5 and secondary pressures near ambient, optimum performance was obtained at a mixing duct area ratio (MAR) of 0.90.

Results of the high-speed performance tests showed that relatively long, straight-wall, C-D nozzles could meet supersonic cruise thrust coefficient goal of 0.982; but the plug, ramp, and shorter C-D nozzles required isentropic contours to reach the same level of performance. The isentropic C-D contours provide the highest performance ( $C_{fg} = 0.992$ ) for a 2.5 area ratio. The two-piece C-D nozzle contour performed about 0.002 lower, and the conventional straight flap was 0.007 lower than isentropic. For a zero flap angle and 4.598 flap length, the isentropic 5-degree plug peak thrust coefficient was 0.987, or 1.5 percent higher than the 15-degree wedge, and 0.5 percent higher than the isentropic 10-degree plug. The 5-degree isentropic SERN ramp thrust coefficient was 0.987, or 0.2 percent higher than the 7.5-degree isentropic ramp, and 0.4 percent higher than the 10-degree isentropic ramp. The effects of wall friction, even with simulated acoustic liner roughness, were less than predicted.

Studies included computational fluid dynamics (CFD) analyses and heat transfer analyses of mixer/ejector nozzles, and one-dimensional (1-D) analyses of ejector nozzle thrust augmentation. The CFD study accurately predicted mixer/ejector pressure distributions and shock locations. The calculations closely predicted the pressure ratio at which the experimentally observed *mode switch* occurs (i.e., switching from predominantly subsonic flow in the mixing duct to predominantly supersonic flow). The CFD studies also showed that the shock location in the mixing duct is dependent on the boundary development along the duct wall, hence a larger than normal number of CFD iterations were needed to achieve solution convergence.

Heat transfer studies showed that a combination of insulation and convective cooling was more effective than film cooling for nonafterburning, low-noise nozzles. Duct and flap temperatures of less than 1000°F could be achieved by convective cooling at a rate of 0.5 percent of total engine flow combined with 0.1-in. thick insulation layer.

The thrust augmentation study indicated potential benefits for use of ejector nozzles in the subsonic cruise mode if the ejector inlet contains a sonic throat plane. A 1-D theory for secondary throat ejectors was developed that accounts for the operation of the ejector over a complete range of back pressures.

## 2. INTRODUCTION

### 2.1 BACKGROUND

As global markets and world populations grow, increased air traffic will follow. Studies indicate that there is an opportunity for a second-generation supersonic transport to become an important part of air transportation in the next century. The most desirable routes for a High-Speed Civil Transport (HSCT) are routes covering long distances, predominantly over water. The number of air passengers on these routes is projected to increase by 600,000 per day by 2015.

To service the increase in air traffic, most airlines would have to purchase additional subsonic aircraft or purchase supersonic aircraft, such as the HSCT. The HSCT will have increased range and faster turnaround time than a subsonic transport. For example, a subsonic aircraft travelling from Los Angeles to Tokyo takes 10.3 hours, while the HSCT will only take 4.3 hours. Therefore, the HSCT aircraft could travel from Los Angeles to Tokyo and return in the same day. This faster turnaround time would alleviate the need for additional aircraft and would open up more arrival/departure times at airports.

While the HSCT passenger would arrive at his destination in half the time of a subsonic transport, this would benefit the passenger only if the fare premium was nominal. Otherwise, the passenger would choose the subsonic transport. The challenge is to develop an economically feasible aircraft while meeting stringent noise and emission guidelines.

During Phase I of the NASA/General Electric/Pratt & Whitney (NASA/GE/P&W) HSCT program, noise-suppressing exhaust nozzle technology for a future HSCT aircraft had progressed to a point where small-scale model testing was needed to provide the data base for predicting thrust and flow coefficients. Previous model testing was concentrated on point designs to show the feasibility of using mixer/ejector nozzles to reach acceptable takeoff noise levels. Acoustic tests indicated that the noise reduction goal was achievable. However, very little test data were available on the effects of mixer/ejector variables on internal mixing and performance. One test conducted in November 1992 at NASA Langley showed that relatively small changes in shroud geometry had large effects on thrust coefficients. Exit traverse data were taken on a few configurations, but not enough to determine if mixing was affected in the same manner as the thrust data. While other ejector nozzle data were available in the literature, most of it was for slot-type ejectors rather than the multi-lobe type needed for complete mixing.

To prepare for the HSCT Phase II engine/nozzle demonstration program, an intermediate step designated as the *Generation 1.5 Program* was initiated by the NASA/GE/P&W team. The subject program was developed to provide a database for accurate prediction of mixing and performance over a large range of mixer/ejector nozzle geometries. It also produced a database on the high-speed performance of several different low-noise nozzle concepts. To supplement the experimental data, computation fluid dynamic (CFD) analyses of mixer/ejectors were conducted, and analytical studies of low-noise nozzle cooling and thrust augmentation were accomplished.

The scope of the work reported herein involved two task orders under the NASA-Lewis Large Engine Technology (LET) Program:

- Task 16 — Generation 1.5 HSCT Nozzle Model Concept Definition and Planning Study
- Task 26 — Generation 1.5 HSCT Exhaust Nozzle Program.

In Task 16, input from a NASA/industry HSCT nozzle team was used to develop geometries and test matrices for proposed experimental evaluations of low-noise nozzle performance models. The primary outputs of that task were test plans for static performance tests in both takeoff, low-noise mode, and the high-speed, convergent-divergent (C-D) mode. Task 26 consisted of the following eight subtasks:

- Parametric Mixer/Ejector Nozzle Performance Tests
- Support of Acoustic Tests in GE and Boeing Facilities
- High-Speed Nozzle Model Performance Tests
- CFD Analysis of GE Two-Dimensional (2-D) Mixer/Ejector Exhaust Nozzle
- CFD Analysis of Wing Wake Effect on 2-D Mixer/Ejector Exhaust Nozzle
- Deliveries — Contractor Report
- Thermal Analysis of Mixer/Ejector Nozzle
- High-Speed Mixer/Ejector Nozzle Thrust Augmentation Study.

The purpose of the subject program was to develop an analytical and experimental data base for a class of exhaust nozzles that operated in two modes. The first is characterized by a low-noise, mixer/ejector mode for takeoff and initial climb, and the second is characterized by a 2-D/C-D mode for transonic and supersonic flight. A typical nozzle configuration is shown in Figure 1. In the takeoff mode, it is necessary to reduce the normal exit velocity from about 2400 to 1500 fps to meet the projected HSCT noise goal. To minimize takeoff thrust losses, a large amount of ambient secondary air is ingested and mixed with the primary engine flow. The secondary flow is pumped into the nozzle by expanding the primary flow so that the mixing plane static pressure is below ambient pressure. The mixing process must be completed in a relatively short distance downstream of the mixing plane to avoid excessive nozzle weight. This is accomplished by using multi-lobe mixers with 8 to 10 lobes between side-walls, both above and below the nozzle centerline (16 to 20 lobes total). Therefore, the potential for performance losses in the mixer/ejector system is high because the primary flow is split into multiple channels, overexpanded to induce secondary flow ingesting, and shocked down during the mixing process. Additional losses can occur in the secondary flow depending on the design of the ejector inlet and secondary mixer lobes. These losses were measured in the Subtask A program by conducting parametric performance tests of over 50 different mixer/ejector model configurations under controlled primary and secondary flow test conditions.

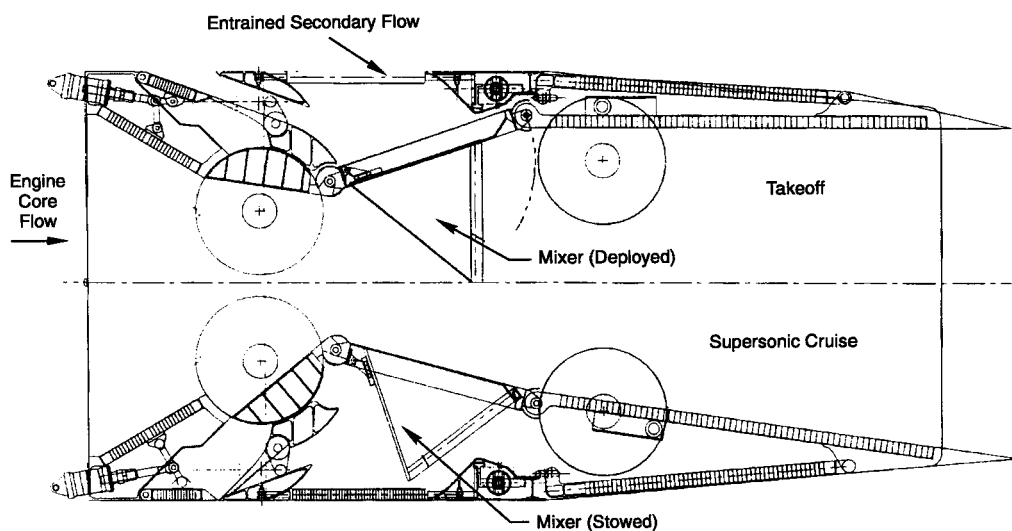


*Figure 1. Typical 2-D/C-D Mixer/Ejector Shown at Takeoff and Supersonic Cruise Positions*

For transonic and supersonic operation, the mixer/ejector concepts are converted to C-D nozzles by shifting the primary throat from the mixer lobes to an inward deployed flap system. Because the C-D flap system makes up the ejector shroud when stowed, the length of the flap system was determined by mixing or by acoustic liner requirements rather than cruise performance. Therefore, the accuracy of existing C-D nozzle performance prediction tools for non-optimum flap geometries was uncertain. Additionally, there was very limited reference data available on 2-D/C-D or plug nozzles at the nozzle pressure ratios of 30 to 40 associated with supersonic climb and cruise. The Subtask C test program was conducted in a NASA altitude facility to measure the thrust coefficients of 2-D/C-D and plug nozzle models of different lengths, contours, and expansion ratios.

In Subtasks D and E, a full Navier-Stokes analysis was conducted on selected 2-D mixer/ejector nozzle geometries with upper and lower ejector chutes aligned or staggered, and with and without simulated wing effects on the upper ejector inlet. Results showed that this type of CFD analysis was a good tool for predicting the effects of ejector geometry on mixing.

Although afterburning is not required in current HSCT engine cycles, gas temperatures as high as 1800°F can occur near the top of climb. A comprehensive thermal analysis of a mixer/ejector nozzle concept was conducted in Subtask G to determine the effects of fan air cooling and thermal protection systems. Results showed that substantial reductions in wall temperatures occurred from a combination of convective cooling and insulation in the convergent section, and insulation only in the divergent section of the nozzle.

The possibility of using the mixer/ejector nozzle to augment thrust in supersonic flight was studied in Subtask H. A one-dimensional (1-D) computer code was developed to analyze the effects of subsonic and supersonic secondary flows on the efficiency of ejector nozzles. Results of the analysis indicate that a significant amount of thrust augmentation is possible at supersonic flight speeds if ejector inlet losses can be minimized. Recommendations were made to conduct wind tunnel testing to verify the analytical thrust augmentation levels.

### 3. MIXER/EJECTOR MODEL TESTS

#### 3.1 BACKGROUND

Subscale model testing was conducted at Boeing's Nozzle Test Facility (NTF) in support of the Generation 1.5 HSCT Nozzle Program to develop a database for mixer/ejector nozzle performance and pumping in the noise suppression operating mode.

Previous testing of mixer/ejector HSCT nozzles included individual nozzles supplied by P&W and GE without any common reference between them. As a result, conclusions were difficult, if not impossible, to determine from the existing database. Thus, it was obvious that a single parametric test was needed to incorporate all of the critical design concerns so that direct comparisons could be made and conclusions drawn.

In support of this effort, various mixer/ejector model designs were provided by P&W and GE in a joint effort to optimize the performance that may be realized in the takeoff mode of operation. The testing was performed at hot-flow conditions with primary flow temperature of 700°F and maximum total pressure of 66 psia. These concepts were tested to measure thrust performance, pumping, and static pressure distributions. In addition, the phenomenon of mode shift was also examined. Mode shift is a condition observed in mixer/ejector nozzles when the flow in the mixing duct transitions from subsonic to supersonic in nature. The occurrence of this condition is usually accompanied by a shift in shroud static pressures. For certain geometries, this shift can be quite drastic, causing a high dynamic load on the shrouds and sidewalls.

The data were used to evaluate the effects of temperature, mixing duct area ratio (MAR), suppressor area ratio (SAR), chute expansion ratio (CER), mixer lobe penetration at the mixing plane (PEN), mixing duct length, mixer length, and the number of mixer lobes (N). Plots and comparisons showing the effects of these variables are included in the body of this report.

Mixer/ejector results showed static thrust augmentation levels of up to 1.05 at secondary flow entrainment levels of 70 percent of primary flow. However, variations in secondary supply pressure showed that thrust coefficients are very sensitive to ejector inlet losses. Of all the variables tested, penetration of the multilobe mixer chutes into the secondary flow had the largest effect. For example, mixers using a penetration of 80 percent produced 10 percent higher thrust coefficients than did those using 100-percent penetration.

#### 3.2 TEST FACILITY DESCRIPTION

Static testing was performed at the Boeing NTF in Seattle, Washington. The test rig, also known as the Large Dual Flow Rig, is shown in Figure 2. Flowrate, pressure, and temperature capabilities of the primary and secondary flows are given. The test cell is ventilated to maintain ambient atmospheric pressure.

The primary and secondary flows are supplied by a common 300 psi source and are both limited to a pressure of 135 psia. The respective maximum flows based on cold flow temperatures are 35 lb<sub>m</sub>/s for the secondary and 25 lb<sub>m</sub>/s for the primary. Both supplies may be independently controlled and are measured using critical flow venturis, which are accurate to +0.25 percent.

The Large Dual Flow Rig is mounted on a three-component strain gage thrust balance to measure axial and side forces up to 3000 lbf and 600 lbf, respectively. The quoted accuracy of the thrust balance is +0.25 percent of full-scale.

A propane burner in the primary stream is capable of providing heated combustion products up to 1200°F.

The data acquisition system incorporates a Hewlett-Packard desktop computer acquisition and control system. Twenty-four channels of analog signal conditioning are available in this 80-channel system, as well as four Scanivalves. Each Scanivalve has 48 pressure ports. Pressures accurate to ±0.25 percent of full-scale may be measured using either 45 or 100 psig transducers. Provisions exist for 160 type K thermocouples.

### 3.3 HARDWARE

Each nozzle assembly consisted of a secondary flow plenum, a transition duct, a two-dimensional (2-D) convergent section, a mixer, a mixing duct comprised of two ejector sidewalls and two ejector shrouds, and shroud brackets. This assembly is shown in Figure 3 and Figure 4. In addition, a charging station duct with total pressure and temperature instrumentation and an adapter duct was supplied to the test facility. The primary choked area ( $A_j$ ) was held constant at 10 in.<sup>2</sup> for all test configurations.

The facility adapter duct served two functions. First, it reduced the flow areas from the facility to the levels required at the model inlet. Second, it added length to the overall model to align the nozzle exit with the Schlieren system. To allow for thermal expansion of the primary duct relative to the secondary duct, a thermal expansion joint was located at the interface between the adapter duct and the charging station. Originally, the model hardware was to be designed for testing at 1000°F. However, due to an error in the design of the thermal expansion joint, 700°F was determined to be the maximum temperature at which this test could be conducted. The transition duct is a circular-to-rectangular transition section designed to reduce the flow area by 10 percent at the 2-D convergent section interface. The 2-D convergence angle was limited to no more than 25 degrees. A secondary plenum was used to establish the secondary flowfield upstream of the mixing plane. The secondary flow inlet to the ejector was bellmouth shaped to minimize pressure losses and was integral with the mixing duct hardware.

Three sets of varying length shrouds and sidewalls were tested to determine the effects of mixing duct length on performance and pumping. Of the three, the mid-length shroud most closely represents the current mixer/ejector nozzle designs.

### 3.4 TEST MATRIX

The test matrix (Figure 5 and Figure 6) was set up to evaluate 16 different mixer designs over a range of suppressor area ratios ( $SAR = A_m/A_j$ ) that were sized to correspond to uncorrected secondary-to-primary flow ratios (entrainment) of 40, 60, 80, and 100 percent. These SARs were based on engine conditions at the design point, a freestream Mach number of 0.32, and an inlet recovery of 95 percent. The matrix of mixers used in this test is shown in Figure 5. Figure 6 summarizes the test configurations and their corresponding mixers. Mixers 1 through 11 represent the parametric portion of the test, while Mixers 12 through 15 are specific geometries of interest for both P&W and GE. Parametric definitions used to describe these configurations are shown in Figure 7 through Figure 9. The mixer designs included variations in lobe penetration, the Mach number of the flow exiting the mixer ( $A_p/A_j$ , or CER variations), the overall length of the mixer ( $L_{mix}/D$ ), and the number of lobes ( $N$ ). Design variations in the ejector include variations in ejector shroud length ( $L_{eject}/D$ ), SAR, and MAR. The test matrix includes all of the configurations that were originally planned for this test. However, as will be explained in the test procedure, not all of these configurations were actually tested. Some were omitted due to hardware problems while others were omitted because of priorities within the allotted test period.

The baseline configuration (using Mixer 3) is defined for  $CER = 1.10$ ,  $SAR = 3.0$ , 20 mixer lobes, and 80-percent penetration. (A mixer base area of 1.0 in.<sup>2</sup> has been assumed for calculating the required mixing plane area.) The penetration for Mixers 1 through 8 is defined at the SAR that provides 80 percent entrainment (uncorrected flow ratio), or  $\omega\sqrt{\tau} = 0.45$ . Mixers 9, 10, and 11 were sized for 80-percent penetration at entrainment levels of 100, 60, and 40 percent, respectively. This corresponds to SAR levels of 3.4, 2.6, and 2.2. Additional SAR variations were achieved for Mixers 3, 6, 10, and 11 by translating the ejector shrouds away from the nozzle centerline. However, when SAR is varied in this manner, the mixer penetration also changes. The mixing duct area ratio ( $MAR = A_g/A_m$ ) was varied by rotating the ejector shrouds while holding the mixing duct inlet area ( $A_m$ ) constant. A baseline MAR of 0.95 was used for all configurations while MARs of 0.8, 0.9, 0.95, and 1.2 were evaluated using Mixers 3 and 8.



As shown in the test matrix (Figure 6), mixers were also evaluated without the mixing duct installed. This is denoted in the matrix as  $SAR = \infty$ . This series of tests was run to determine a baseline performance level for each mixer.

### 3.5 INSTRUMENTATION

Data were recorded both for facility instrumentation and for hardware instrumentation. Facility instrumentation included primary and secondary flows and thrust. Total temperatures and pressures for both the primary and secondary flows were measured at the charging station using the instrumentation designed so that the probes were located on centers of equal area. Thus, a simple mathematical average was used to determine the average temperatures and pressures, yielding area-averaged total conditions.

Hardware instrumentation consisted of static and total pressure taps located in the mixer primary and secondary lobes and in the mixing duct (Figures 10 through 14). Mixer pressure instrumentation (Figures 10 through 12) was used to determine the Mach number of the primary flow as it exited from the mixer to evaluate the primary and secondary flow uniformity, and to measure the secondary flow total pressure at (or near) the mixing plane. By locating pressure taps on the exterior surface of the mixer at the mixer exit, information on the secondary flow Mach number at the mixing plane was achieved. Some mixers contained 20 static pressure taps, while others contained only 14 to reduce instrumentation costs and hardware complexity. Static pressure taps were also located throughout the mixing duct in axial lines centered on both primary and secondary mixer lobes (Figures 13 and 14). To accommodate mixers with both 16 and 20 lobes, different quadrants of the ejector shrouds were instrumented to line up with the different mixers. In this manner, a single set of shrouds was used with all the mixers. Pressure instrumentation on the shrouds started at the bellmouth to provide information regarding the secondary flow entrance Mach number and continued to the end of the shroud and sidewall. A total of 60 static pressure taps were located in this section.

### 3.6 TEST PROCEDURE

Primary nozzle pressure ratios ( $NPR = P_{t_p}/P_a$ ) of 1.2, 2.0, 2.5, 3.0, 3.5, 4.0, and 4.5 were evaluated for most configurations included in this test. At each primary pressure ratio, secondary pressure ratios ( $SNPR = P_{t_s}/P_a$ ) corresponding to cutoff, 0.6, 0.9, 1.0, 1.15, and 1.30 were also tested. (Cutoff is the secondary pressure that results when the secondary flow supply is shut off [ $W_s = 0$ ]). In this manner, a total of 42 data points were recorded for each configuration and temperature tested. These points were collected by setting a constant NPR with the secondary flow shut off (cutoff) and then increasing the secondary flow up to a maximum secondary pressure ratio of 1.3. Then the NPR was increased to its next value and the procedure was repeated. This method of collecting data provided consistent results since the set point was always attained by increasing the pressure of the primary and/or secondary flows. Due to the magnitude of data collected and because the test facility was calibrated for increasing pressures only, hysteresis effects were not examined.

During this portion of the test, it was observed that all the mixers deflected to some extent, causing the flow coefficient ( $Cd_p$ ) to be greater than 1.0 for nearly every mixer. Several mixers deflected enough to cause stress fractures to develop at the lobe exit. As failures were encountered, test points were deleted from the test matrix, and the remaining configurations were reprioritized.

Towards the end of the test, certain mixers were tested with the mixing duct removed ( $SAR = \infty$ ). This series of tests was intended to provide baseline performance data of the mixers and was conducted at primary flow supply temperatures of both ambient (70°F) and 700°F. The secondary flow was turned off for these configurations.

Schlieren video of the exit flow was recorded during testing. Typically, 10 seconds of video were recorded for each data point. To aid in analyzing this data after the completion of the test, the configuration number and supply pressures were recorded on the video.

### 3.7 DISCUSSION OF RESULTS

The purpose of the first part of the test was to determine the effects of temperature on performance, pumping, static pressures, and mode shift so that an appropriate primary flow temperature could be selected for the remainder of the test. Mode shift is a condition observed in mixer/ejector nozzles when the flow in the mixing duct transitions from subsonic to supersonic in nature. The occurrence of this condition is usually accompanied by a shift in shroud static pressures. For certain geometries, this shift can be quite drastic, causing a high dynamic load on the shrouds and sidewalls. The operating point at which this mode shift occurs is referred to as the critical point. To clarify, critical operation is the condition at which the overall flow at some point in the mixing duct behaves as sonic flow even though the secondary flow itself may not be choked. This operational point is defined by the compound compressible flow equations summarized in Reference 1. Any condition above the critical point is defined as supercritical (secondary flow approaches choked) while any below critical is defined as subcritical (secondary flow is unchoked). Since it is usually a good practice to design mixers to operate critically, off-design conditions could realistically include both supercritical and subcritical points. The baseline model (Figure 15) was tested at temperatures of 70, 500, 700, and 1000°F. This data indicated that the performance and pumping are not affected by primary total temperature when the mixer/ejector is operating in the critical or supercritical mode. However, they are affected when operating in the subcritical mode. Therefore, this test should have been conducted at the highest possible temperature of 1000°F to most closely approximate the actual operating conditions, particularly for subcritical modes of operation. However, due to a hardware problem that prohibited testing at 1000°F, the decision was made to limit the test temperature of all subsequent tests to 700°F. It was assumed that this temperature would provide accurate data since the temperature effects between 700°F and 1000°F are small, and since the design point of a mixer/ejector nozzle is normally near the critical point, where the temperature effects are small anyhow. Except where otherwise noted, all subsequent performance, pumping, and pressure data are shown at 700° F.

During testing of the various mixers, it was observed that the nozzle flow coefficient ( $C_{d_p}$ ) was greater than 1.0 and increased with NPR. Initially, it was believed that a leak existed in the primary flow supply. However, closer observation indicated that the problem was not a leak. Rather, the mixers deflected under pressure. The trailing-edge of the mixers was extremely thin (0.015 in.) to minimize the effects of base drag on nozzle performance. This thin trailing edge did not provide the necessary strength, and resulted in mixers that deflected under load. This caused primary choked areas that varied with NPR. Several mixers deflected enough to cause stress fractures to develop at the lobe exit. In every case, the mixers that exhibited failures were either designed for 100-percent penetration (square corners in the lobes) or used convergent chutes. The convergent/divergent mixers with less than 100-percent penetration had additional material thickness at the throat location that provided the necessary strength, and the rounded lobes prevented stress concentrations from developing. As a result, none of these mixers failed. Performance and pumping data have been corrected to account for deflection.

Of primary interest in the test are the effects of SAR, MAR, CER, PEN, mixer length, shroud length, number of lobes, and mixer chute shape on performance, pumping (entrainment), and mode shift. The performance, as discussed in this report, is defined as the measured thrust normalized by the ideal thrust of the primary flow:

$$C_{FG} = \frac{F_{\text{measured}}}{F_{idp}}$$

In this manner,  $C_{FG}$  may be greater than 1.0. The pumping (entrainment) is the temperature-corrected secondary-to-primary flow ratio scaled to a nominal effective primary choked flow area of 10 in<sup>2</sup>.

$$WTF_{LC} = (\omega\sqrt{\tau})_{cor} = \frac{W_{s'}}{W_p'} \sqrt{\frac{T_{ts}}{T_{tp}}}$$

where  $W_p'$  and  $W_{s'}$  are the corrected primary and secondary flow rates as described in Appendix 3-C. This scaled entrainment ratio allows comparisons of data obtained for various configurations by removing the minor shifts that resulted from mixer deflections.

### 3.7.1 Discussion of Performance and Pumping

As mentioned earlier, data from the baseline model (summarized in Figure 15) indicated that performance and pumping are not affected by primary total temperature when the mixer/ejector is operating in the critical or supercritical mode ( $NPR > 3$  at  $SNPR = 1.0$ ). However, performance and pumping are affected when operating in the subcritical mode ( $NPR < 3$ ). In the subcritical mode, primary temperature increases cause the performance to decrease. It is important to note that the baseline configuration, which is similar to the current mixer types and designs being considered for the HSCT program, demonstrated performance levels ( $C_{FG}$ ) at  $T_{tp} = 700^\circ\text{F}$  of approximately 1.040 at the design pressure ratio of 3.5 with secondary total pressure equal to ambient.

Figure 16 and Figure 17 show the effect of SAR on nozzle performance and pumping. In addition, Figure 18 compares the performance with the shrouds and sidewalls removed ( $SAR = \infty$ ). The SAR values shown in Figure 18 are included for reference only, as they have no significance without shrouds and sidewalls ( $SAR = \infty$ ). These figures indicate that, neglecting the secondary flow entrainment (pumping), the best performance is obtained by the mixer used for the lowest SAR (shortest vertical lobes), and the worst performance is obtained by the mixer used for the highest SAR (tallest vertical lobes). However, this trend reverses when entrainment is considered since the increased pumping achieved by the higher SARs produces a thrust improvement that more than offsets the thrust decrement caused by the taller lobes.

Performance and pumping data for MAR variations were collected for two mixer configurations: the baseline mixer (mixer  $L/D = 1.0$ ) and a shortened mixer (mixer  $L/D = 0.6$ ). This data is shown in Figure 19 and Figure 20, respectively. For both mixer lengths, the optimum nozzle performance is achieved for  $MAR = 0.90$  to  $0.95$  at the HSCT nozzle design point ( $NPR = 3.5$ ,  $SNPR = 1.0$ ). The pumping at the design point is only slightly affected by changes in MAR for  $MAR > 0.90$ . However, the lowest MAR (0.80) experiences a degradation in pumping due to the decreased exit/controlling area. Although a MAR of either 0.90 or 0.95 could be used with little difference in thrust,  $MAR = 0.90$  is recommended since it provides the highest thrust while minimizing the tendency and severity of mode shift (see discussion on effects of MAR on static pressures/ mode shift in Section 3.7.2).

The data for the effects of chute expansion ratio ( $CER = A_p/A_j$ ) are shown as a function of NPR for constant SNPR in Figure 21, and as a function of SNPR for constant NPR in Figure 22 and Figure 23. These data were plotted in this manner to aid in understanding the effect that the inlet recovery may have on the selection of the design CER. The CER for optimum performance is directly related to the local pressure ratio ( $P_{tp}/P_s$ ) at the exit of the mixer. For high exit pressure ratios provided by high NPR or by low SNPR, the highest CER of 1.25 would prove to be beneficial. In contrast, low exit pressure ratios provided by low NPR, or by high secondary pressures, may benefit by use of a convergent mixer. However, in the region of operation anticipated for the HSCT nozzle ( $NPR = 2.5$  to  $3.5$  and  $SNPR = 0.9$  to  $1.1$ ), a mixer using an expansion ratio of 1.10 would prove to be most beneficial. For comparison, the effects of CER on mixer-only performance are included in Figure 24.

The effects of penetration on performance and pumping are shown in Figure 25 and Figure 26 for SARs of 3.0 and 3.4, respectively. In addition, the performance of the mixers without the shrouds and sidewalls installed is shown in Figure 27. (The same four mixers are used to provide variations in penetration for both SAR settings.) The penetration values shown in this figure are consistent with those for a SAR of 3.4. They are included for reference only since penetration has no significance without shrouds and sidewalls ( $PEN = 0$ ). In the absence of secondary flow and the mixing duct, the performance is maximized by using shorter mixer lobes (Figure 27). That is, the taller the lobes, the lower the performance. However, Figure 25 and Figure 26 show that the pumping increases with escalating penetration (up to 80 percent). The thrust increase due to the increased secondary flow more than compensates for the thrust loss caused by the taller lobes. The net effect is that the performance increases with rising penetration up to 80 percent. The 100-percent penetration mixer encounters a significant thrust loss, possibly for the following reasons:

1. The 100-percent penetration mixer has no gap in the secondary flowpath near the shrouds where the secondary flow may pass with minimal losses. Rather, all the secondary flow must pass through the secondary lobes where the associated losses are likely to be much higher.
2. The lobe shapes were more square rather than rounded. This squared shape, particularly around the leading-edges of the lobes into both the primary and secondary flow, are likely to result in high losses. This effect could be reduced or eliminated by better shaping of the lobe leading edges.

Two mixer lengths (mixer  $L/D = 0.6$  and  $1.0$ ) were evaluated, with the results shown in Figure 28 and Figure 29. The long mixer performs approximately 1 percent better than the short mixer at the design point, and about the same at higher NPRs (Figure 28). Comparison of the pumping and performance data indicates that the improved performance is the result of improved pumping. Thus, losses in the secondary flow are crucial to the overall nozzle performance. Lengthening the mixer decreases the secondary losses and yields a benefit in pumping and performance.

Three mixing duct lengths (shroud  $L/D = 2.2$ ,  $3.0$ , and  $6.0$ ) were evaluated for the short mixer, with the results shown in Figure 30. As expected, the shortest mixing duct provides the highest performance, at least at  $NPR < 3.25$ . However, at higher NPRs, the three shroud lengths perform approximately the same. The corresponding pumping data reveals that both the mid and long mixing ducts pump at the same level, and that both pump slightly better than the short mixing duct.

The number of mixer lobes employed is an important design consideration since existing acoustic data indicates that more lobes improve mixing effectiveness and reduce noise. However, the performance of the 16-lobe mixer is considerably better (by 1.5 percent at the design point) than that of the 20-lobe mixer (Figure 31). This indicates that the additional mixing provided by the 20-lobe mixer results in a net loss in thrust relative to a 16-lobe mixer. Figure 32 compares the performance of the 16- and 20-lobe mixers without the mixing duct installed.

Mixer lobe (chute) shaping was investigated for the potential benefit in nozzle thrust it may provide. The results of shaping the mixer lobes are shown in Figure 33 and Figure 34. These data indicate that shaping may be used to improve gross performance by as much as 3 percent, although the net benefit in performance is somewhat less in forward flight due to the ram drag of the additional secondary flow. This indicates that, while the effect of lobe shaping on acoustic attenuation may not be determined from this test, lobe shaping may certainly be used to enhance nozzle performance.

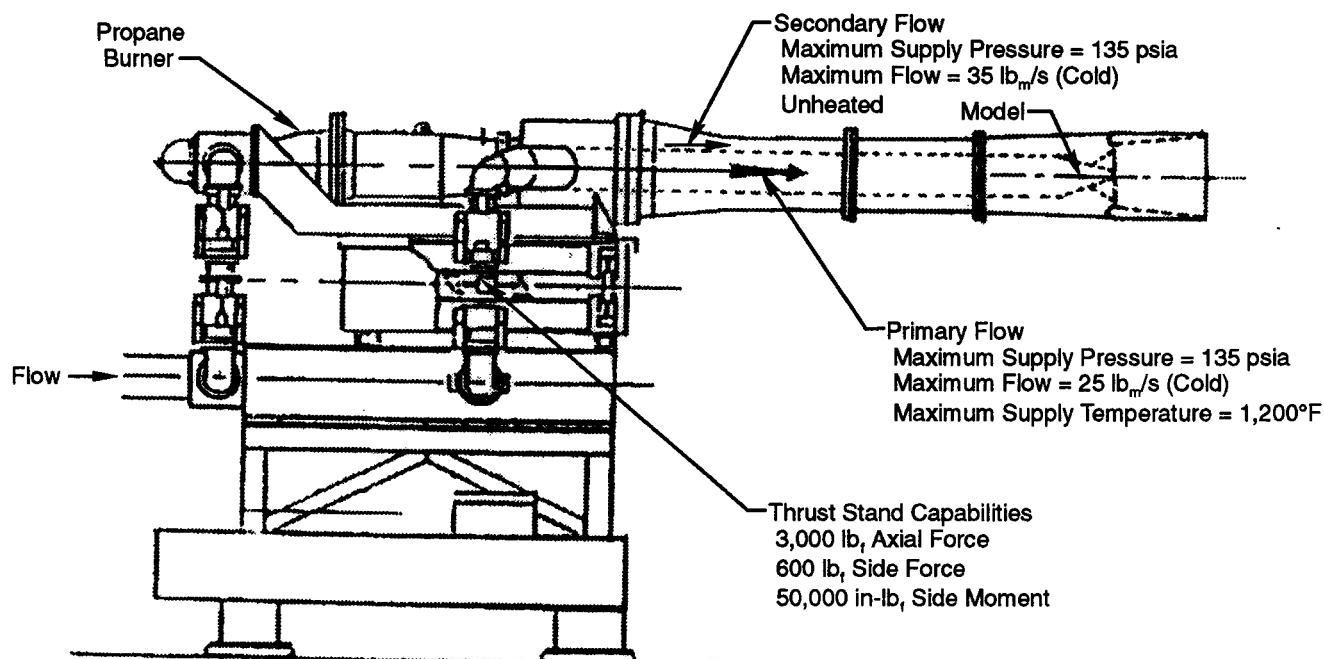
The effects of SNPR on performance and entrainment are shown in Figure 35 through Figure 38 for SARs of 2.2, 2.6, 3.0, and 3.4. These data indicate that at the test condition of  $MAR = 0.95$ ,  $CER = 1.1$ ,  $PEN = 80$  percent, and  $N = 20$ , performance and entrainment increase with increasing SNPR. Thus, performance may be improved by increasing SNPR either by improving the inlet recovery or by pressurizing the secondary flow.

Of interest for future testing of mixer/ejector nozzles is the effect of mixer lobe stiffening pins on the nozzle performance. Mixers 12 and 14 were tested both with and without stiffening pins in the secondary chutes. These mixers were tested at Boeing's NTF without stiffening pins. They were then repaired, pins were installed

(Figure 39), and testing was repeated at Fluidyne's Channel 14 thrust stand. In addition, Mixer 15 was strengthened with pins prior to its initial testing at Fluidyne. The results of these tests for Mixer 12 are shown in Figure 40. As can be seen, pins located in the secondary chutes contribute to a 3 percent loss in  $C_{FG}$  at NPR = 3.5 and an associated decrease in entrainment.

For comparison, Figure 41 is included to show the agreement in the data obtained by Boeing's NTF and Fluidyne's Channel 14 for the baseline model. The close agreement between these facilities, particularly at low temperature-corrected entrainment (high NPR) provides confidence in the data obtained by either of the facilities.

Flow coefficient data (obtained at Fluidyne's Channel 14 thrust stand) for Mixers 12, 14, and 15 are shown in Figure 42. Mixer 12 is a 100-percent penetration mixer with CER = 1.1 and no center gap, while Mixers 14 and 15 are 88-percent penetration mixers with CER = 1.0. These mixers were selected for demonstrating typical flow coefficients since they were all repaired with stiffening pins located in the secondary lobes. These pins added stiffness sufficient to prevent mixer deflections under load, and therefore yielded flow coefficients that did not change appreciably with increasing NPR. All flow coefficient data is based on a physical throat area of 10 in<sup>2</sup>. Since this area could not be determined directly from measurements, the actual levels are somewhat uncertain. However, data shows that mixers with squared lobes and no center gap will most likely exhibit low flow coefficients, while well-designed mixers could yield flow coefficients as high as 0.98.



73191.cdr

Figure 2. Boeing Nozzle Test Facility

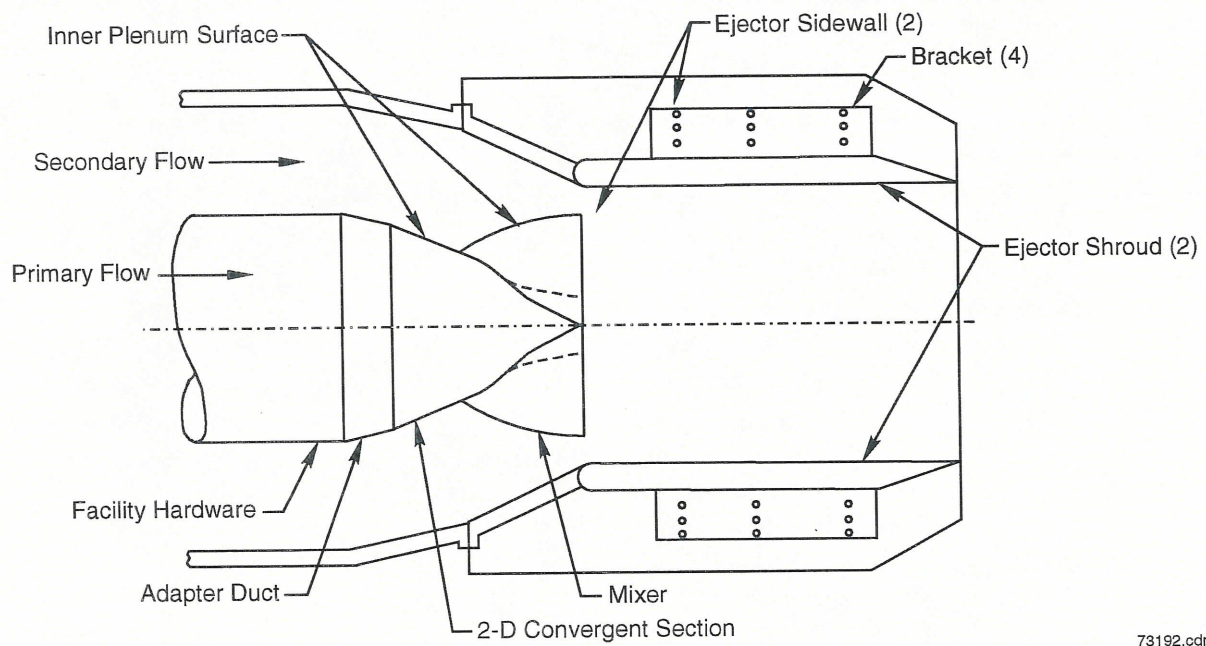


Figure 3. Nozzle Assembly

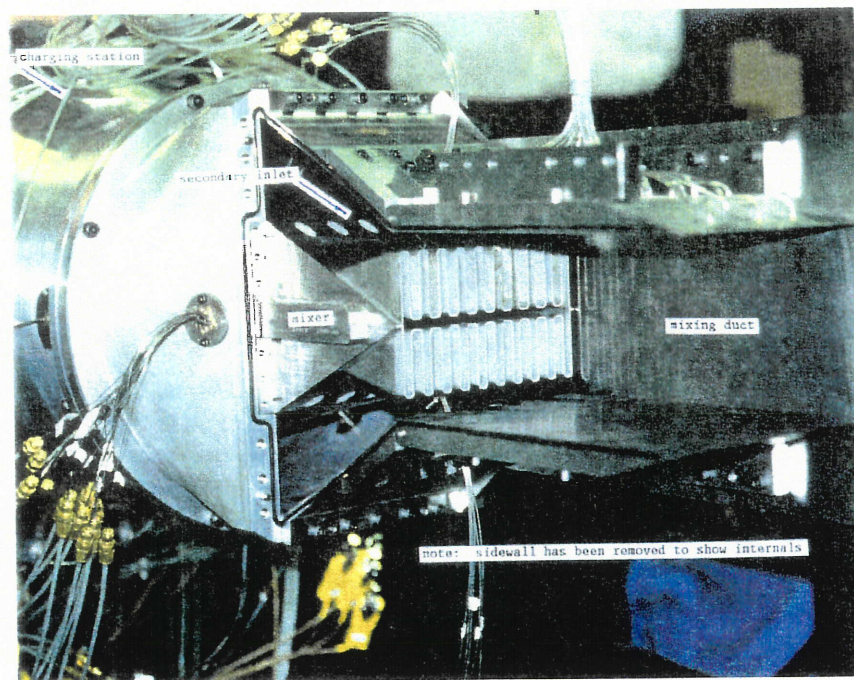


Figure 4. Nozzle Installation

LP Preparation %	Mixer L/D	Lobe Count	Mixer Summary												
			SAR CER	2.2 1.00	2.6 1.00	3.0 1.00	3.4 1.00	2.2 1.10	2.6 1.10	3.0 1.10	3.4 1.10	2.2 1.25	2.6 1.25	3.0 1.25	3.4 1.25
60	1.0	20				2				1					
80	1.0	20								3				4	
100	1.0	20								5					
80	1.0	16								6				7	
80	0.6	20								8					
80	1.0	20									9				
80	1.0	20						11	10						
80	1.0	20													
P&W Mixer Concept						13 14 15									
100	0.6	20								12					
GE Mixer Concepts															
80	1.0	20													
88	0.6	20													
88	0.6	20													

73193.cdr

Figure 5. HSCT Generation 1.5 Mixer Summary



Mixer No.	Mid-Length Shroud																Short Shroud			Long
	Shroud L/D																2.20			6.00
	3.00																			
	SAR CER	∞ 1.00	2.2 1.00	2.6 1.00	3.0 1.00	3.4 1.00	∞ 1.10	2.2 1.10	2.6 1.10	3.0 1.10	3.4 1.10	∞ 1.25	2.2 1.25	2.6 1.25	3.0 1.25	3.4 1.25	3.0 1.00	3.0 1.10	3.0 1.25	3.0 1.10
	MAR = 0.95																			
1																				
2																				
3																				
4																				
5																				
6																				
7																				
8																				
9																				
10																				
11																				
12																				
13																				
14																				
15																				
16																				
	MAR = 0.80																			
1																				
3																				
5																				
8																				
	MAR = 0.90																			
1																				
3																				
5																				
8																				
	MAR = 1.20																			
1																				
3																				
5																				
8																				

Note: Configurations in bold text denote those actually tested

73194.cdr

Figure 6. HSCT Generation 1.5 Test Matrix



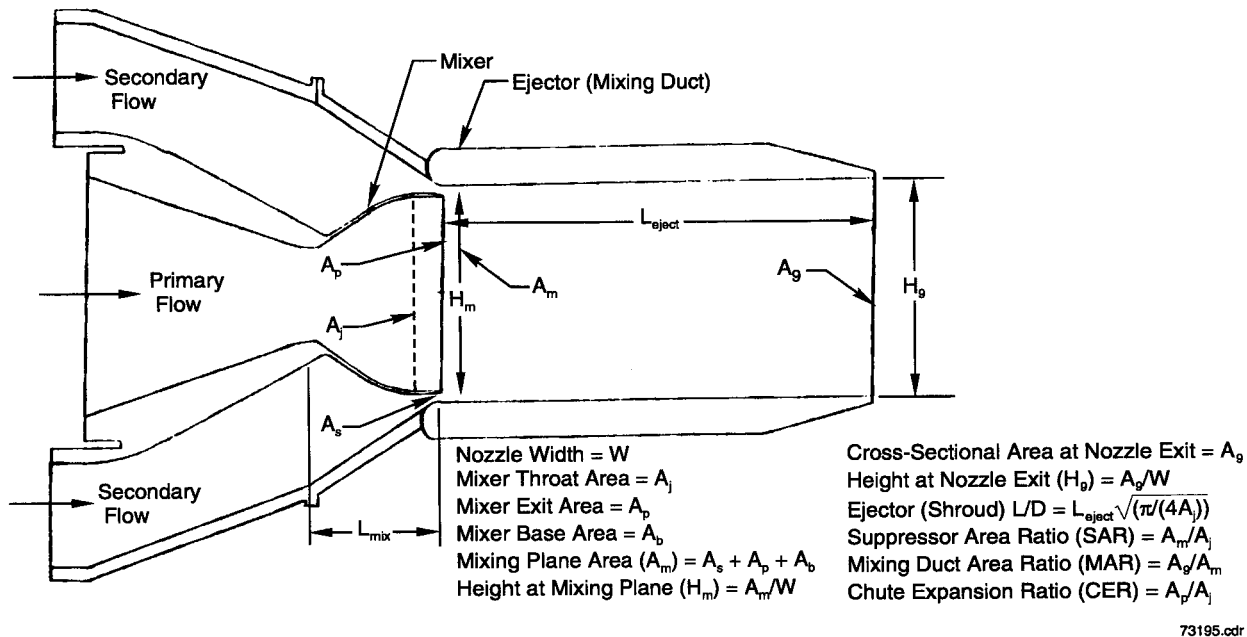


Figure 7. Mixer/Ejector Rig for Generation 1.5 Performance Tests

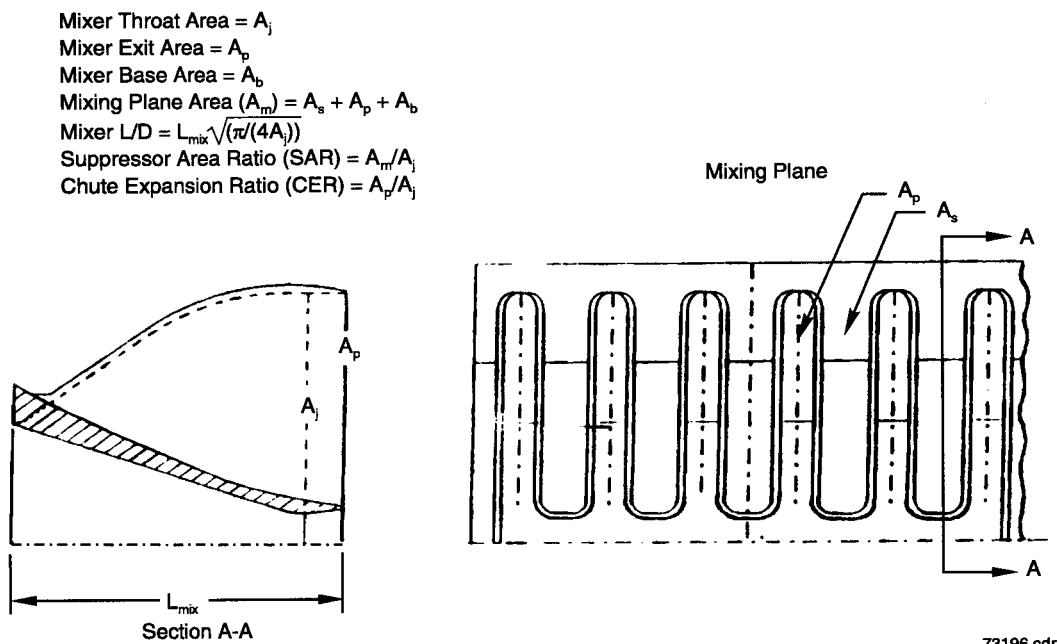
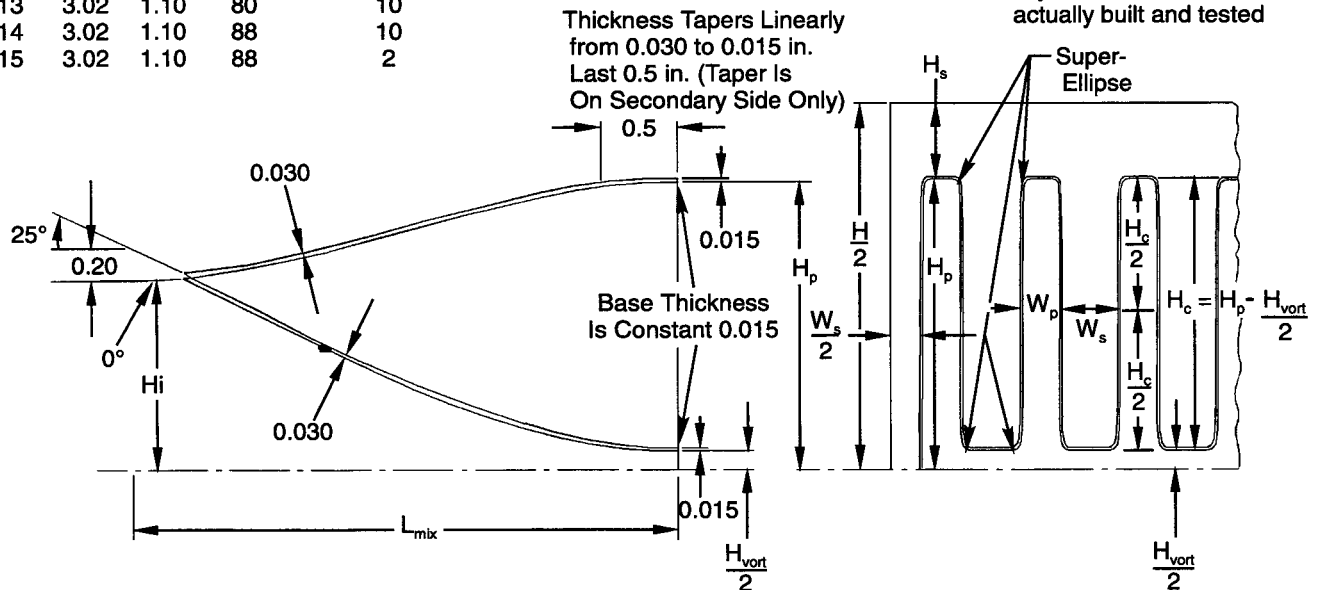


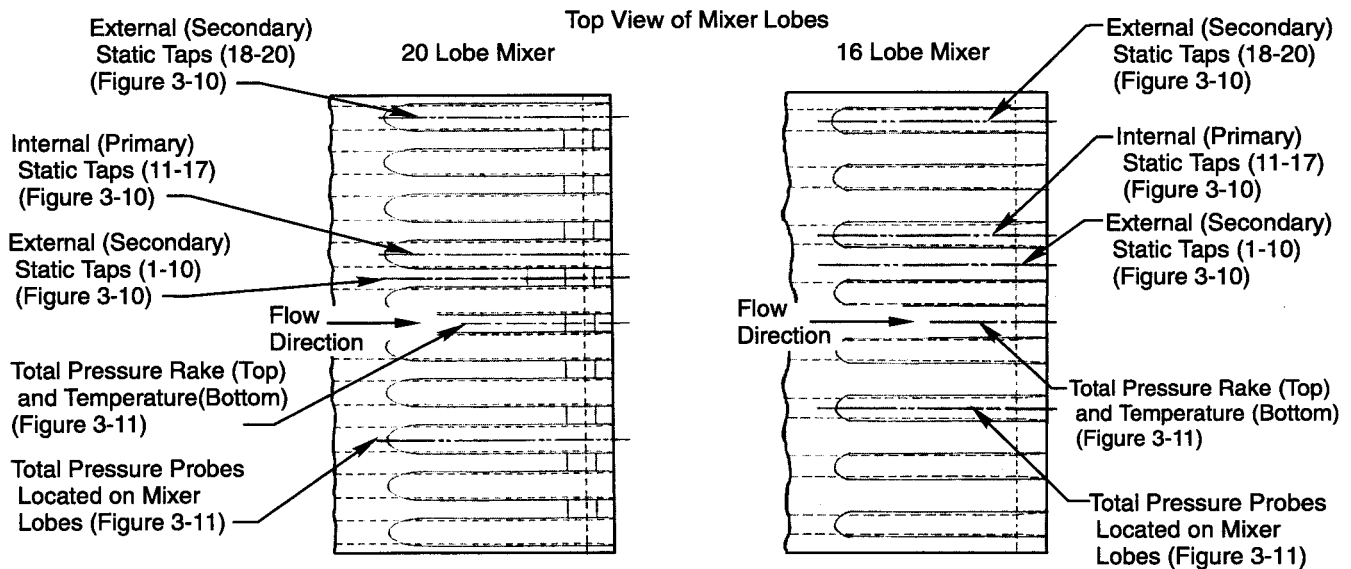
Figure 8. Mixer for Generation 1.5 Performance Tests

Mixer	SAR	CER	PEN (%)	Exit Super-Ellipse Coefficient
13	3.02	1.10	80	10
14	3.02	1.10	88	10
15	3.02	1.10	88	2



73197.cdr

Figure 9. Geometric Definition for Aerodynamically Shaped Mixers



73198.cdr

Figure 10. Mixer Instrumentation Locations

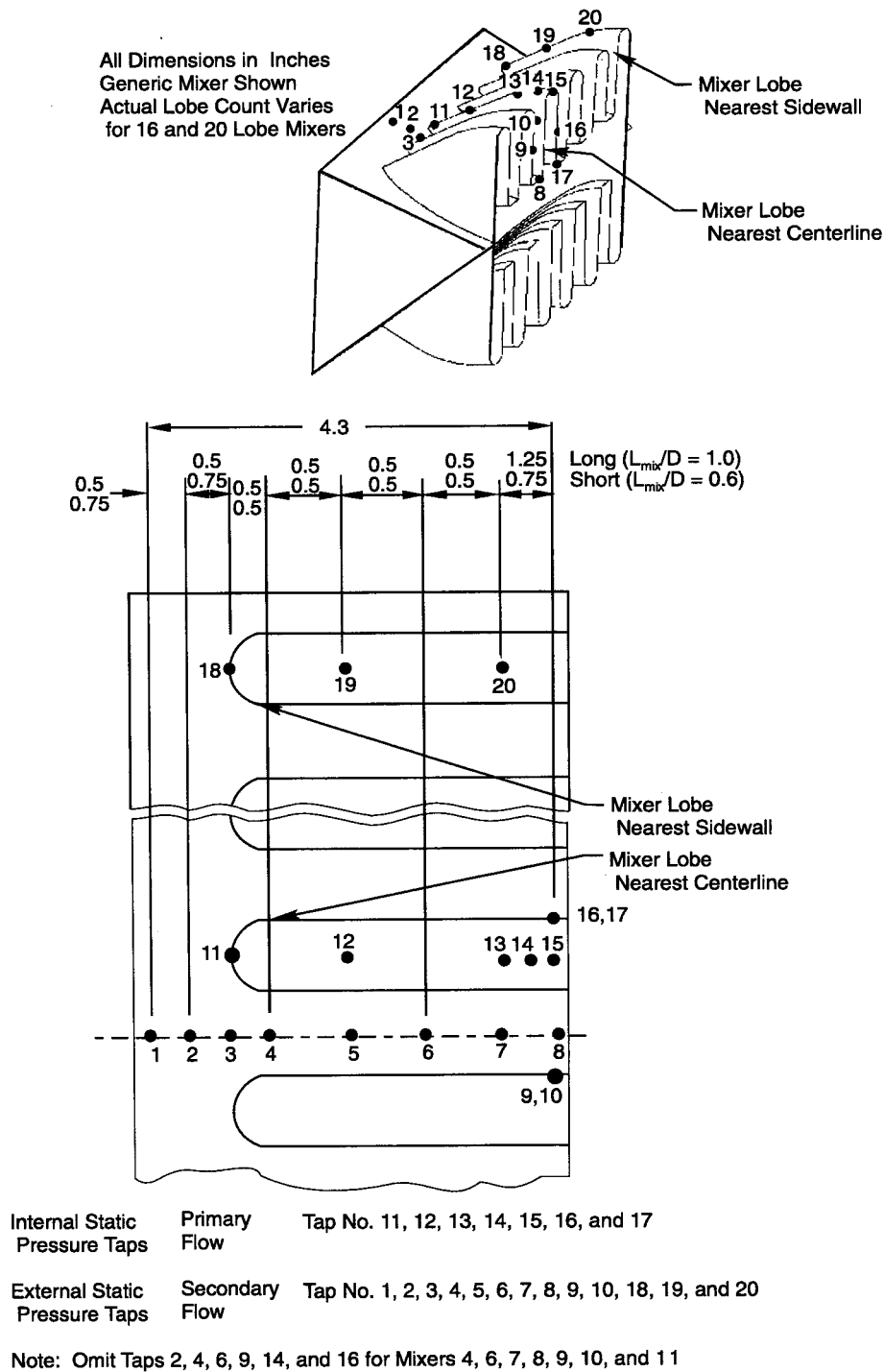
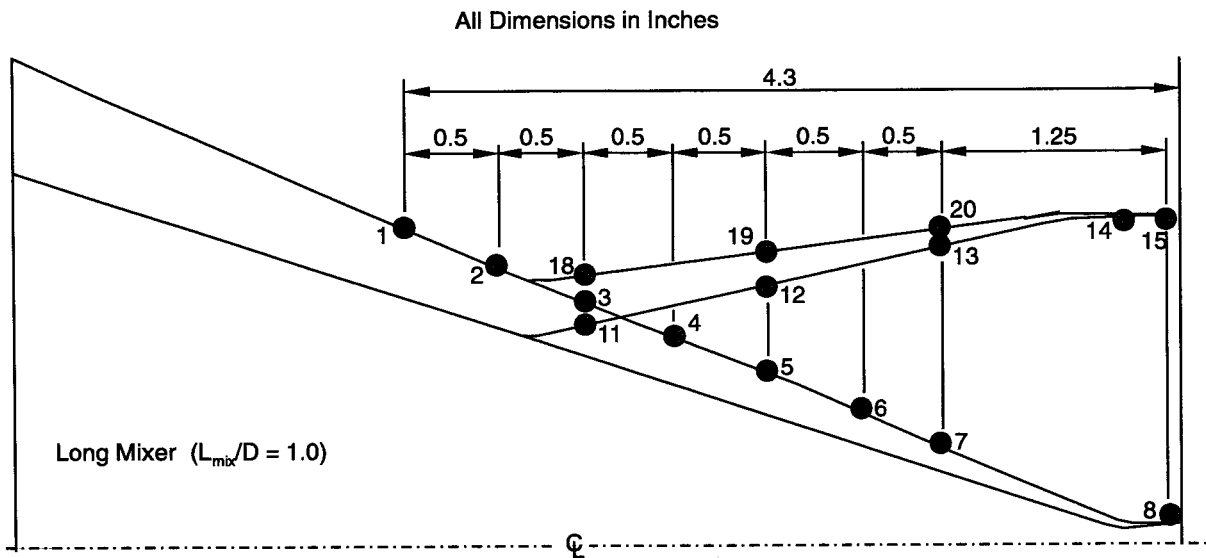
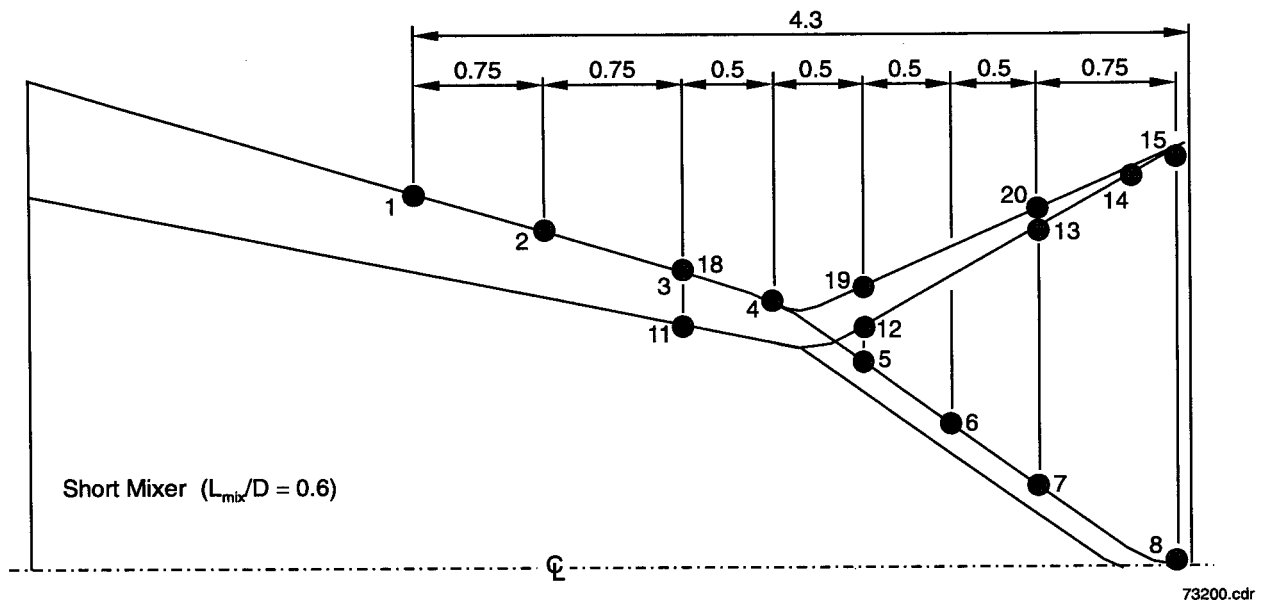


Figure 11. Mixer Instrumentation — Static Pressure Taps  
a) Relative Position of Static Pressures Shown on Mixers



Note: Omit Taps 2, 4, 6, 9, 14, and 16 for Mixers No. 4, 6, 7, 8, 9, 10, and 11



*Figure 11 (Concluded). Mixer Instrumentation — Static Pressure Taps  
b) Static Pressure Positions Shown on Mixer Cutaway View*

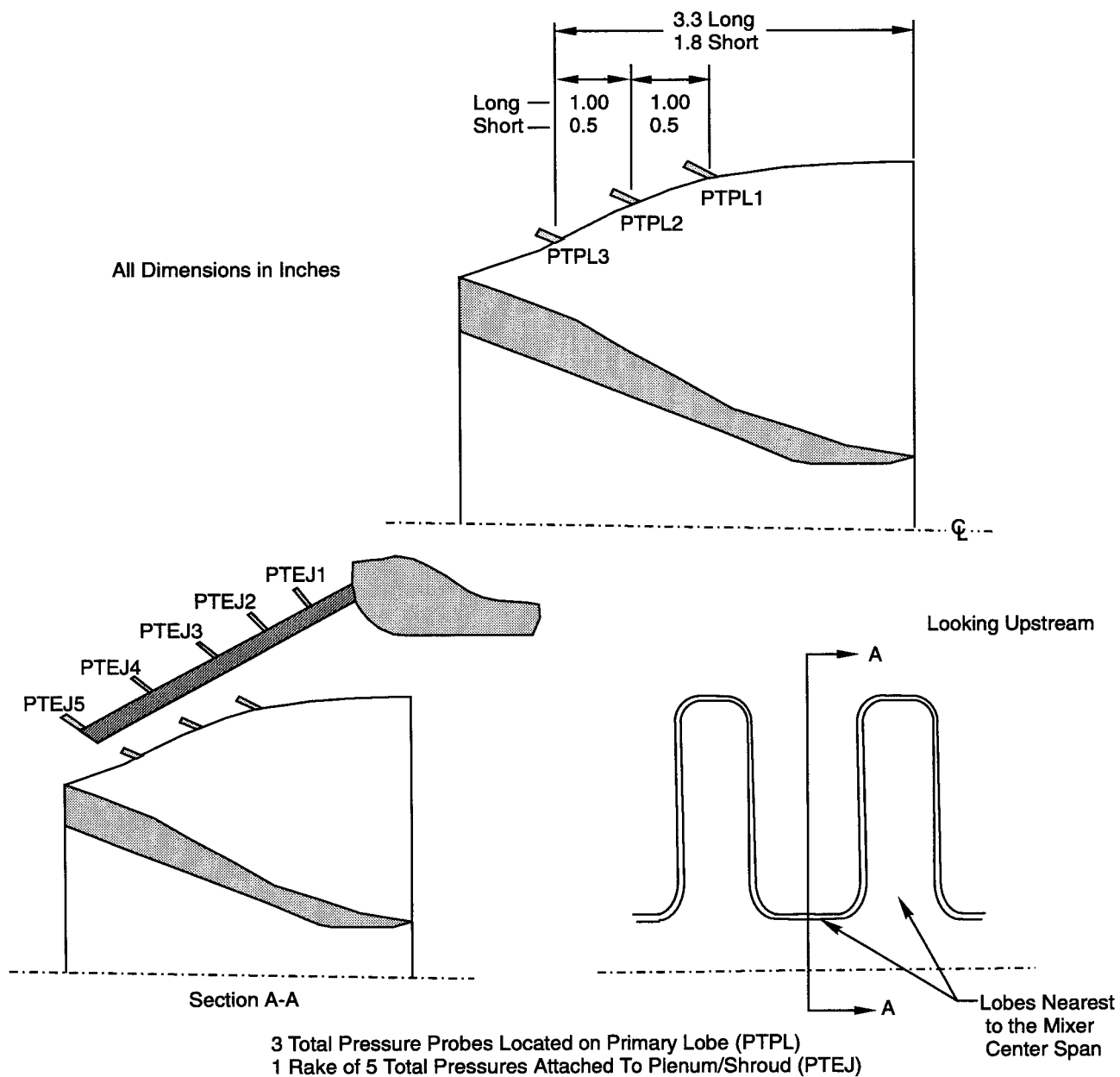


Figure 12. Mixer Total Pressure Probe Locations

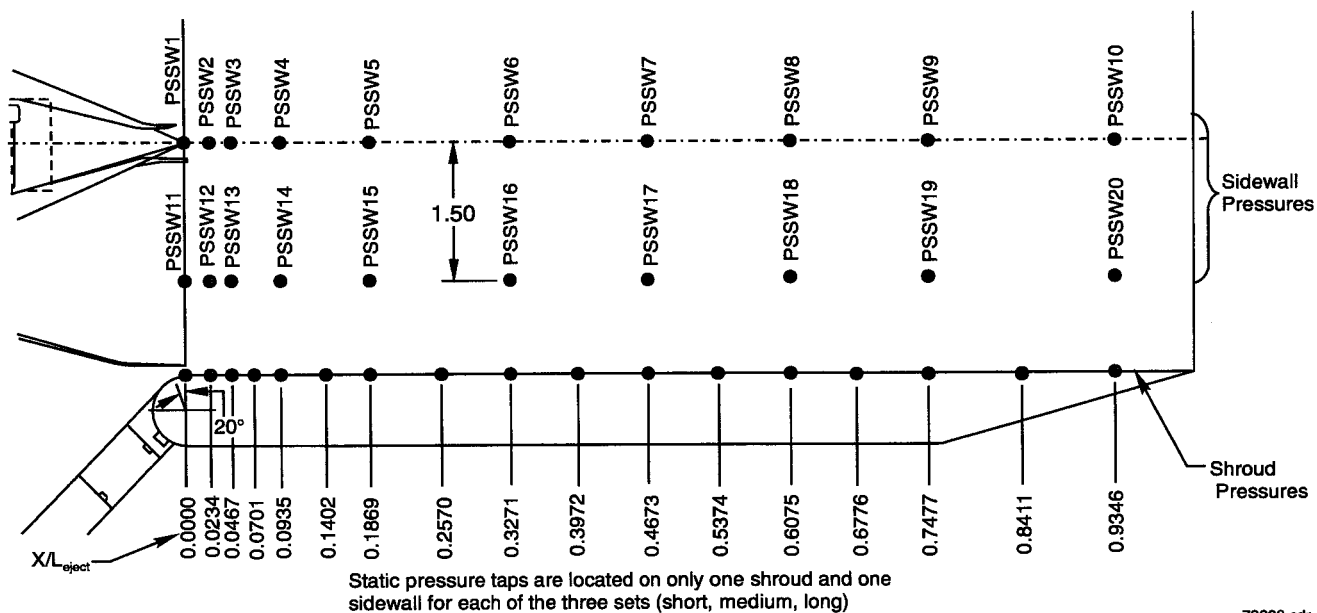


Figure 13. Ejector Shroud and Sidewall Static Pressure Taps

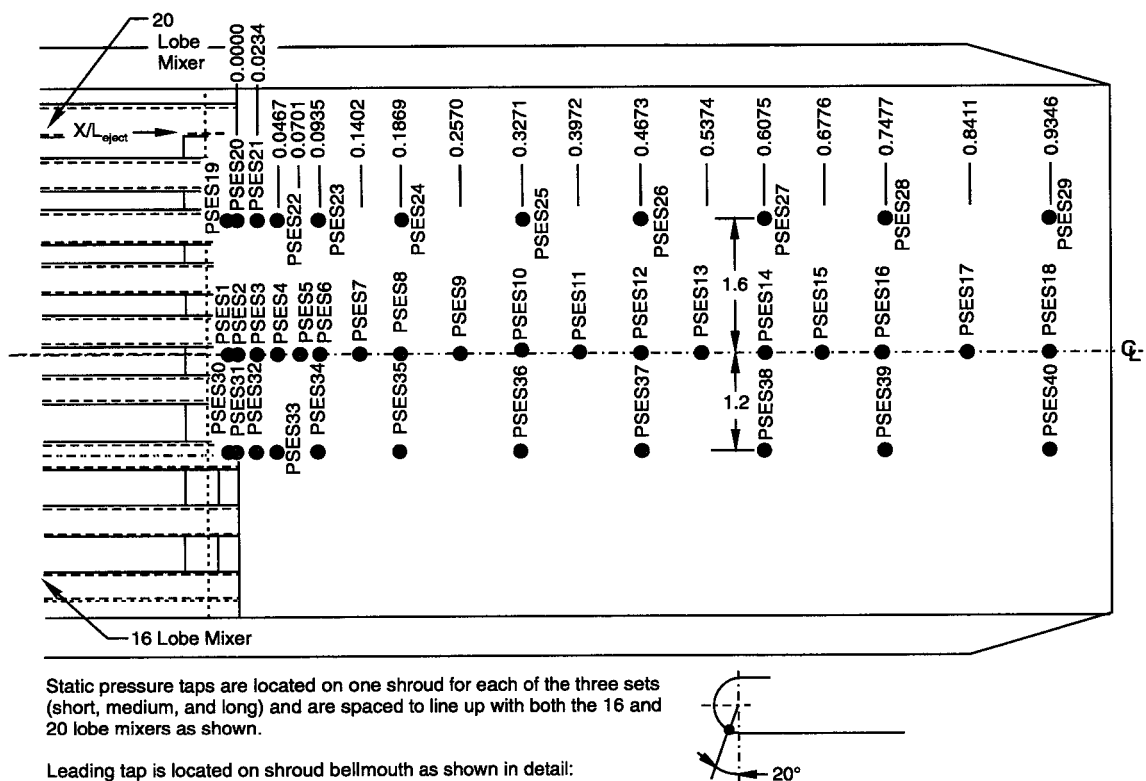
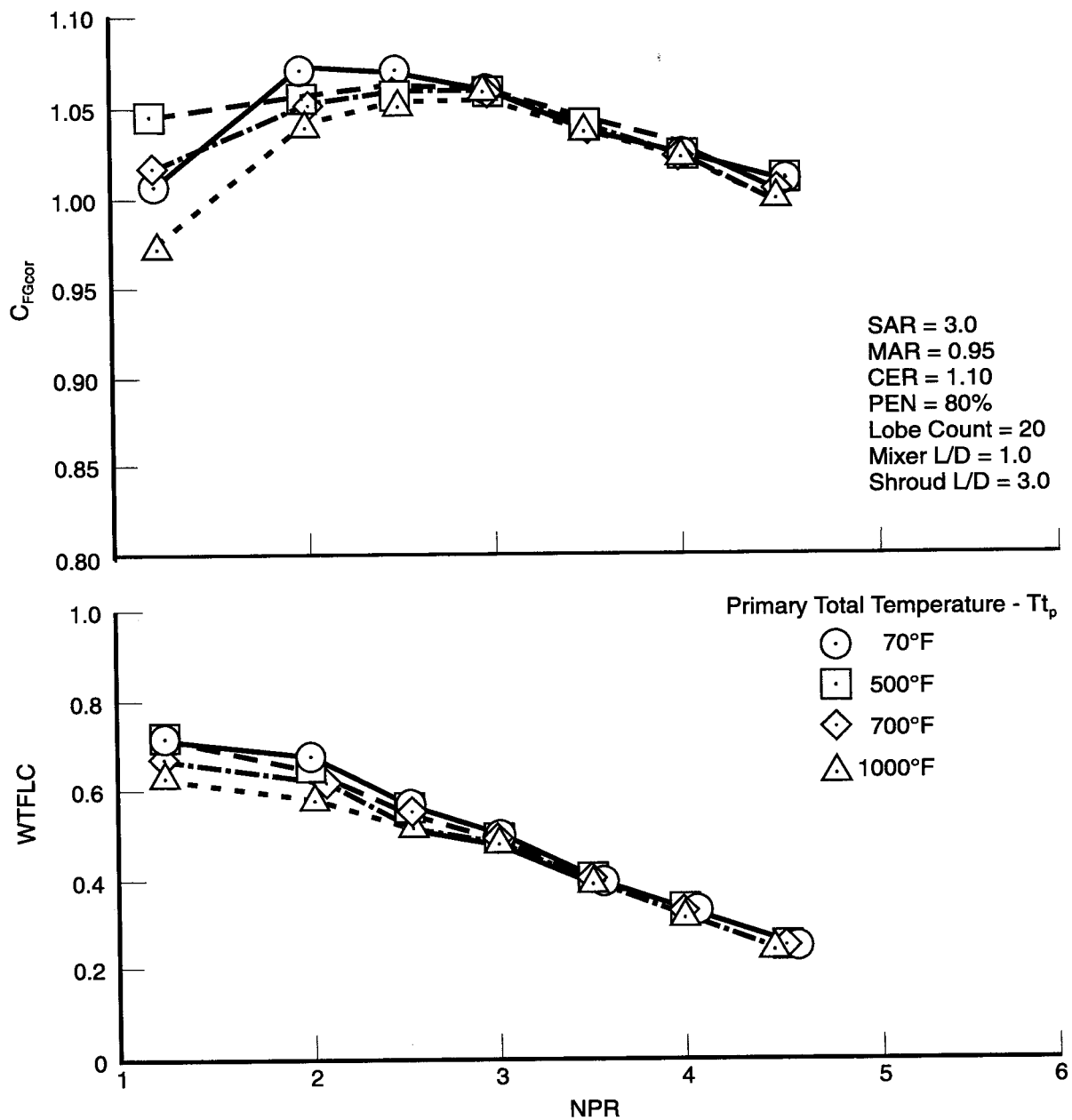
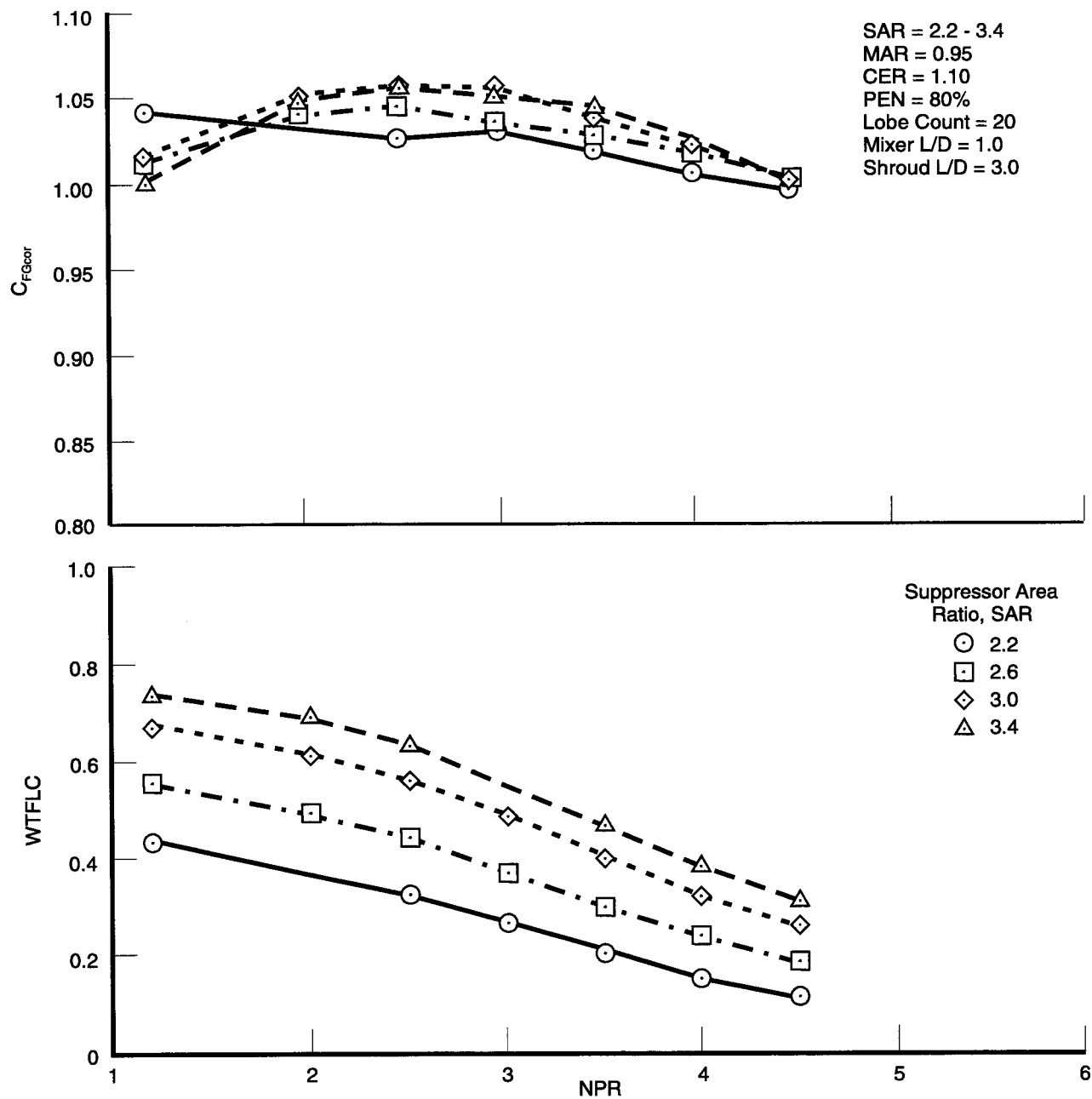


Figure 14. Ejector Shroud Static Pressure Taps



73205.cdr

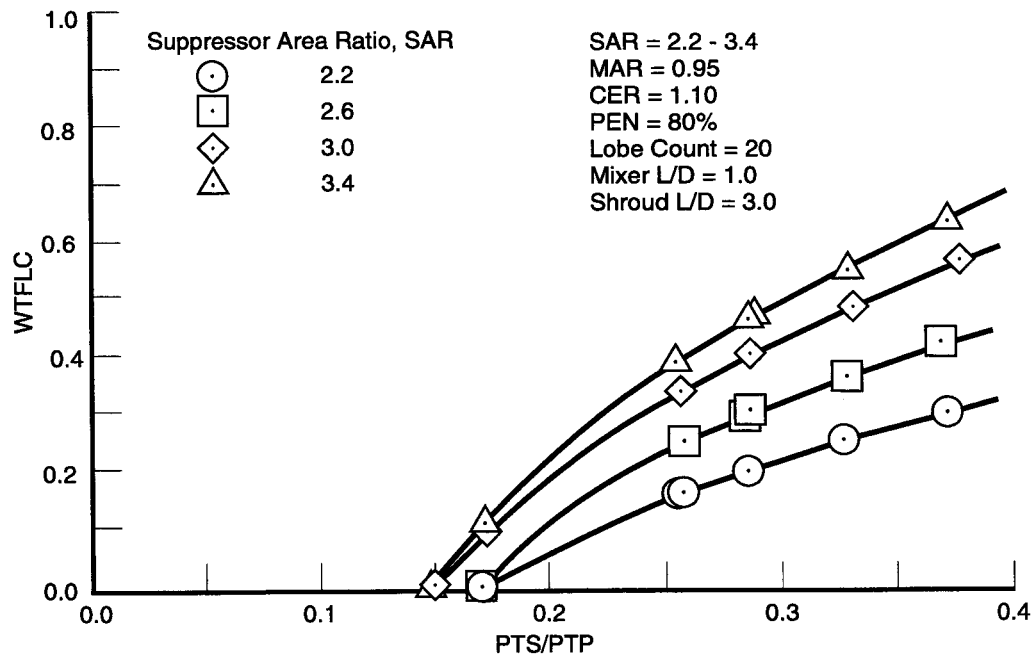
*Figure 15. Comparison of Corrected Performance and Entrainment Effects of Primary Total Temperature at SNPR = 1.0 for Baseline Configuration*



73206.cdr

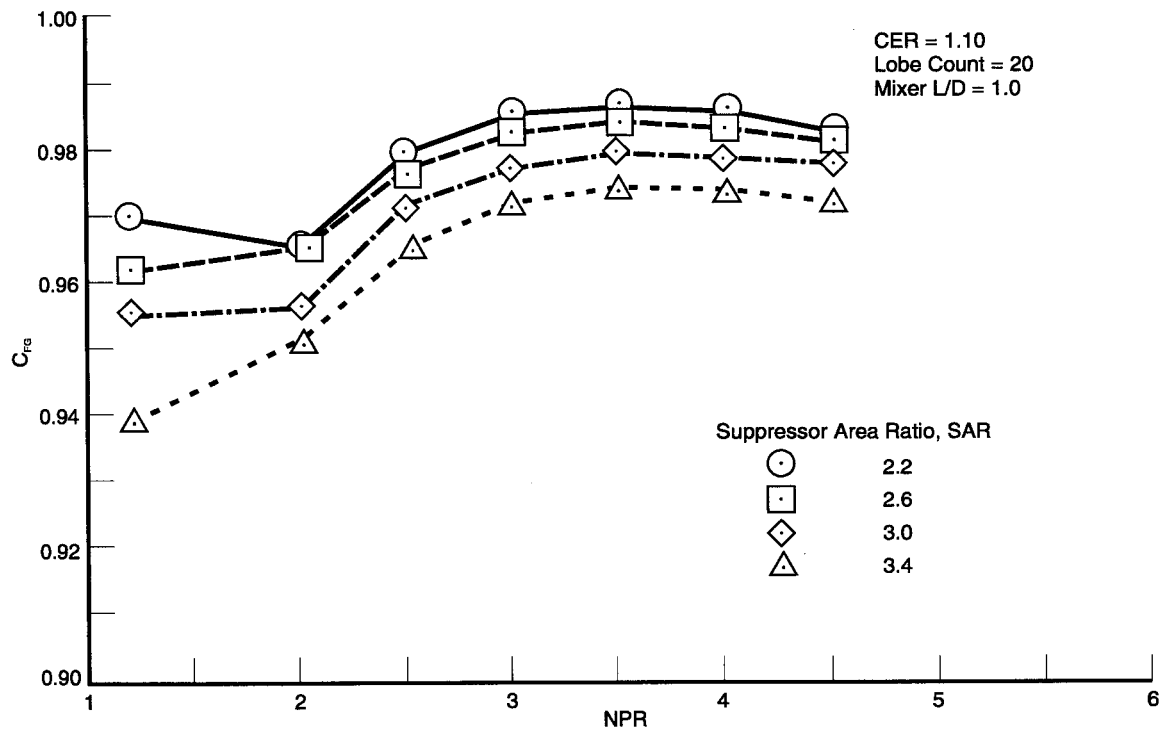
Figure 16. Comparison of Corrected Performance and Entrainment  
 Effects of SAR at SNPR = 1.0 and  $T_{tp} = 700^{\circ}F$





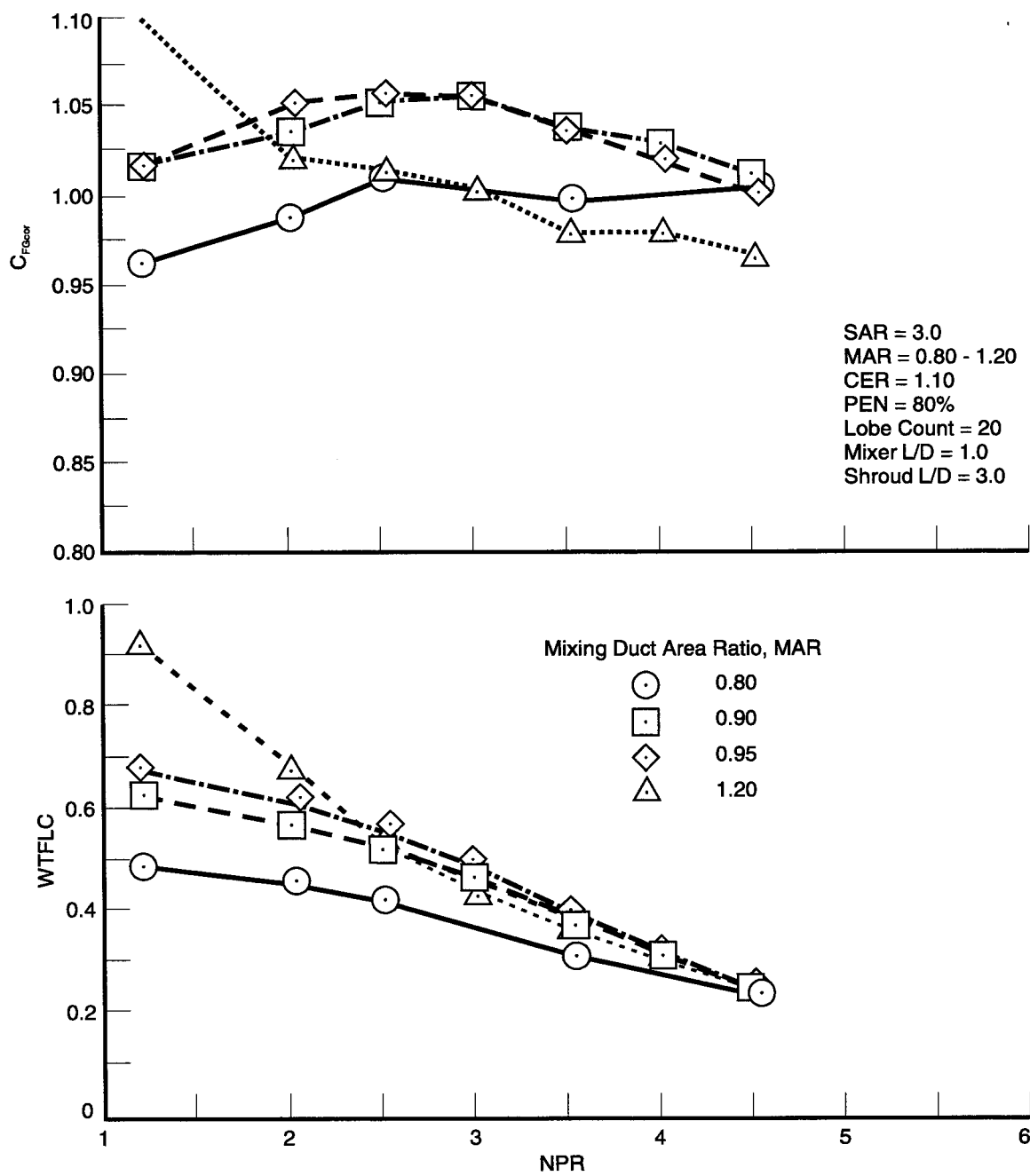
73207.cdr

Figure 17. Comparison of Corrected Entrainment  
Effects of SAR at NPR = 3.5 and  $T_{tp} = 700^{\circ}\text{F}$



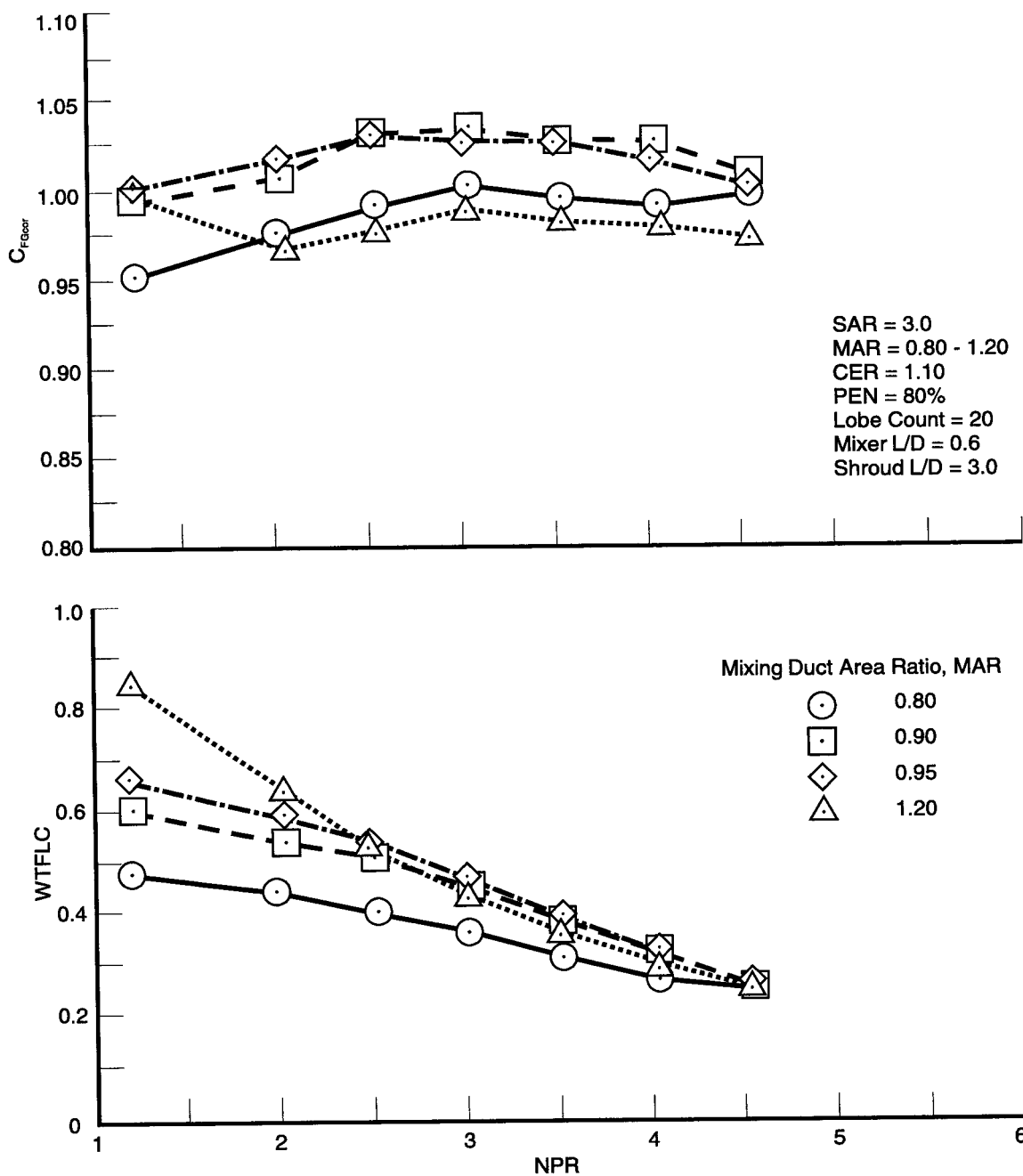
73208.cdr

Figure 18. Mixer-Only Nozzle Performance  
Effects of Mixer Lobe Height (SAR),  $T_{tp} = 700^{\circ}\text{F}$



73209.cdr

Figure 19. Comparison of Corrected Performance and Entrainment Effects of MAR at SNPR = 1.0, Mixer L/D = 1.0, and  $T_{tp} = 700^{\circ}F$



73210.cdr

Figure 20. Comparison of Corrected Performance and Entrainment  
Effects of MAR at SNPR = 1.0, Mixer L/D = 0.6 and  $T_{tp} = 700^{\circ}F$

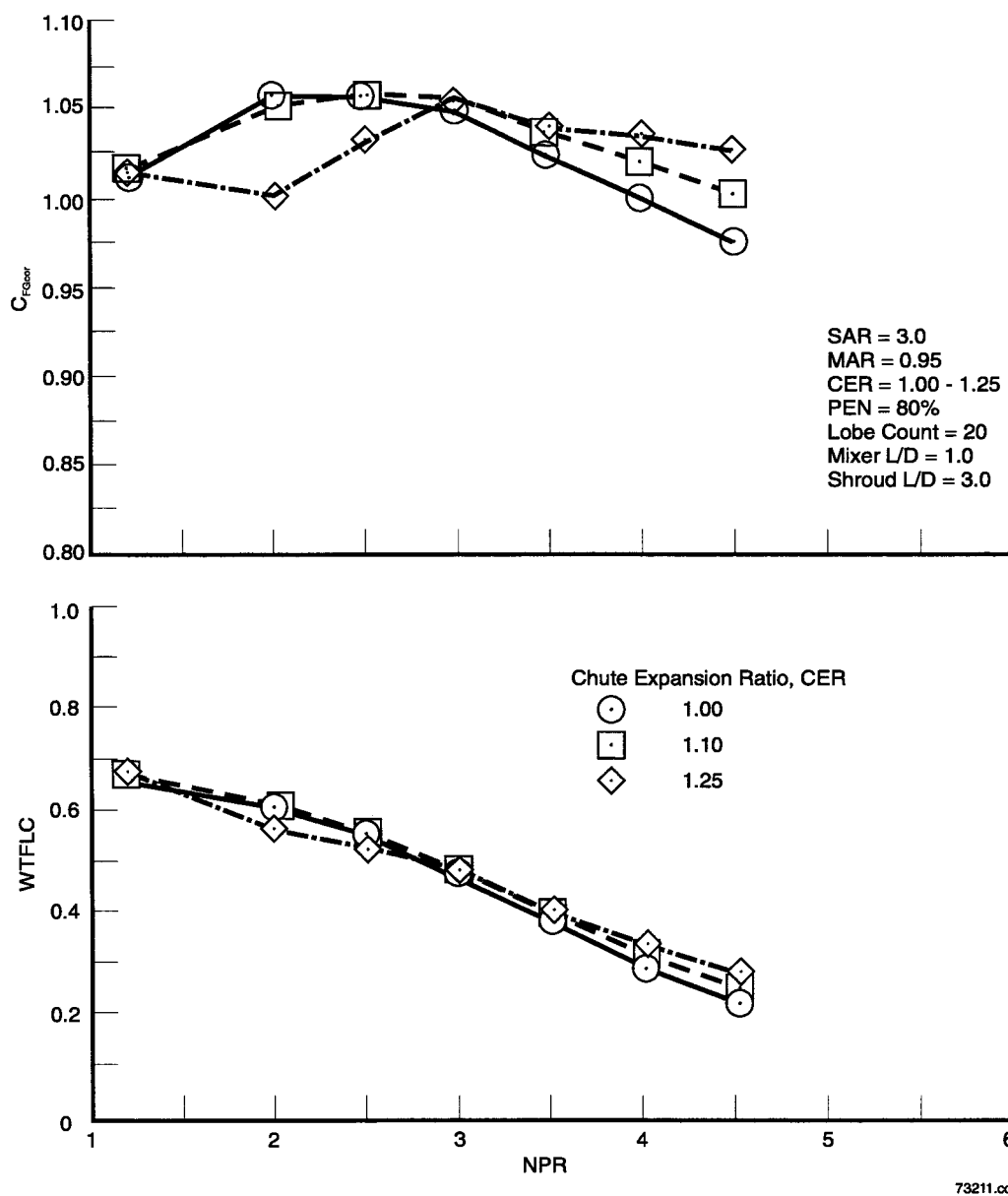


Figure 21. Comparison of Corrected Performance and Entrainment Effects of CER at SNPR = 1.0 and  $Tt_p = 700^\circ\text{F}$

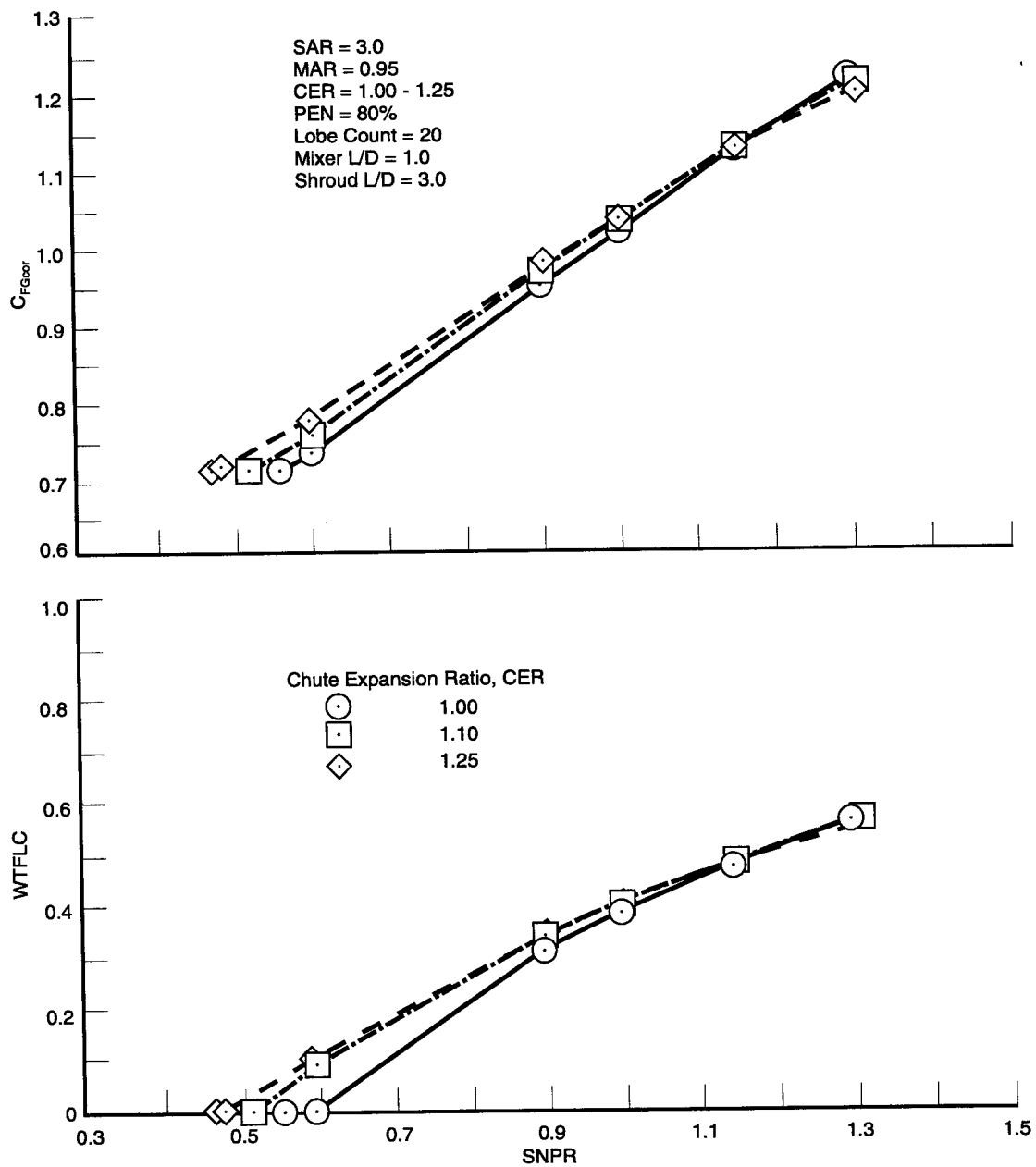


Figure 22. Comparison of Corrected Performance and Entrainment Effects of CER at NPR = 3.5 and  $T_t = 700^\circ\text{F}$

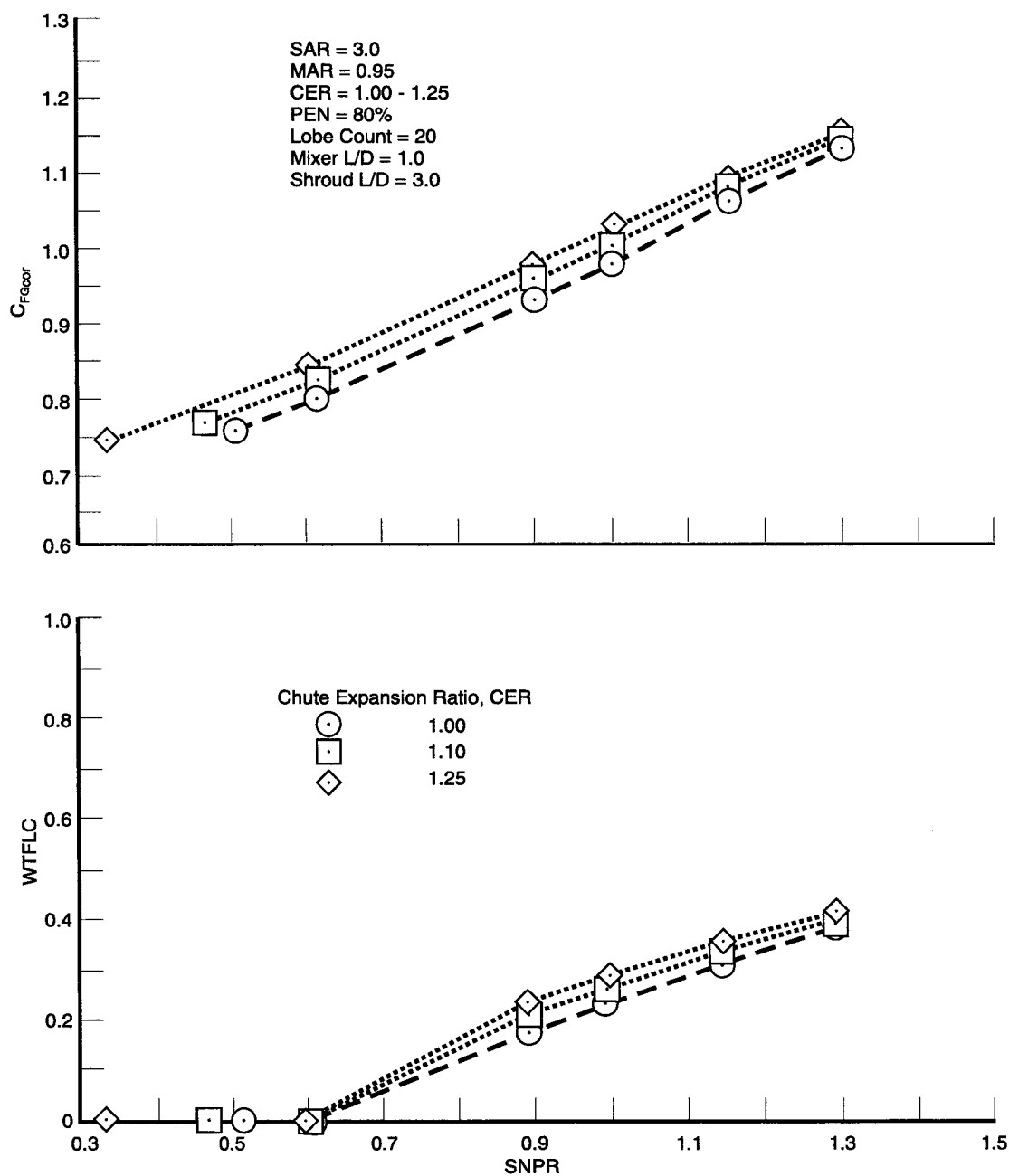
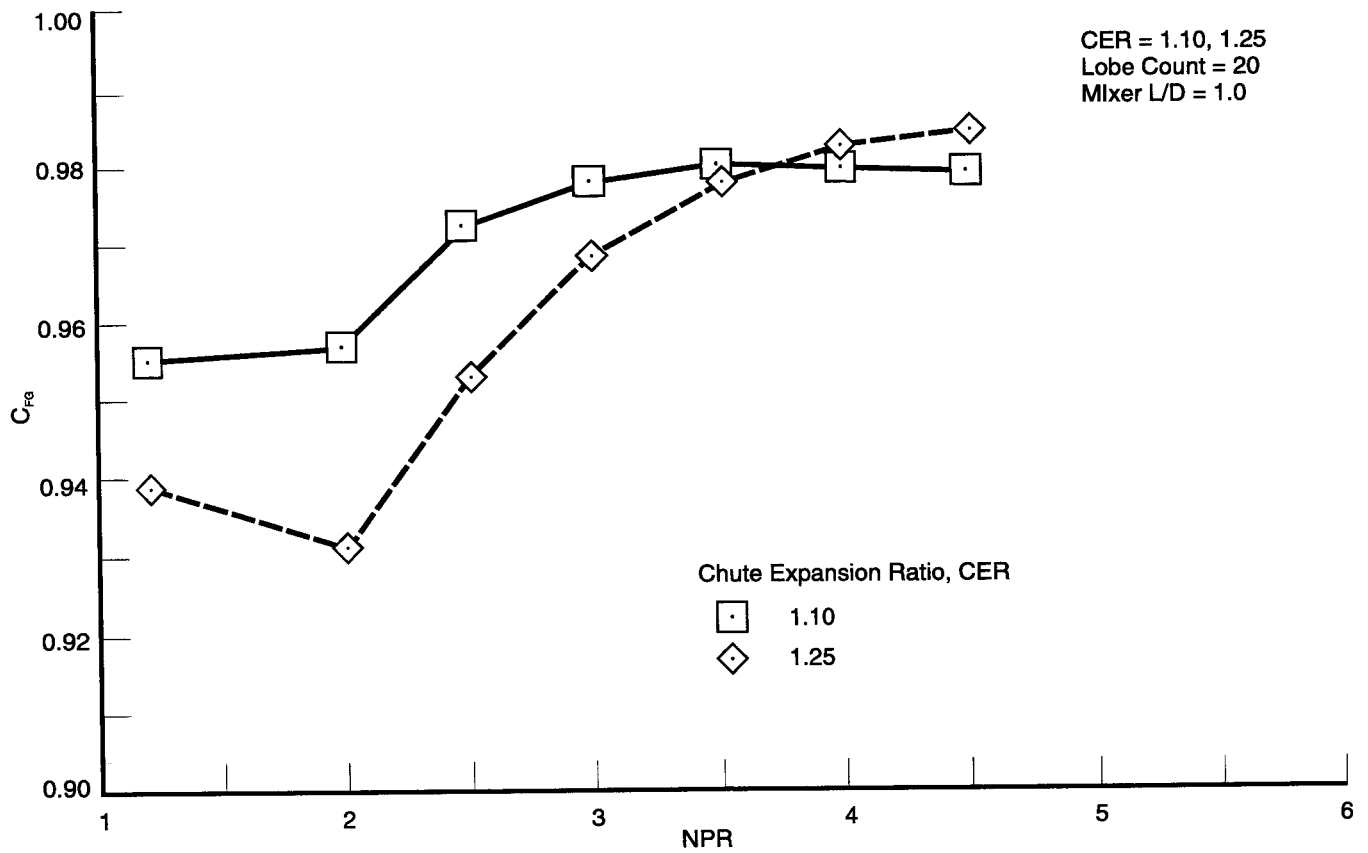


Figure 23. Comparison of Corrected Performance and Entrainment Effects of CER at NPR = 4.5 and  $T_{tp} = 700^{\circ}F$



73214.cdr

*Figure 24. Mixer-Only Nozzle Performance  
 Effects of CER at  $T_{tp} = 700^{\circ}\text{F}$*

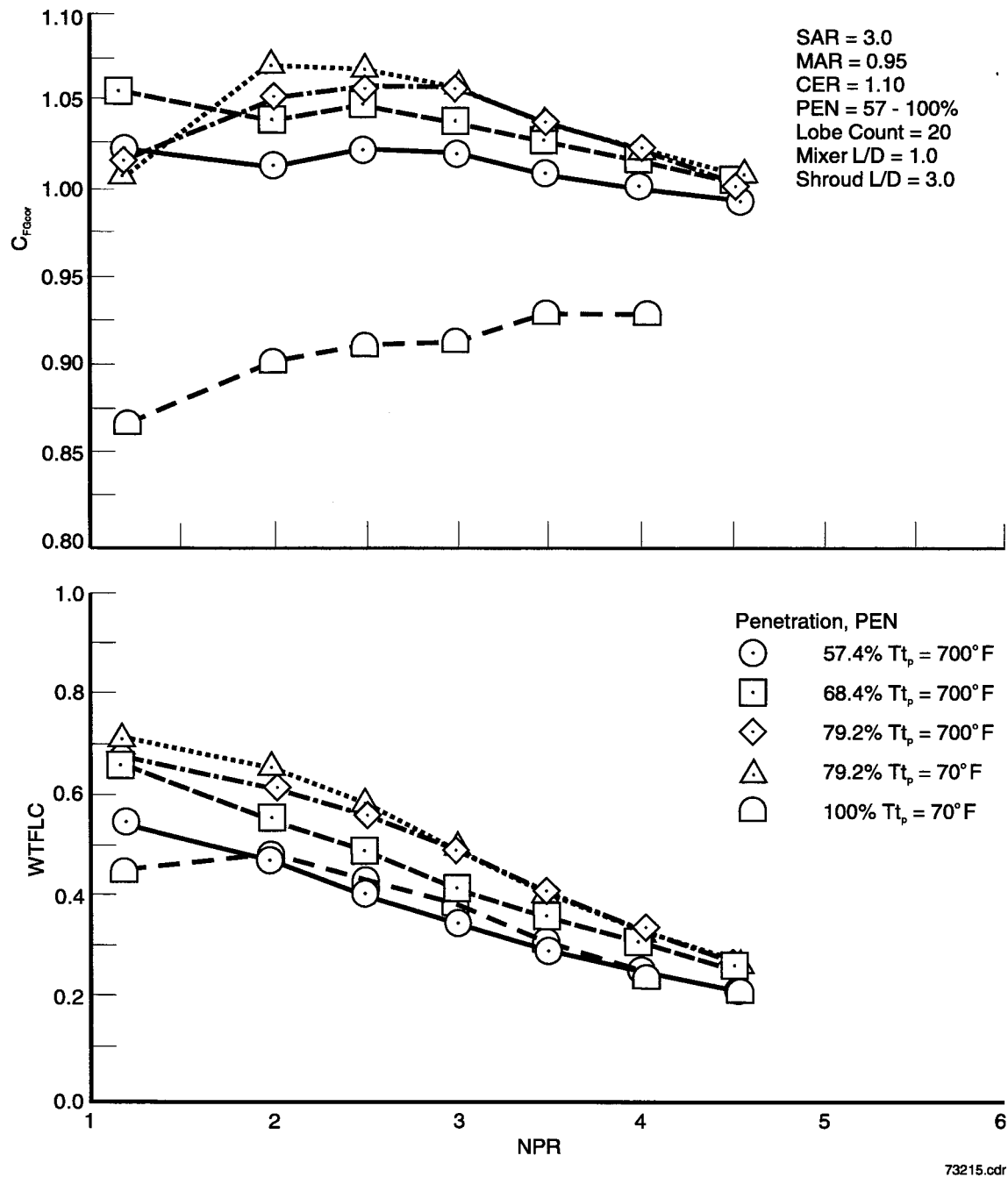


Figure 25. Comparison of Corrected Performance and Entrainment  
Effects of Penetration at SNPR = 1.0, SAR = 3.0



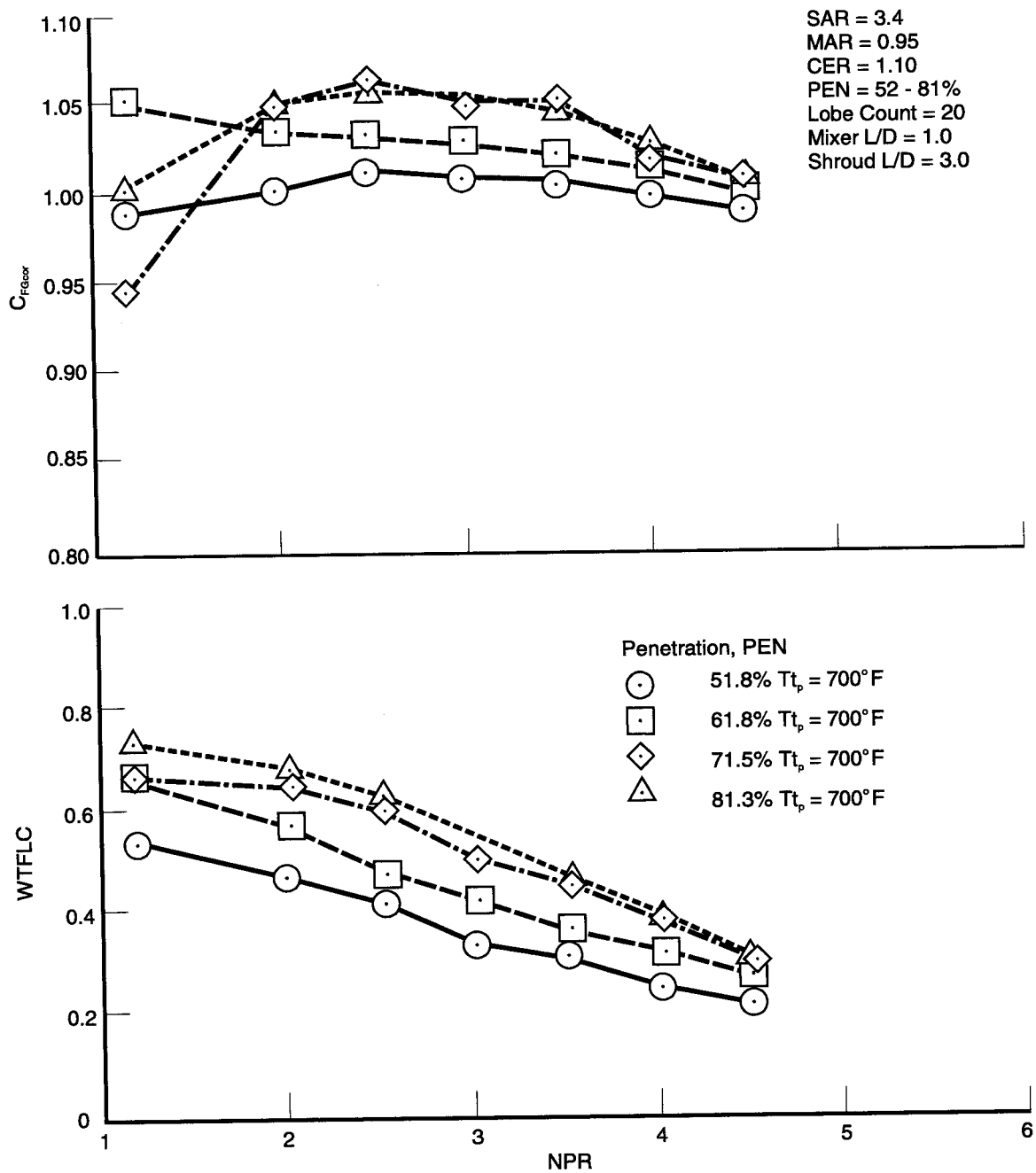


Figure 26. Comparison of Corrected Performance and Entrainment  
Effects of Penetration at SNPR = 1.0, SAR = 3.4, and  $T_{tp} = 700^\circ F$

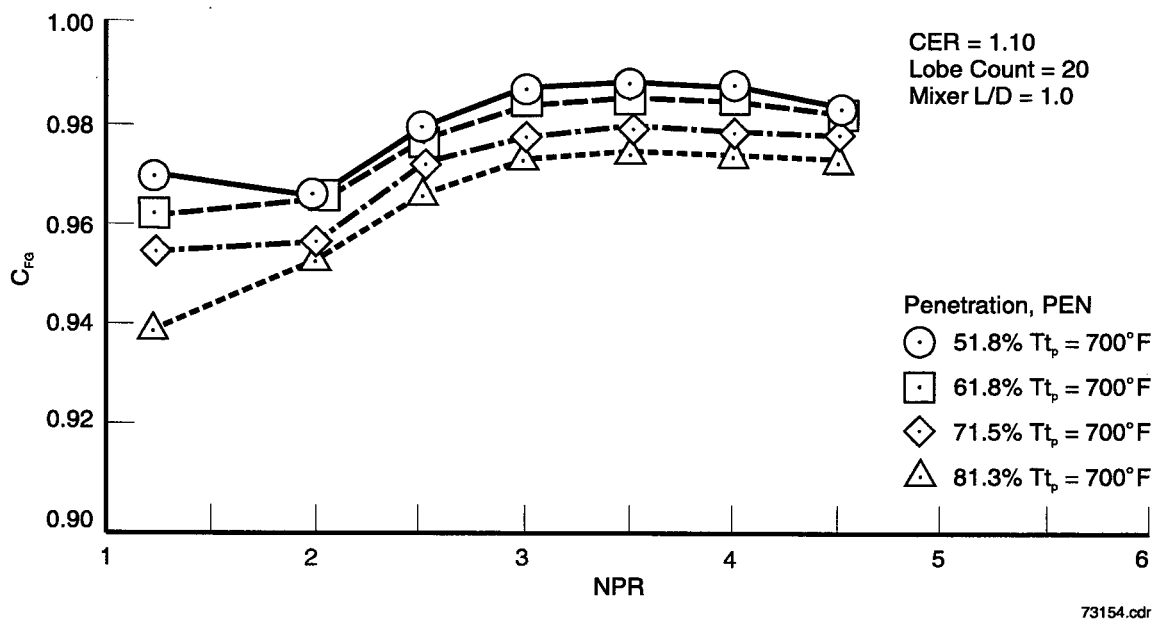
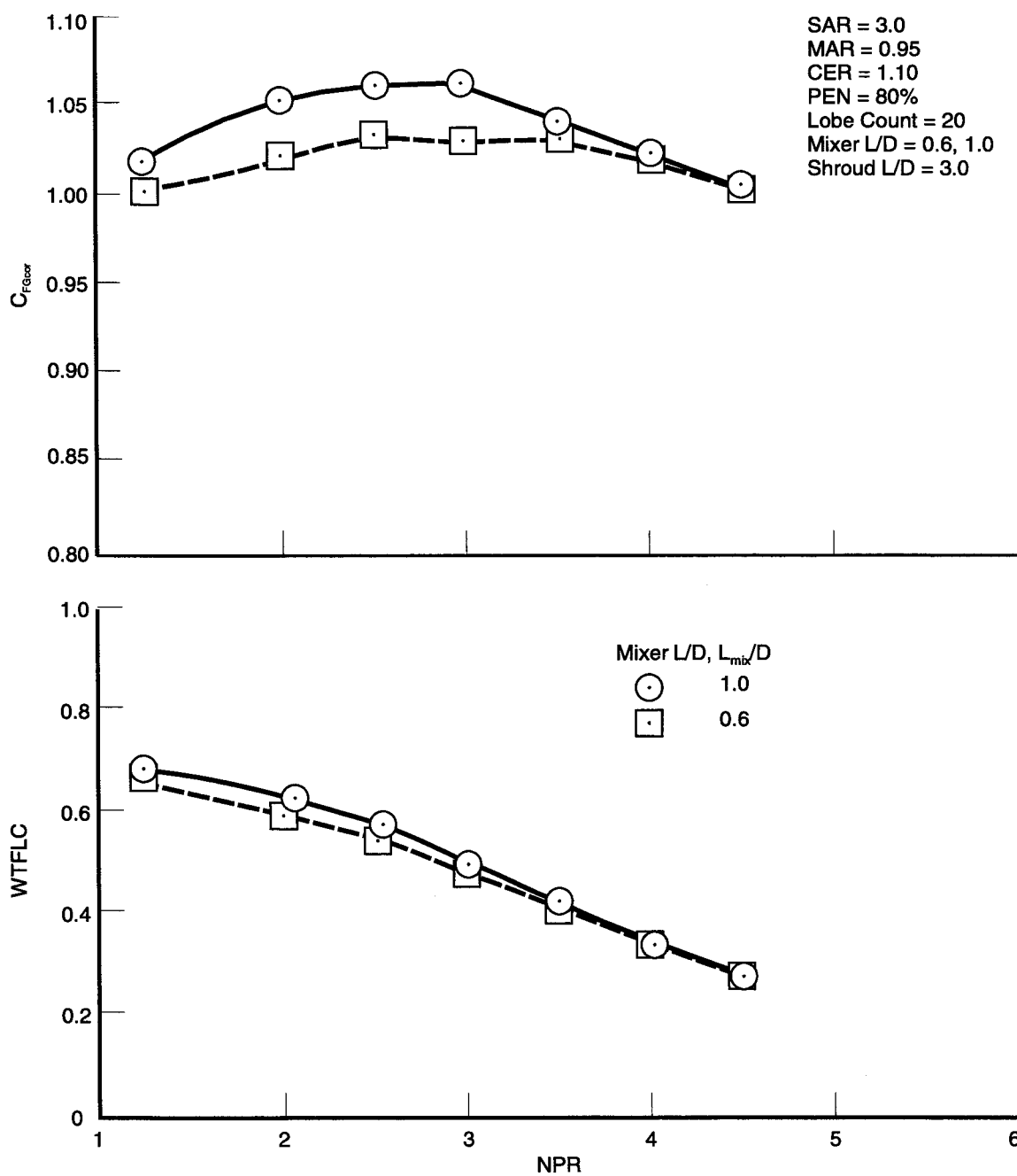
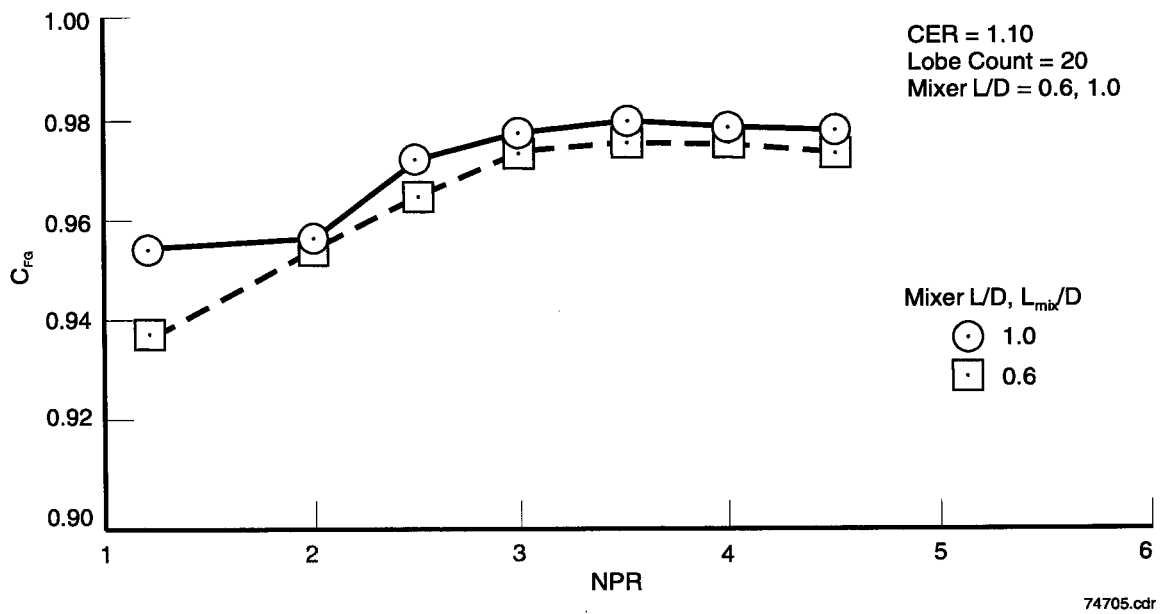


Figure 27. Mixer-Only Nozzle Performance  
Effects of Mixer Lobe Height (Penetration),  $T_p = 700^\circ\text{F}$

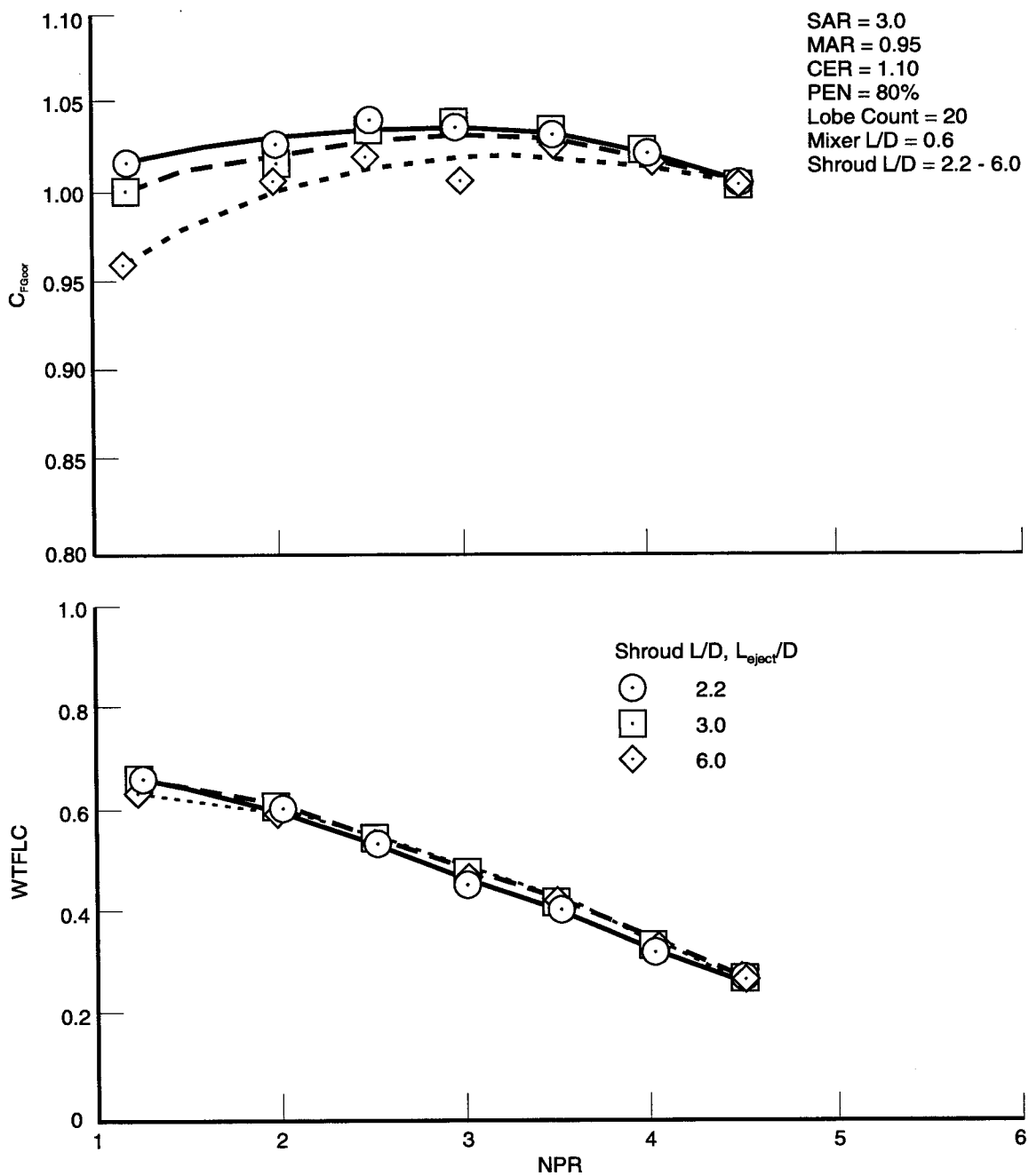


74704.cdr

Figure 28. Comparison of Corrected Performance and Entrainment  
 Effects of Mixer L/D at SNPR = 1.0 and  $T_{tp} = 700^\circ F$

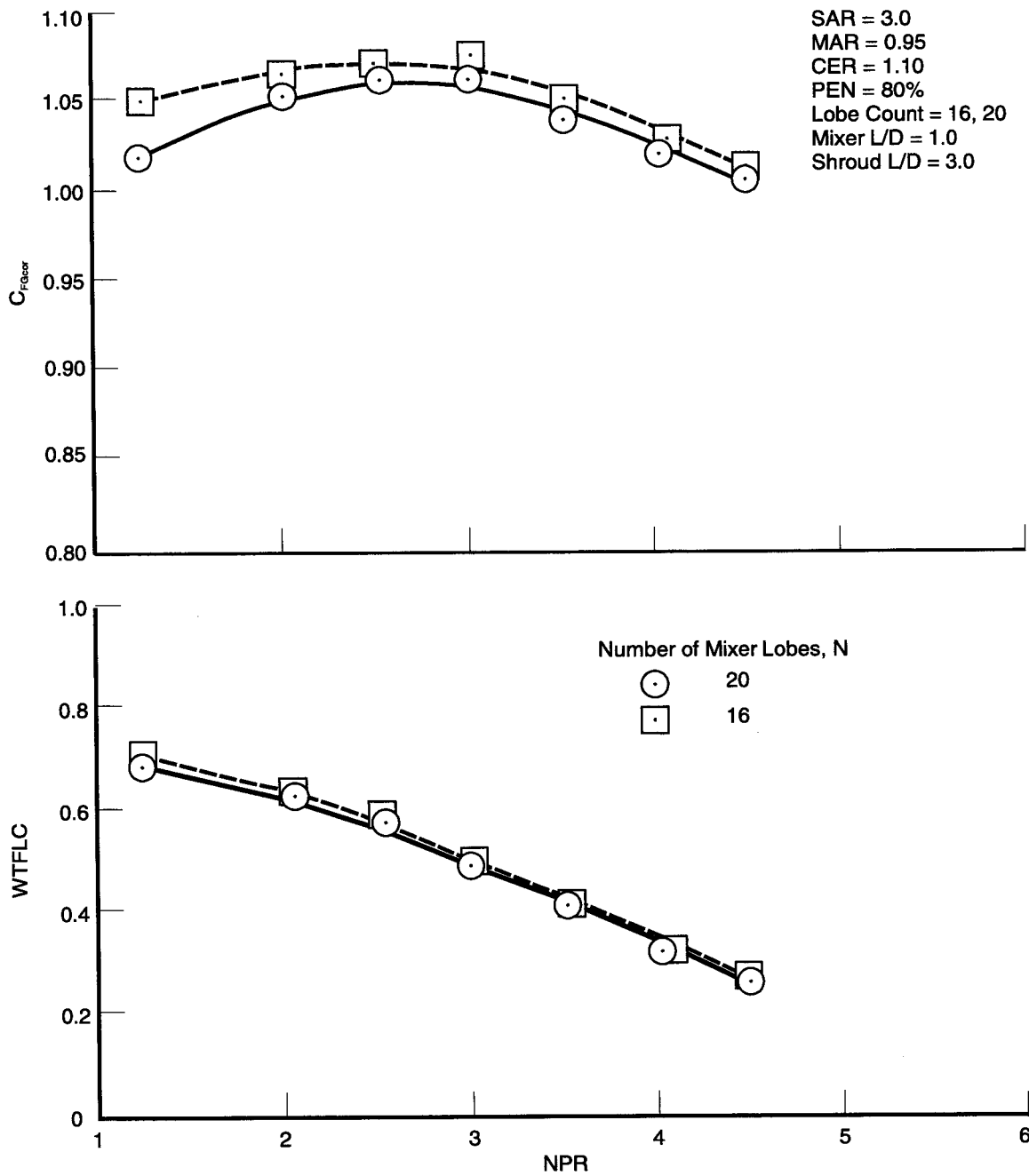


*Figure 29. Mixer-Only Nozzle Performance  
Effects of Mixer L/D at  $T_t = 700^\circ F$*



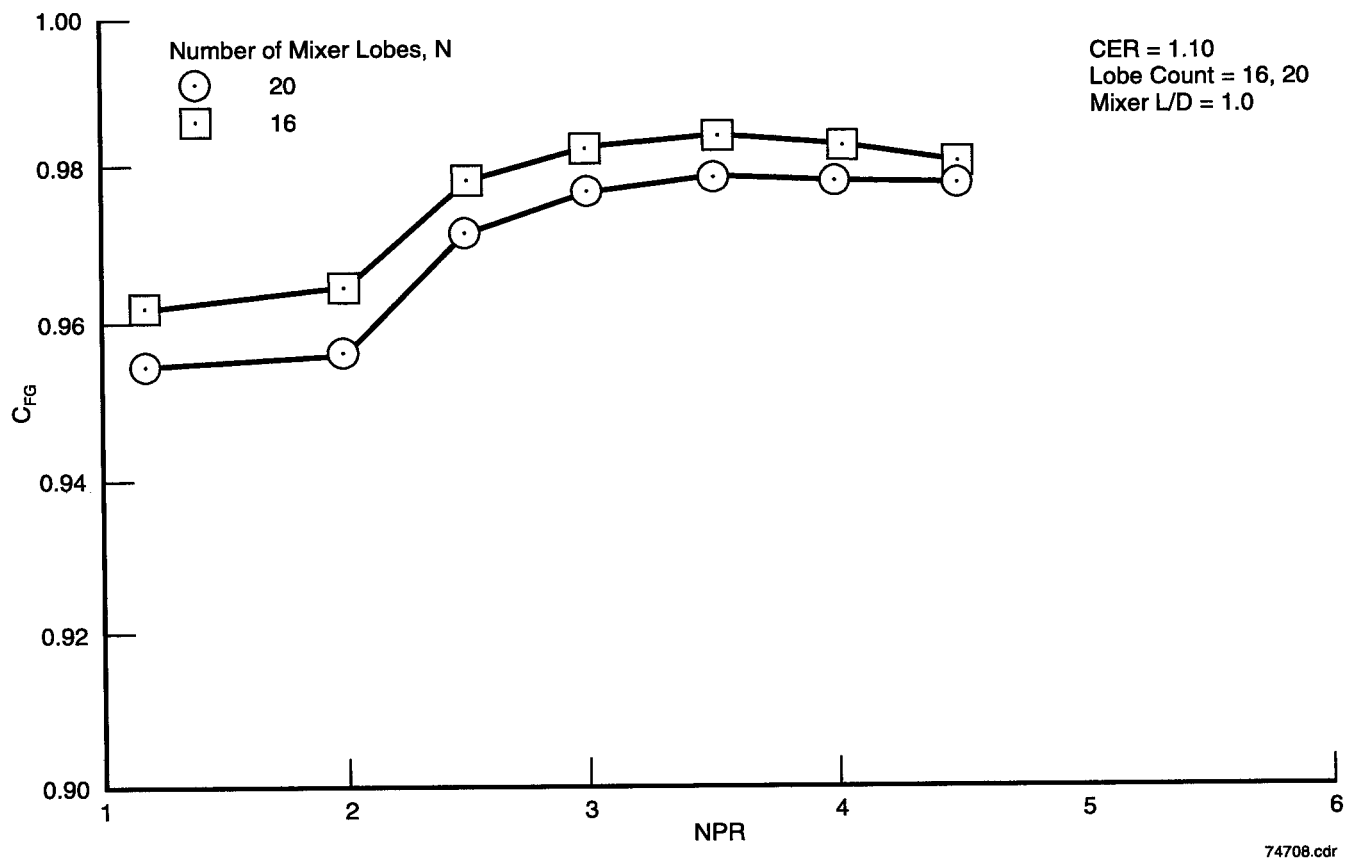
74706.cdr

Figure 30. Comparison of Corrected Performance and Entrainment  
Effects of Shroud L/D at SNPR = 1.0 and  $T_{tp} = 700^\circ F$

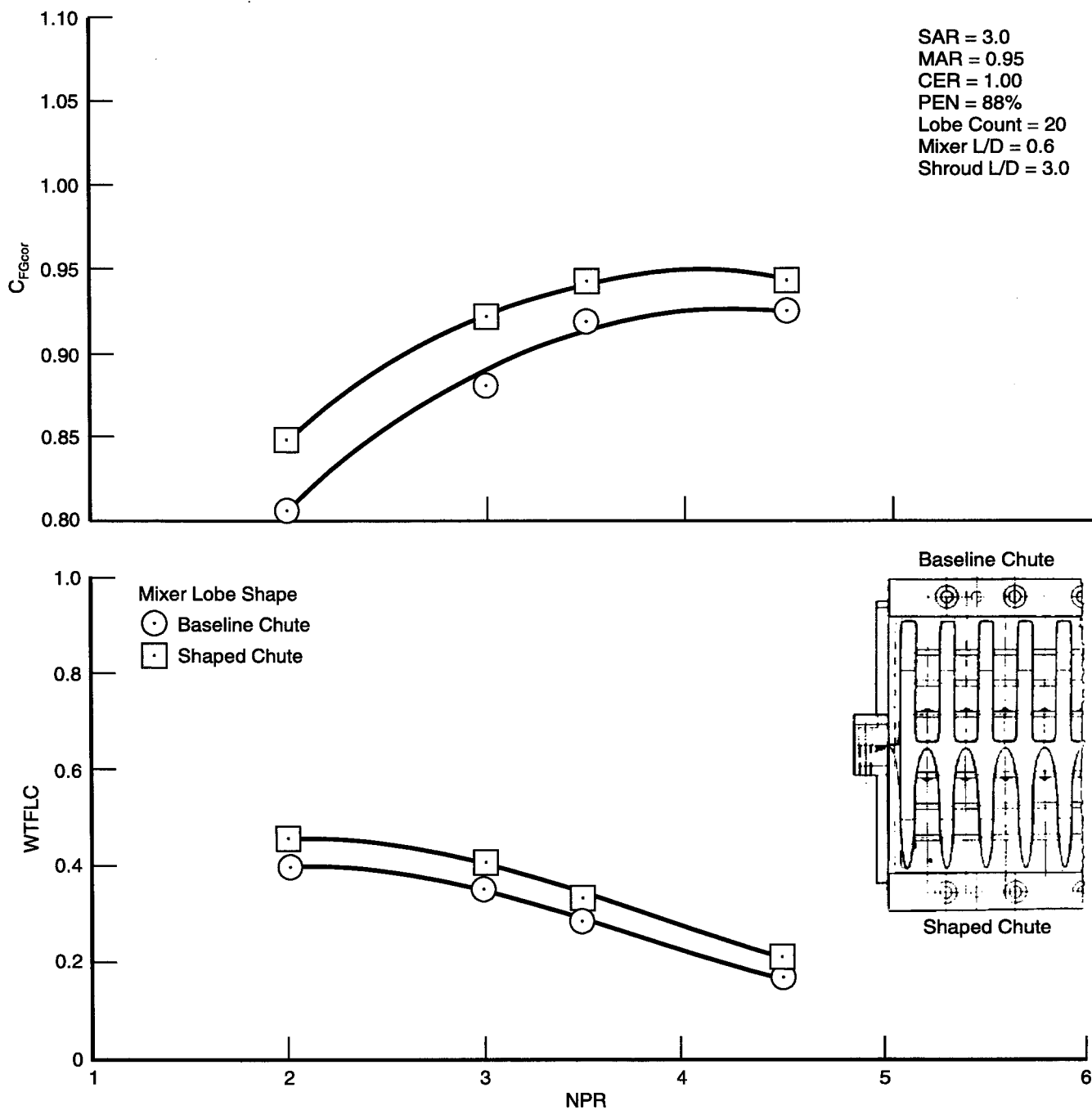


74707.cdr

Figure 31. Comparison of Corrected Performance and Entrainment Effects of Lobe Count at SNPR = 1.0, SAR = 3.0, and  $T_{tp} = 700^{\circ}F$



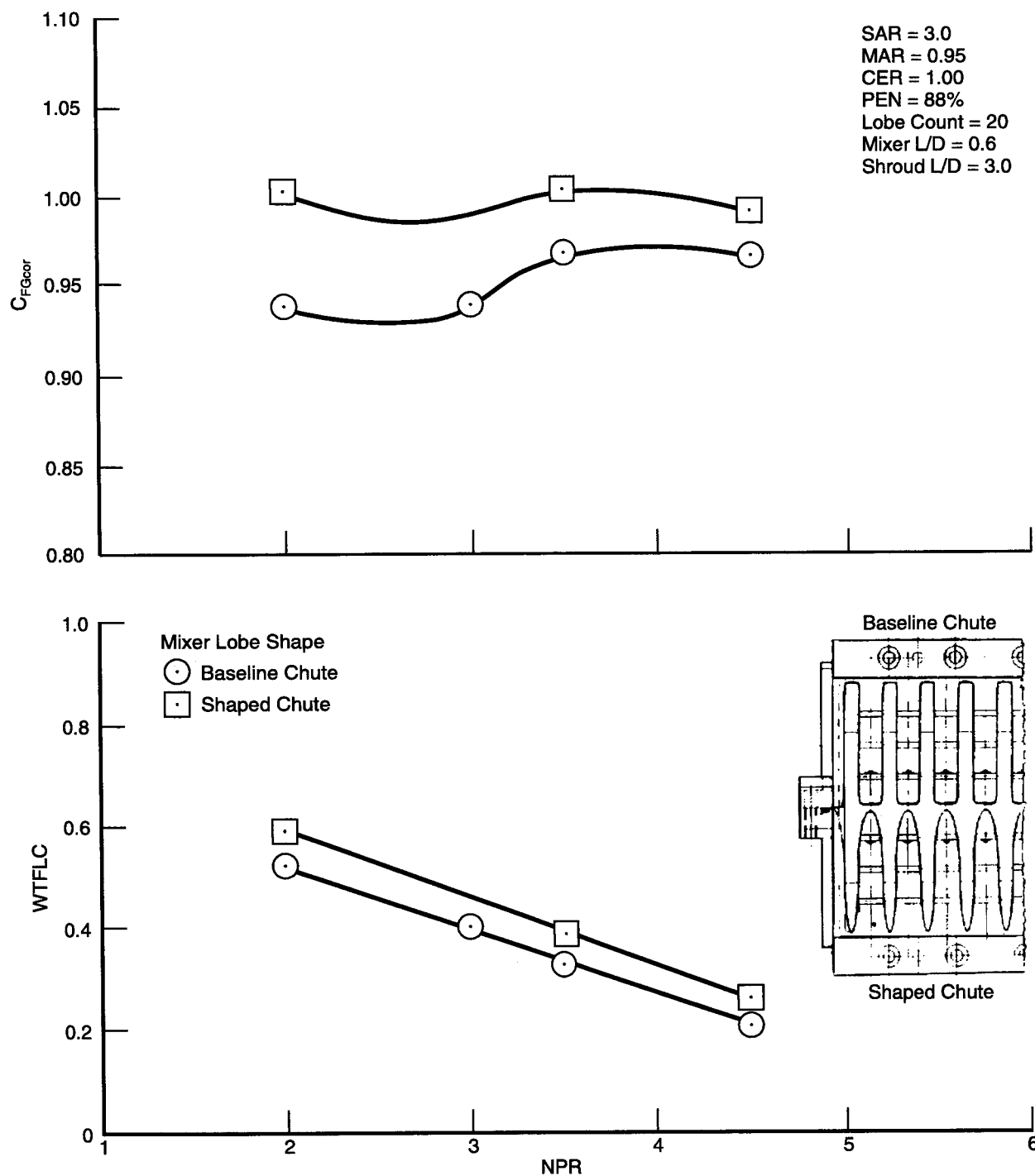
*Figure 32. Mixer-Only Nozzle Performance  
Effects of Mixer Lobe Count at  $T_{tp} = 700^{\circ}F$*



74709.cdr

*Figure 33. Comparison of Corrected Performance and Entrainment Effects of Chute Shaping at SNPR = 0.9 and  $T_t_p = 70^\circ F$*





74710.cdr

*Figure 34. Comparison of Corrected Performance and Entrainment Effects of Chute Shaping at SNPR = 1.0 and  $Tt_p = 70^\circ\text{F}$*

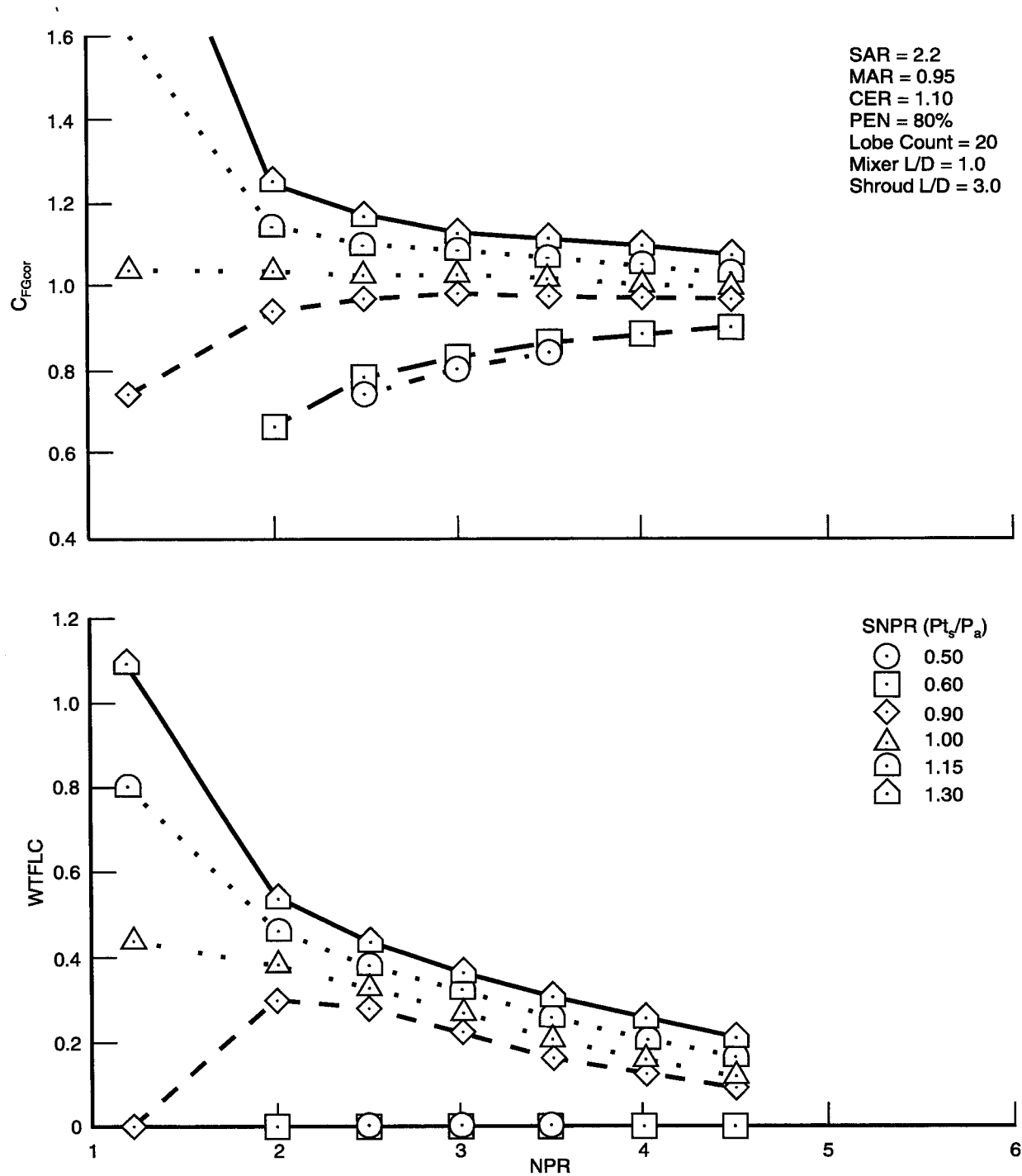


Figure 35. Comparison of Corrected Performance and Entrainment  
 Effects of SNPR for SAR = 2.2 and  $T_{tp} = 700^\circ F$

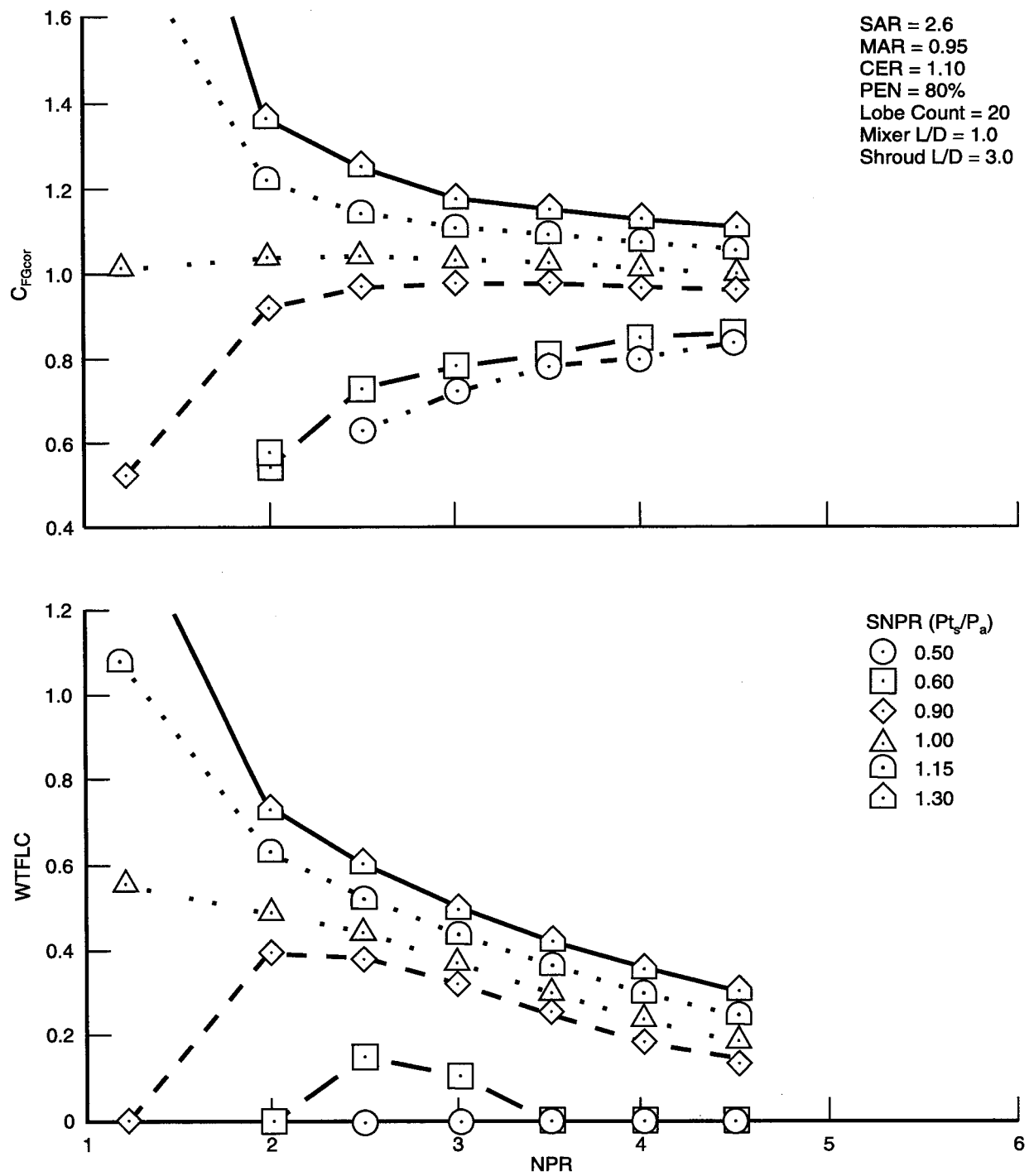
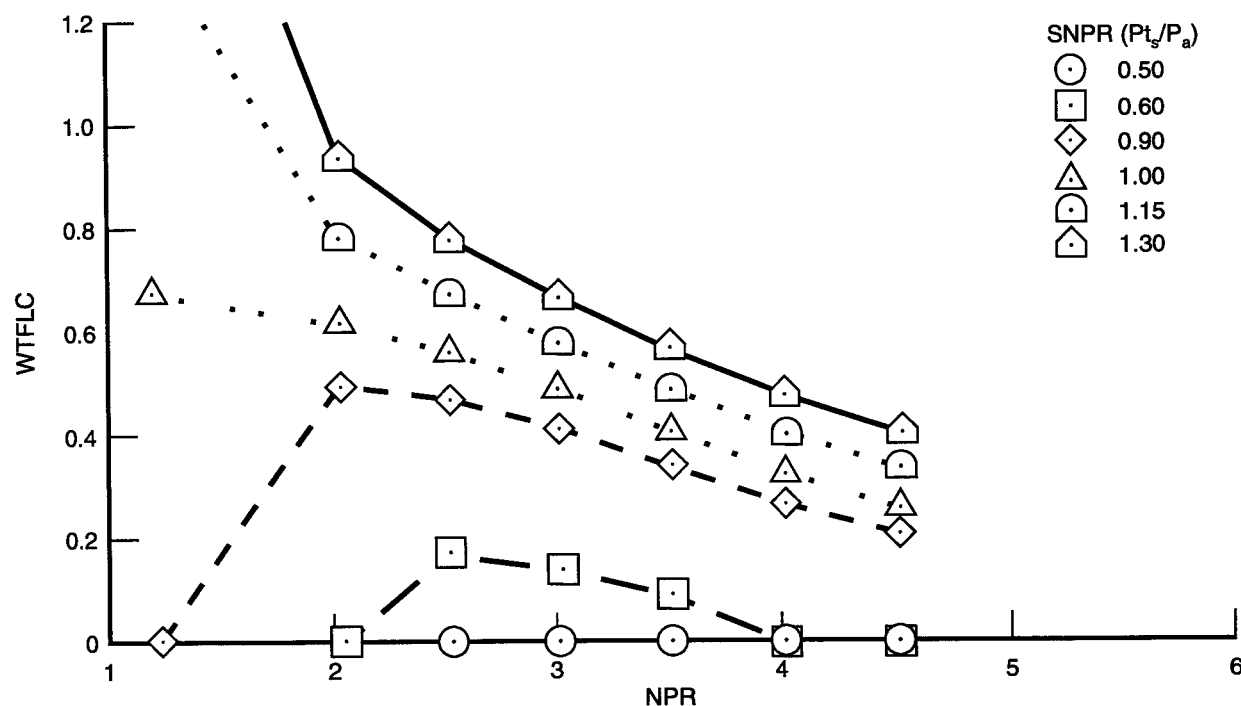
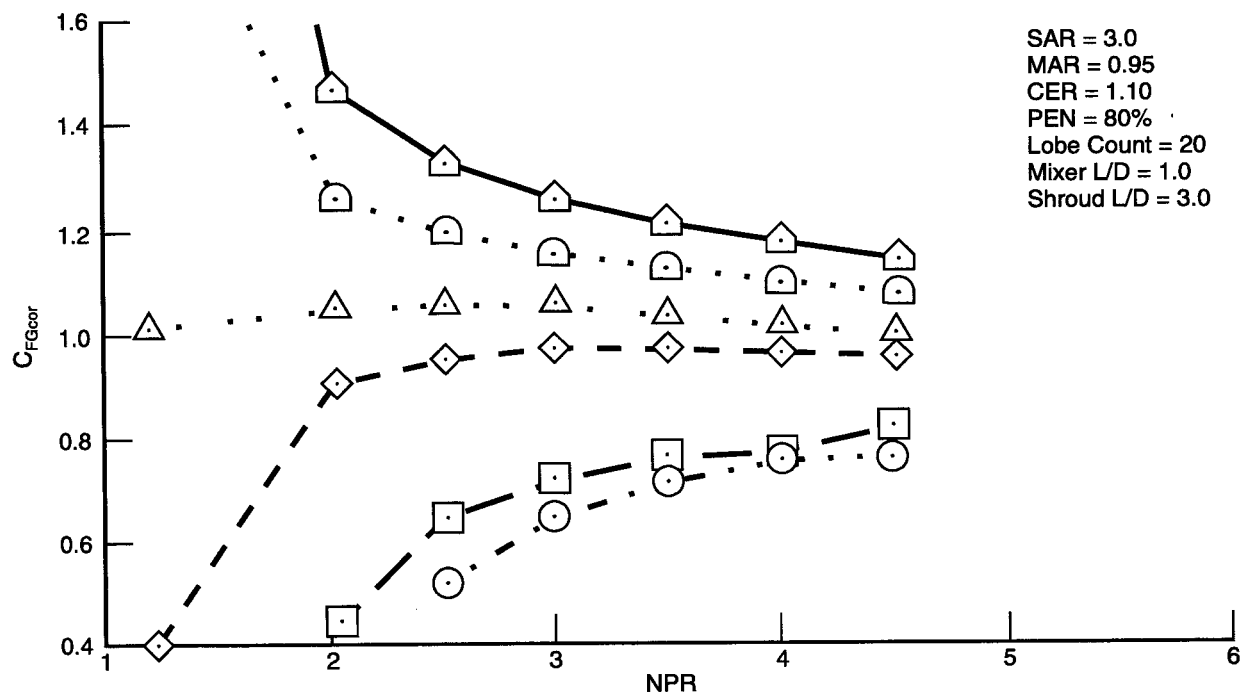
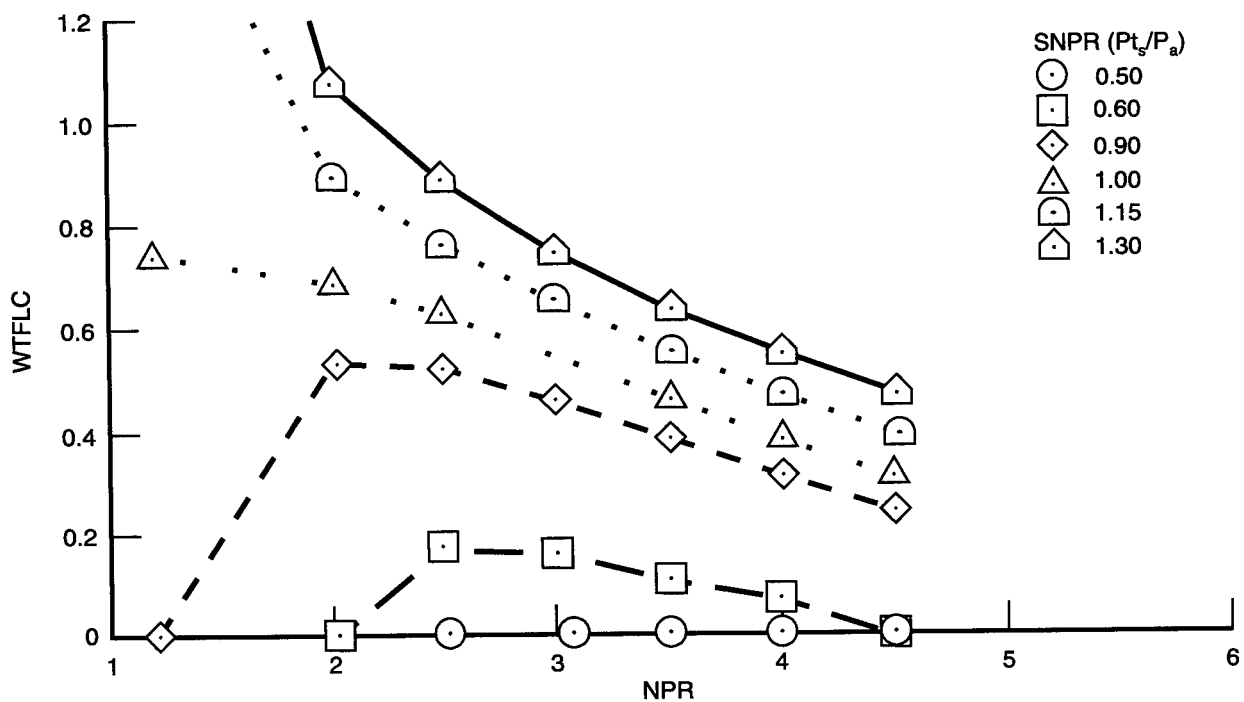
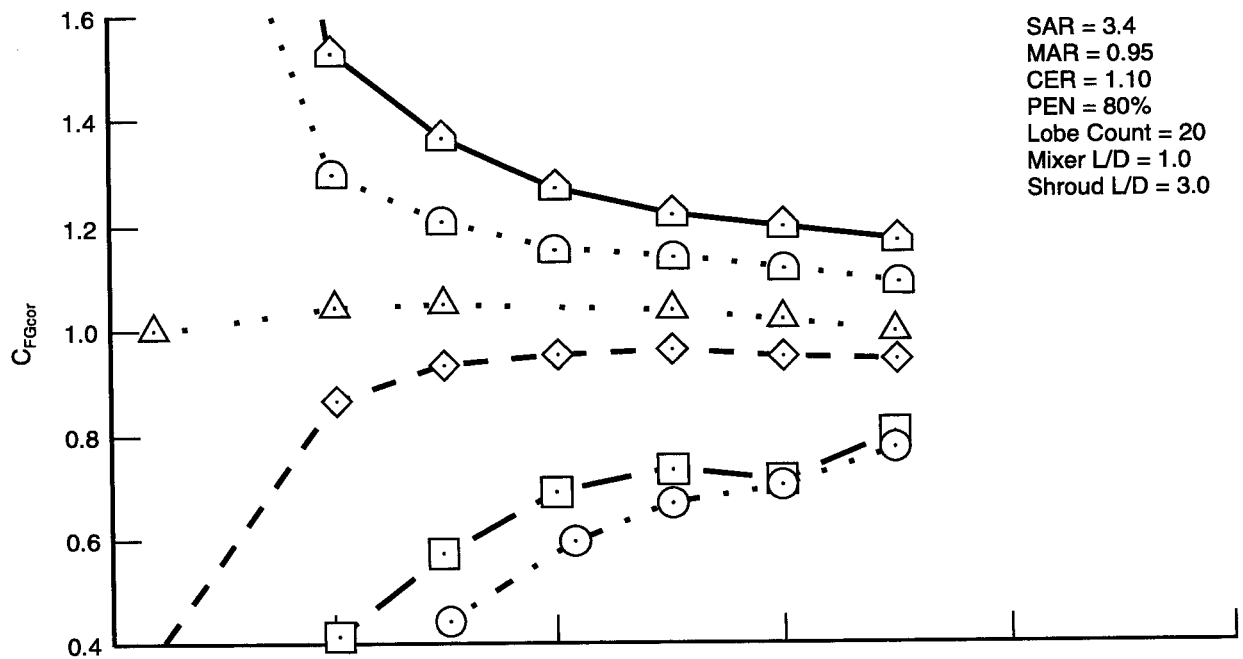


Figure 36. Comparison of Corrected Performance and Entrainment  
 Effects of SNPR for SAR = 2.6 and  $T_{tp} = 700^\circ F$



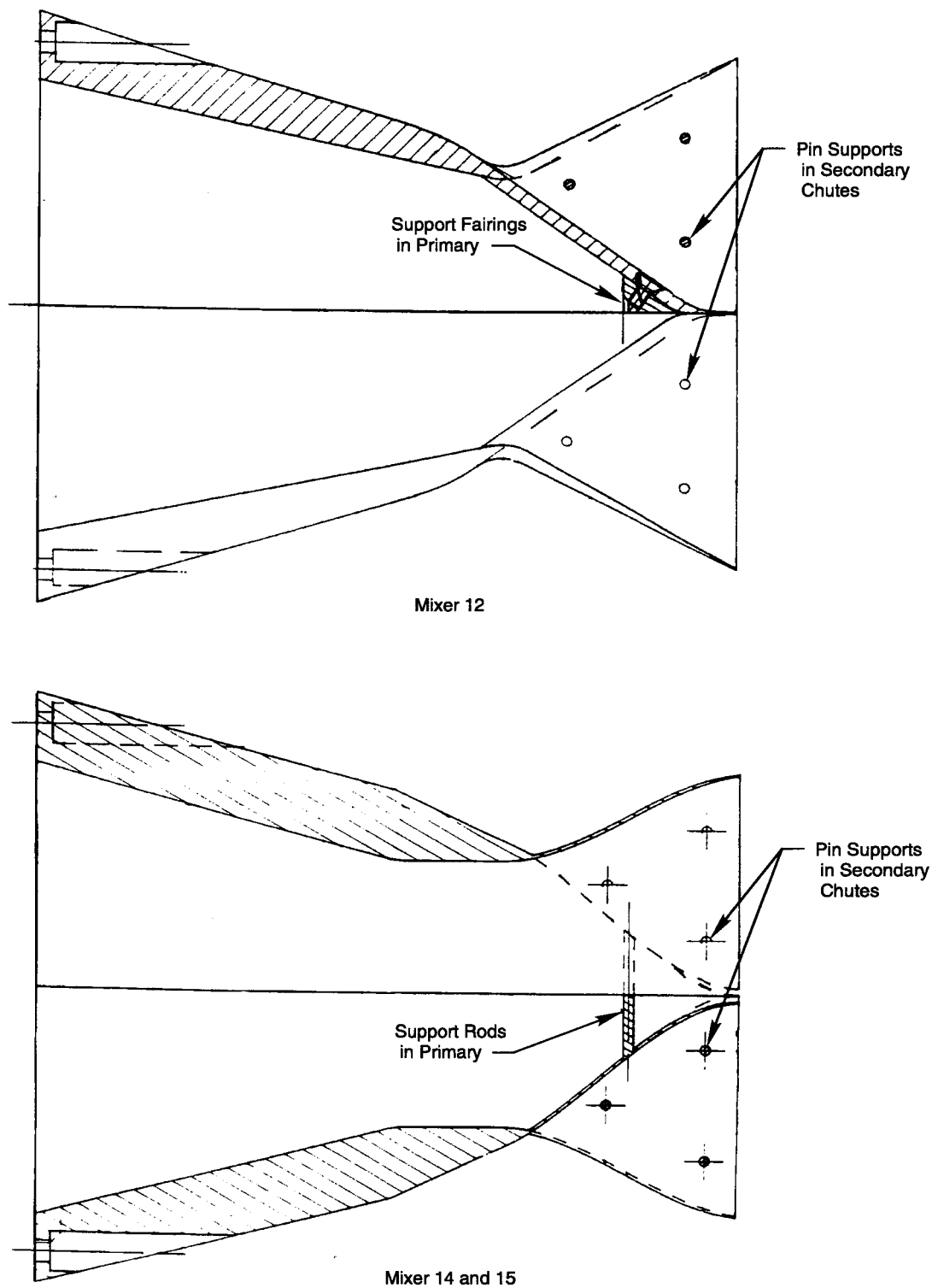
74713.cdr

Figure 37. Comparison of Corrected Performance and Entrainment Effects of SNPR for SAR = 3.0 and  $T_{t_p} = 700^\circ F$



74714.cdr

Figure 38. Comparison of Corrected Performance and Entrainment Effects of SNPR for SAR = 3.4 and  $T_{tp} = 700^\circ\text{F}$



74715.cdr

*Figure 39. Pin Supports Used for Mixers 12, 14, and 15*

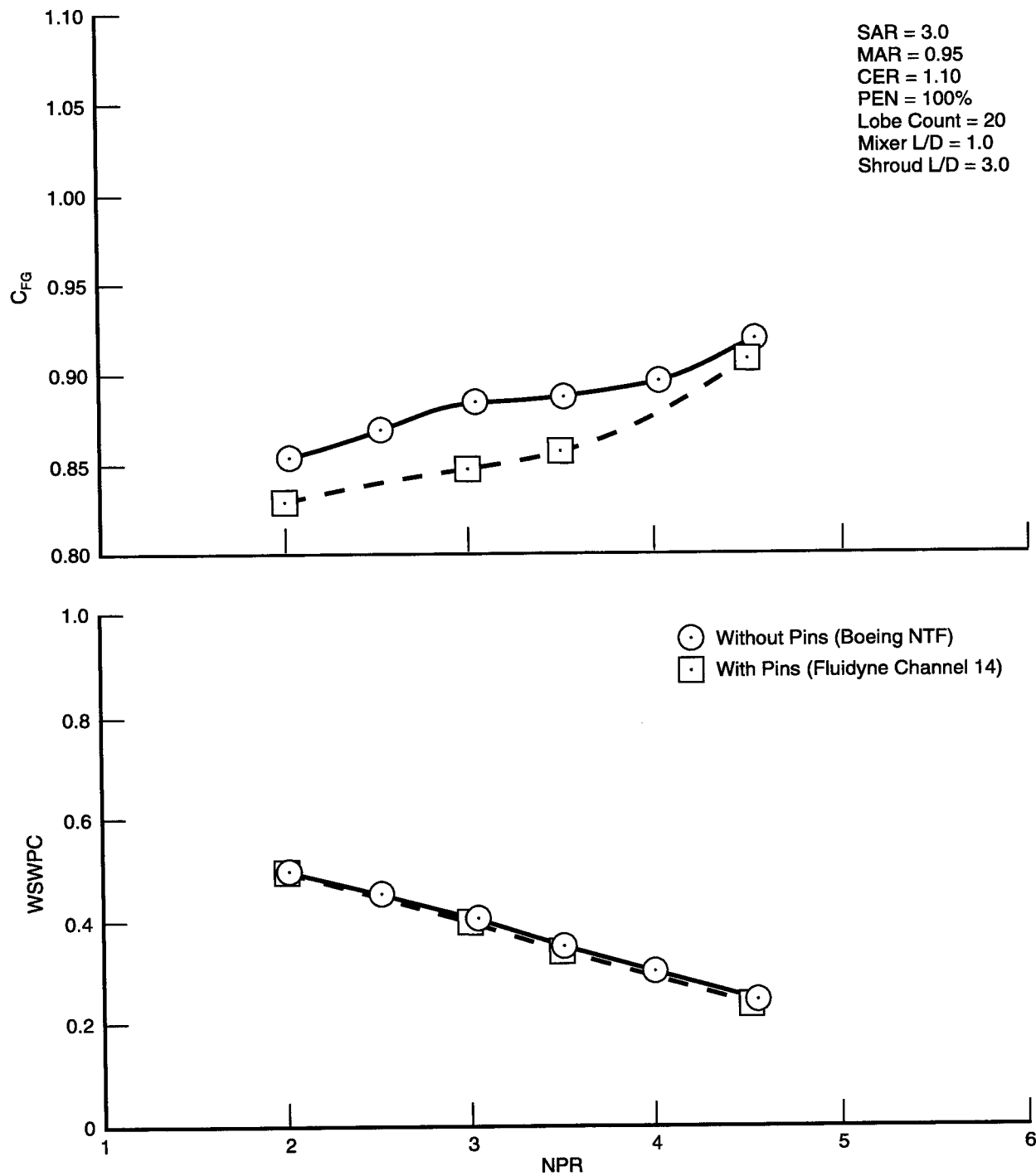
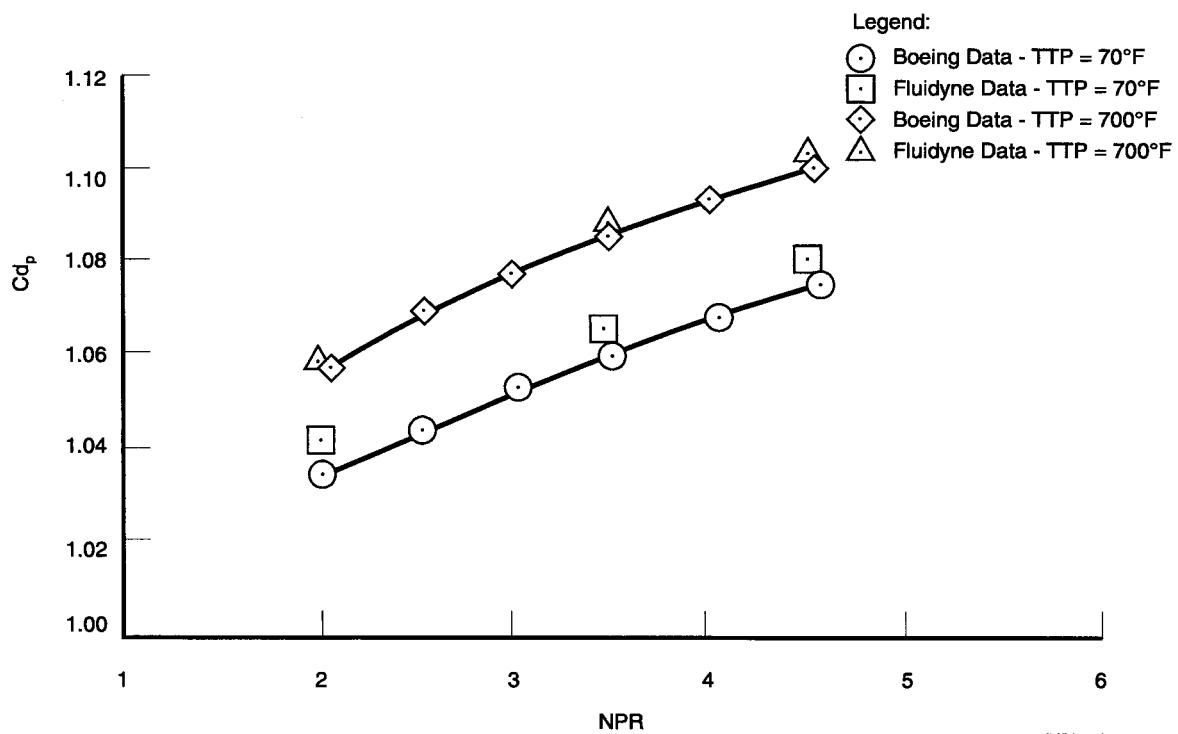
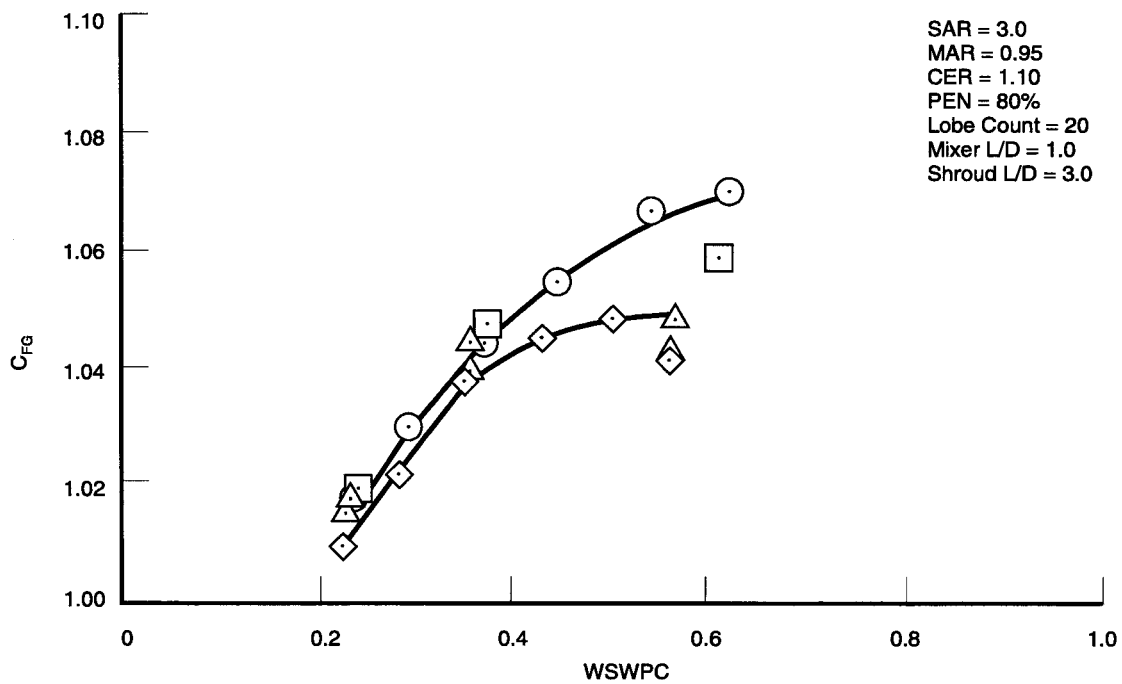


Figure 40. Comparison of Corrected Performance and Entrainment  
 Effects of Support Pins in Mixer 12 Secondary Chutes for SNPR = 1.0 and  $Tt_p = 70^\circ F$



74717.odr

Figure 41. Comparison of Boeing and Fluidyne Data —  
 Baseline Configuration Performance and Flow Coefficient for SNPR = 1.0 and  $T_{tp} = 700^\circ\text{F}$



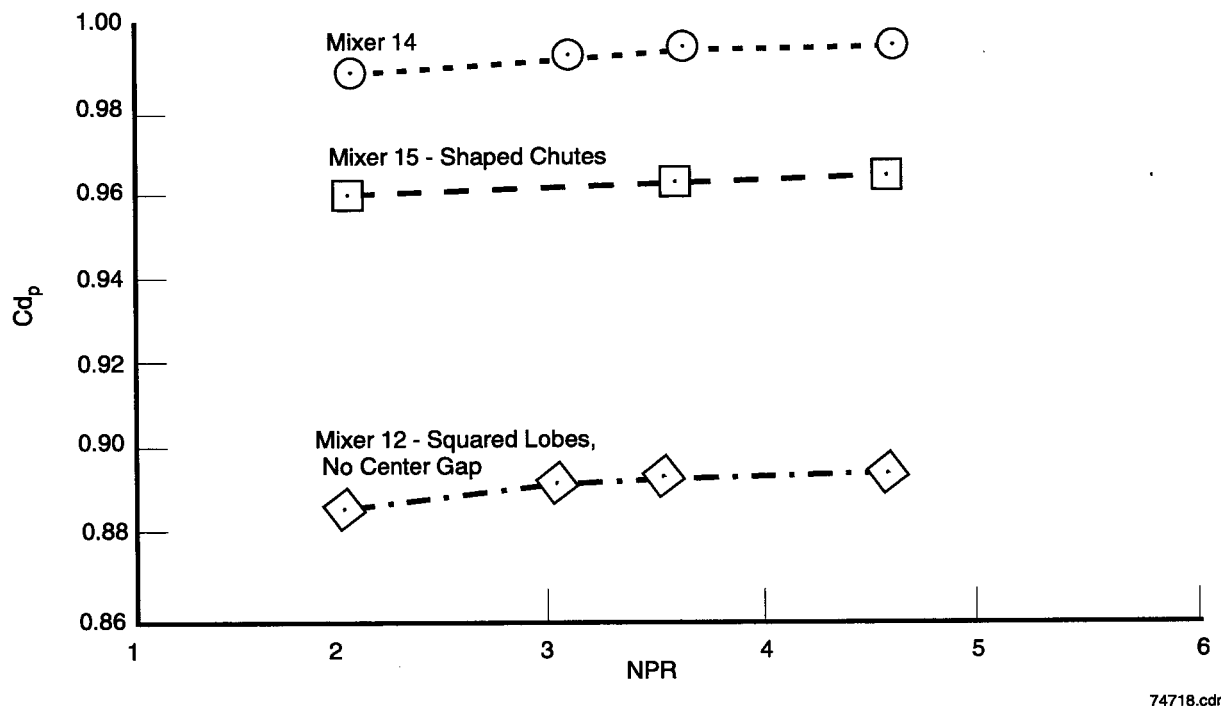


Figure 42. Flow Coefficient Data for Mixers with Stiffening Pins in Secondary Chutes  
Recorded in Fluidyne's Channel 14

### 3.7.2 Discussion of Static Pressures/Mode Shift

The mode shift, as revealed by the ejector shroud static pressure distributions, did not occur for every configuration. Even when it did occur, it was not always characterized by a sudden shift in pressure level between the subsonic and the supersonic compound compressible flow solutions. Thus, understanding what causes this shift and what prevents it could prove to be very valuable in the design of mixer/ejector nozzles.

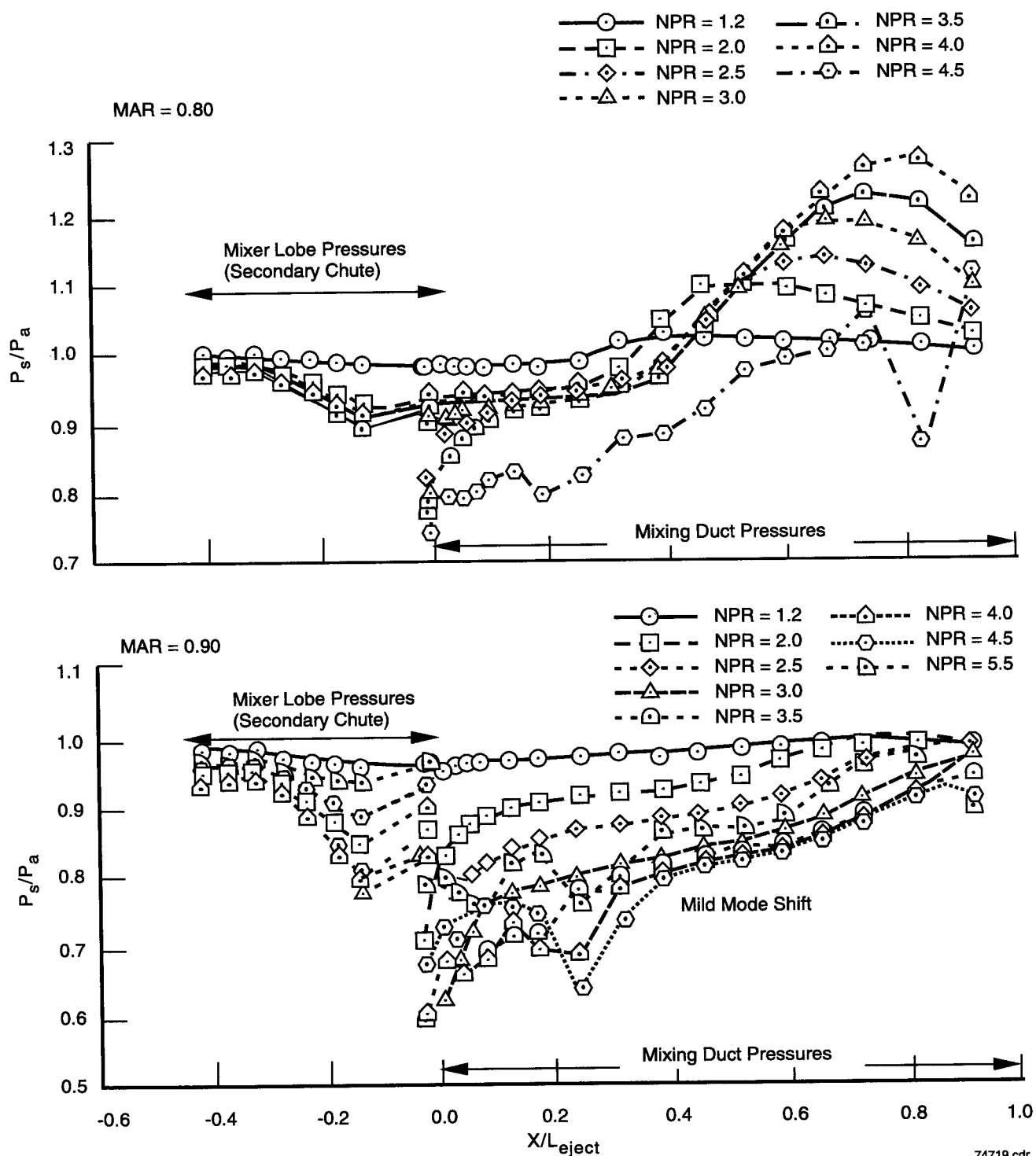
The data indicates that the variables MAR, SAR, PEN, and shroud length are the principle parameters that may be used to limit or enhance the mode shift of the flow in the mixing duct. Mixers 3 and 8, which represented the baseline mixer and a shortened baseline, respectively, were both tested at four different MARs (0.80, 0.90, 0.95, and 1.20). The pressure distributions are shown in Figure 43 and Figure 44 for comparison. These MAR sweeps indicate that as MAR increases, the nozzle pressure ratio at which the mode shift occurs (critical NPR) decreases as shown in Figure 45. At the maximum MAR of 1.2, the mode shift occurs at nozzle pressure ratios as low as 2. At the minimum MAR of 0.80, the mode shift does not occur at all over the range of NPRs tested, presumably because the mixing duct is convergent with the minimum area (sonic velocity) at the exit of the mixing duct. Even when the mode shift does occur at intermediate values of MAR, the shift in pressure level does not necessarily present a problem in ejector shroud or sidewall loads.

The mode shift severity was probably most influenced by the combination of SAR and PEN. Figure 46 shows the effect of penetration on the mixer and mixing duct static pressures. These pressures indicate that the severity of the mode shift increases with increasing penetration. At low penetrations (less than 80 percent), no mode shift occurred. At 80-percent penetration, the mode shift begins to occur, and at 100-percent penetration, the mode shift is observed to be severe. As shown in Figure 47, lobe penetrations of 100 percent always produced a severe shift in static pressure as the flow shifted from subsonic to supersonic, regardless of the flow angle at the mixer exit. (i.e., two mixers were tested at 100-percent penetration; one with axially directed flow at the mixer exit [Mixer 5], and

one with the exit flow directed into the ejector shrouds [Mixer 12]). Figure 48 shows static distributions for SARs ranging from 2.2 to 3.4 (PEN = 0.80). While SAR does not affect the critical NPR, it does affect the severity of the mode shift. The lower SAR values undergo a much more severe mode shift than do the higher SARs. Various combinations of SAR and PEN had varying effects on the mode shift severity. As shown in Figure 49, lower values of SAR required lower penetrations to avoid severe mode shifts. Conversely, higher SARs could use higher penetrations while avoiding severe mode shifts.

The relationship between complete mixing and mode shift is demonstrated by using a long mixing duct (shroud  $L/D = 6$ ) relative to the mid-length duct (shroud  $L/D = 3$ ). This data, shown in Figure 50, indicates that while the mode shift occurred at a nozzle pressure ratio of 3.5 for either shroud length, the severity of the corresponding shift in static pressures is much greater for the long shroud (more complete mixing). This data suggests that the severity of the mode shift may be directly related to the mixedness of the flow.

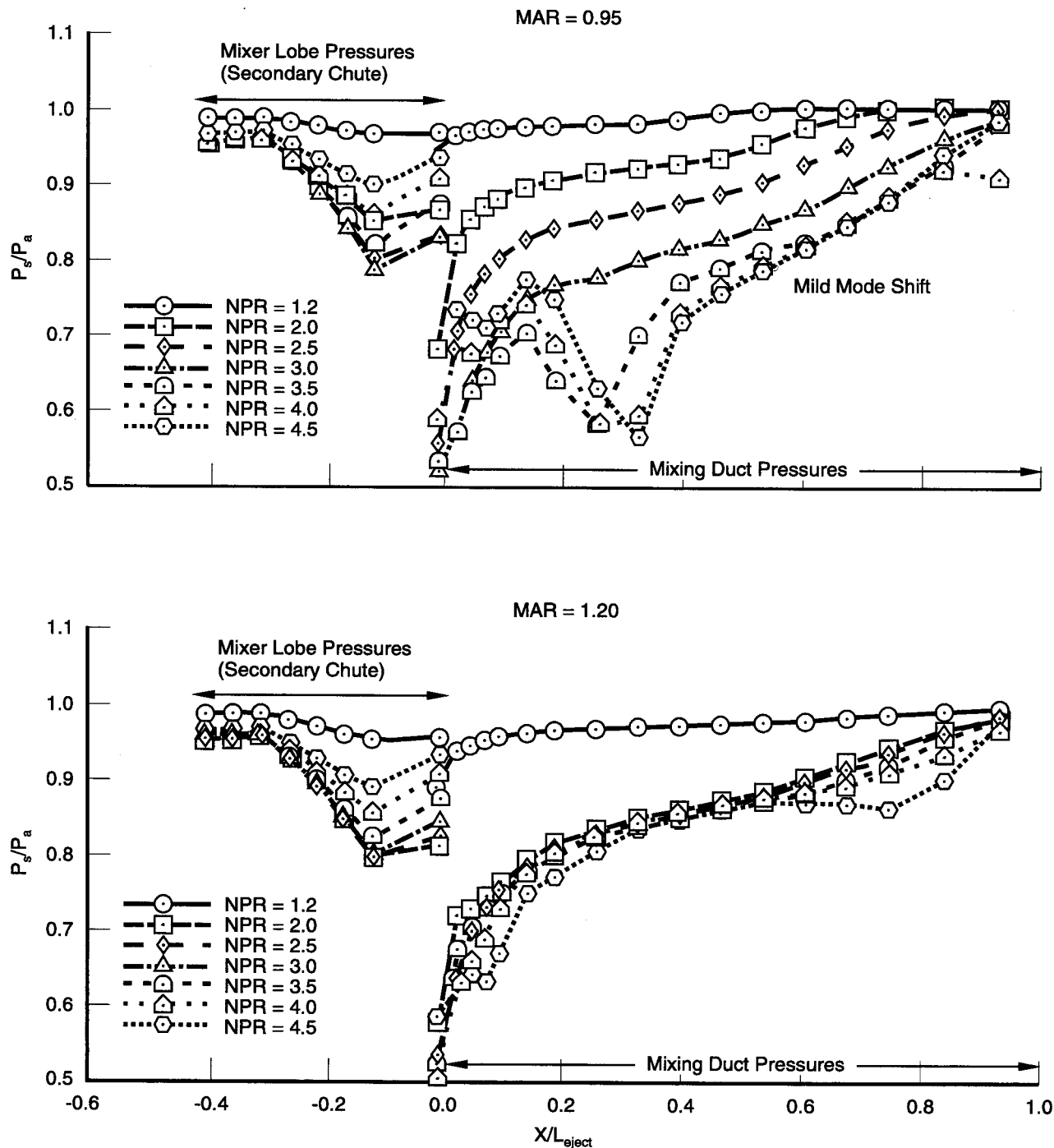
Primary flow total temperature affects the critical NPR by raising it slightly with increases in temperature (Figure 51). Figure 52 shows the mixing duct static pressure variations for temperatures ranging from 70°F to 1000°F. For low temperatures (70°F), the mode shift occurred at a nozzle pressure ratios of 2.5 to 3.0, while at higher temperatures (500°F to 1000°F), the critical NPR was near 3.0 to 3.5. In addition to the critical NPR, the severity of the mode shift was also affected. The static pressures associated with the supersonic solution in the mixing duct decrease with increasing temperature, leading to a larger shift in static pressure (more severe mode shift) as the primary flow temperature increases.



74719.cdr

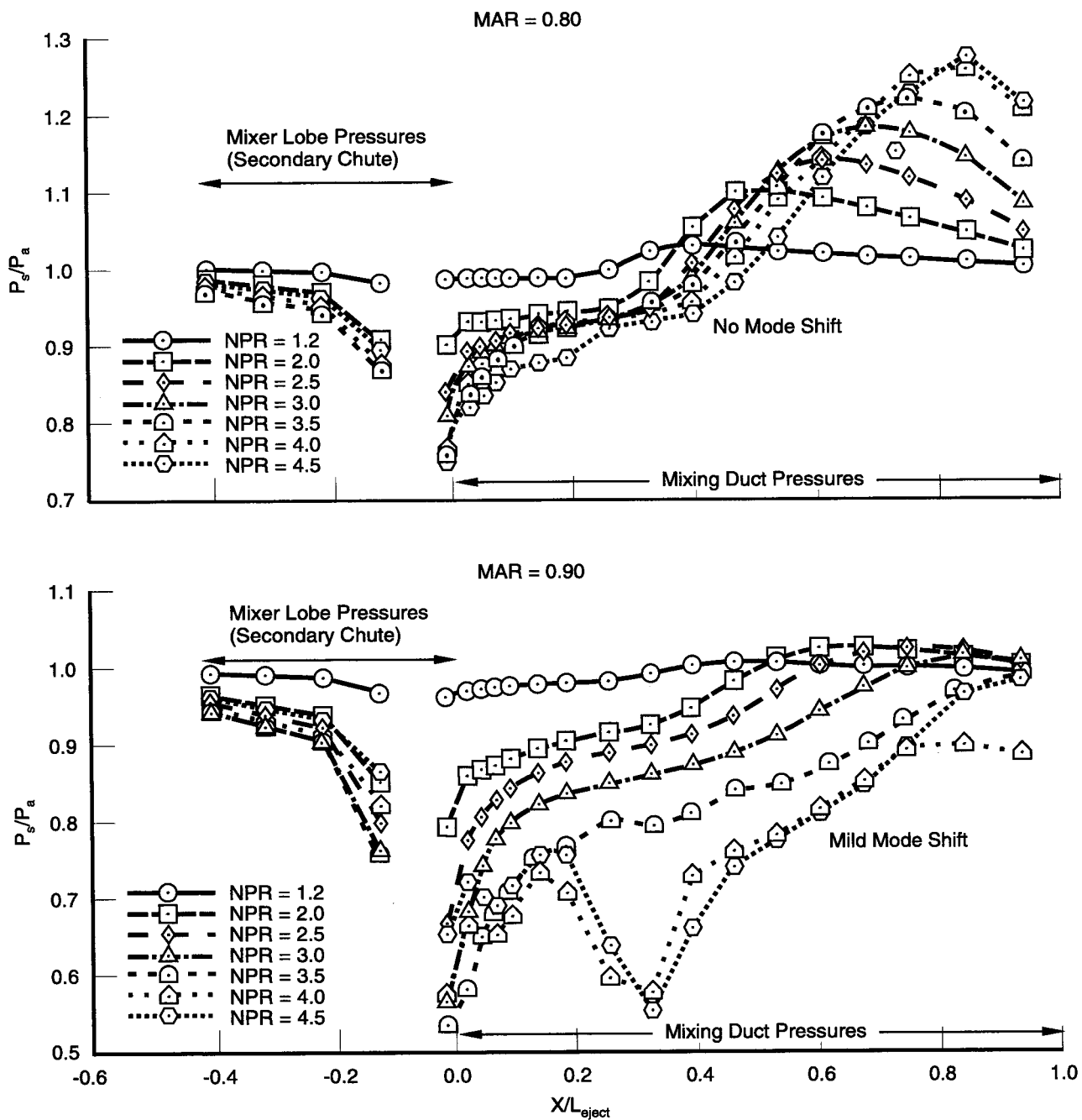
Figure 43. Mixer External and Shroud Internal Static Pressures —  
Effect of MAR Using Long Mixer

$SAR = 3.0$ ,  $CER = 1.1$ ,  $PEN = 80\%$ , 20 Lobes,  $L_{mix}/D = 1.0$ ,  $L_{eject}/D = 3.0$ ,  $SNPR = 1.0$ ,  $T_{t_p} = 700^\circ F$



74720.cdr

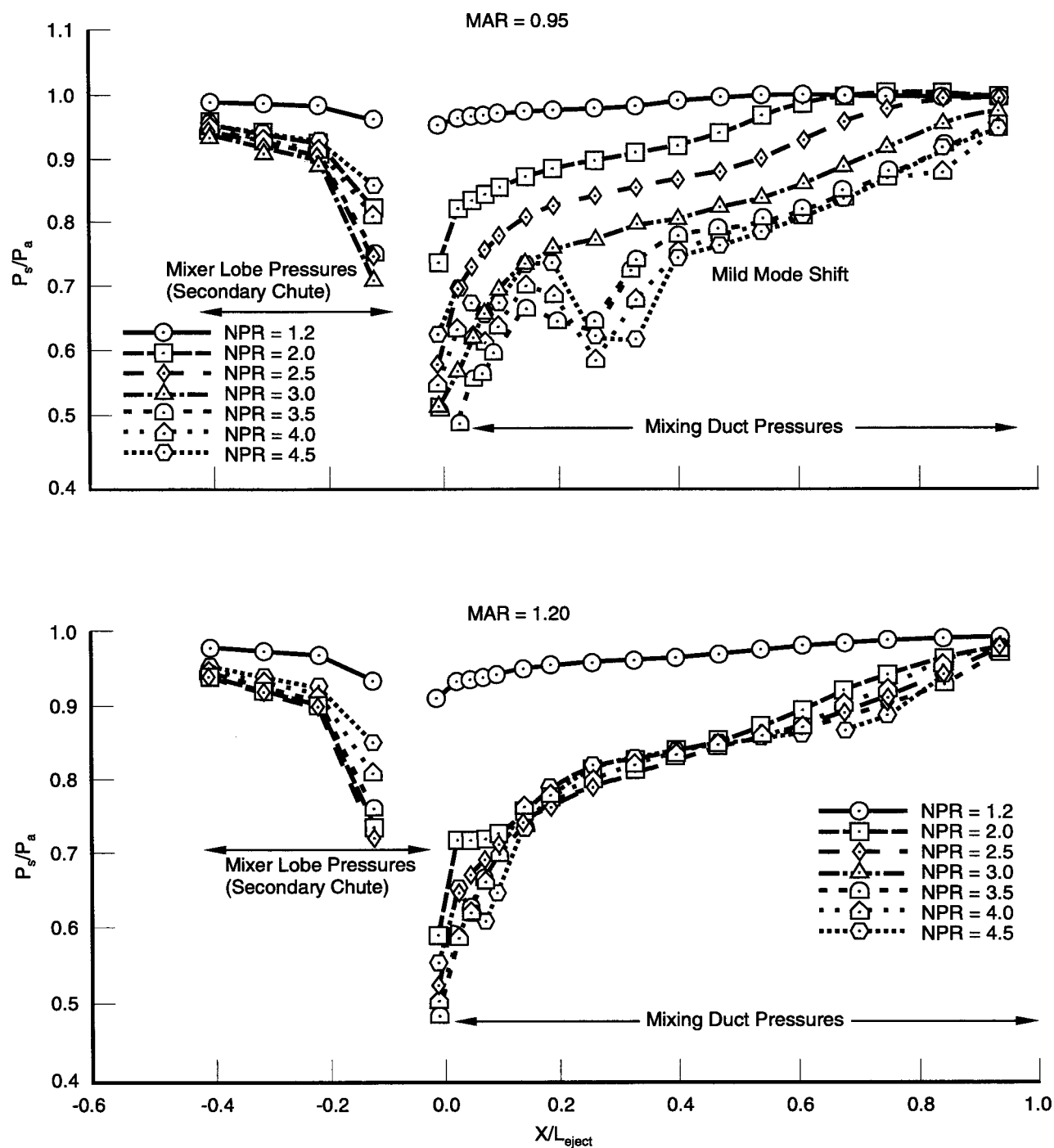
*Figure 43 (Concluded). Mixer External and Shroud Internal Static Pressures —  
Effect of MAR Using Long Mixer  
SAR = 3.0, CER = 1.1, PEN = 80%, 20 Lobes,  $L_{mix}/D = 1.0$ ,  $L_{eject}/D = 3.0$ , SNPR = 1.0,  $T_{tp} = 700^\circ F$*



74721.cdr

Figure 44. Mixer External and Shroud Internal Static Pressures —  
Effect of MAR Using Short Mixer

$SAR = 3.0$ ,  $CER = 1.1$ ,  $PEN = 80\%$ , 20 Lobes,  $L_{mix}/D = 0.6$ ,  $L_{eject}/D = 3.0$ ,  $SNPR = 1.0$ ,  $T_{tp} = 700^\circ F$



74722.cdr

Figure 44 (Concluded). Mixer External and Shroud Internal Static Pressures —  
 Effect of MAR Using Short Mixer  
 $SAR = 3.0$ ,  $CER = 1.1$ ,  $PEN = 80\%$ , 20 Lobes,  $L_{mix}/D = 0.6$ ,  $L_{eject}/D = 3.0$ ,  $SNPR = 1.0$ ,  $T_{tp} = 700^\circ F$

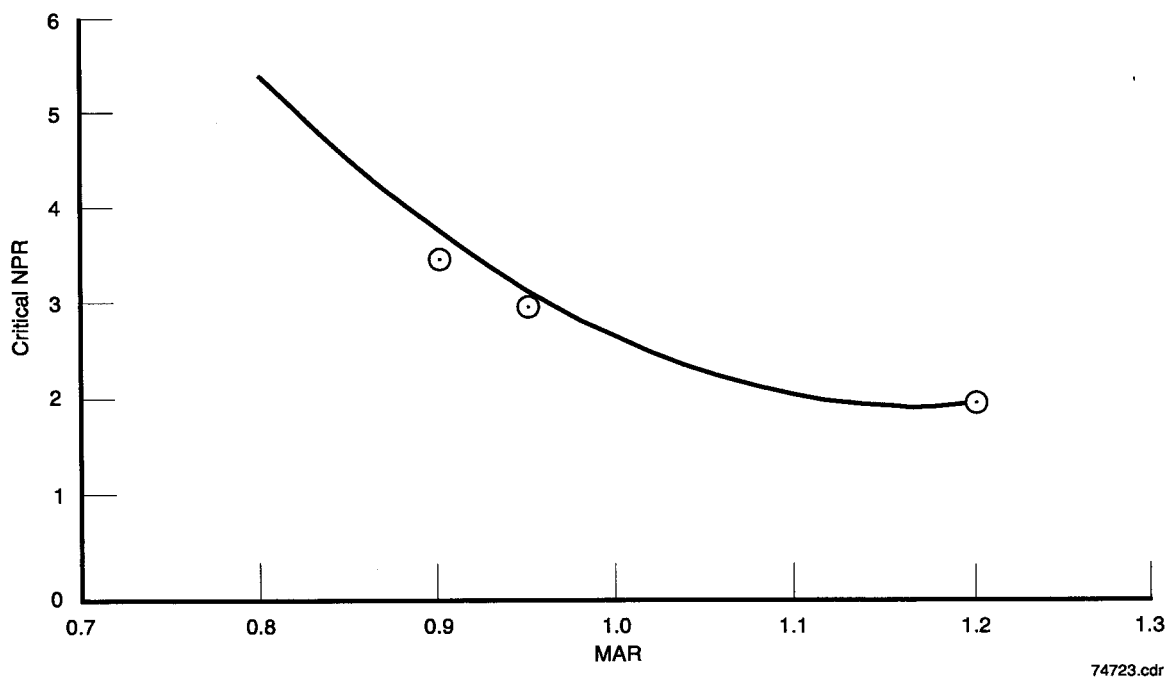
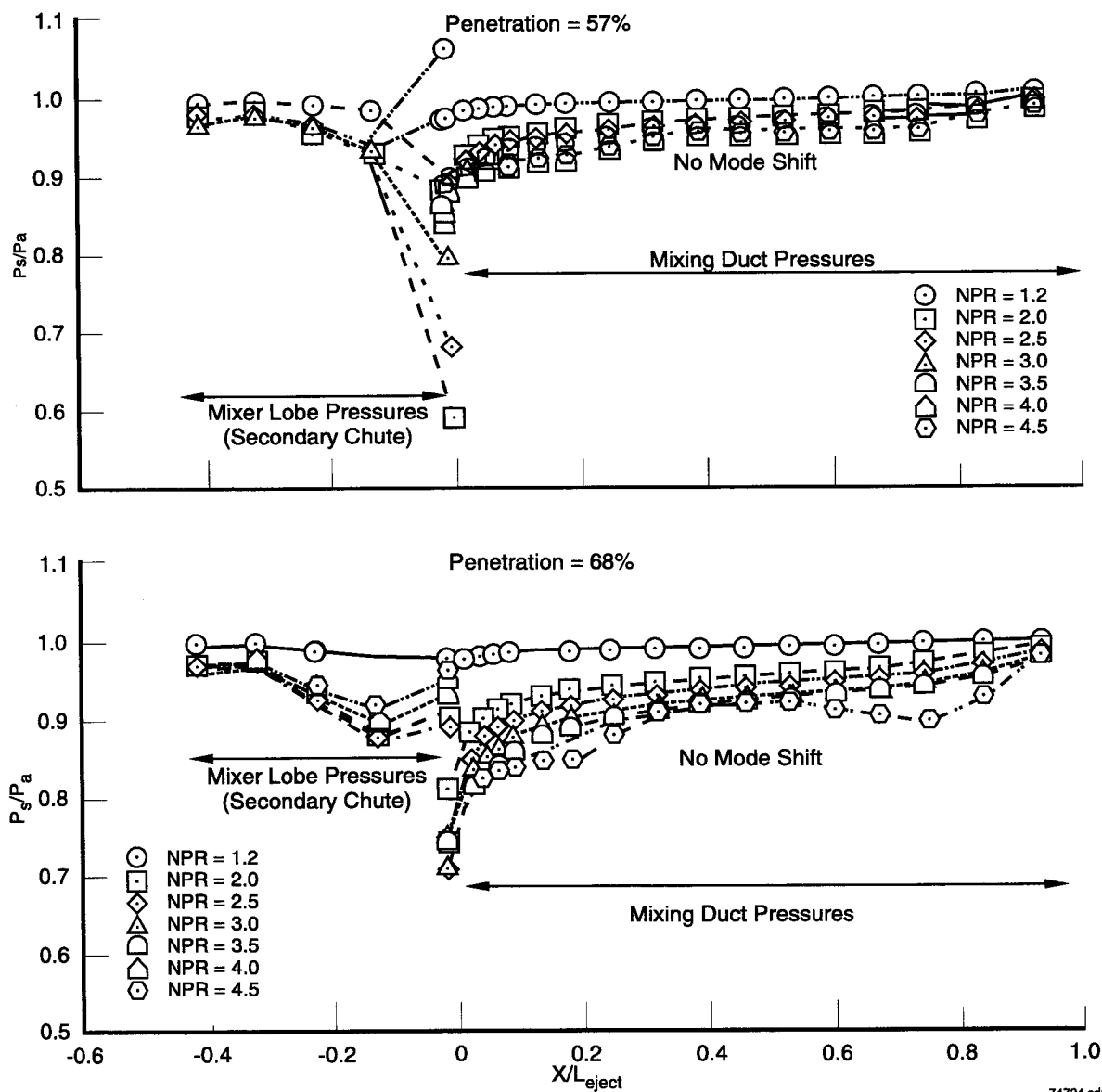


*Figure 45. Effect of MAR on Mode Shift Pressure Ratio*  
 $SAR = 3.0$ ,  $CER = 1.1$ ,  $PEN = 80\%$ , 20 Lobes,  $L_{mix}/D = 1.0$ ,  $L_{eject}/D = 3.0$ ,  $SNPR = 1.0$ ,  $Tt_p = 700^\circ F$

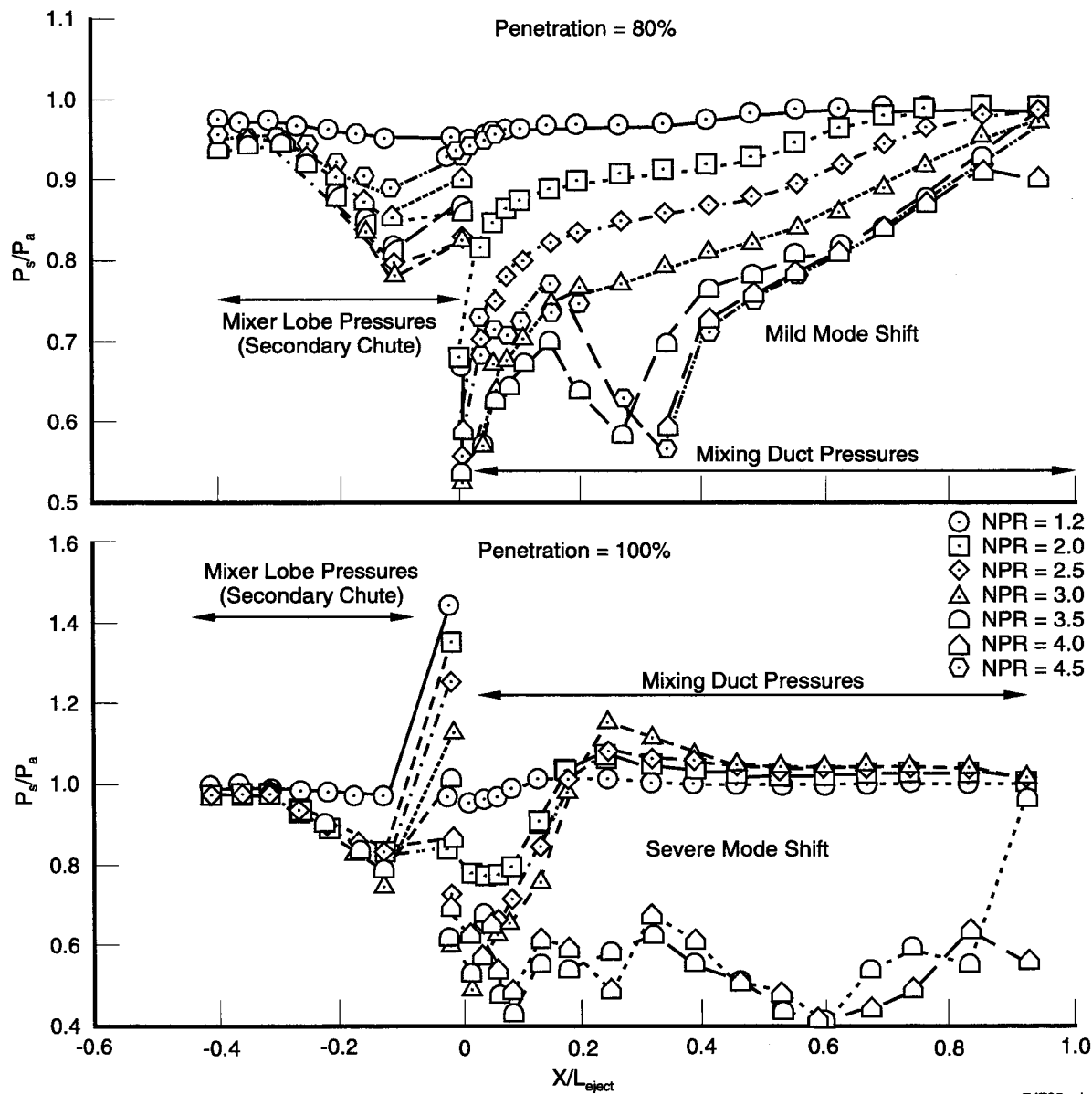


74724.cdr

Figure 46. Mixer External and Shroud Internal Static Pressures —  
Effect of Penetration

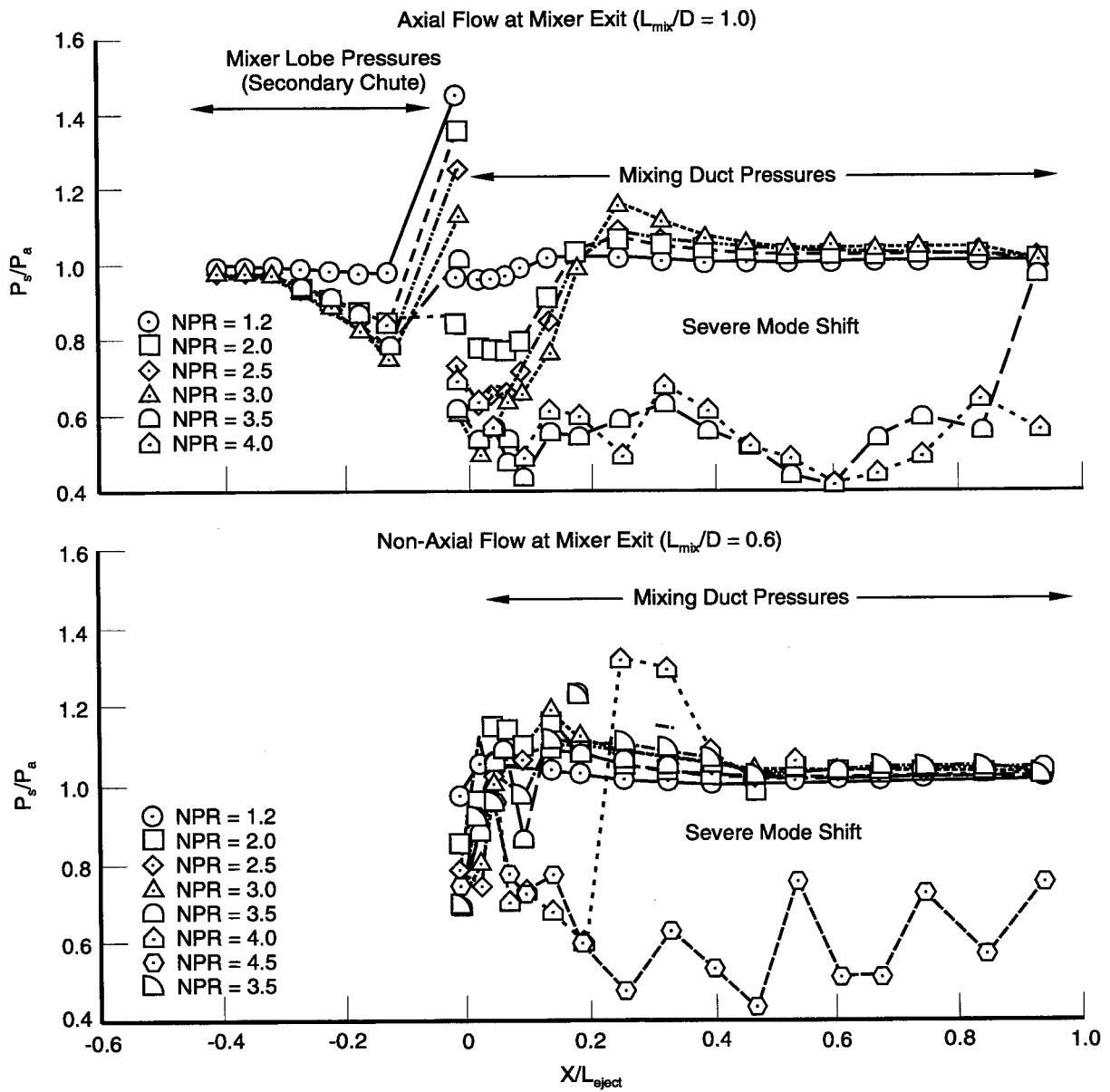
$SAR = 3.0$ ,  $CER = 1.1$ ,  $MAR = 95\%$ , 20 Lobes,  $L_{mix}/D = 1.0$ ,  $L_{eject}/D = 3.0$ ,  $SNPR = 1.0$ ,  $T_t = 700^\circ F$





74725.cdr

**Figure 46 (Concluded). Mixer External and Shroud Internal Static Pressures —**  
**Effect of Penetration**  
*SAR = 3.0, CER = 1.1, MAR = 95%, 20 Lobes,  $L_{mix}/D = 1.0$ ,  $L_{eject}/D = 3.0$ , SNPR = 1.0,  $T_{tp} = 700^\circ F$*



74726.cdr

*Figure 47. Mixer External and Shroud Internal Static Pressures —  
Effect of Axial Versus Nonaxial Mixer Exit Flow*  
*SAR = 3.0, CER = 1.1, MAR = 0.95, PEN = 100%, 20 Lobes,  $L_{eject}/D = 3.0$ , SNPR = 1.0,  $T_{tp} = 70^\circ F$*

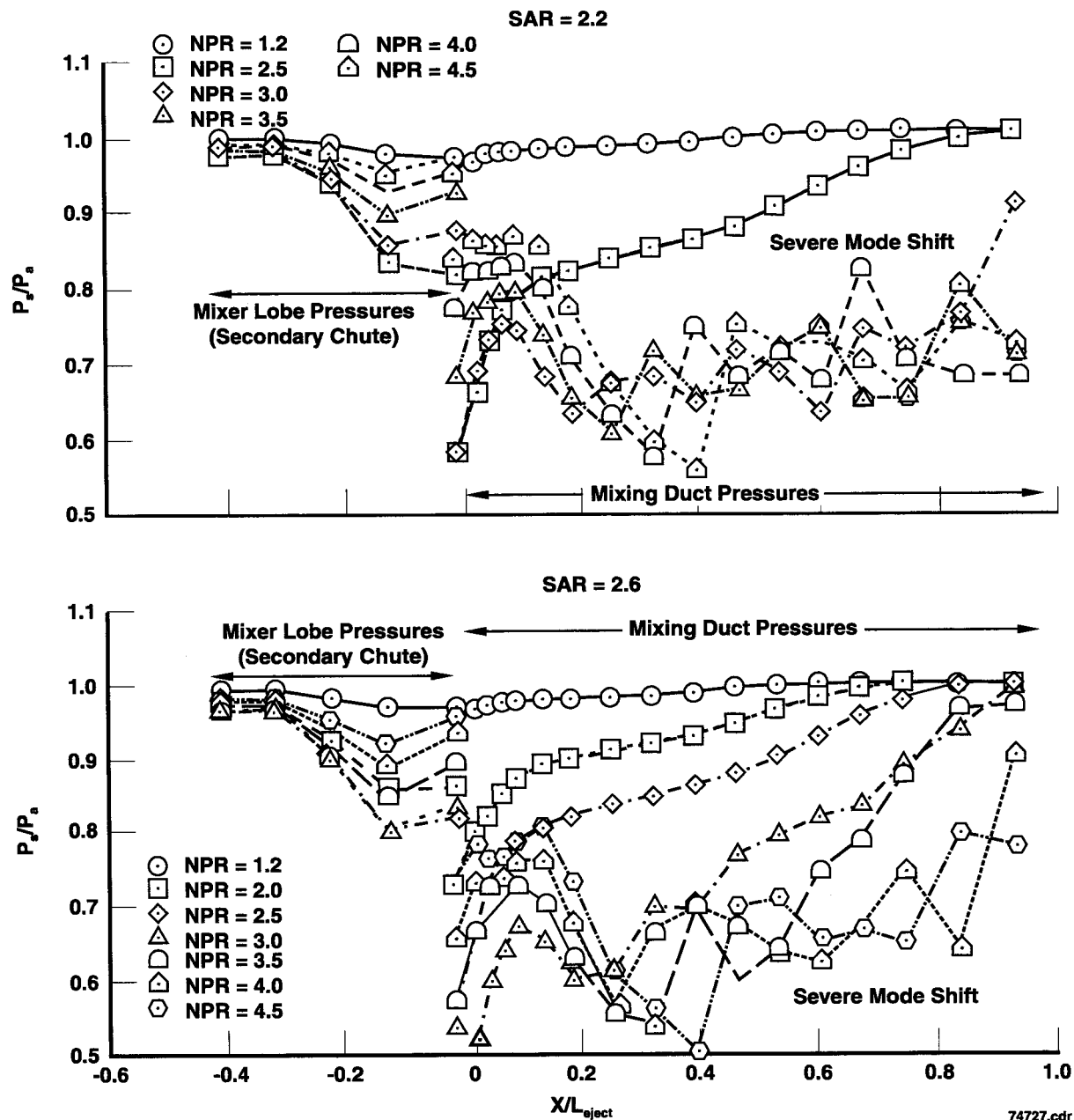
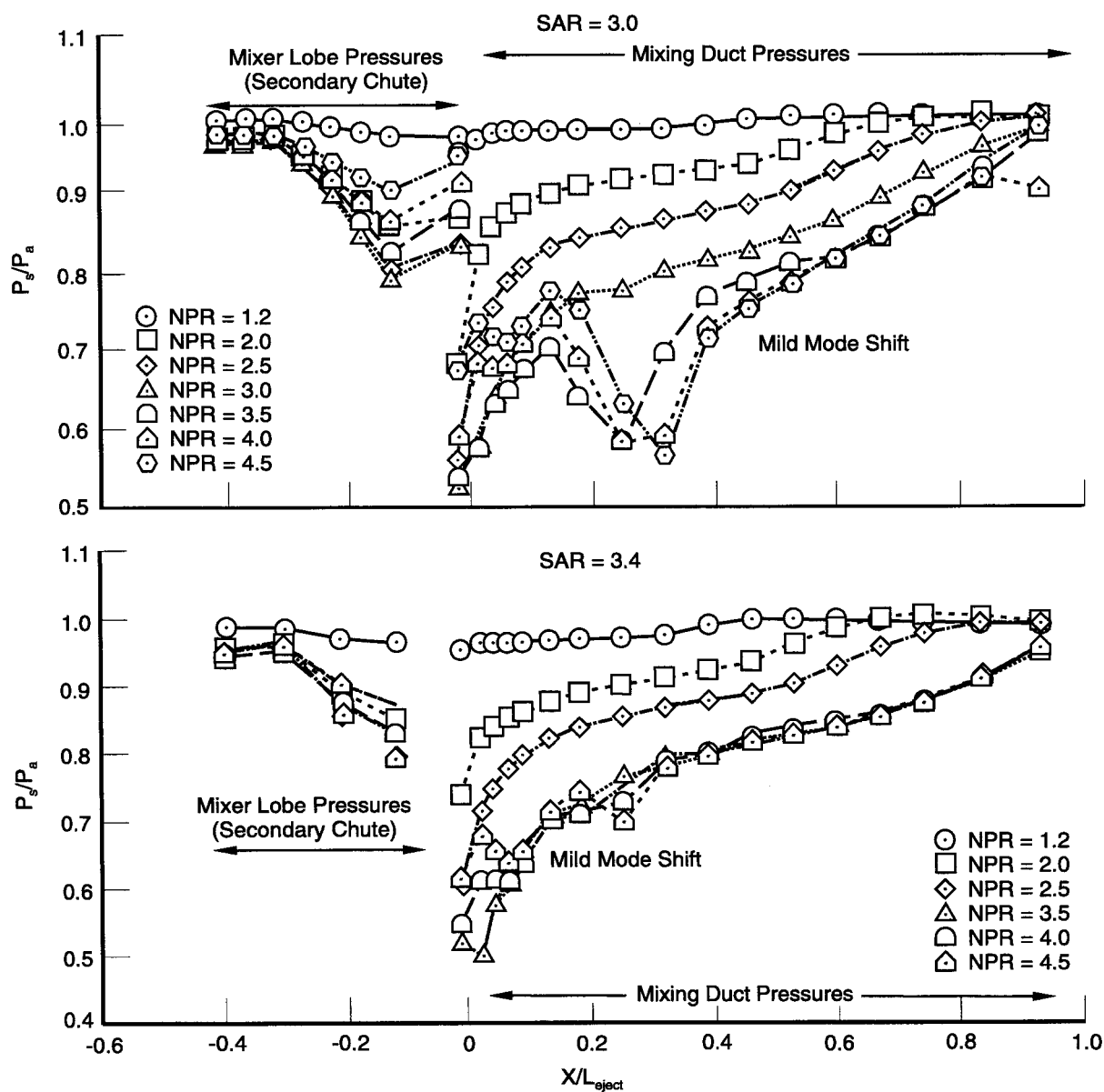


Figure 48. Mixer External and Shroud Internal Static Pressures —  
Effect of SAR

$CER = 1.1$ ,  $MAR = 0.95$ ,  $PEN = 80\%$ , 20 Lobes,  $L_{mix}/D = 1.0$ ,  $L_{eject}/D = 3.0$ ,  $SNPR = 1.0$ ,  $T_{tp} = 700^\circ F$



74728.cdr

*Figure 48 (Concluded). Mixer External and Shroud Internal Static Pressures —  
Effect of SAR  
CER = 1.1, MAR = 0.95, PEN = 80%, 20 Lobes,  $L_{mix}/D = 1.0$ ,  $L_{eject}/D = 3.0$ , SNPR = 1.0,  $Tt_p = 700^\circ F$*

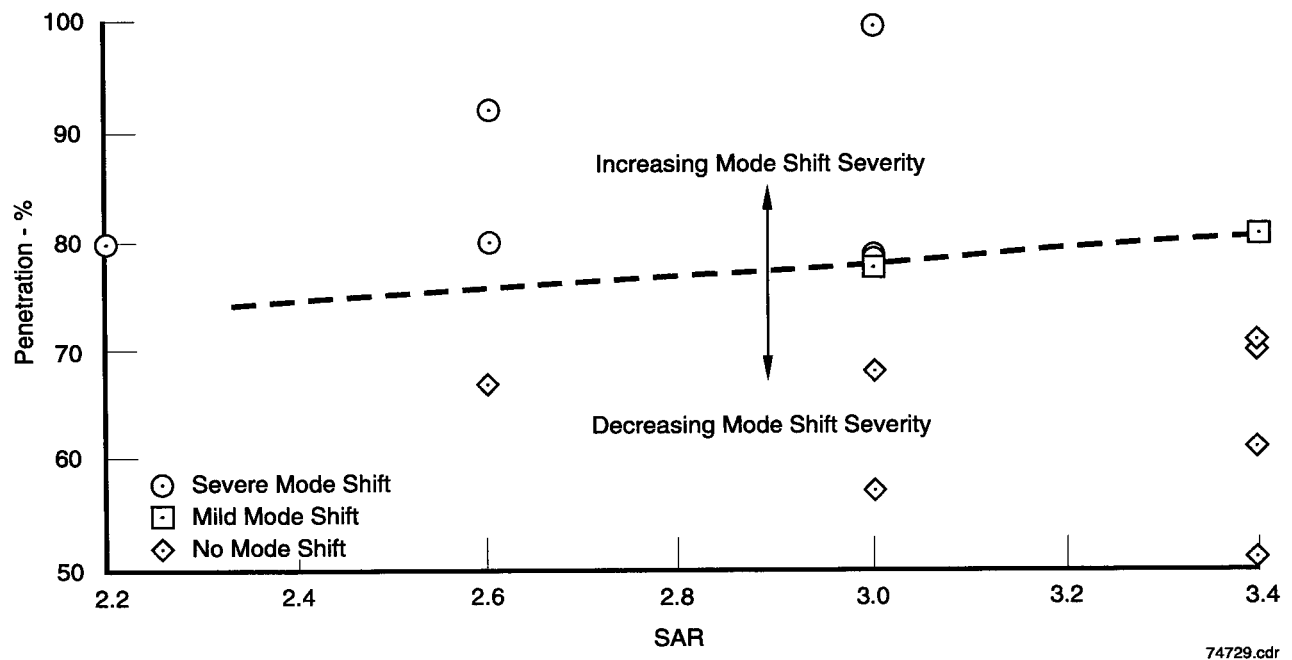
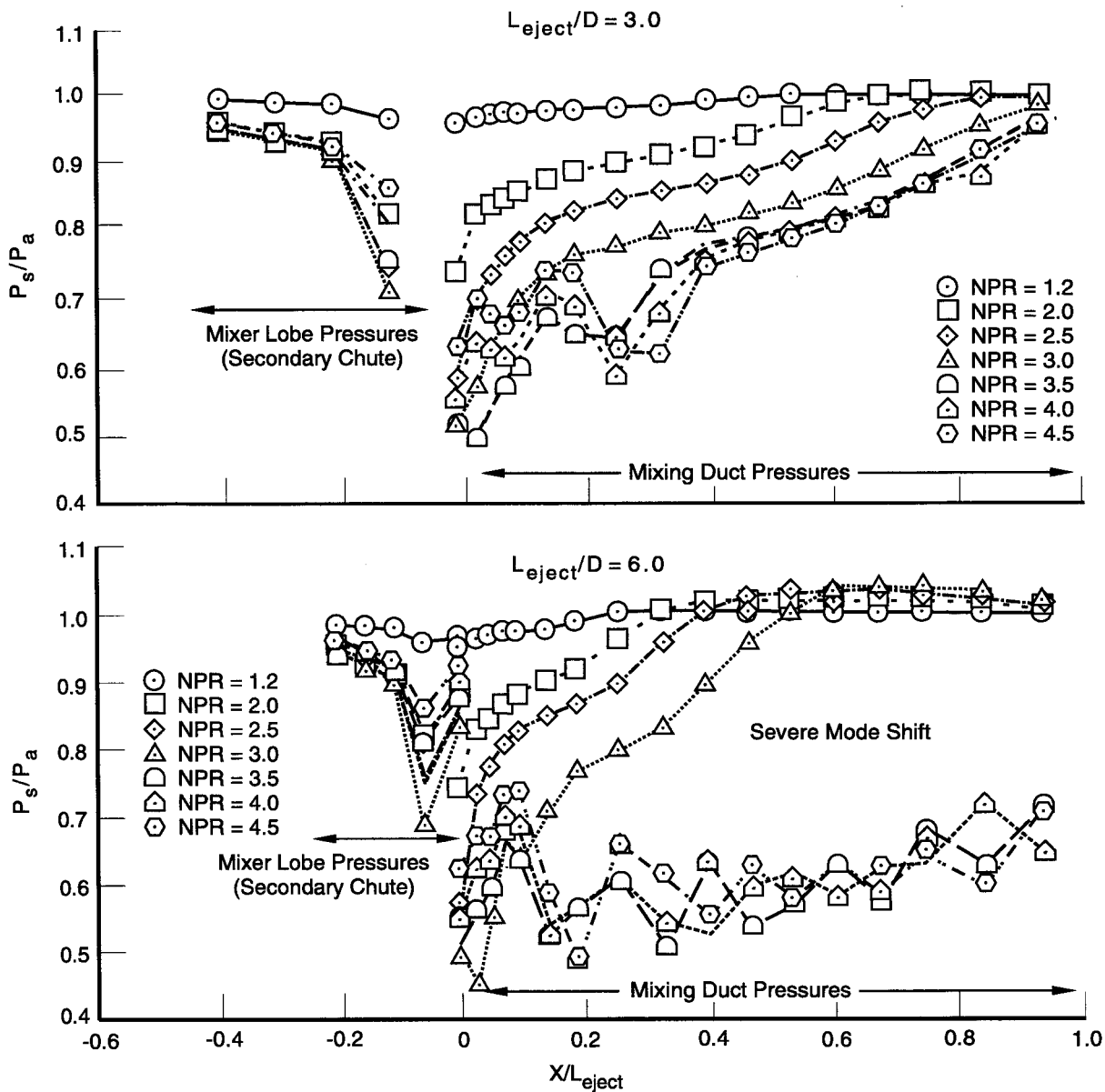


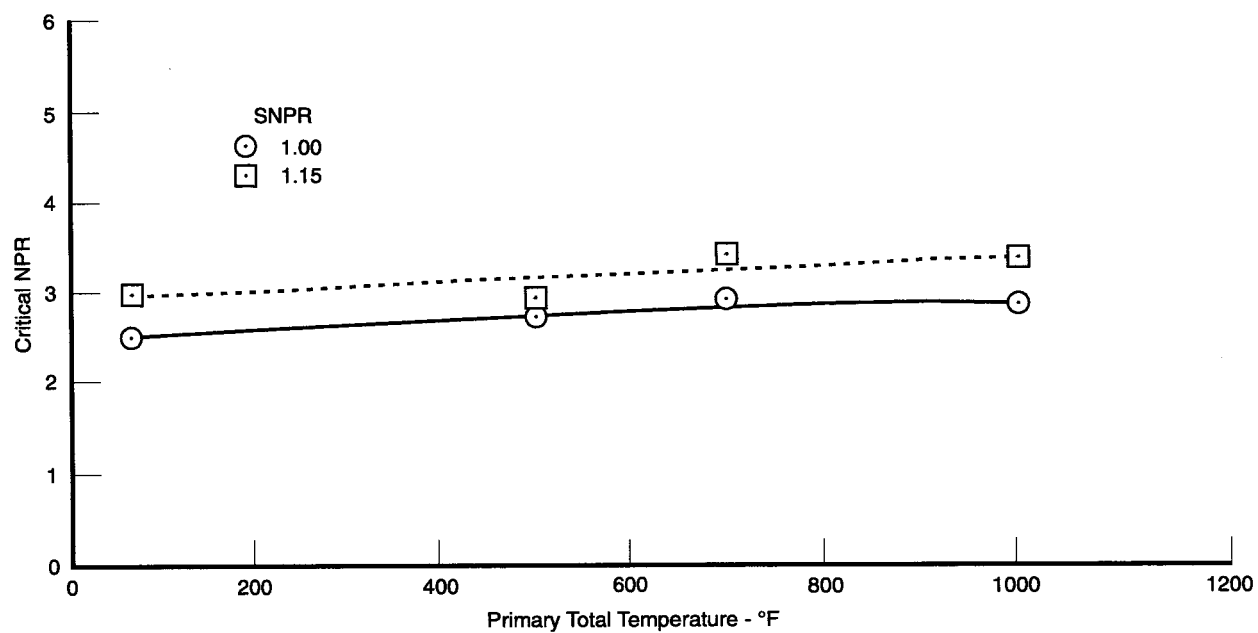
*Figure 49. Mode Shift Trends*  
 $CER = 1.1$ ,  $MAR = 0.95$ , 20 Lobes,  $L_{mix}/D = 1.0$ ,  $L_{eject}/D = 3.0$ ,  $SNPR = 1.0$ ,  $T_{tp} = 700^{\circ} F$



74732.cdr

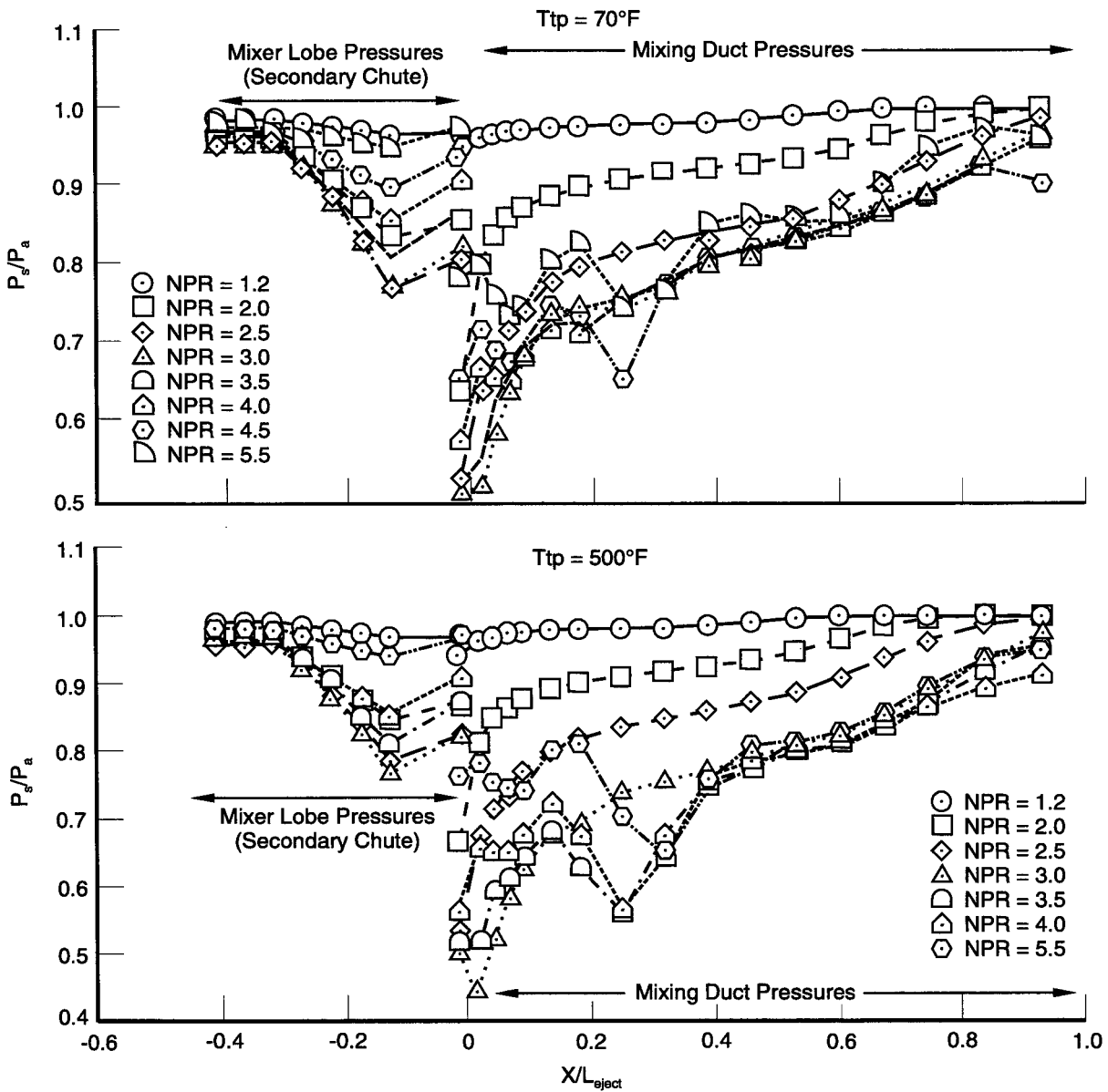
Figure 50. Mixer External and Shroud Internal Static Pressures —  
Effect of Mixing Duct Length

$SAR = 3.0$ ,  $CER = 1.1$ ,  $MAR = 0.95$ ,  $PEN = 80\%$ , 20 Lobes,  $L_{mix}/D = 1.0$ ,  $SNPR = 1.0$ ,  $T_{tp} = 700^\circ F$



74731.cdr

*Figure 51. Effect of Primary Total Temperature on Mode Shift Pressure Ratio*  
*SAR = 3.0, CER = 1.1, MAR = 0.95, PEN = 80%, 20 Lobes,  $L_{mix}/D = 1.0$ ,  $L_{eject}/D = 3.0$ , SNPR = 1.0*

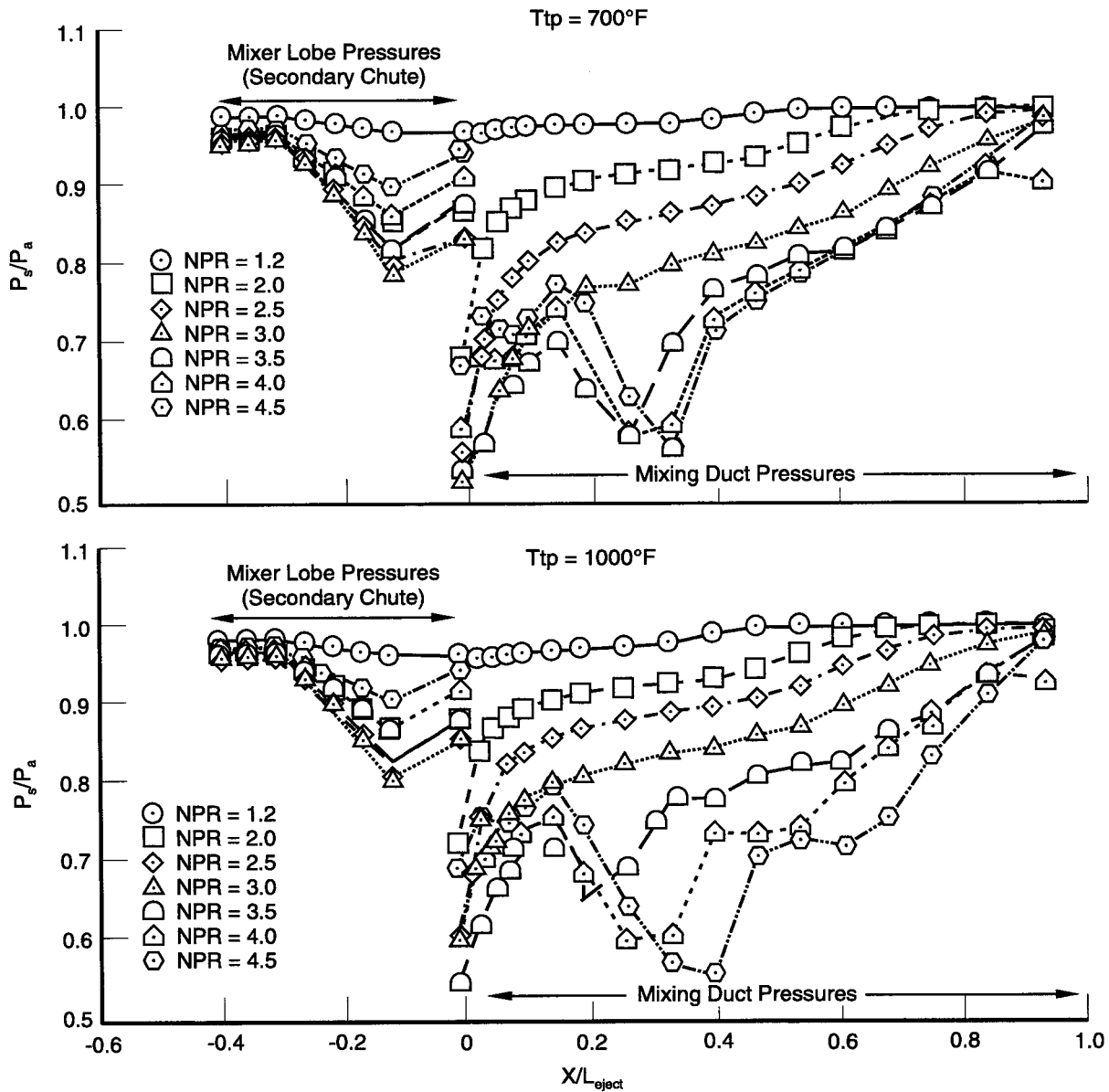


74730.cdr

Figure 52. Mixer External and Shroud Internal Static Pressures —  
Effect of Temperature

$SAR = 3.0$ ,  $CER = 1.1$ ,  $MAR = 0.95$ ,  $PEN = 80\%$ , 20 Lobes,  $L_{mix}/D = 1.0$ ,  $L_{eject}/D = 3.0$ ,  $SNPR = 1.0$





74733.cdr

Figure 52 (Concluded). Mixer External and Shroud Internal Static Pressures —  
Effect of Temperature  
 $SAR = 3.0$ ,  $CER = 1.1$ ,  $MAR = 0.95$ ,  $PEN = 80\%$ , 20 Lobes,  $L_{mix}/D = 1.0$ ,  $L_{eject}/D = 3.0$ ,  $SNPR = 1.0$

### 3.7.3 Discussion of Schlieren Photography

Schlieren videography was recorded at nozzle pressure ratios greater than or equal to 3.5 for most test configurations. Schlieren data were obtained to illustrate the differences in exit shock structures caused by variations in NPR, SNPR, MAR, PEN, and SAR. The baseline configuration is not included in this series of photos since the Schlieren system was not operational during the early part of the test. Even without this baseline configuration, however, the trends are readily visible. Figure 53 is included to describe what is being shown in the Schlieren photos.

The Schlieren photos indicate that, as would be expected, the exit shock structure becomes apparent at the condition at which the mode shift occurs. It then increases in strength and moves upstream (closer to the nozzle exit) as the exit velocity increases further. Figure 54 shows that this trend is observed with increasing nozzle pressure ratio while Figure 55 shows it with increasing secondary pressure ratio. Likewise, Figure 56 shows this trend with increasing MAR, and Figure 57 shows it with increasing penetration (at the design NPR and SNPR). The effects of SAR on the exit shock structure are shown in Figure 58 for a constant 80 percent penetration. SAR affects the shape and strength of the exit shocks but does not affect the presence of the mode shift, at least not for the range of SARs tested. Consistent with the static pressure data, the Schlieren photos indicate that, while SAR does affect the severity of the mode shift, it doesn't affect the critical NPR. The effects of primary total temperature are shown in Figure 59. For a given NPR and SNPR, the mode shift appears to be less severe at the higher temperature. However, considering that the pressure data indicates that the critical NPR increases from 3.0 at 70°F to 3.5 at 700°F, the Schlieren is probably showing a less severe mode shift at the higher temperature simply because it was taken at the critical NPR whereas it was taken above the critical NPR for the lower temperature. Thus, the Schlieren results are consistent with the static pressures in indicating the presence and strength of the mode shift.

Based on the results of the Schlieren photography, and consistent with the results of the static pressure data, the mode shift is very sensitive to the mixer lobe penetration and is affected to a lesser degree by MAR. Suppressor area ratio contributes to the severity of the mode shift but does not affect the nozzle pressure ratio at which it occurs.

## 3.8 CONCLUSIONS

Previous testing of mixer/ejector nozzles in support of the HSCT program included individual nozzles and single point designs supplied by P&W and GE without any common reference between them. As a result, conclusions were difficult, if not impossible, to determine from the existing database. Thus, it was obvious that a single parametric test was needed to incorporate all of the critical design concerns so that direct comparisons could be made and conclusions drawn. This test was a much-needed parametric test which was conducted as a joint effort between P&W and GE.

This test successfully demonstrated the aerodynamic viability of a mixer/ejector nozzle for the HSCT program. The baseline geometry demonstrated gross thrust performance levels (normalized by the ideal thrust of the primary flow) of approximately 1.04 for secondary pressures near ambient and an NPR of 3.5. By using a 16-lobe mixer, this performance could be expected to go as high as 1.055 since the 16-lobe mixer has been shown to provide a thrust benefit of 1.5 percent over the baseline 20-lobe mixer. For the design point of NPR = 3.5 and secondary pressures near ambient, optimum performance was obtained at a MAR of 0.90. A long mixer was found to be effective in minimizing the secondary losses. Although a short mixing duct may be beneficial to maximize the performance at lower NPRs, the mixing duct length is not a critical performance concern at and above the design nozzle pressure ratio.

Since the data has shown that secondary losses are critical to the overall nozzle performance, it is important that these losses be minimized to provide the best aerodynamic design. Thus, the design of the secondary inlets are critical to the actual levels of thrust attained for the HSCT nozzle.

Mode shift is a condition observed in mixer/ejector nozzles when the flow in the mixing duct transitions from subsonic to supersonic in nature. The occurrence of this condition is usually accompanied by a shift in shroud static pressures. For certain geometries, this shift can be quite drastic, causing a high dynamic load on the shrouds and sidewalls. Although the mode shift may not always be eliminated entirely, its effects may be greatly reduced by applying the results of this test. This test revealed the following trends:

- The tendency for mode shift was basically eliminated at MARs of less than 0.90.
- The tendency to mode shift was closely related to penetration. High penetrations (100 percent) caused severe mode shifts while lower penetrations reduced the severity of and the tendency to mode shift.
- The tendency for mode shift was related to shroud length (mixing duct length). The longer the shroud, the greater the severity of and the tendency to mode shift.

### 3.9 RECOMMENDATIONS

Typical gross thrust performance levels (normalized by the ideal thrust of the primary flow) for the baseline configuration operating at the anticipated HSCT design point are approximately 1.04. This performance may be improved by using a mixer with fewer than 20 lobes or by shaping the lobes to provide better secondary flow aerodynamics. Mixer lobe penetrations of greater than 80 percent reduce nozzle performance and should be avoided unless they are necessary for achieving the required acoustic suppression. If this is the case, then trade studies between nozzle performance and acoustic suppression would be required.

Although the phenomenon of mode shifting in the mixing duct has been demonstrated in previous tests and has been found to induce a sudden change in internal static pressures, this testing has shown that it is possible to experience a mode shift without the associated pressure shift. Thus, the mode shift is not necessarily undesirable and may be controlled by following certain design guidelines, outlined as follows:

- Mixing duct area ratio should be limited to a maximum value of 0.90 (which is also beneficial for optimum performance).
- Penetration should be limited to a maximum value of 80 percent and should be further reduced at lower levels of SAR.
- Shroud length (mixing duct length) should be minimized. The longer the shroud, the greater the tendency for mode shift.

Based on the results from this test, it is recommended that additional acoustic testing be conducted to determine the actual effects of mixer lobe count, penetration, and chute shaping on noise suppression since the optimum acoustic design point may not coincide with the optimum aerodynamic design point. Design trade-offs must be understood so that they may be used to provide the best combination of acoustic suppression and nozzle performance.

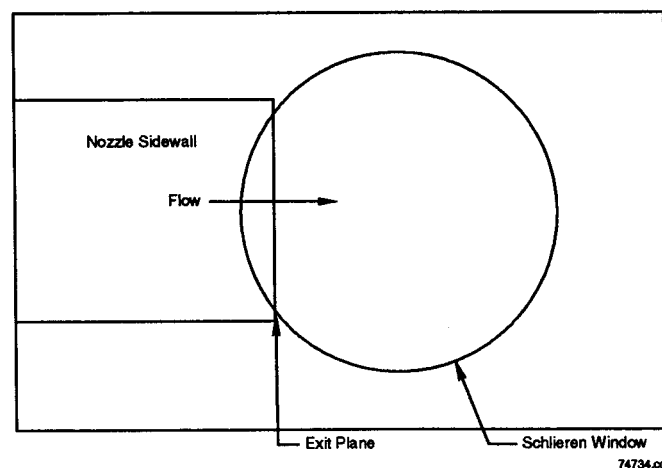
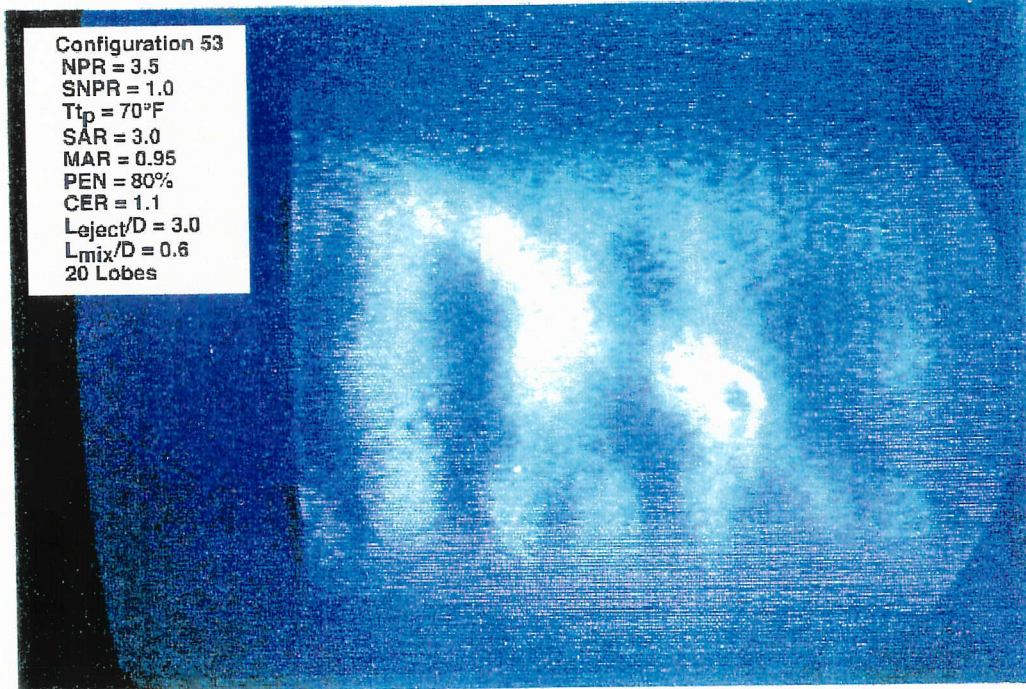


*Figure 53. View Shown in Typical Schlieren Photograph*

a) NPR = 3.5



b) NPR = 4.5

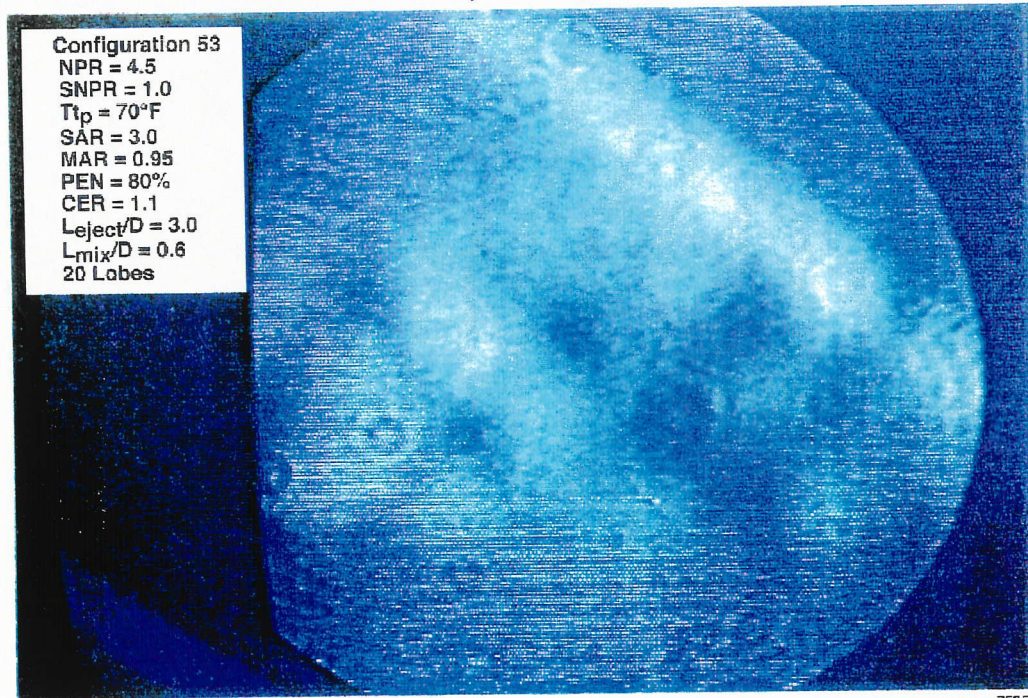
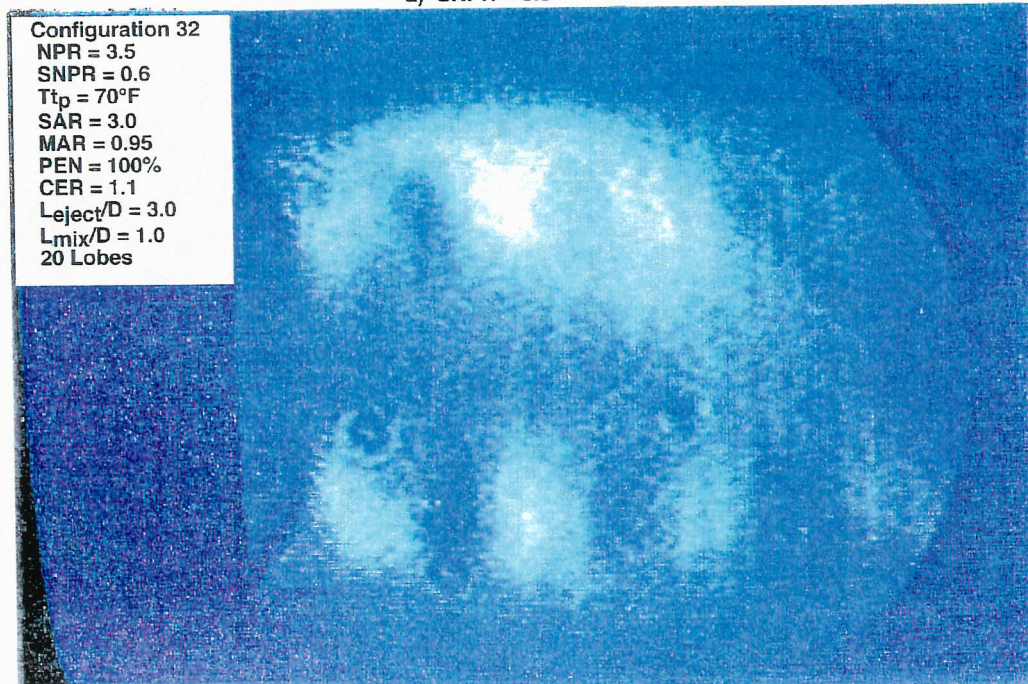


Figure 54. Schlieren Photography Showing NPR Effects



a) SNPR = 0.6



b) SNPR = 0.9

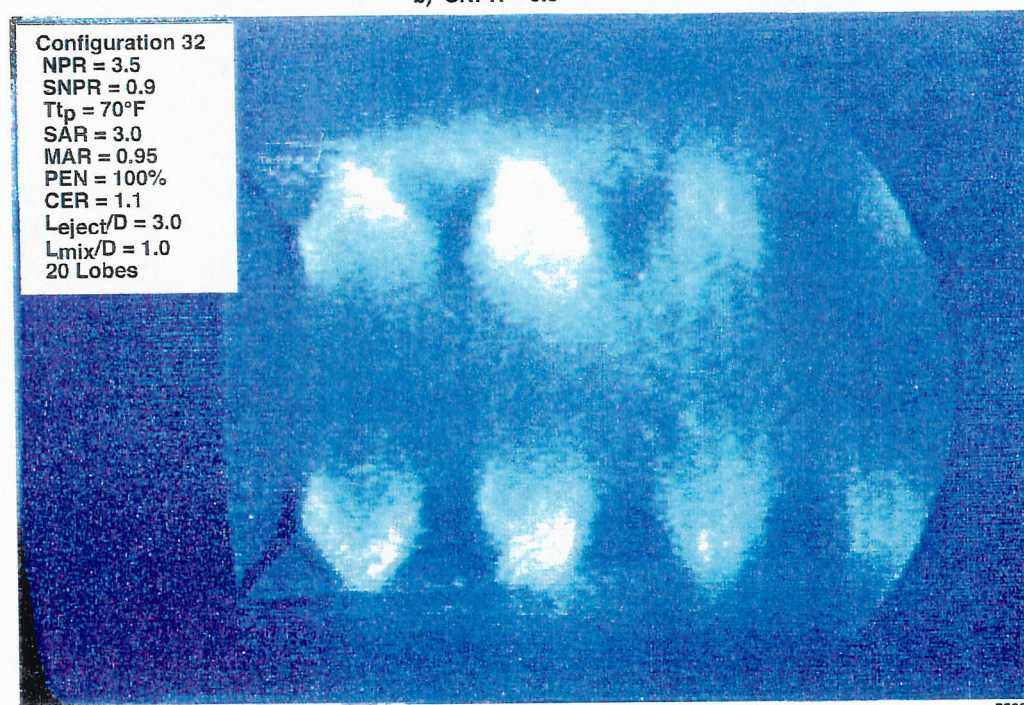
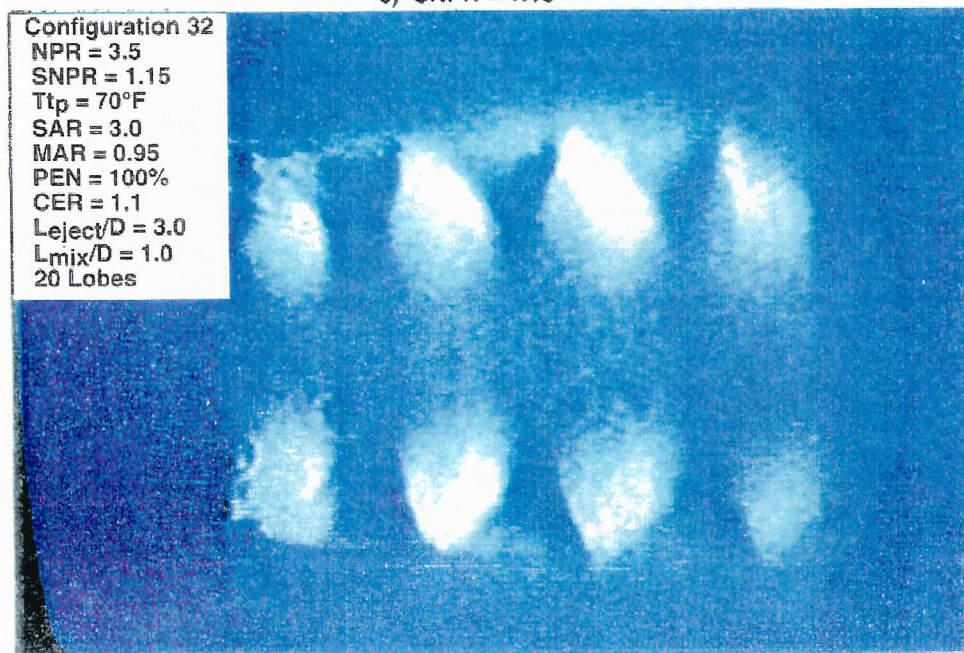


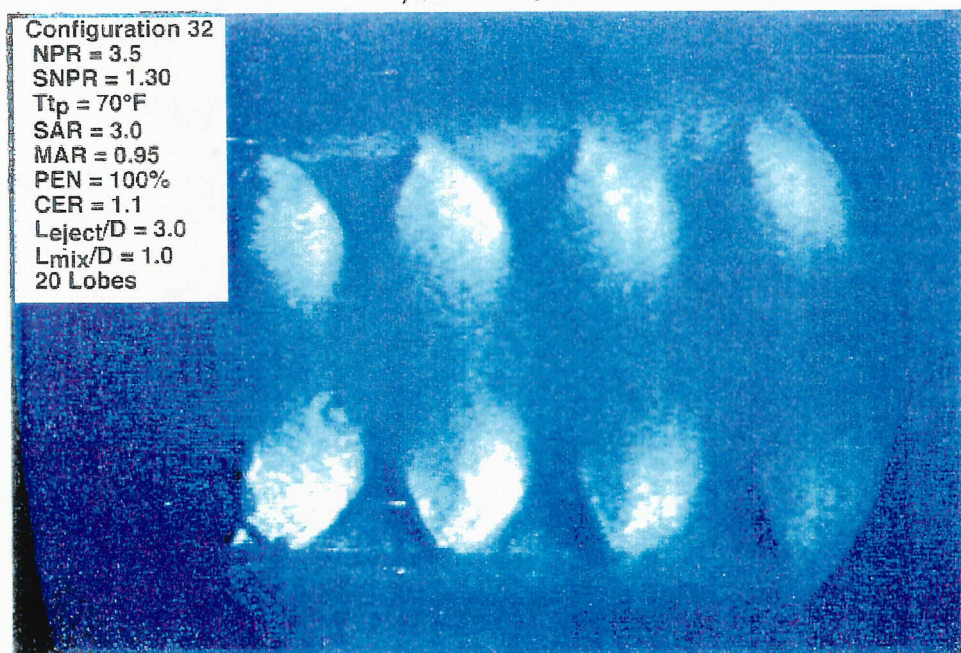
Figure 55. Schlieren Photography Showing SNPR Effects



c) SNPR = 1.15



d) SNPR = 1.30

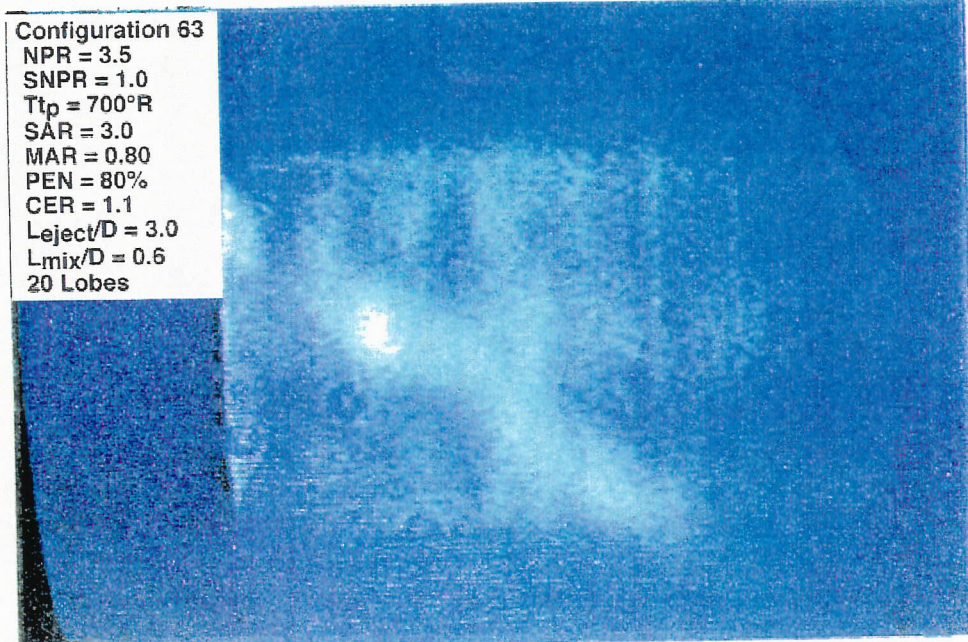


75954

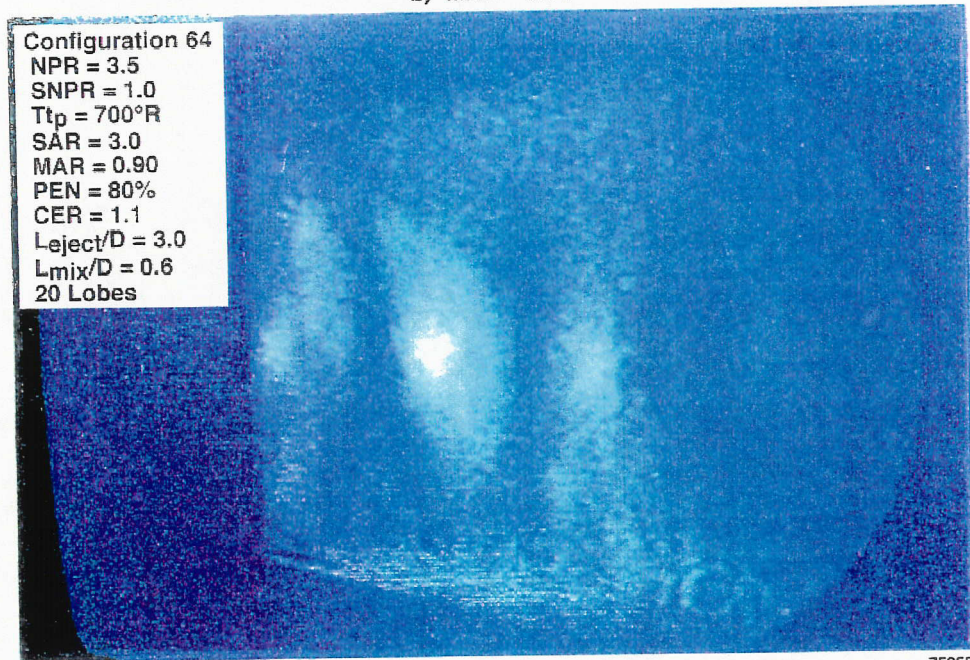
Figure 55 (Concluded). Schlieren Photography Showing SNPR Effects



a) MAR = 0.80



b) MAR = 0.90

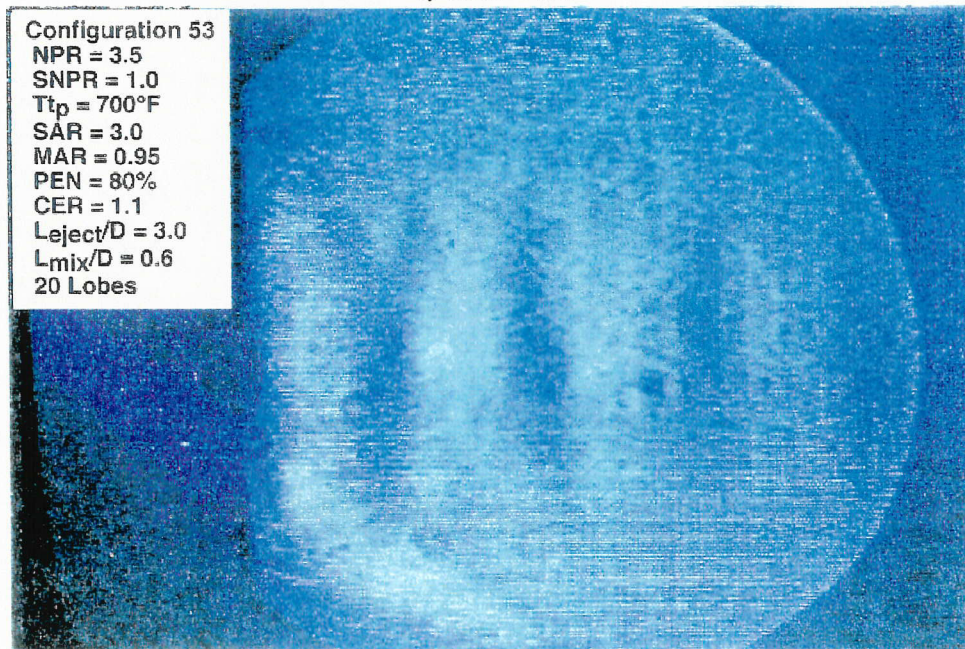


75965

Figure 56. Schlieren Photography Showing MAR Effects



c) MAR = 0.95



d) MAR = 1.20

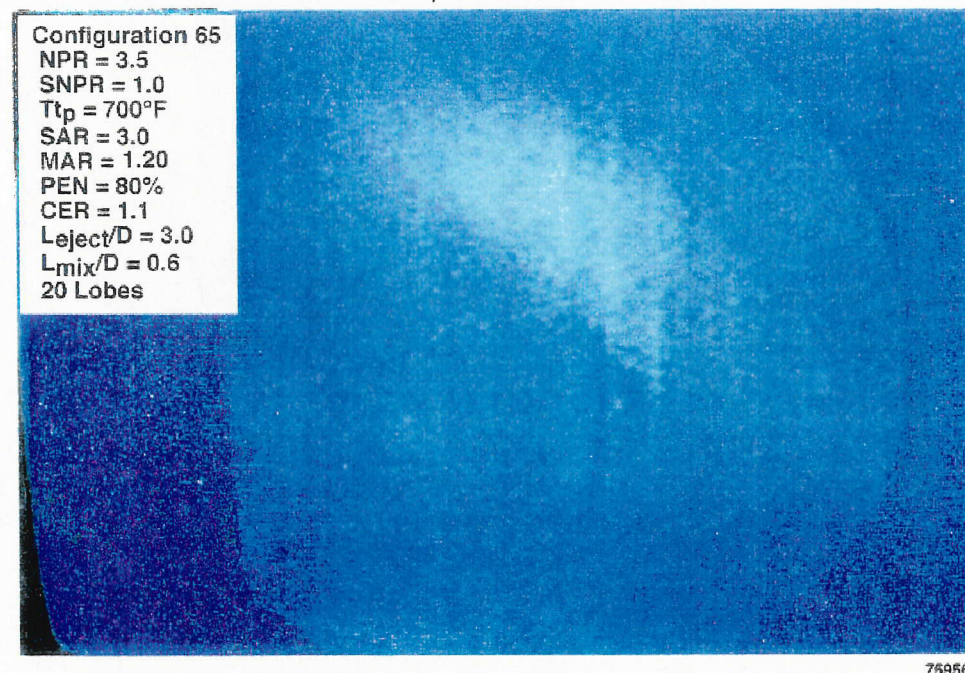
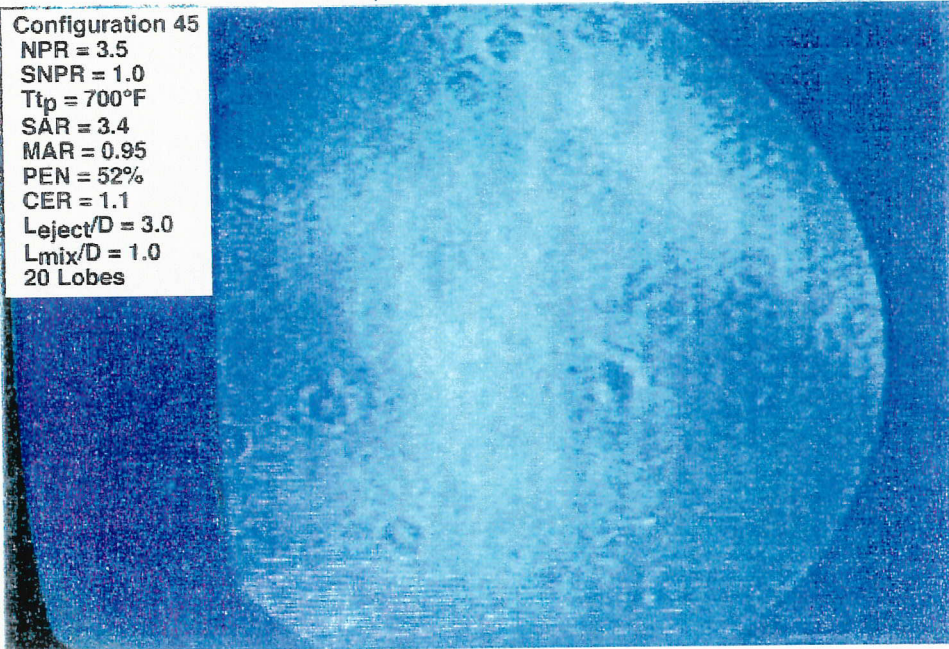


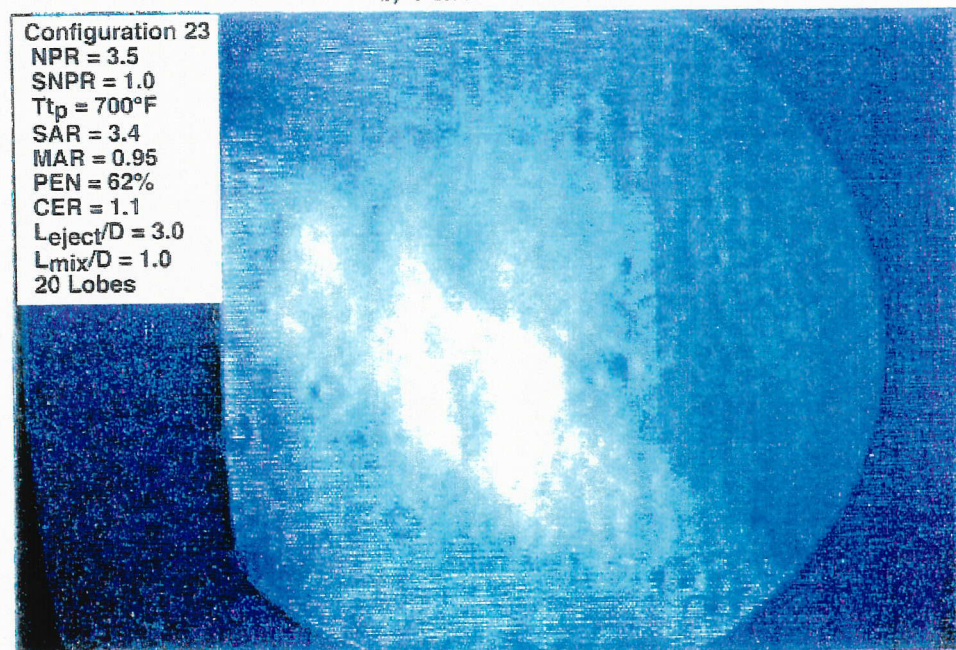
Figure 56 (Concluded). Schlieren Photography Showing MAR Effects



a) Penetration = 52%



b) Penetration = 62%

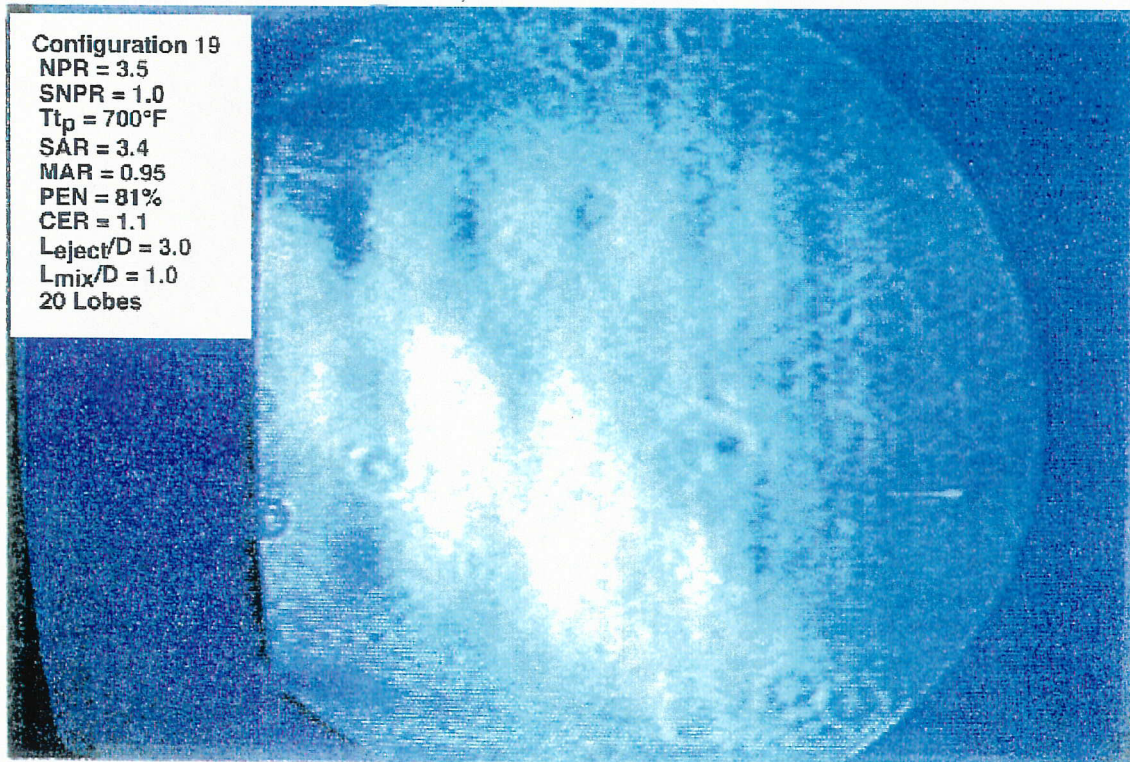


75957

Figure 57. Schlieren Photography Showing Penetration Effects



c) Penetration = 81%

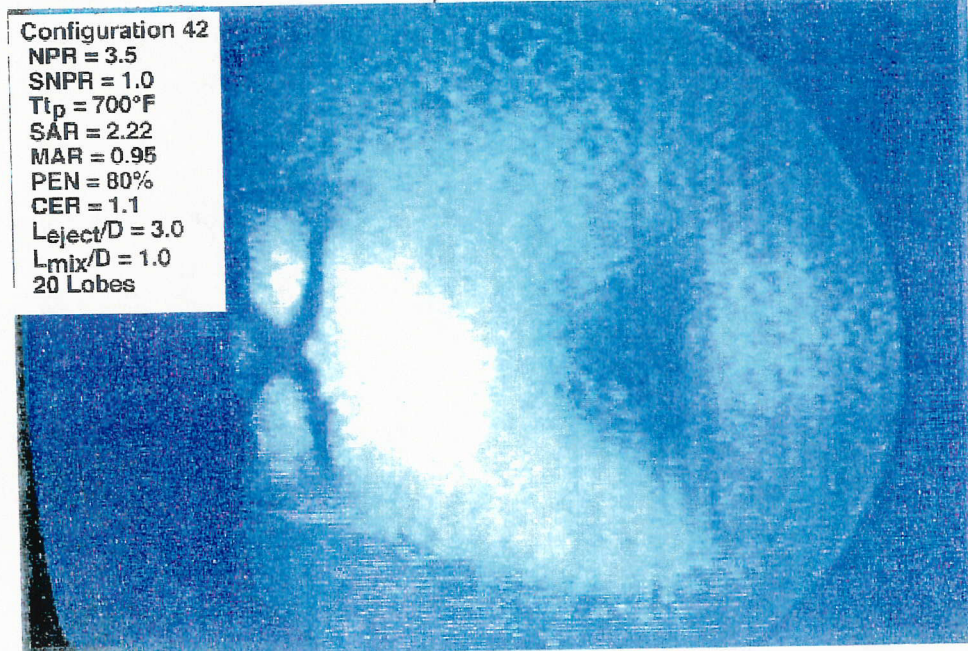


75958

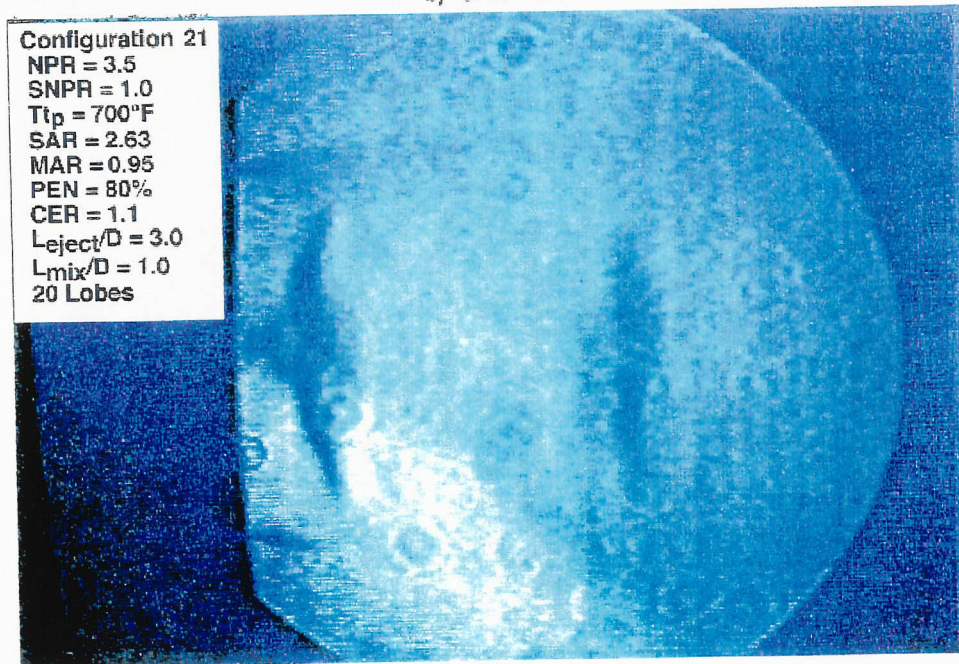
*Figure 57 (Concluded). Schlieren Photography Showing Penetration Effects*



a) SAR = 2.2



b) SAR = 2.6



77554

Figure 58. Schlieren Photography Showing SAR Effects



b) SAR = 3.4

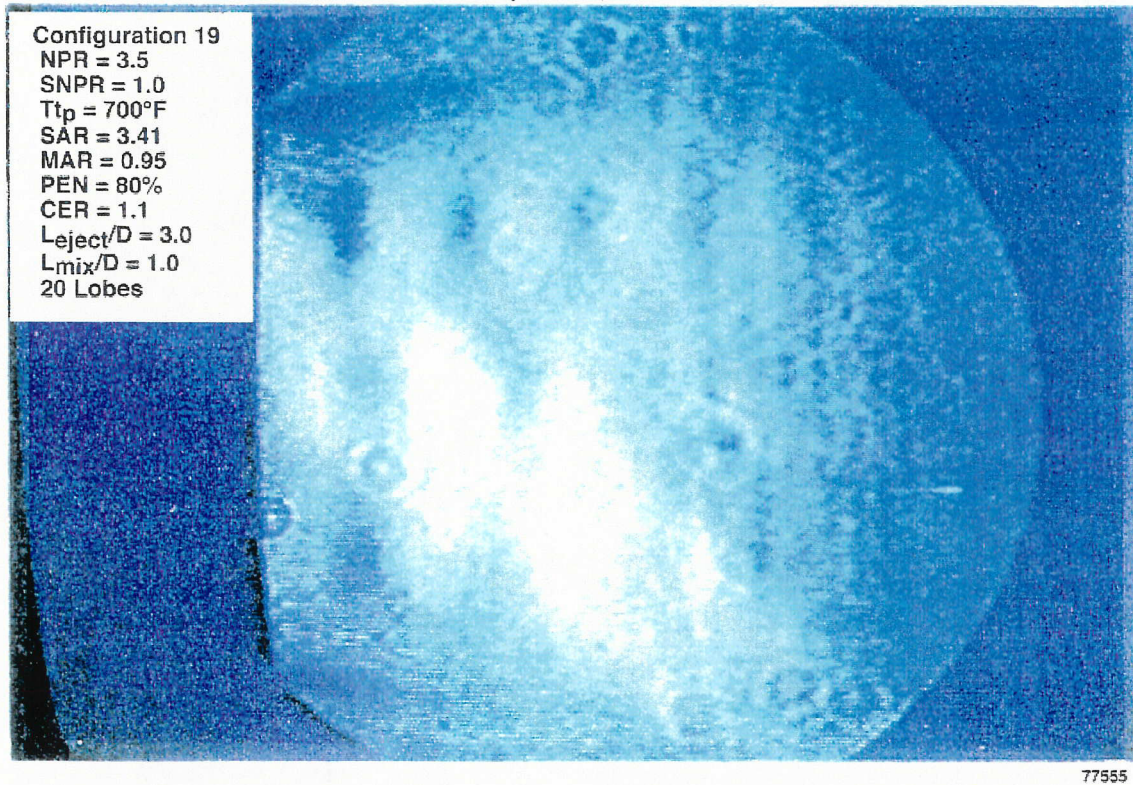
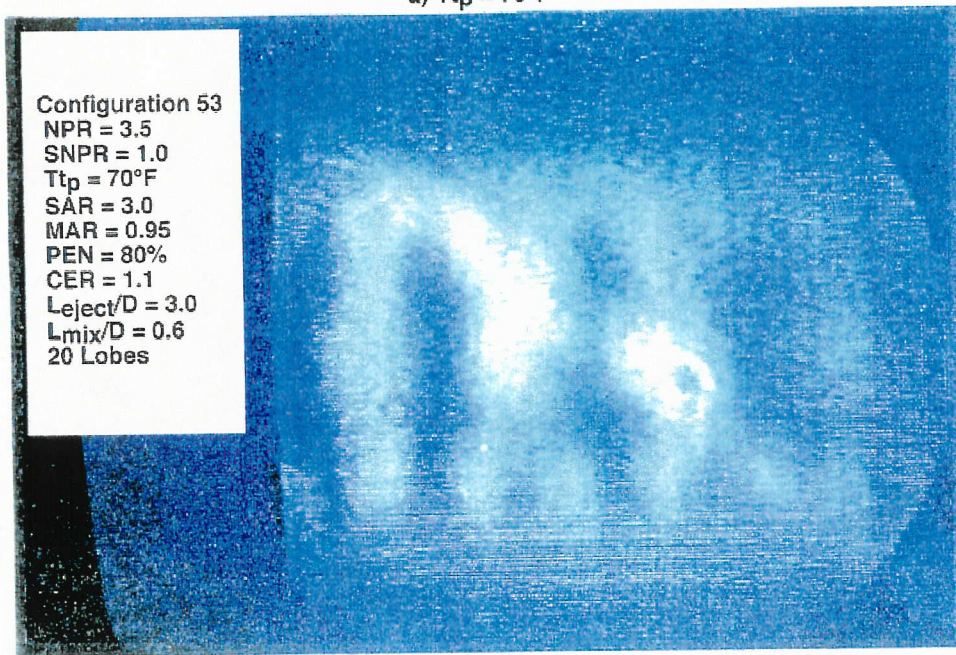


Figure 58 (Concluded). Schlieren Photography Showing SAR Effects



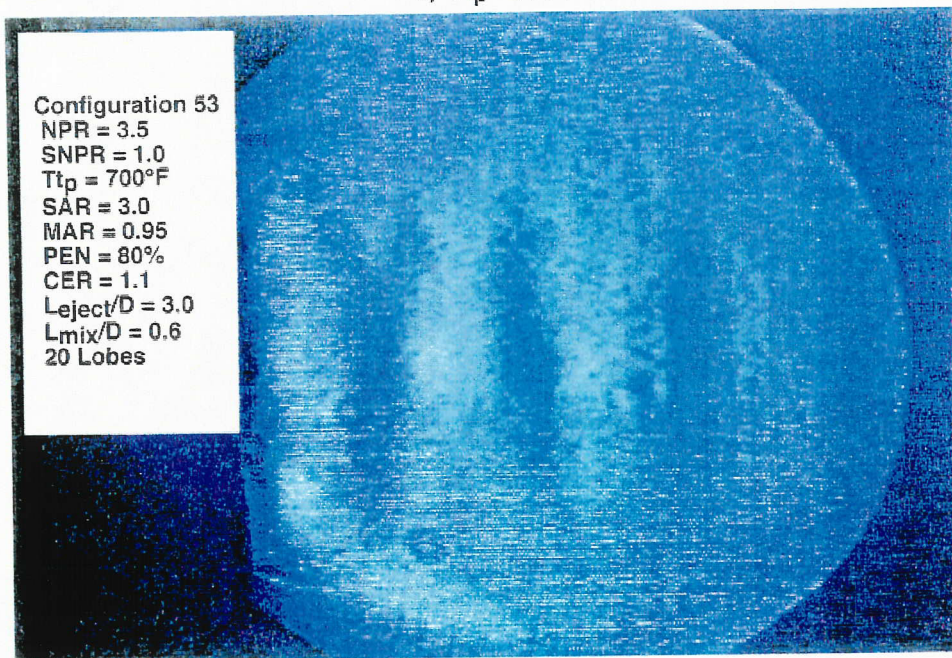
a)  $T_{tp} = 70^{\circ}\text{F}$

Configuration 53  
NPR = 3.5  
SNPR = 1.0  
 $T_{tp} = 70^{\circ}\text{F}$   
SAR = 3.0  
MAR = 0.95  
PEN = 80%  
CER = 1.1  
 $L_{\text{eject}}/D = 3.0$   
 $L_{\text{mix}}/D = 0.6$   
20 Lobes



b)  $T_{tp} = 700^{\circ}\text{F}$

Configuration 53  
NPR = 3.5  
SNPR = 1.0  
 $T_{tp} = 700^{\circ}\text{F}$   
SAR = 3.0  
MAR = 0.95  
PEN = 80%  
CER = 1.1  
 $L_{\text{eject}}/D = 3.0$   
 $L_{\text{mix}}/D = 0.6$   
20 Lobes



77556

Figure 59. Schlieren Photography Showing Temperature Effects

## APPENDIX 3-A

### TERMS AND DEFINITIONS

#### **Aerodynamic Terms**

$Cd_p = W_p/W_{idp}$	Primary Flow Coefficient
$C_{FG} = F/F_{idp}$	Thrust Coefficient
$C_{FGcor} = F'/F_{idp}'$	Thrust Coefficient Corrected to Constant $A_j$
$CR_p = W_p/W_p'$	Primary Flow Correction Ratio (used to scale primary flow to constant $A_jCd=10 \text{ in.}^2$ )
$CR_s = W_s/W_s'$	Secondary Flow Correction Ratio (used to scale secondary flow to constant $A_jCd=10 \text{ in.}^2$ )
$F$	Measured Thrust ( $lb_f$ )
$F'$	Thrust Corrected to Constant $A_j$ ( $lb_f$ )
$F_{idp}$	Ideal thrust ( $lb_f$ )
$F_{idp}'$	Ideal Thrust Corrected to Constant $A_j$ ( $lb_f$ )
$NPR = P_{t_p}/P_a$	Nozzle Pressure Ratio (primary)
$P_a$	Ambient Pressure (psia)
$P_e$	Calculated Exit Static Pressure (psia)
$P'$	Exit Static Pressure Corrected to Constant $A_jCd$ (psia)
$P_s$	Static Pressure (psia)
$P_s/P_a$	Static Pressure Normalized by Ambient Pressure (dimensionless)
PSES01–PSES40	Static Pressure Header for Taps Located on the Mixing Duct Shroud (psia)
PSSW01–PSSW20	Static Pressure Header for Taps Located on the Mixing Duct Sidewall (psia)
PTEJ01–PTEJ05	Total Pressure Header for Probes Located on the Secondary Inlet Total Pressure Rake (psia)
PTPL01–PTPL03	Total Pressure Header for Probes Located on the Mixer Lobes in the Secondary Flow (psia)
$P_{t_p}$	Primary Total Pressure (psia)
$P_{t_s}$	Secondary Total Pressure (psia)
$T_{t_p}$	Primary Total Temperature ( $^{\circ}R$ )
$T_{t_s}$	Secondary Total Temperature ( $^{\circ}R$ )
$SNPR = P_{t_s}/P_a$	Secondary Nozzle Pressure Ratio
$V_e$	Calculated Exit Velocity (ft/s)

$V'$	Exit Velocity Corrected to Constant $A_jCd$ (ft/s)
$W_{idp}$	Primary Ideal Flow Rate (lbm/s)
$W_p$	Primary Flow Rate (lbm/s)
$W_p'$	Corrected Primary Flow Rate (lbm/s) (scaled to constant $A_jCd = 10 \text{ in.}^2$ )
$W_s$	Secondary Flow Rate (lbm/s)
$W_s'$	Corrected Secondary Flow Rate (lbm/s) (scaled to Constant $A_jCd = 10 \text{ in.}^2$ )

$$WSWPC = \omega\sqrt{\tau} = \frac{W_s}{W_p} \sqrt{\frac{Tts}{Ttp}}$$

Temperature-Corrected Flow Ratio

$$WTFLC = (\omega\sqrt{\tau})_{cor} = \frac{W_s'}{W_p'} \sqrt{\frac{Tts}{Ttp}}$$

Temperature-Corrected Flow Ratio of Flows

Corrected to  $10 \text{ in.}^2$  Primary Choked Flow Area

### **Geometric Terms**

$A_b$	Base Area of Mixer ( $\text{in.}^2$ )
$A_j = A_8$	Physical Primary Choke Area ( $\text{in.}^2$ )
$A_jCd$	Aerodynamic Primary Choke Area (flow area, $\text{in.}^2$ )
$A_m$	Cross-sectional Area of Mixing Plane ( $\text{in.}^2$ )
$A_p$	Cross-sectional Area of Primary at Mixer Exit ( $\text{in.}^2$ )
$A_s$	Cross-sectional Area of Secondary at Mixer Exit ( $\text{in.}^2$ )
$ASAR = A_m/(A_jCd)$	Aerodynamic Suppressor Area Ratio
$A_9$	Cross-sectional Area at Nozzle Exit ( $\text{in.}^2$ )
$CER = A_p/A_j$	Chute Expansion Ratio, or expansion ratio of primary flow at the exit of the mixer chutes
$D = \text{SQRT}(4*A_j/\pi)$	Equivalent Diameter of Throat (in.)
$H_m = A_m/W$	Height of Mixing Plane (in.)
$H_9 = A_9/W$	Height of Nozzle Exit (in.)
$L_{eject}$	Shroud Length, or Mixing Duct Length (in.)
$L_{mix}$	Mixer Length (in.)
$MAR = A_9/A_m$	Mixing Duct Area Ratio
Mixer $L/D = L_{mix}/D$	Length of Mixer Chutes Normalized by the Equivalent Diameter of the Primary Choked Area

$SAR = A_m/A_j$

Suppressor Area Ratio

shroud  $L/D = L_{eject}/D$

Length of Mixing Duct Normalized by the  
Equivalent Diameter of the Primary Choked Area

$PEN = \text{penetration}$

Mixer Lobe Height Normalized by the Height of the  
Mixing Plane (expressed in percent)

$W$

Width of Nozzle Flowpath (in.)

$X/L_{eject}$

Distance Downstream of Mixing Plane  
Normalized by the Shroud Length (dimensionless)



## **APPENDIX 3-B**

### **HISTORICAL BACKGROUND FOR GEN 1.5 TESTING**

In NASA/industry meetings prior to the start of this program, discussions indicated that noise-suppressing exhaust nozzle technology for a future high-speed civil transport aircraft had progressed to a point where small-scale model testing was needed to provide the data base for predicting thrust coefficients. Previous model testing had been concentrated on point designs to show the feasibility of using mixer/ejector nozzles to reach acceptable takeoff noise levels. Acoustic tests had indicated that the noise reduction goal was achievable. However, very little test data was available on the effects of mixer/ejector variables on internal mixing and performance. One test conducted in November 1992 at NASA-Langley showed that relatively small changes in shroud geometry had large effects on thrust coefficients. Exit traverse data was taken on a few configurations, but not enough to determine if mixing was affected in the same manner as the thrust data. Hence, this program was initiated to provide an approach to developing a data base that will allow accurate prediction of mixing and performance over a large range of mixer/ejector nozzle geometries.

Based on existing HSR performance data, P&W worked with GEAE and Boeing to identify geometric and aerodynamic variables that would have the greatest effect on the performance and mixing of current mixer/ejector designs. The industry team came up with 28 mixer/ejector test variables, and each company prioritized the list of variables. The list of variables and the company prioritizations are shown in Table 1. Only the variables that were considered to be of high priority by at least one company were selected, as shown in Table 2. This process resulted in ten geometric variables being selected for development into a test matrix. Existing computational fluid dynamic (CFD) codes were then used to assist in the definition of the mixer/ejector model hardware needed to evaluate these variables. Model hardware approaches and test facilities to perform parametric testing of the important mixer/ejector variables were identified.

Based on the results of the above study, a test plan for the performance model tests in the selected facility was prepared. The test plan included a description of all model hardware, a definition of typical model and facility instrumentation requirements, a test matrix, and a test procedure. Requirements for data reduction and analysis were also defined.

Table 1. Gen 1.5 Aero Mixing and Performance Model Test – List of All Geometric Variables

Item	Parameter	Aero – Mixing			Thrust Coefficient			Data Elsewhere
		Boeing	GEAE	P&W	Boeing	GEAE	P&W	
1	Lobe Count		High	2- High		High	9 - Medium	
2	Lobe Penetration	5 - High	Medium	5 - High	5 - High	Medium	10-Med	
3	Mixer Pri Inlet Mach							
4	Mixer Pri Area Ratio	1 - High	High	3 - High	1 - High	High	1- High	
5	Mixer Length						2 - High	
6	Chute Stagger							
7	Tailor Chute Spacing		High	Medium				
8	Axial Versus Vortical Mixer			4 - High				P&W/Langley Tests
9	Nonuniform Chutes			Medium				
10	Serrated (Vented) Chutes	Medium	Medium		Medium			
11	Vortex Generators	Medium	Medium		Medium	Medium		
12	Splayed Chutes						8 - Medium	
13	Wave Neutral Chutes		High			High		
14	Cascades in Chutes							
15	Chute Exit Angles	Medium	High	Medium	Medium	High	4 - High	
16	Shroud Length	4 - High		Medium	4 - High		7 - Medium	
17	Shroud Area Ratio	3- High			3 - High			GEAE/Langley Tests
18	Shroud Contouring					High	3 - High	
19	Shroud Friction							
20	Inlet Ramp Angle							
21	Inlet Scoop							
22	Boundary Layer Control	Medium			Medium			
23	Upstream Swirl						5 - High	
24	Mixer CFD Screening			1 - High				Part of Model Design
25	With and W/O Splitter	Medium		Medium	Medium		6 - Medium	
26	Tone Injection Rods							
27	Acoustic Splitter in Lobes	6 - High			6 - High			
28	Amix/Aprimary	2 - High			2 - High			P&W/Langley Tests

Priority 1 = High

*Table 2. Gen 1.5 Aero Mixing and Performance Tests — High Priority Variables*

<i>From Boeing/GEAE/P&amp;W Nozzle and Acoustic Input (25 November 1992)</i>				
<i>No.</i>	<i>Item</i>	<i>Parameter</i>	<i>No. of High Priorities</i>	<i>Comments</i>
1	4	Mixer Primary Area Ratio	6	
2	1	Lobe Count	3	
3	15	Chute Exit Angles	3	
4	7	Tailored Chute Spacing	1	
5	18	Shroud Contouring	2	
6	2	Lobe Penetration	3	
7	23	Upstream Swirl	1	
8	24	Mixer CFD Screening	1	Part of Model Design
9	13	Wave Neutralizing Chutes	2	
10	5	Mixer Length	1	
11	16	Shroud Length	2	
12	17	Shroud Area Ratio	2	GEAE/Langley Tests
13	8	Axial/Vortical Mixer	1	P&W/Langley Tests
14	28	Amix/Aprimary	2	P&W/Langley Tests
15	27	Acoustic Splitter in Lobes	2	
Priority 5 = High				

## APPENDIX 3-C

### METHODOLOGY FOR CORRECTING GEN1.5 DATA TO CONSTANT THROAT AREA

This appendix provides a detailed description of the correction methodology applied to the data to correct for the mixer deflections.

The data was scaled to a constant primary choked physical area of 10.31 in.<sup>2</sup> and an effective flow area of 10.0 in.<sup>2</sup> (Cd=0.97).

$A_{j_{cold}} = 10.0$	(area used in original data reduction to calculate Cdp)
$A_j = 10.31$	
$A_j C_d = 10.0$	(scaled effective flow area to maintain constant SAR over range of data)
$A_p = A_j * C_{ER}$	(primary flow area at exit of mixer chutes)
$A_{s_{nom}} = A_m - A_b - A_p$	(nominal, undeflected secondary area)
$A_{s_{act}} = A_m - A_b - A_{j_{cold}} * C_{ER} * (1 + [C_d - 0.97])$	(actual, deflected secondary area)
$CR_s = A_{s_{act}} / A_{s_{nom}}$	(correction ratio for sec. area)
$CR_p = (A_{j_{cold}} * C_{d_p}) / (A_j C_d)$	(correction ratio for pri. area)
$(\omega \sqrt{\tau})_{cor} = \frac{W_s CR_p}{W_p CR_s} \sqrt{\frac{T_{t_s}}{T_{t_p}}}$	
$SAR_{nom} = A_m / (A_j C_d)$	(nominal undeflected SAR)
$SAR_{act} = A_m / A_{j_{cold}} * C_{d_p}$	(actual deflected SAR)

This methodology was used to scale the pumping data to a constant primary choked effective flow area of 10 in.<sup>2</sup>, which corresponds to a physical choked area of 10.31 in.<sup>2</sup> and a flow coefficient of 0.97. In this manner, the corrected data reflects a corrected aerodynamic SAR ( $ASAR = A_m / A_j C_d$ ), which is equal to the undeflected physical SAR ( $SAR = A_m / A_{j_{cold}}$ ).

To determine the sensitivity of the data correction to the assumed flow coefficient, the data were also corrected to an assumed flow coefficient of 1.00. This comparison revealed that the data correction is relatively insensitive to small differences in the assumption of flow coefficient.

Performance data were corrected by scaling the exit pressure and velocity based on the known trends as determined from data. First, Configurations 42, 21, 3, and 19 were used to calculate the exit pressure and exit velocity, based on the raw data, as a function of ASAR. These curves (Figures 60 through 65) were then used to scale each data point to its nominal ASAR value by first calculating the actual exit conditions and then scaling them to the corrected ASAR level using the relationship as follows:

$$V' = V_e \left( \frac{V_2}{V_1} \right)$$

where  $V'$  is the corrected velocity;  $V_1$  is the velocity read from the curve at the corresponding NPR, SNPR, and measured ASAR;  $V_2$  is the velocity read from the curve at the corresponding NPR, SNPR, and scaled nominal ASAR; and  $V_e$  is the velocity calculated for a particular data point. This same procedure was also used for the exit static pressure.

$$P' = P e^{\left(\frac{P_2}{P_1}\right)}$$

Then the corrected thrust may be calculated by the relationship

$$F' = m'V' + (P' - P_a)A_e$$

where  $m'$  is the total of the corrected primary and secondary flows,  $V'$  is the corrected exit velocity, and  $P'$  is the corrected exit pressure. Likewise, the ideal thrust is corrected to the scaled primary mass flow.

$$F_{idp}' = W_p' V_{idp} \quad (W_p' = W_p / CR_p)$$

Then the corrected thrust ratio is given by the relationship:

$$C_{FGCor} = \frac{F'}{F_{idp}'}$$

The data reduction equations are summarized in the following paragraphs.

#### Entrainment Correction to Adjust for Mixer Deflections

Mixing Plane Area	AM = Measured Value
Mixer Base Area	AB
Corrected Nozzle Primary Area	AJC = 10.31
Corrected Nozzle Flow Area	ASTAR = 10.00
Corrected Mixer Exit Area	AP = AJC * CER (CER=1.10)
Nominal Secondary area (Corrected)	ASNOM=AM-AB-AP
Actual Secondary Area (As Tested)	ASACT=AM-AB-10.0*(1.+[CDP-0.97])*CER
Secondary Flow Correction Ratio	CRS = ASACT/ASNOM
Primary Flow Correction Ratio	CRP = 10.0*CDP/ASTAR
Area-Corrected Flow Ratio	WTFLC=WS/WP*SQRT(TTSAV/TTPAV)*CRSP/CRS

#### Performance Correction to Adjust for Mixer Deflections

##### Step 1: Calculate Exit Pressure and Velocity as Functions of ASAR

Mass-Averaged Total Temperature	TTAV = (WP*TTP+WS*TTS)/(WP+WS)
Mass-Averaged Gamma	GAMMA = (WP*GAMMAP+WS*GAMMAS)/(WP+WS)
Exit Area	AE = AM*MAR

Measured Thrust	$FMEAS = CFG * FIP$
Iteration Counter	$KOUNT = 1$
Gas Constant	$R = 53.35$
First Iteration (Guess Mn)	$MN = 1.0$
Tt/Ts (Isentropic Flow)	$TTOTS = 1.0 + (GAMMA - 1.) / 2. * MN^{**2}$
Static Temperature	$TS = TTAV / TTOTS$
Speed of Sound	$C = SQRT(GAMMA * R * 32.2 * TS)$
Calculate Exit Velocity (Base on Assumed Mn)	$V1 = C * MN$
Calculate Corresponding Exit Static Pressure	$PE = PAMB + (FMEAS - (WS + WP) * V1 / 32.2) / AE$
Calculate Density	$RHO = (PE / TS) * (144. / R)$
Calculate Exit Velocity (Based on Continuity)	$V2 = (WS + WP) / (RHO * AE) * 144.$
Compare Velocities	$IF(ABS(V2 - V1) / V2.GT. 0.001.AND.KOUNT.LT.500)THEN$
Re-adjust Mn for Next Iteration	$MN = V2 / C$
Re-adjust Iteration Counter	$KOUNT = KOUNT + 1$
Final Calculation of Mn	$MN = V2 / C$
Final Calculation of Ve	$VE = V2$
Final Calculation of Exit Total Pressure	$PTE = PE * (1.0 + GAMMA - 1.) / 2. * MN^{**2} * (GAMMA / [GAMMA - 1.])$
Final Calculation of Ps/Pa	$PSPA = PE / PAMB$

**CALCULATED VALUES OF EXIT PRESSURE AND VELOCITY ARE SHOWN AS FUNCTIONS OF ASAR IN FIGURES 60 THROUGH 65.**

**Step 2: Calculate Exit Pressure and Velocity of Each Data Point and Adjust to Corrected, Nominal ASAR Using the Relationships Shown in Figures 60 Through 65.**

Using methodology in Step 1, calculate Ve and Pe at a particular data point

Read Velocity and Pressure Corresponding to Actual ASAR from Curves, Interpolating as Required	$V1, P1 = f(NPR, SNPR, \text{measured ASAR})$
--	---

Read Velocity and Pressure Corresponding to Corrected, Nominal ASAR from Curves, Interpolating as Required	$V_2, P_2 = f(\text{NPR}, \text{SNPR}, \text{corrected ASAR})$
--	--

Adjust Velocity to Account for ASAR Scaling	$V_e' = V_e * (V_2/V_1)$
---	--------------------------

→ Adjust Pressure to Account for ASAR Scaling	$P_e' = P_e * (P_2/P_1)$
---	--------------------------

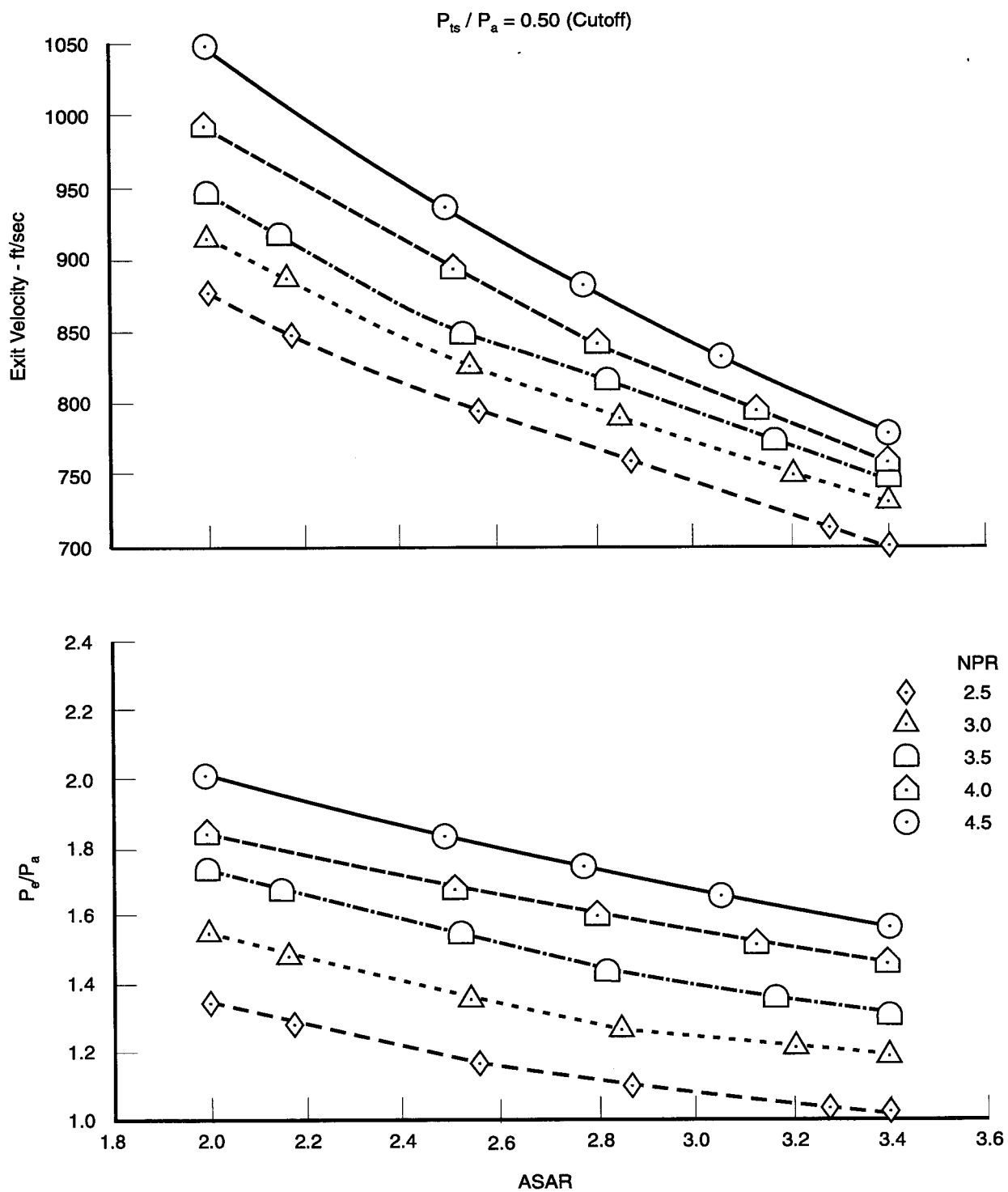
Adjust Primary Flow to Account for ASAR Scaling	$W_p' = W_p/CR_p$
---	-------------------

Adjust Secondary Flow to Account for ASAR Scaling	$W_s' = W_s/CR_s$
---	-------------------

Calculate Adjusted Thrust	$F' = (W_p' + W_s') * V_e'/g + (P_e' - P_a) * A_e$
---------------------------	--

Calculate Adjusted Ideal Thrust ( $V_{idp} = f(\text{NPR}, \text{gamma})$ )	$F_{idp}' = W_p' * V_{idp}$
--	-----------------------------

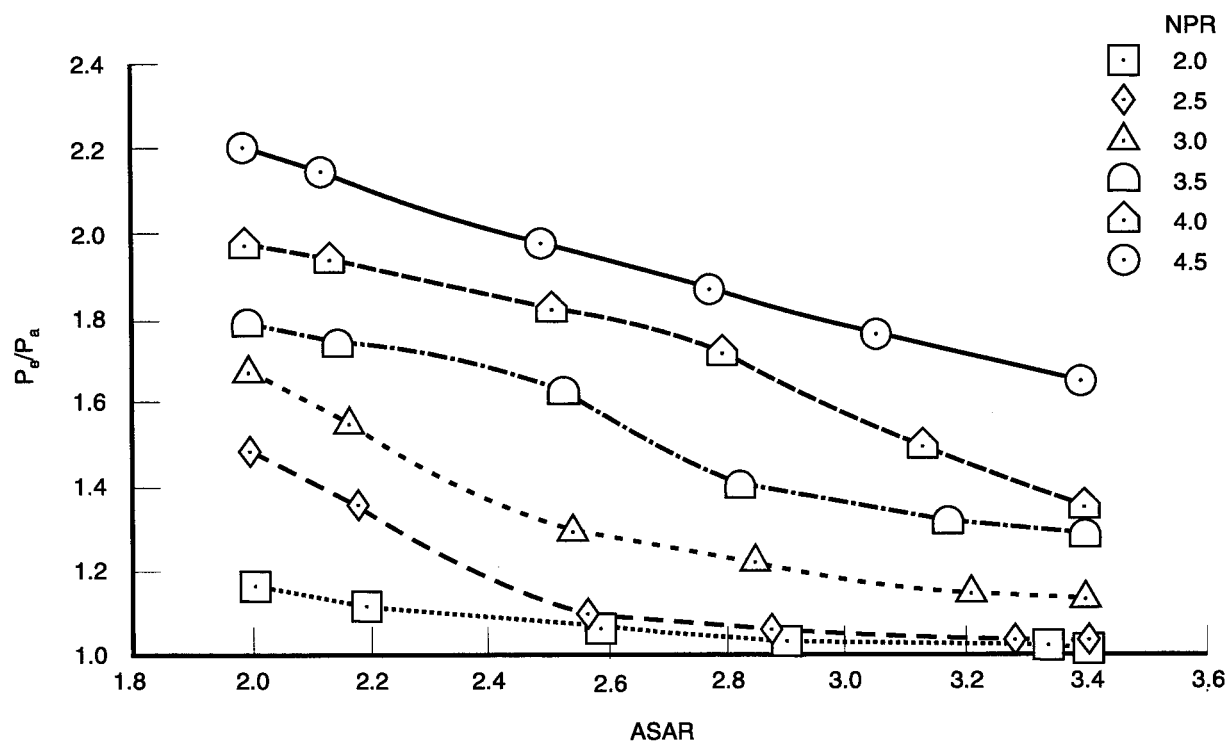
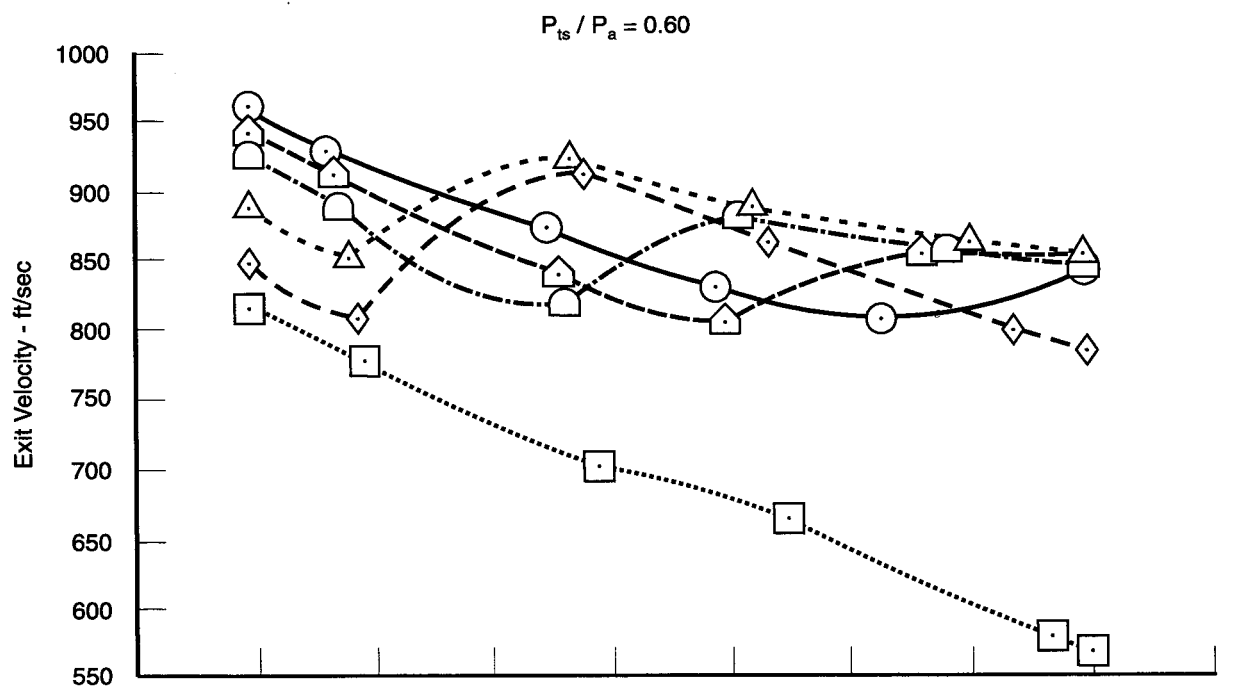
Calculate Adjusted Thrust Coefficient	$CFGCOR = F'/F_{idp}'$
---------------------------------------	------------------------



74802.cdr

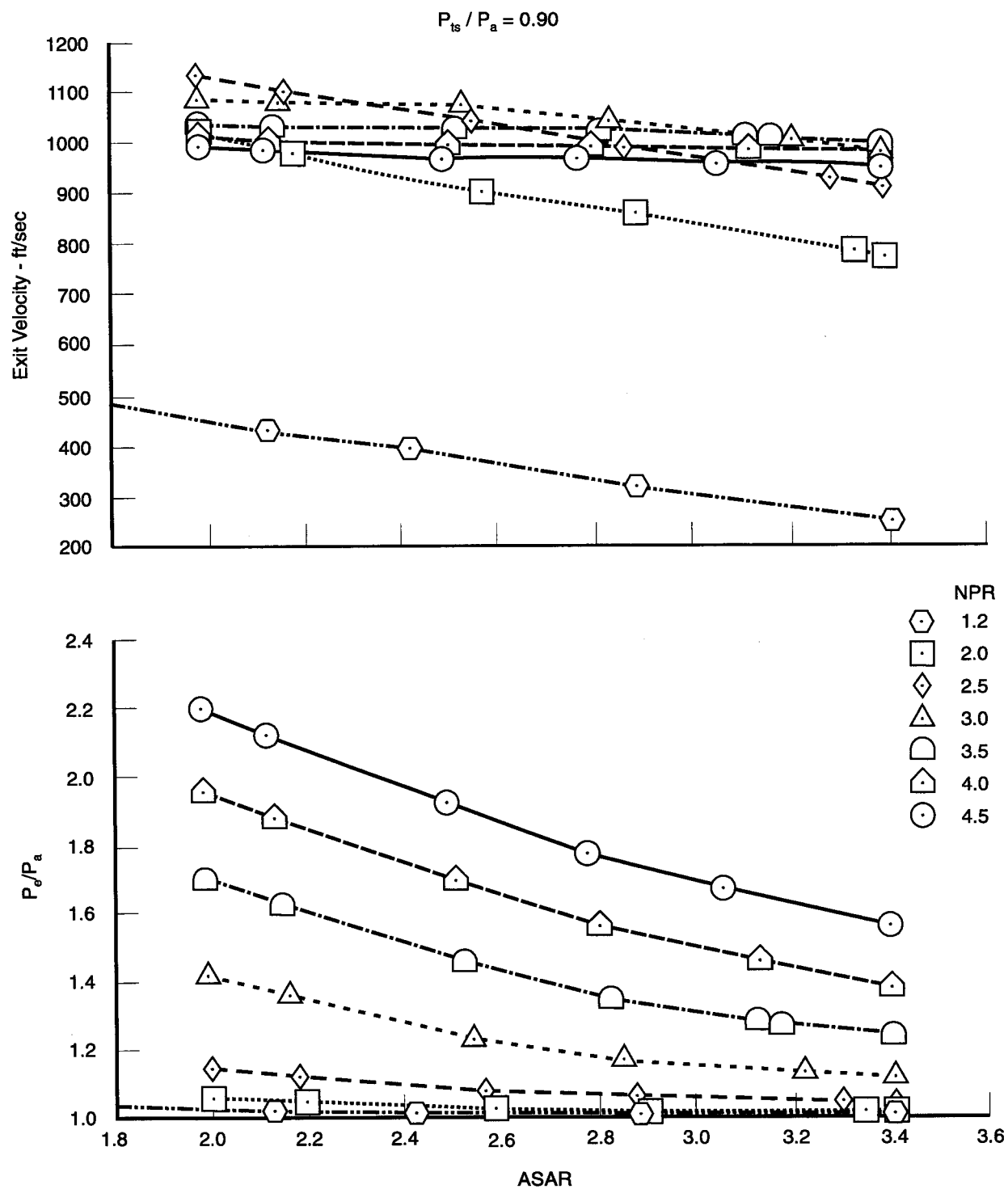
Figure 60. Exit Velocity and Static Pressure Versus ASAR





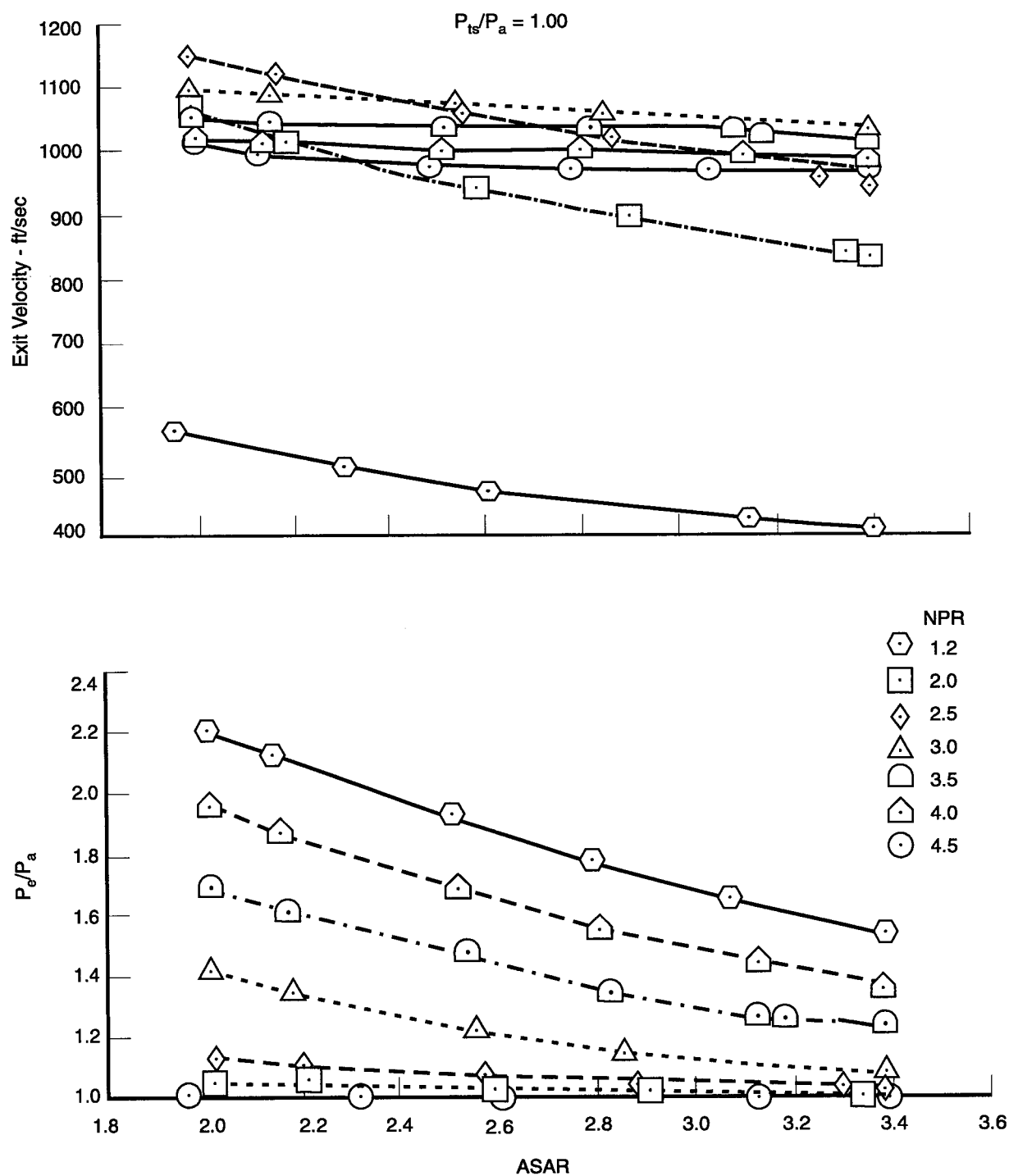
74803.cdr

Figure 61. Exit Velocity and Static Pressure Versus ASAR



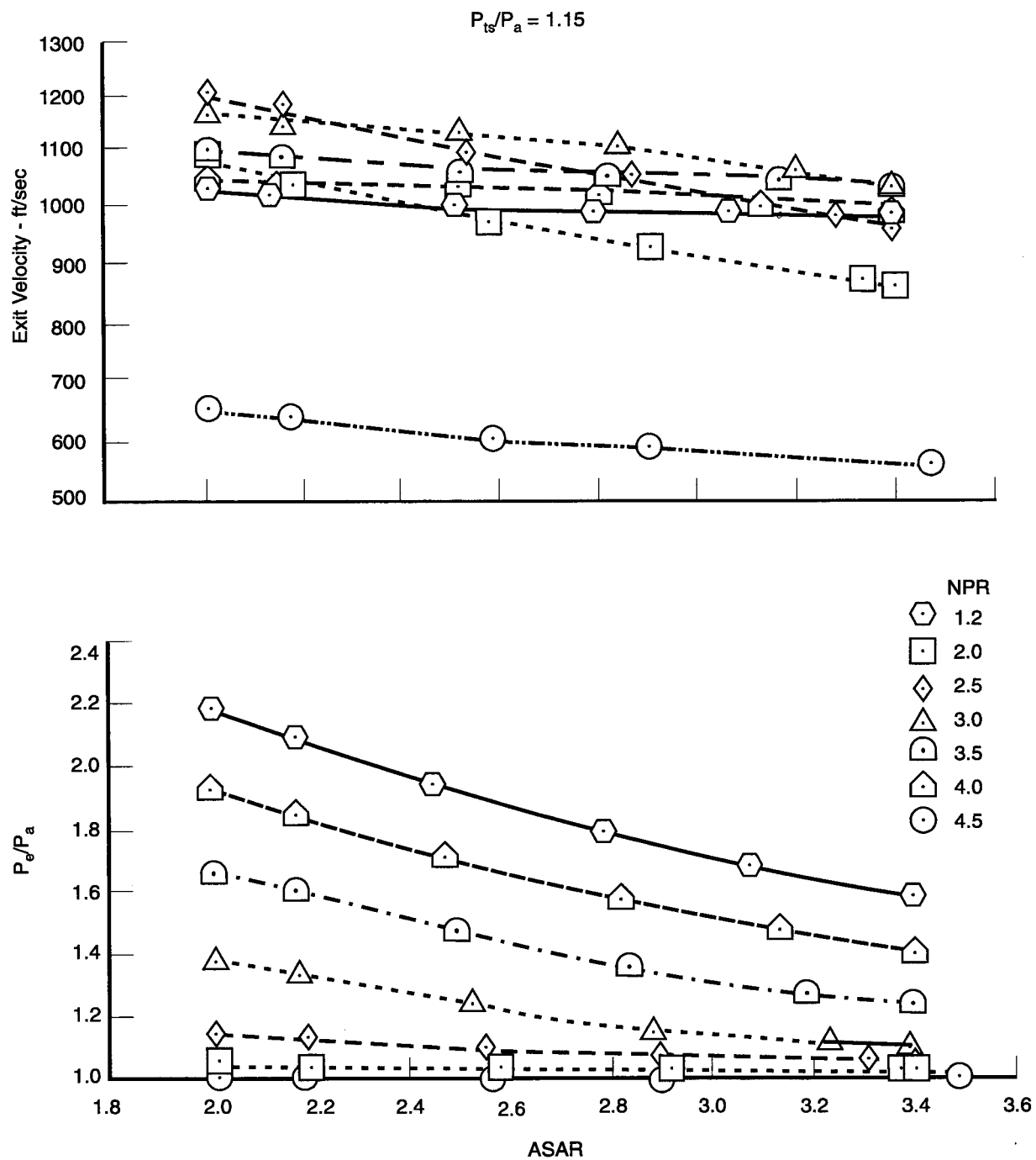
74804.cdr

Figure 62. Exit Velocity and Static Pressure Versus ASAR



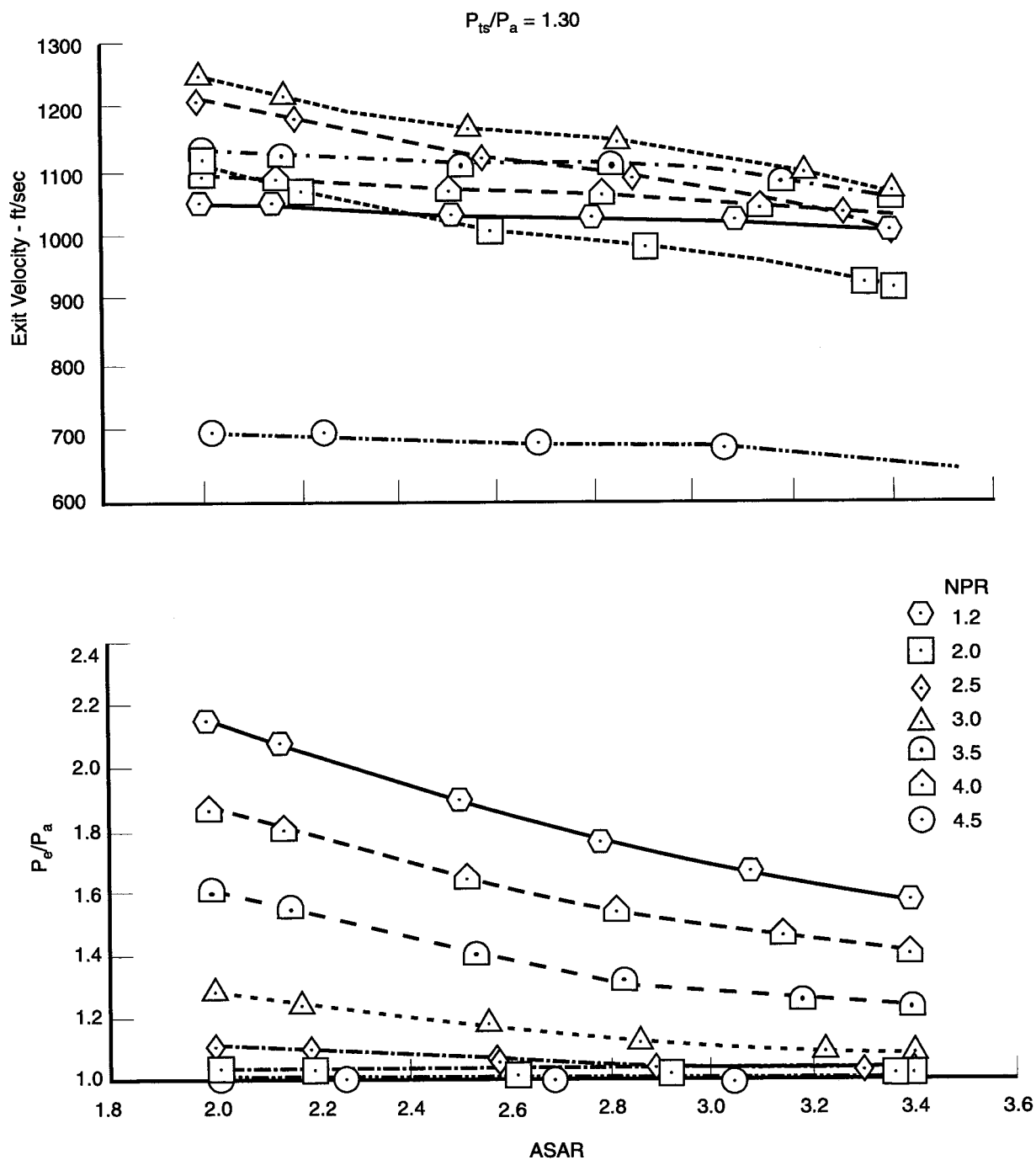
74805.cdr

Figure 63. Exit Velocity and Static Pressure Versus ASAR



74806.cdr

Figure 64. Exit Velocity and Static Pressure Versus ASAR



74807.cdr

Figure 65. Exit Velocity and Static Pressure Versus ASAR

## REFERENCES

1. Arthur Bernstein, William Heiser, and Charles Hevenor, *Compound Compressible Nozzle Flow*, AIAA Paper No. 66-663, 13 June 1966.

## 4. HIGH-SPEED MODEL TESTS

Three economic barriers to a viable High Speed Civil Transport (HSCT) are range and payload capability, operating costs, and manufacturing costs. Both fuel consumption and cruise performance effect these barriers. If the aircraft does not meet cruise performance, the aircraft will burn fuel less efficiently, and operating costs will increase while range and payload capabilities decrease. In developing the propulsion system for the HSCT, the need for a supersonic cruise database was identified. A subscale model test was planned to create this database for three current nozzle concepts.

The objective of this subscale model test was to obtain supercruise performance data for the three nozzle concepts to create a database for the HSCT program. This database will be used to predict performance for the systems studies funded by NASA and will support ongoing design work.

Results of the high-speed performance tests showed that relatively long, straight wall, convergent-divergent (C-D) nozzles could meet supersonic cruise thrust coefficient goals; but the plug, ramp and shorter C-D nozzles required isentropic contours to reach the same level of performance. The effects of wall friction, even with simulated acoustic-liner roughness, were less than predicted.

In the first half of 1994, Pratt and Whitney (P&W) and General Electric Aircraft Engines (GEAE) completed testing of the Generation 1.5 High-Speed Performance Test at the NASA Lewis Research Center (NASA LeRC) CE-22 stand. The model fabrication, testing, and data analysis was funded under NASA-LeRC Large Engine Technology (LET) contract NAS3-26618, Task 26, Subtask C. Two nozzle concepts were tested in Phase I: A P&W Two-Dimensional Convergent-Divergent (2-D/C-D) nozzle with and without a splitter, and a GEAE Two-Dimensional Plug Nozzle (2-D Plug). Phase II of this test included the GEAE Single Expansion Ramp Nozzle (SERN) and the completion of the 2-D/C-D Nozzle test matrix.

### 4.1 TEST APPARATUS AND METHOD

Cold flow aero performance was measured for each configuration at the NASA LeRC CE-22 nozzle thrust stand. This stand was calibrated using standard American Society of Mechanical Engineers (ASME) nozzles before testing. During the test, the ASME nozzle runs were repeated to detect any shifts or problems in the thrust and flow measurements. The thrust coefficient ( $C_{fg}$ ) and flow coefficient ( $C_d$ ) measurements are each accurate to within  $\pm 0.25$  percent. Each nozzle model contained static pressure taps on the centerline of the flap or plug surfaces and on the centerline of the walls. Typical tap locations are shown later in this section.

Three types of 1/7th-scale HSCT nozzle concepts were tested: a 2-D/C-D, a 2-D Plug, and a 2-D SERN. These models were fabricated and instrumented by Fluidyne Engineering Inc. of Minneapolis, MN. The circular-to-rectangular transition duct mates to NASA-LeRC hardware and was the same for all three nozzle concepts. The transition duct changes the flow from axisymmetric to two-dimensional (2-D) flow. For each nozzle configuration, the upper right (starboard) was instrumented with static pressure taps.

#### 4.1.1 Two-Dimensional/Convergent-Divergent (2-D/C-D) Nozzle

The 2-D/C-D nozzle was designed for a mixer/ejector turbofan engine cycle. At takeoff, a forced mixer is deployed into the core flow to mix supersonic core flow with subsonic ambient flow (Figure 66). The mixing of the two streams will reduce the exit velocity of the flow and jet noise at the exit. During supersonic cruise, the nozzle becomes a standard 2-D/C-D nozzle with a stowed mixer. The divergent section of the nozzle was treated with acoustic liner (Figure 66).

The 2-D/C-D model baseline configuration had smooth, straight flaps, and a varied divergent flap length and area ratio (Figure 67). This nozzle has a throat area ( $A_j$ ) of 19.75 in.<sup>2</sup> with area ratios ( $A_e/A_j$ ) of 1.1 to 3.5, and divergent flap lengths of 10, 14, and 18 in. The divergent flap lengths were chosen to cover a range of HSCT 2-D/C-D nozzles that are currently being designed. Because certain engine cycles require large amounts of acoustic liner material to reach the noise goals, a splitter configuration was added to determine the effects of the splitter on

performance. This configuration had a different convergent section to maintain a constant throat area of 19.75 in.<sup>2</sup> between the configurations. The splitter configuration was tested at an area ratio of 3.5 and a flap length of 18 in. Photographs of the baseline and splitter configurations are shown in Figure 68 through Figure 71.

The 2-D/C-D baseline configuration was tested with rough internal surfaces in an effort to determine performance losses due to rough acoustic liners at different area ratios. Only the divergent section of the flaps and sidewalls are rough. The convergent section and throat radius are smooth. The separate rough flaps and sidewalls were machined in a crisscross diamond pattern similar to knurling the surface 10 mils deep and approximately 0.05 in. apart for Roughness A, and 10 mils deep and 0.015 in. apart for Roughness B (Figure 72). After initial testing showed that the performance of the Roughness A flap was the same as the smooth flap, it was modified to the Roughness C configuration shown in Figure 73. The latter was tested to evaluate the effects of grooves associated with the stowed mixer of the nozzle concept shown in Figure 66.

The curved and two piece 2-D/C-D flaps are point designs providing the best performance for a given area ratio ( $A_e/A_j = 2.5, 3.0, \text{ and } 3.5$ ) and a divergent flap length of 10 in. From an operational standpoint, the isentropic contours are unrealistic, but do provide a baseline. The curved flap is a truncated isentropic contour optimized for an area ratio and flap length. The two-piece flap was designed using the divergent flap leading- and trailing-edge angles from the isentropic contour. This flap design is similar to the supercruise position of the current downstream mixer (DSM) design (Figure 66). Photographs of the curved and two-piece flaps are shown in Figure 74 and Figure 75.

Instrumentation sketches showing pressure tap numbers and locations for the 2-D/C-D flaps are shown in Figure 76 and Figure 77.

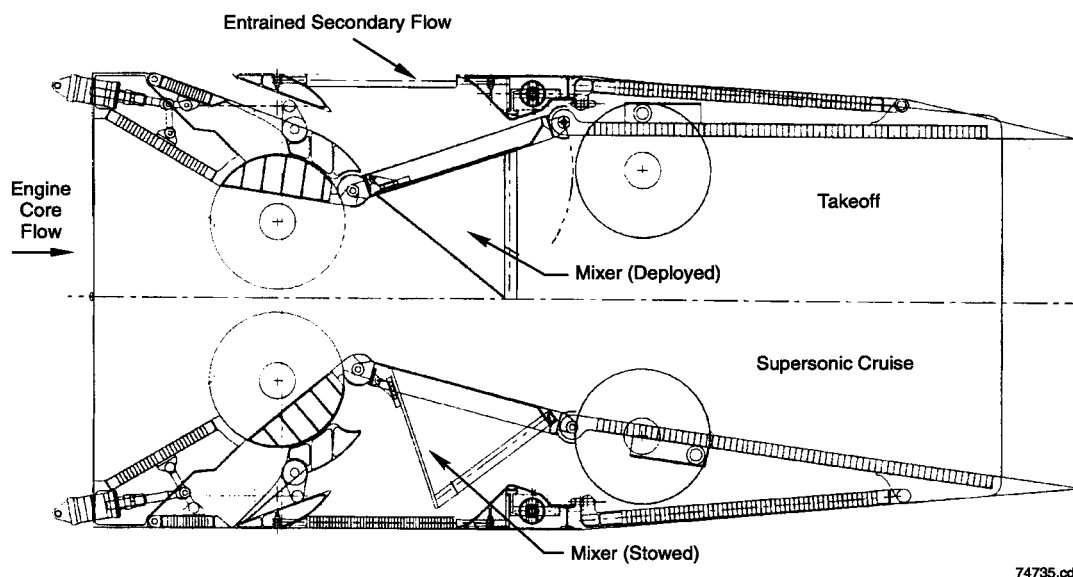
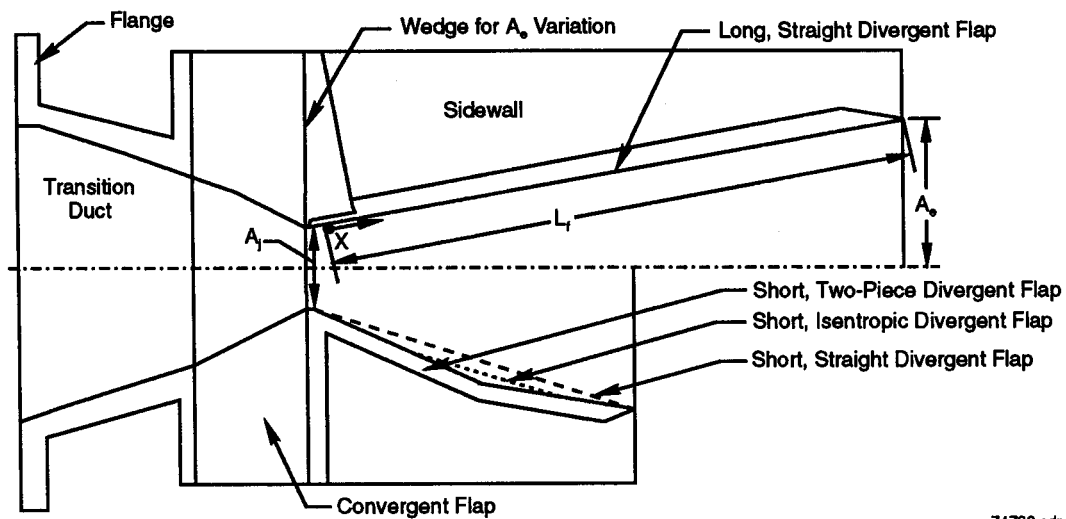


Figure 66. Typical 2-D/C-D Mixer/Ejector Shown at Takeoff and Supersonic Cruise Positions



<i>Flap Length (<math>L_f</math>)</i> (in.)	<i>Flap Contour</i>	<i>Area Ratio</i> $A_e/A_j$	<i>Splitter</i>	<i>Divergent</i> <i>Section Finish</i>
10	Straight	1.1, 1.3, 2.5, 3.0, 3.5	No	Smooth
	Isentropic	2.5, 3.0, 3.5	No	Smooth
	Two Piece	2.5, 3.0, 3.5	No	Smooth
14	Straight	1.1, 1.3, 2.5, 3.0, 3.5	No	Smooth
18	Straight	1.1, 1.3, 2.5, 3.0, 3.5	No	Smooth
		3.5	Yes	Smooth
		1.1, 1.3, 3.5	No	Roughness A & B
		1.3, 2.5, 3.0, 3.5	No	Roughness C



74736.odr

Figure 67. 2-D/C-D Model Configuration Geometry Variations

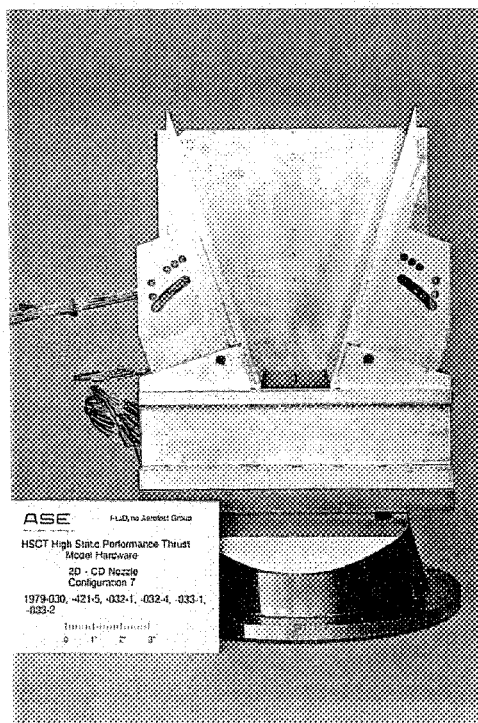


Figure 68. 2-D/C-D Nozzle — Short, Straight Flap Configuration ( $L_f = 10$  in.)

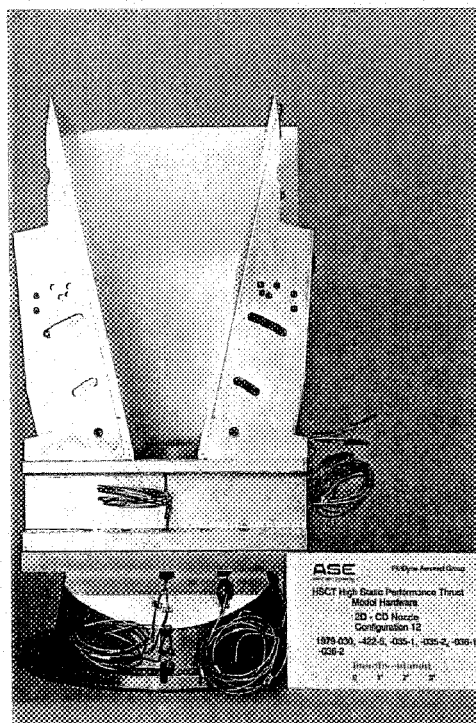


Figure 69. 2-D/C-D Nozzle — Medium, Straight Flap Configuration ( $L_f = 14$  in.)

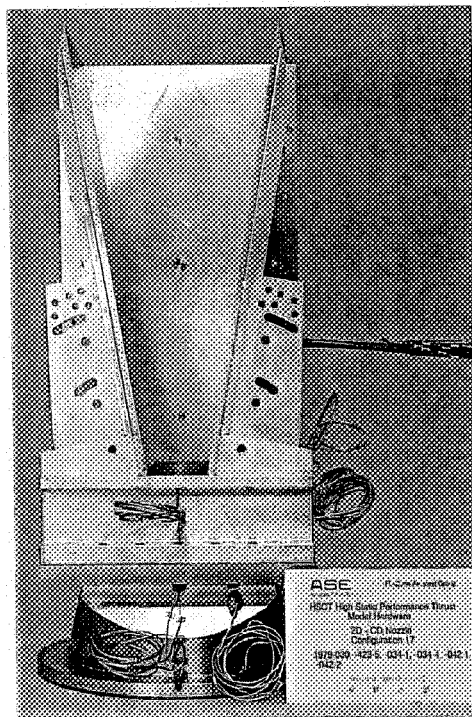


Figure 70. 2-D/C-D Nozzle — Long Straight Flap Configuration ( $L_f = 18$  in.)

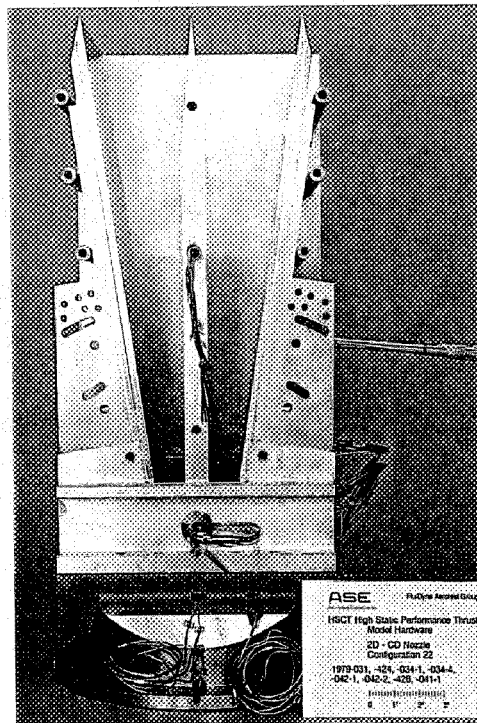
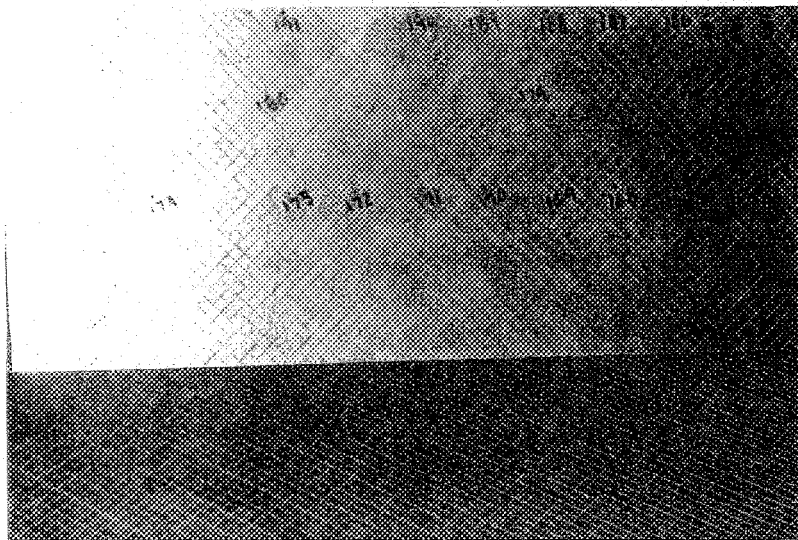
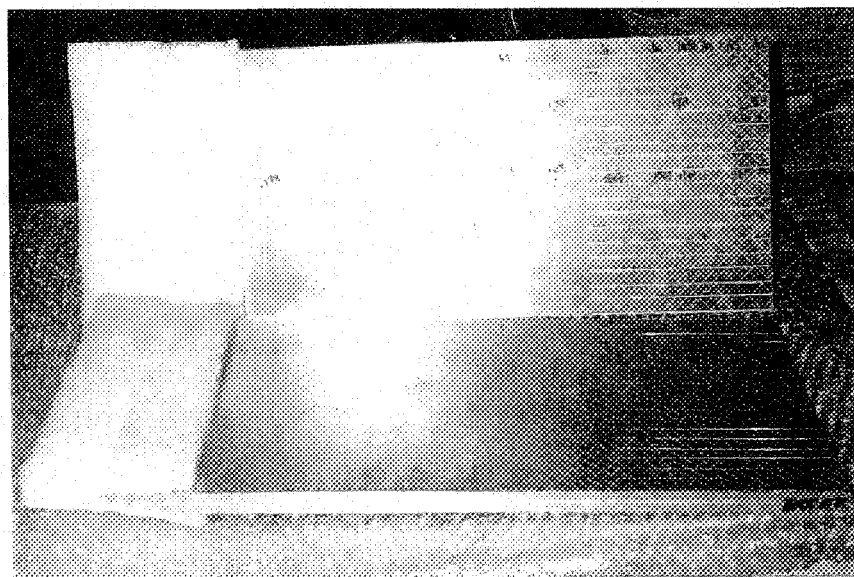


Figure 71. 2-D/C-D Nozzle — Long Straight Flap with Splitter Configuration ( $L_f = 18$  in.,  $A_e/A_j = 3.5$ )



*Figure 72. 2-D/C-D Nozzle — Rough Flap ( $L_f = 18$  in., Roughness B)*



*Figure 73. 2-D/C-D Nozzle — Rough Flap ( $L_f = 18$  in., Roughness C)*

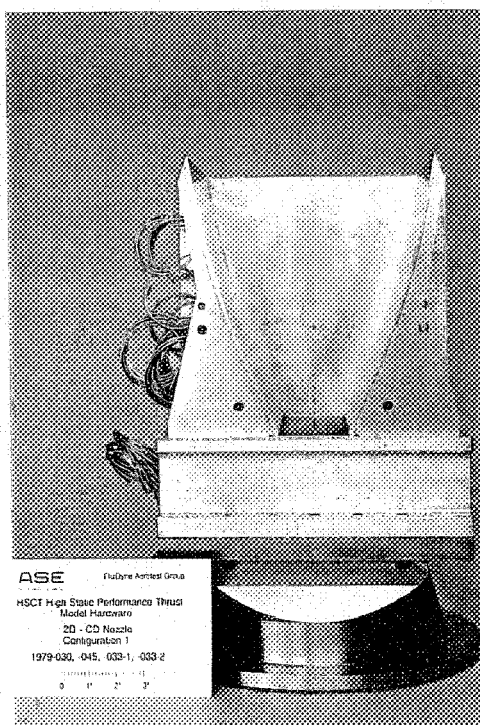


Figure 74. 2-D/C-D Nozzle — Isentropic Flap ( $L_f = 10$  in.)

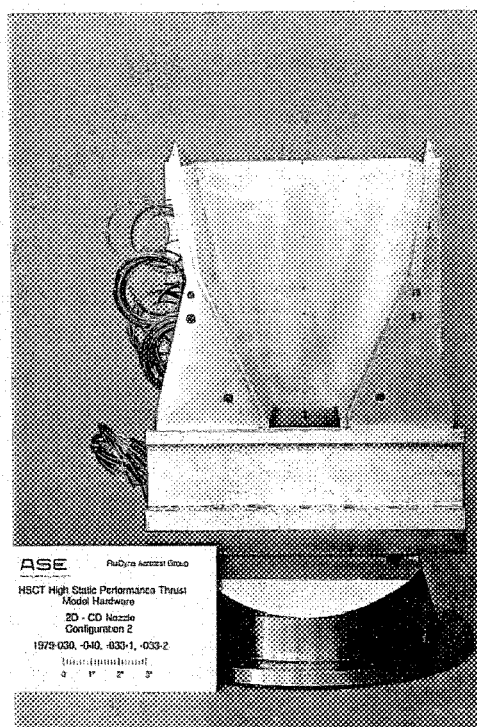
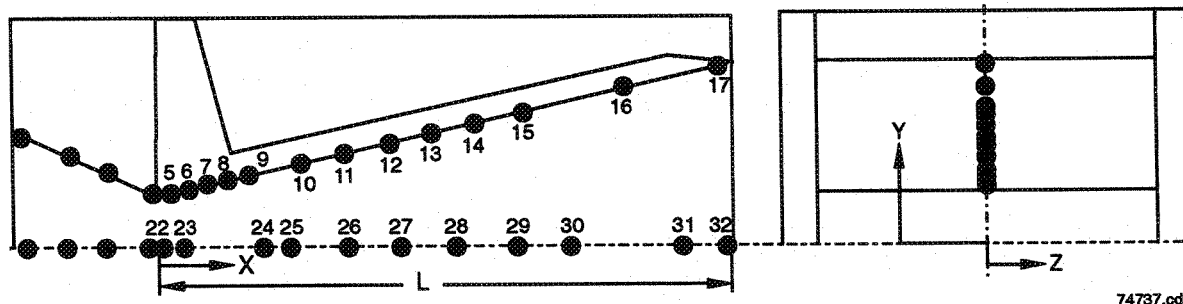


Figure 75. 2-D/C-D Nozzle — Two-Piece Flap ( $L_f = 10$  in.)

Orifice	Orifice X/L	Location Z/L	Type of Pressure	Orifice	Orifice X/L	Location Z/L	Type of Pressure
5	0.02	0	Flap	22	0.009	0	Sidewall
6	0.06	0	Flap	23	0.044	0	Sidewall
7	0.1	0	Flap	24	0.184	0	Sidewall
8	0.14	0	Flap	25	0.232	0	Sidewall
9	0.18	0	Flap	26	0.327	0	Sidewall
10	0.26	0	Flap	27	0.42	0	Sidewall
11	0.34	0	Flap	28	0.515	0	Sidewall
12	0.42	0	Flap	29	0.61	0	Sidewall
13	0.5	0	Flap	30	0.704	0	Sidewall
14	0.58	0	Flap	31	0.984	0	Sidewall
15	0.66	0	Flap	32	0.976	0	Sidewall
16	0.82	0	Flap				
17	0.98	0	Flap				

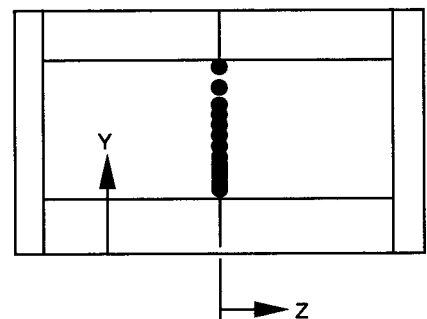
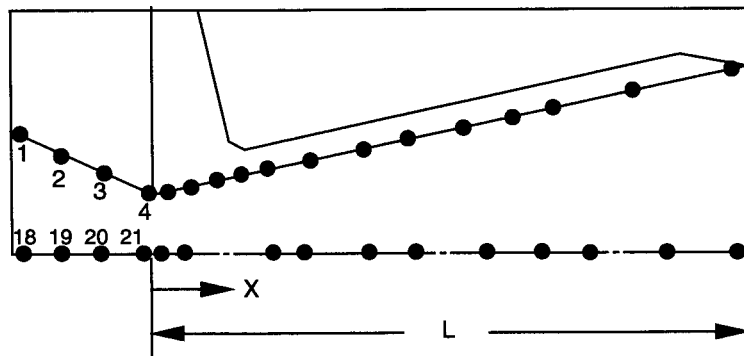


74737.odr

Figure 76. 2-D/C-D Divergent Flap Pressure Tap Instrumentation

<i>Length <math>L_f</math></i>	<i>Orifice</i>	<i>Orifice X/L</i>	<i>Location Z/L</i>	<i>Type of Pressure</i>
10	1	-0.318	0	Flap
10	2	-0.218	0	Flap
10	3	-0.118	0	Flap
10	4	-0.018	0	Flap
14	1	-0.227	0	Flap
14	2	-0.156	0	Flap
14	3	-0.084	0	Flap
14	4	-0.013	0	Flap
18	1	-0.176	0	Flap
18	2	-0.121	0	Flap
18	3	-0.065	0	Flap
18	4	-0.01	0	Flap

<i>Orifice</i>	<i>Orifice X/L</i>	<i>Location Y/L</i>	<i>Type of Pressure</i>
18	-0.318	0	Sidewall
19	-0.218	0	Sidewall
20	-0.118	0	Sidewall
21	-0.018	0	Sidewall
18	-0.227	0	Sidewall
19	-0.156	0	Sidewall
20	-0.084	0	Sidewall
21	-0.013	0	Sidewall
18	-0.176	0	Sidewall
19	-0.121	0	Sidewall
20	-0.065	0	Sidewall
21	-0.01	0	Sidewall



Convergent Flaps

74738.cdr

Figure 77. 2-D/C-D Convergent Flap Pressure Tap Instrumentation

### 4.1.2 Two-Dimensional (2-D) Plug Nozzle

The 2-D Plug Nozzle was designed for the Fluid Shield engine cycle. At takeoff, ambient secondary flow is entrained through a forced mixer into the core flow to mix with the supersonic core flow (Figure 78). The mixing of the two streams will reduce the exit velocity of the flow and therefore the jet noise at the exit. To further reduce the jet noise during takeoff, the Fluid Shield engine cycle provides air downstream of the chute/core mixing plane. The Fan-on-Blade (FLADE) secondary flow is cut off after takeoff and the ambient secondary flow is no longer entrained. The internal plug and short divergent flaps control the expansion of the corestream. During supersonic cruise, the throat area is controlled by a convergent flap and the crown of the plug.

The 2-D plug model baseline configuration (Figure 79) used a plug surface with a supersonic cruise design point isentropic contour truncated such that the trailing edge was at a 5-degree angle. The flap had a straight surface with a length determined by wave cancellation for the complete isentropic plug contour. For consistency, the throat area was 19.75 in.<sup>2</sup>

Configuration variables included a plug with the isentropic contour truncated at a 10-degree angle and a straight plug (wedge) at a 15-degree angle. Flap length variations of 75 and 50 percent of the baseline length, and flap angles of -15, -10, 0, and 10 degrees were tested. Flap length and angle variations covered an area ratio range ( $A_e/A_j = 1.7$  to 4.0). Photographs of the baseline and different plug contours are shown in Figure 80 through Figure 82.

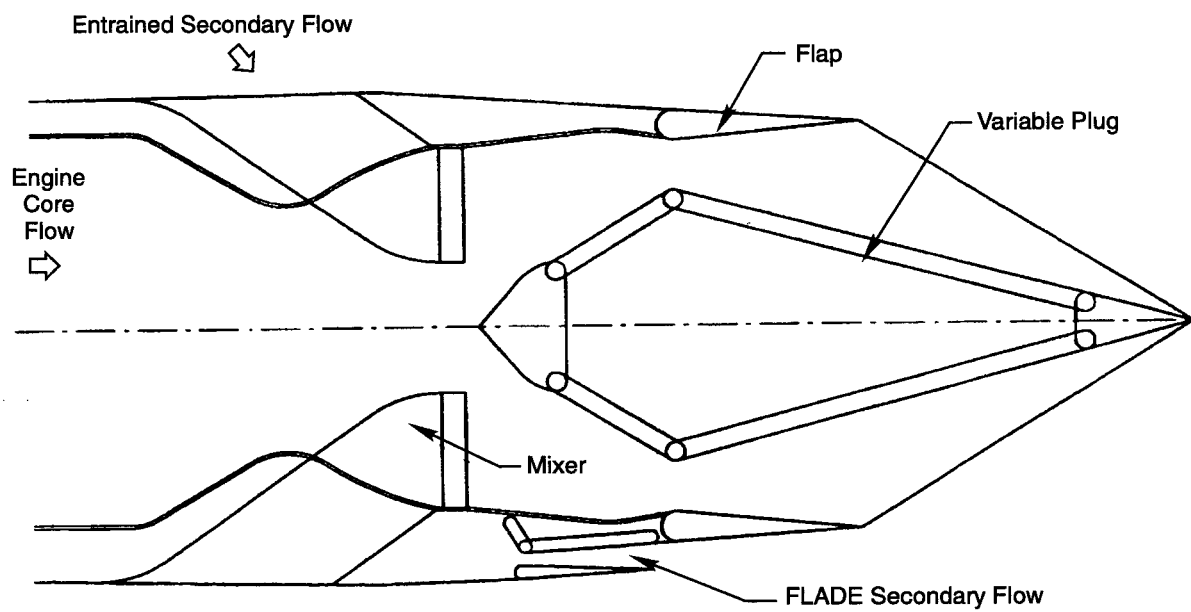
### 4.1.3 Single Expansion Ramp Nozzle (SERN)

The SERN was also designed for the Fluid Shield engine cycle. Similar to the 2-D Plug nozzle concept for this engine cycle, the mixer entrains ambient secondary air to mix with the supersonic core flow, and the FLADE secondary flow is provided downstream of the chute/core mixing plane to help reduce noise. During supersonic cruise (Figure 83), the lower flap controls both the throat area ( $A_j$ ) and exit area ( $A_e$ ), and the length of the flap is determined by supersonic cruise performance and takeoff noise suppression effectiveness. By introducing the FLADE flow close to the exit plane of the ejector chutes, the nozzle acoustic effectiveness is maximized. The divergent ramp was designed to optimize performance at supersonic cruise. Four different ramp contours were tested along with lower flap length and angle variations.

The SERN model baseline configuration (Figure 84) used a ramp surface with a supersonic cruise design point isentropic contour truncated so that the trailing edge was at a 5-degree angle. The flap had a straight surface with a length determined by wave cancellation for the complete isentropic ramp contour. For consistency, the throat area was 19.75 in.<sup>2</sup>

Configuration variables included ramp truncation angle (and therefore length) for the isentropic contour of 7.5 and 10 degrees, and a ramp with a surface composed of two straight sections (flex ramp) using the leading-edge angle from the isentropic contour and a trailing-edge angle. Flap length variations of 75 and 50 percent of the baseline length, and flap angles of -15, -10, 0, 5, 10, and 15 degrees were tested. Flap length and angle variations covered an area ratio range ( $A_e/A_j = 1.5$  to 4.25). Photographs of the baseline and different expansion ramp contours are shown in Figure 85 through Figure 88.





74739.CDR

*Figure 78. 2-D FLADE Plug Nozzle*

Plug Contour Truncation Angle	Flap Length ( $L_f$ ) (in.)	Cowl Angle, $\Theta$ Degrees	Internal Area Ratio	Overall Area Ratio
			$\frac{A_e}{A_j}_I$	$\frac{A_e}{A_j}_O$
Isentropic (5 degrees)	2.479	-15, -10, 0, 10	1.28, 1.44, 1.80, 2.12	2.54, 2.72, 3.24, 3.58
	3.719	-15, 0, 10	1.37, 2.15, 2.65	2.45, 3.24, 3.76
	4.958	-15, -10, 0, 10	1.39, 1.73, 2.43, 3.13	2.2, 2.54, 3.24, 3.93
Isentropic (10 degrees)	2.479	-15, 0	1.28, 1.80	2.72, 3.24
	3.719	-15, 0	1.37, 2.15	2.45, 3.24
	4.958	-15, -10, 0, 10	1.39, 1.73, 2.43, 3.13	2.2, 2.54, 3.93, 3.24
Wedge (15 degrees)	2.479	-15, 0	1.0, 1.53	2.72, 3.24
	3.719	-15, 0, 10	1.0, 1.80, 2.31	2.45, 3.24, 3.76
	4.958	-15, -10, 0, 10	1.0, 1.36, 2.07, 2.75	2.2, 2.54, 3.24, 3.93

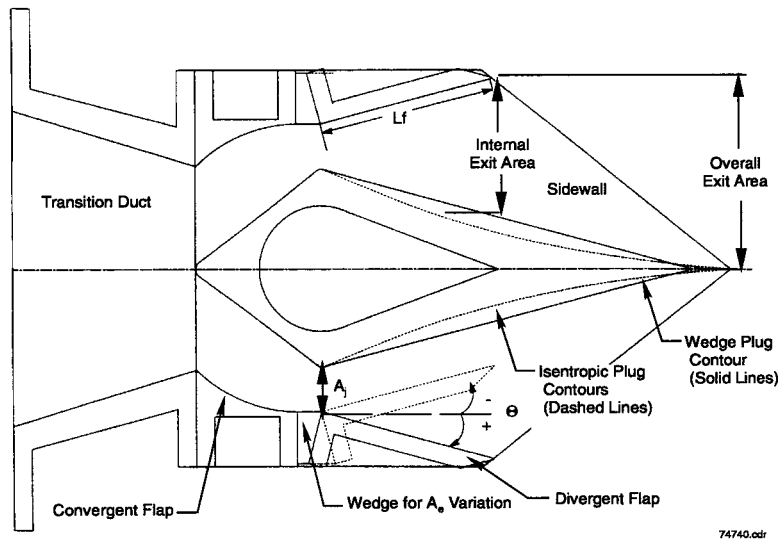


Figure 79. 2-D Plug Model Configuration Geometry Variations

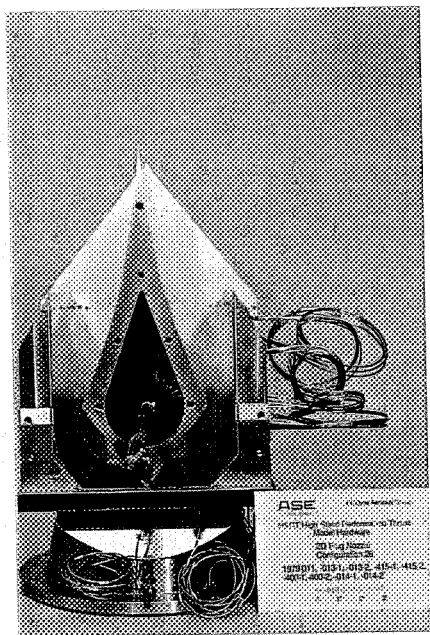


Figure 80. 2-D Plug Nozzle — 5-Degree Isentropic Plug (Baseline)



Figure 81. 2-D Plug Nozzle — 10-Degree Isentropic Plug

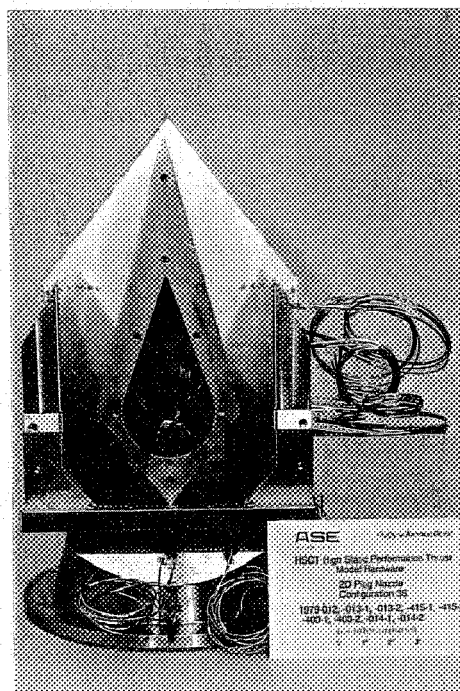


Figure 82. 2-D Plug Nozzle — 15-Degree Wedge

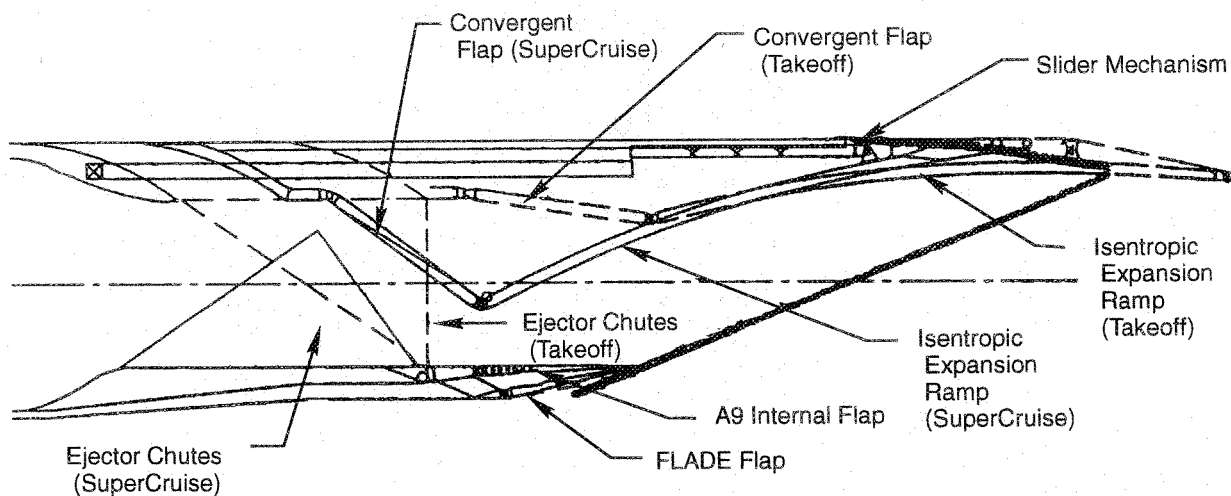


Figure 83. 2-D FLADE SERN with an Isentropic Expansion Ramp

Ramp Contour Truncation Angle	Flap Length ( $L_f$ ) (in.)	Flap Angle, $\Theta$ Degrees	Internal Area Ratio	Overall Area Ratio
			$\frac{A_e}{A_j}\bigg)_I$	$\frac{A_e}{A_j}\bigg)_O$
Isentropic (5 degrees)	4.920	-15	1.26	2.65
	7.379	-15, 0	1.34, 2.14	2.38, 3.18
	9.839	-15	1.36	2.12
Isentropic (7.5 degrees)	4.920	-15	1.26	2.49
	7.379	-15, 0, 10	1.34, 2.14, 2.65	2.22, 3.02, 3.55
	9.839	-15, 0	1.36, 2.43	1.95, 3.02
Isentropic (10 degrees)	4.920	-15	1.26	2.29
	7.379	-15, 0, 10	1.34, 2.14, 2.65	2.0, 2.83, 3.35
	9.839	-15, 0	1.36, 2.43	1.76, 2.83
Flex (15 degrees)	7.379	-15, 0	1.41, 2.23	2.29, 2.83

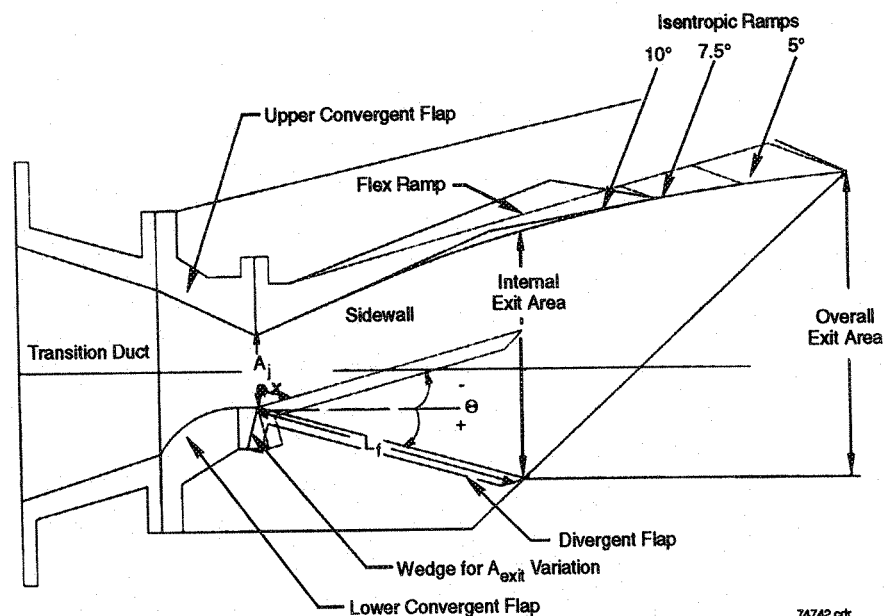


Figure 84. SERN Model Configuration Geometry Variations

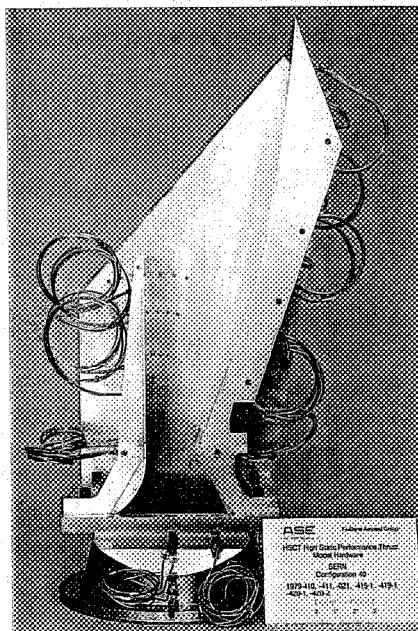


Figure 85. SERN with a 5-Degree Isentropic Ramp

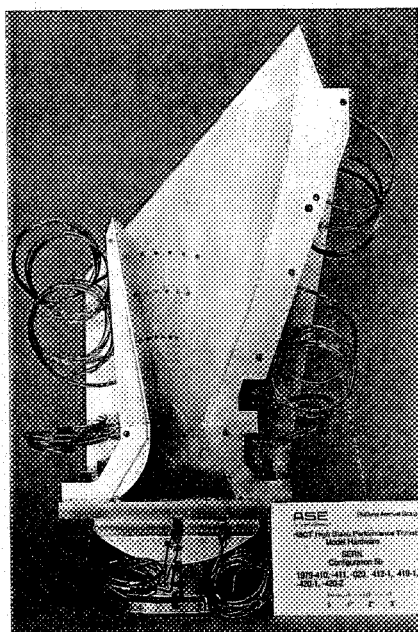


Figure 86. SERN with a 7.5-Degree Isentropic Ramp

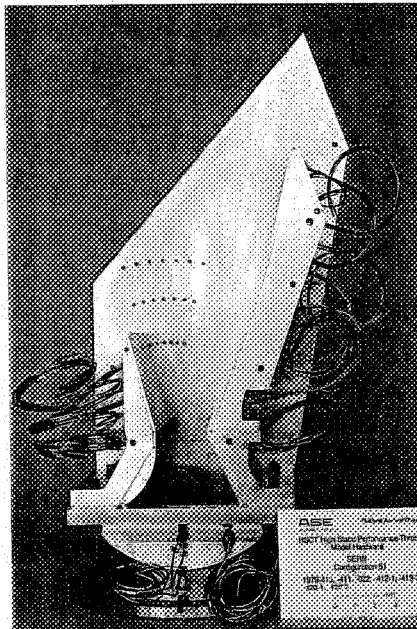


Figure 87. SERN with a 10-Degree Isentropic Ramp

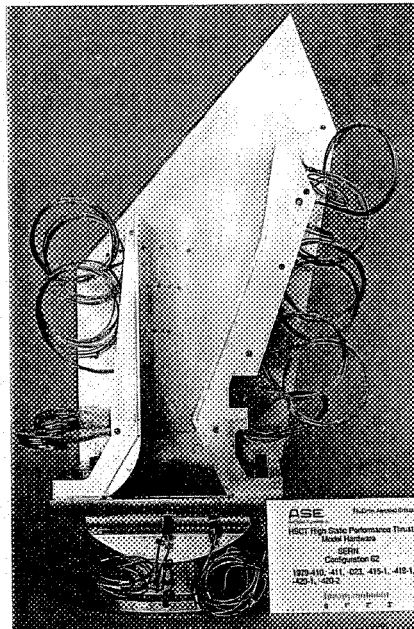


Figure 88. SERN with Flex Ramp

## 4.2 FACILITY DESCRIPTION

Testing was conducted at the CE-22 aeropropulsion test facility located in the Engine Research Building at NASA LeRC (1). The stainless steel altitude tank has a 7.5 ft internal diameter and is 23 ft long (Figure 89). The tank is of two-part construction, with the aft portion moveable to allow access to the model. An inflatable rubber seal is used to prevent leakage at the joint between the two sections.

The facility primary flow system is capable of providing 40 psig of unheated air at 35 lb/sec up to a simulated altitude of 48,000 ft. The secondary flow system can provide heated air at 40, 125, or 450 psig. The model exhaust can be controlled at ambient or altitude conditions.

The facility has the capability to measure thrust up to 3000 lb in the axial direction and up to 1000 lb in the vertical direction. The thrust stand load cells (2 axial and 3 vertical) are calibrated using standard ASME nozzles and dead weight. Calibration coefficients of the cells are entered into the data acquisition system, which provides online thrust calibrations prior to testing.

The ESCORT D data acquisition system is located in the control room for secured programs. The electronically scanned pressure system can provide up to 400 steady-state pressure measurements up to 45 psig. Ninety-six temperature measurements are available for type K thermocouples. Signal conditioners are also available to support individual strain gage type measurements. A color Schlieren system is available for qualitative airflow analysis.

The 2-D/C-D nozzle model with long, rough, straight flaps at an area ratio of 1.1 is shown in the CE-22 Test Facility (Figure 90).

## 4.3 TEST DATA VALIDATION

During testing, efforts were made to ensure the quality of the data by placing external static taps on the flanges. The location of the nozzle exit with respect to the collector was varied during testing.

External pressure taps were located around the model in an effort to detect a pressure gradient that would adversely affect the thrust measurement. The pressure taps were hooked up to a 15 psi ESP module.

The measured pressure gradient across the external flanges did not cause a large change in thrust coefficient (0.05 percent for the following example). Therefore, this effect on the thrust coefficient was considered negligible and the data was not corrected for this effect.

For example, the force on the convergent flange at an NPR of 15.5 for the 2-D/C-D nozzle model (with long, straight, and smooth flaps [ $A_c/A_j = 2.5$ ]):

$$\Delta P = 2.2622 - 2.2551 = 0.0071 \text{ psi}$$

$$A = 11 \times 10 - 49.4 = 60.6 \text{ in.}^2$$

$$F_{fl} = 60.6 \times 0.0071 = 0.43026 \text{ lbf}$$

$$\Delta C_{fg} = \frac{0.43026}{896.71} = 0.0005$$

During the first week of testing, the vacuum stream thrust coefficient ( $C_s$ ) was found to vary during each run where the nozzle was not separated. The  $C_s$  should be constant for a 2-D/C-D nozzle as long as the flow is not separated off the walls. This suggested that the location of the collector relative to the model exit was affecting the thrust measurements. The first five configurations were run at two locations. The first model exit location was 5 in. from the collector, and the second was 10 in. The difference in the thrust coefficient ( $C_{fg}$ ) was 0.10 percent, while the  $C_s$  was constant for the configurations tested at 10 in. From this, the decision was made to run all configurations at least 10 in. from the collector for the 2-D/C-D nozzles.



A similar exercise was done for the 2-D Plug and SERN configurations. In both cases, the model exits were 4 and 9 in. from the collector, and the shorter distance produced steadier performance. The difference in the thrust coefficient was again 0.10 percent.

## 4.4 RESULTS AND DISCUSSION

### 4.4.1 2-D/C-D Nozzle

The isentropic contours provide the highest performance for a given area ratio (Figure 91). From an operability standpoint, these contours are unrealistic, but they do provide a baseline. The two-piece nozzle contour is similar to the current DSM design and performs higher than a conventional straight flap. In comparison, the longer straight flaps (with a flap length [ $L_f$ ] of 14 and 18 in.) perform higher than the short, straight flap at area ratios above 2.0.

#### 4.4.1.1 2-D/C-D Nozzle Flap Contour Effects

Static pressure measurements were taken along the nozzle for each point. The static pressures measured along the centerline of the flap show the effects of the different types of flaps on the flow field. These pressure distribution differences can explain some of the differences in performance for the different configurations. For example, the pressure distribution for the short flaps with various contours (Figure 92) shows the straight flap has higher pressures on the forward portion of the divergent flap. In the same region, the isentropic and two-piece contours have roughly the same pressure distribution because the initial angles are the same. This difference in pressure distribution can be related to the difference in performance for the three contours.

A more detailed look at the performance difference of the different flap contours (Figure 93) shows the isentropic contours perform better than the straight (0.8 percent) and two-piece flaps (0.4 percent) for nozzle pressure ratios above 15, and the performance benefit of the two-piece flaps over the straight flaps is approximately 0.4 percent. The flap static pressure data show that all three nozzles are separated at NPRs of less than 15, and therefore, the performance trends vary due to this separation.

The flow separation is seen in the flap pressure distributions. Separation occurs when the nozzle is operating at a pressure ratio much below that required to produce perfect expansion. The oblique shock formed to recompress the flow to the correct back pressure starts to move inside the nozzle, and the flow separates from the flaps. The flap contour (Figure 92) not only influences where the separation occurs, but also influences at what pressure ratio it occurs. The isentropic flap (Figure 94, Area A) and the two-piece flap (Figure 94, Area B) behave in a similar manner since they were designed with the same angles at the leading and trailing edges of the divergent flap. Both contours show separation for pressure ratios of 5 and below, while the straight flap (Figure 94, Area C) shows separation for pressure ratios up to 10. In comparing the separation of the isentropic and two-piece flap, the axial location on the flap where separation occurs is different. At an NPR of 5, the flow stays attached to the isentropic flap longer than to the two-piece flap. This is due to the gradual angle change of the isentropic flap compared to the constant angle on the forward section of the two-piece flap.

The isentropic contours provide the highest performance ( $C_{fg} = 0.992$ ) for a 2.5 area ratio. The two-piece nozzle contour performed about 0.002 lower, and the conventional straight flap was 0.007 lower than isentropic.

#### 4.4.1.2 2-D/C-D Nozzle Flap Length Effects

The flap length was varied for the straight flaps. The performance for the long flaps (with an  $L_f$  of 18 in.) is 0.8 percent higher than the short ( $L_f = 10$  in.) flaps due to the higher divergence losses of the shorter flap at an area ratio of 3.5 (Figure 95). The additional skin friction due to the longer flaps is small compared to the divergence losses of the short flaps. On the other hand, when comparing the medium ( $L_f = 14$  in.) and the long flaps, the additional skin friction drag of the long flaps negates the decrease in divergence losses so that the performance for both flaps is within 0.2 percent.

Unlike the pressure distribution of the different flap contours, the pressure distributions for the smooth straight flaps at an area ratio of 3.5 do not explain the performance differences as the flap length varies because of friction drag effects (Figure 96). The effects of divergence angle are clearly shown in this figure. For the same area ratio,

the divergence angle decreases as the flap length increases. For the low divergence angle (long flap), the flow recompresses to a higher pressure after the sonic line than it does for the other flap lengths.

The peak performance for long flaps at an area ratio of 3.5 and an NPR of 27.5 was 0.988, or 0.8 percent higher than the short flaps due to the higher divergence losses of the shorter flap.

#### **4.4.1.3 2-D/C-D Nozzle Splitter Configuration**

Due to acoustic requirements, many early designs contained a splitter to shorten the flap without decreasing the amount of acoustic material. At an area ratio of 3.5, a long splitter configuration was tested. This configuration had the same throat area and divergent flap length as the long flap configuration. The splitter configuration performed lower than the baseline configuration (0.5 percent) at the same area ratio (Figure 97). At the lower NPRs, the flow separation for the splitter configuration was different. The flow separated off both the flap and the splitter at an NPR of 5 with each jet acting separately. This produces higher thrust because the flow is not as overexpanded.

#### **4.4.1.4 2-D/C-D Nozzle Flap Roughness Effects**

Additional skin friction drag due to the rough acoustic liners is a concern. In an effort to quantify the performance loss due to surface roughness, two generic rough flaps were tested at various area ratios. The actual acoustic liner material is not modeled by the two generic flaps because of the boundary layer scaling effects and the lack of an identified acoustic material. The rough flaps were designed with a generic diamond pattern that varied the boundary layer distribution (Figure 72).

The equivalent sand grain height is a parameter first developed by Nikuradse in the early 1900s, and was used by Schlichting (2) to relate skin friction drag loss to surface roughness for a fully rough flat plate. The higher equivalent sand grain height (roughness) creates greater turbulence in the boundary layer and, therefore, more skin friction drag. From the thrust data and equivalent sand grain height,  $k_s$  can be calculated using the following equation:

$$C_f = \left[ 2.87 + 1.58 \log \left( \frac{x_f}{k_s} \right) \right]^{-2.0}$$

Performance results from the test show the less dense roughness pattern (Roughness A) performs higher than the more dense pattern (Roughness B) at a given area ratio. Both roughness patterns perform below the smooth flap (Figure 98). As area ratio increases, the performance difference between the rough and the smooth flap decreases. For the larger area ratio (3.5), the boundary layer thickness is a smaller percentage of the total flow at the exit than it is for the area ratio of 1.3. Therefore, the roughness has a greater effect on the thrust coefficient for the lower area ratios.

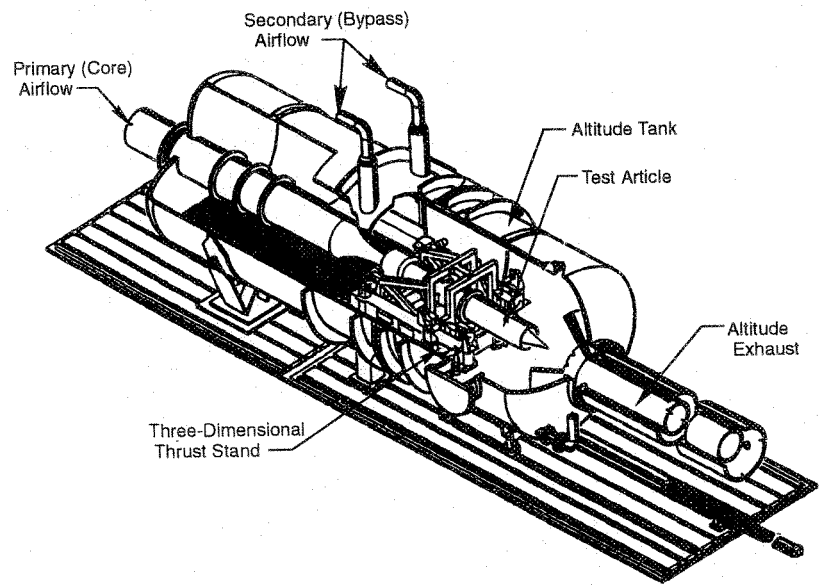
Another set of long flaps designated as Roughness C and machined to model the grooves created when the mixer is stowed performed 0.75 percent lower than the smooth baseline flaps at an area ratio of 1.1, and 0.35 percent lower at an area ratio of 3.5. Similar to roughness Pattern B, roughness Pattern C has a greater effect on the thrust coefficient at the lower area ratios.

Roughness effects from the tests of the knurled long flap showed a 0.002  $C_{fg}$  loss for area ratios between 2.5 and 3.5, but up to 0.0075 loss at 1.1 to 1.3 area ratios.

## **4.5 2-D PLUG NOZZLE**

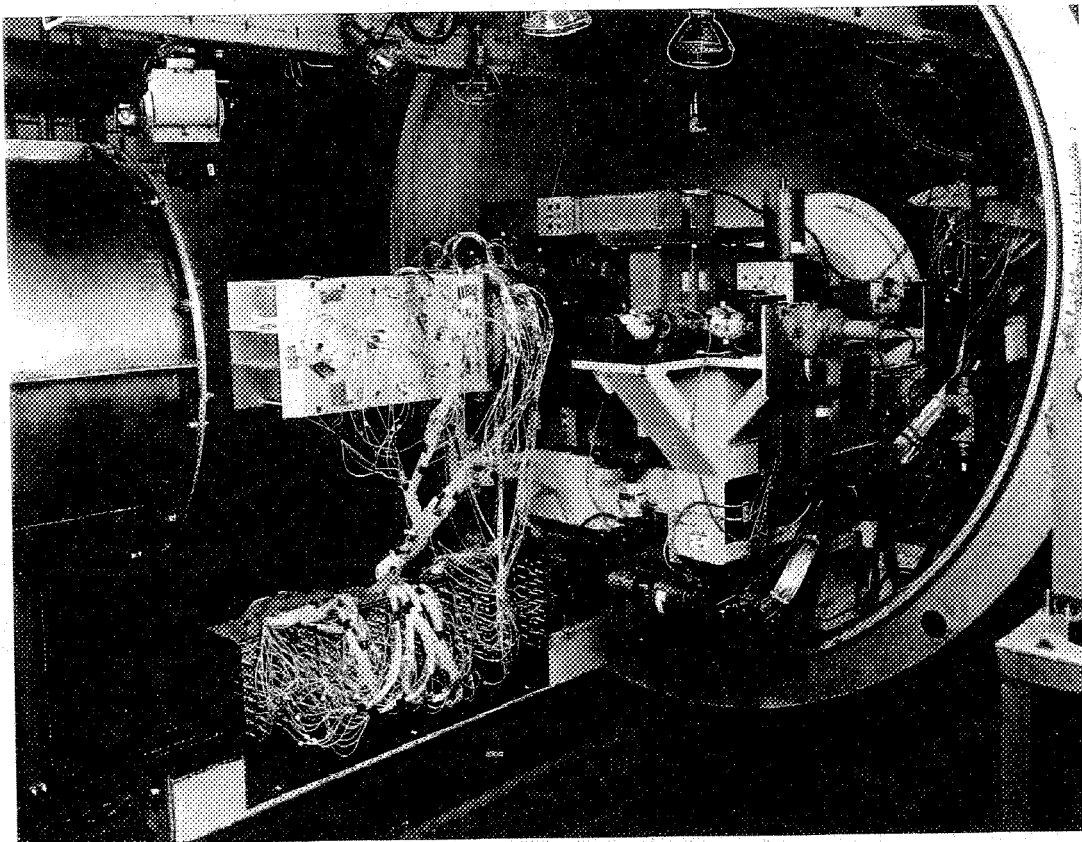
The peak performance of the isentropic plugs was higher than the straight wedge at all of the flap angles and lengths (Figure 99). The performance for the isentropic plugs peaked at a flap angle of 0 degrees, and continued to rise for the straight wedge as the cowl angle increased.

For a flap angle of 0 degrees and a flap length of 4.958 in., the isentropic 5-degree plug peak was 0.987  $C_{fg}$ , or 1.5 percent higher than the 15-degree wedge, and 0.5 percent higher than the isentropic 10-degree plug (Figure 100).

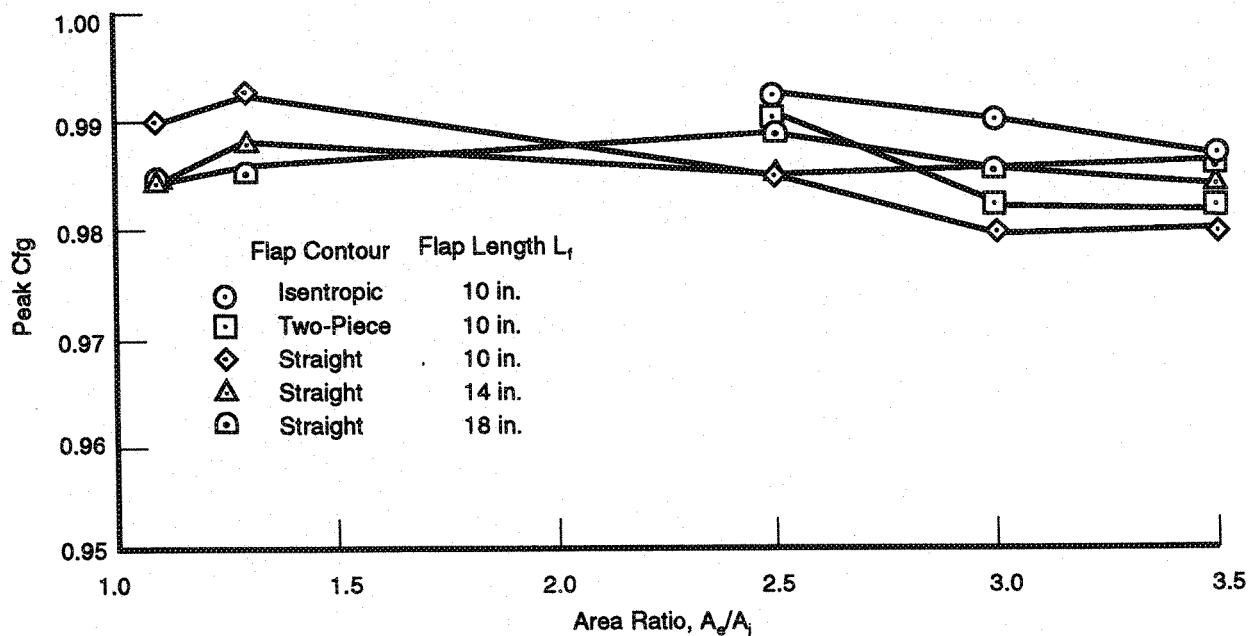


74743.cdr

*Figure 89. CE-22 Test Facility*

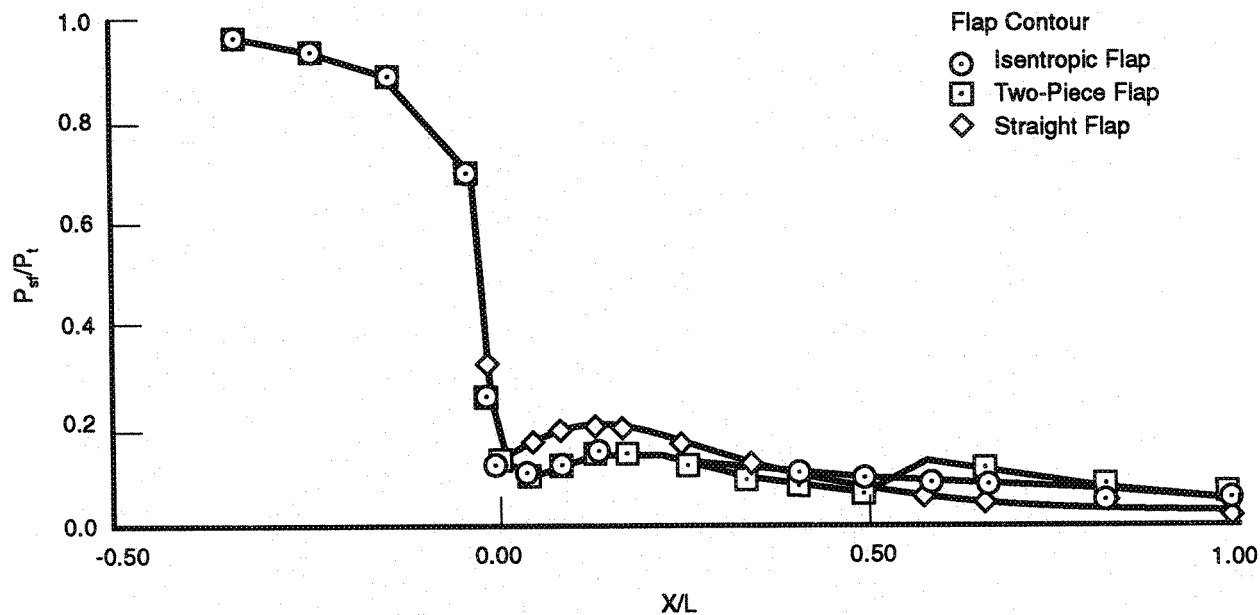


*Figure 90. 2-D/C-D Nozzle Model Mounted in CE-22 Test Facility*



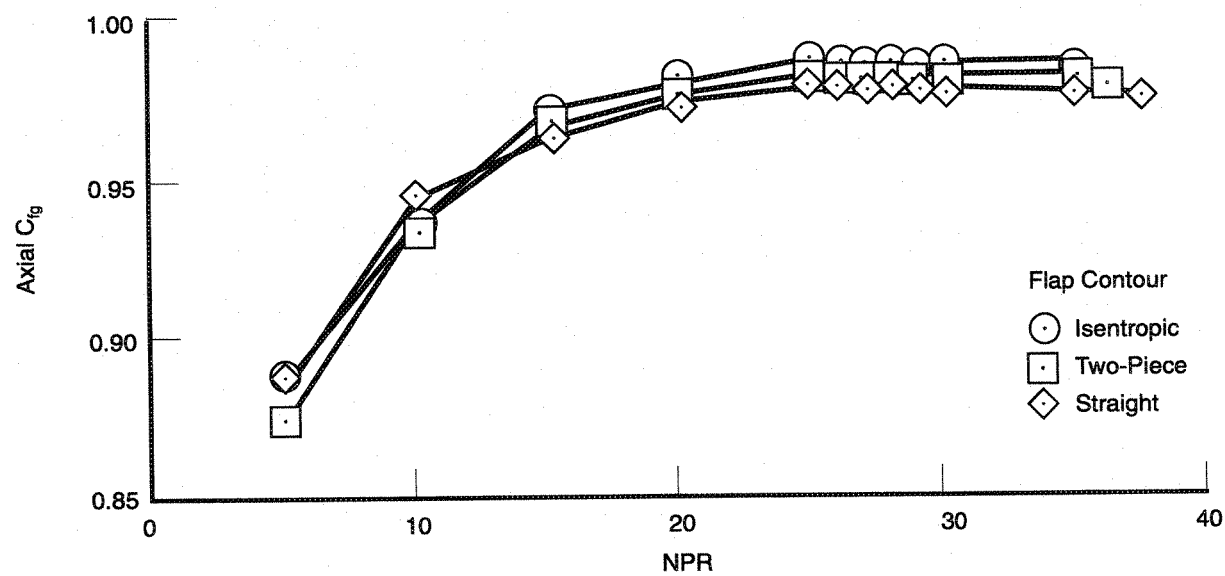
74744.odr

Figure 91. Peak Performance of 2-D/C-D Nozzles



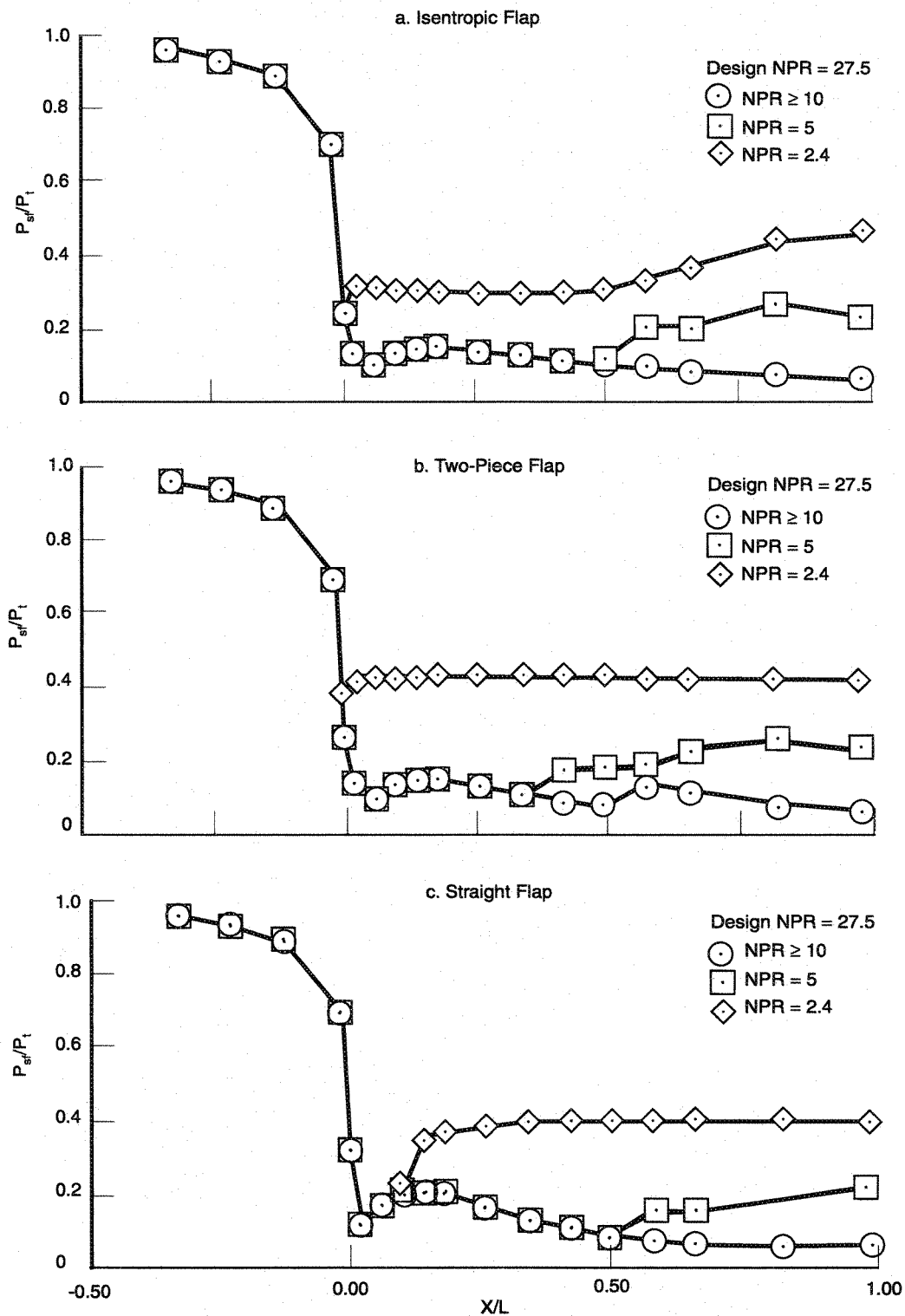
74745.odr

Figure 92. Comparison of 2-D/C-D Nozzle Flap Contour Centerline Pressure Distributions ( $L_f = 10$  in.,  $A_e/A_j = 3.5$ ,  $NPR = 27.5$ )



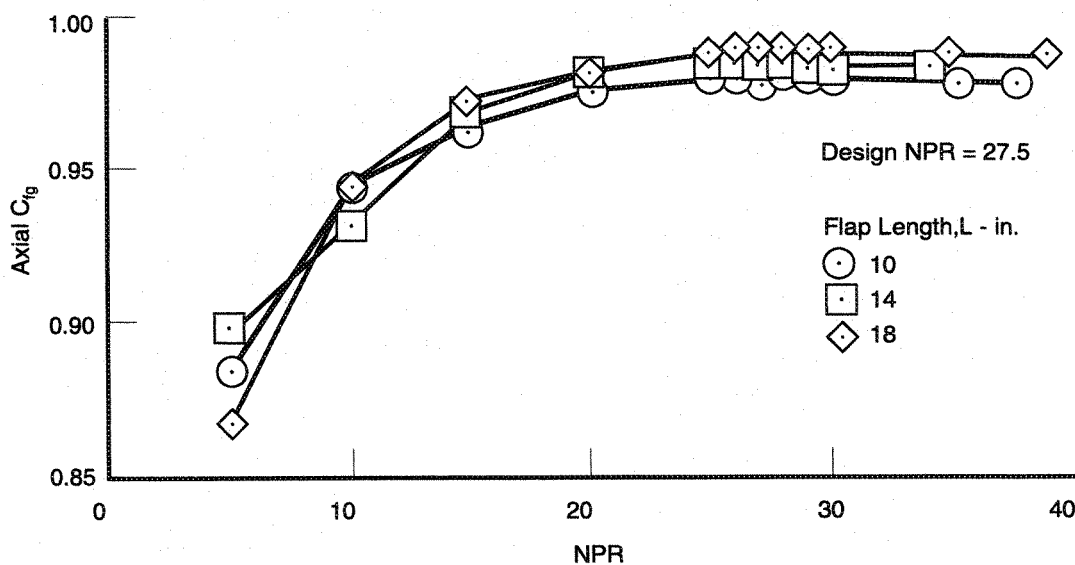
74746.cdr

Figure 93. Effect of 2-D/C-D Nozzle Flap Contour on Axial Performance  
 $(L_f = 10 \text{ in.}, A_e/A_j = 3.5)$



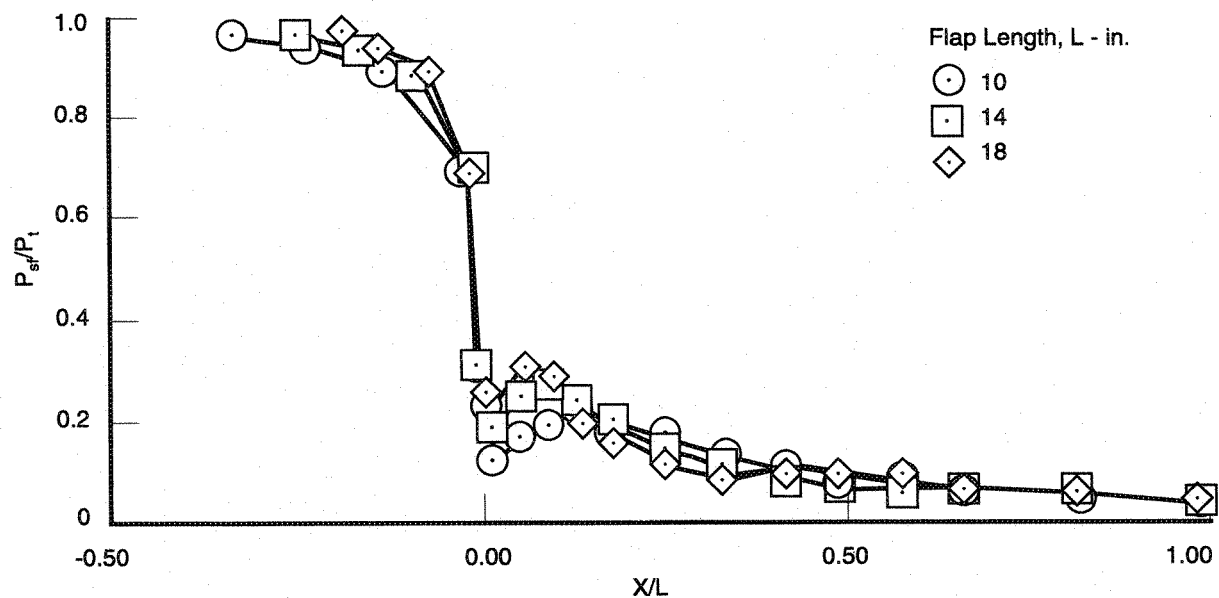
74747.cdr

Figure 94. Comparison of Separation Due to Different Flap Contours for the 2-D/C-D Nozzle ( $L_f = 10$  in.,  $A_e/A_j = 3.5$ )



74748.cdr

Figure 95. Effect of 2-D/C-D Nozzle Flap Length on Performance (Straight Flap,  $A_e/A_j = 3.5$ )



74749.cdr

Figure 96. Effect of 2-D/C-D Nozzle Flap Lengths on Centerline Flap Pressure Distributions (Straight Flap,  $A_e/A_j = 3.5$ , NPR = 27.5)

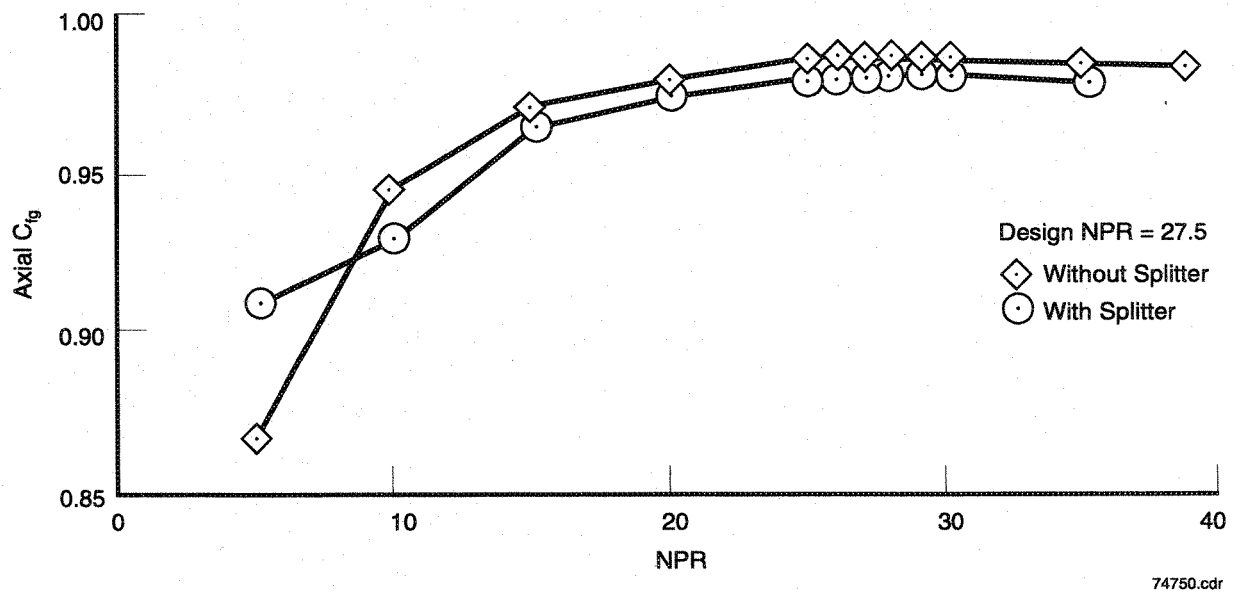


Figure 97. Effect of Splitter on Performance of the 2-D/C-D Nozzle  
 (Straight Flap,  $L_f = 18$  in.,  $A_e/A_j = 3.5$ )

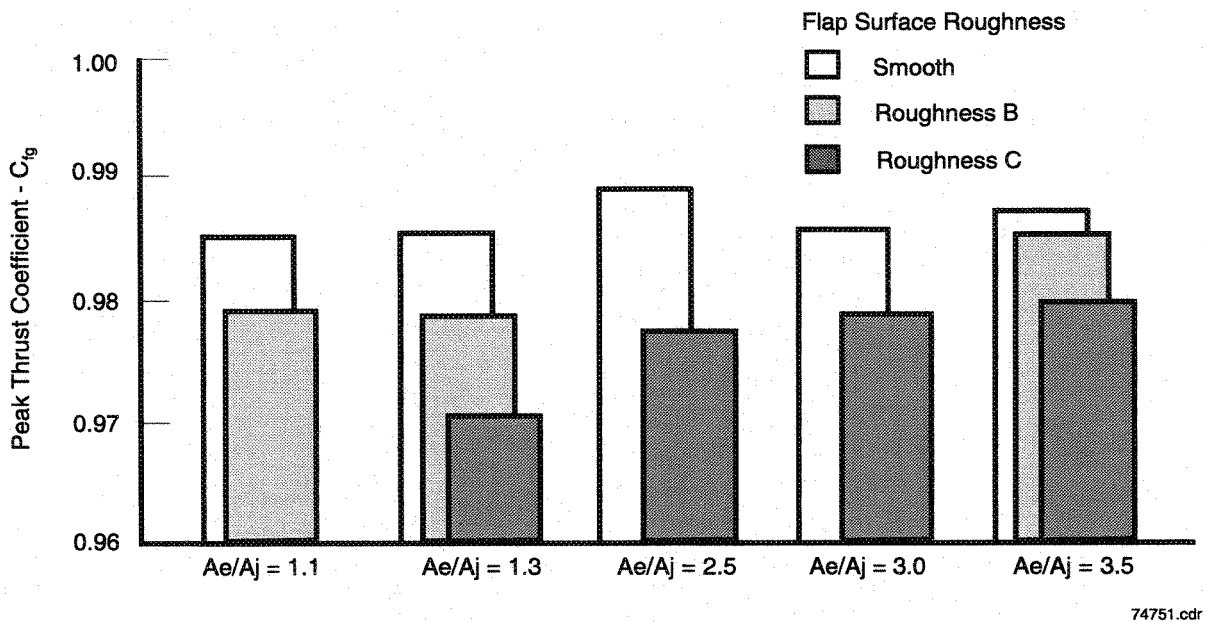
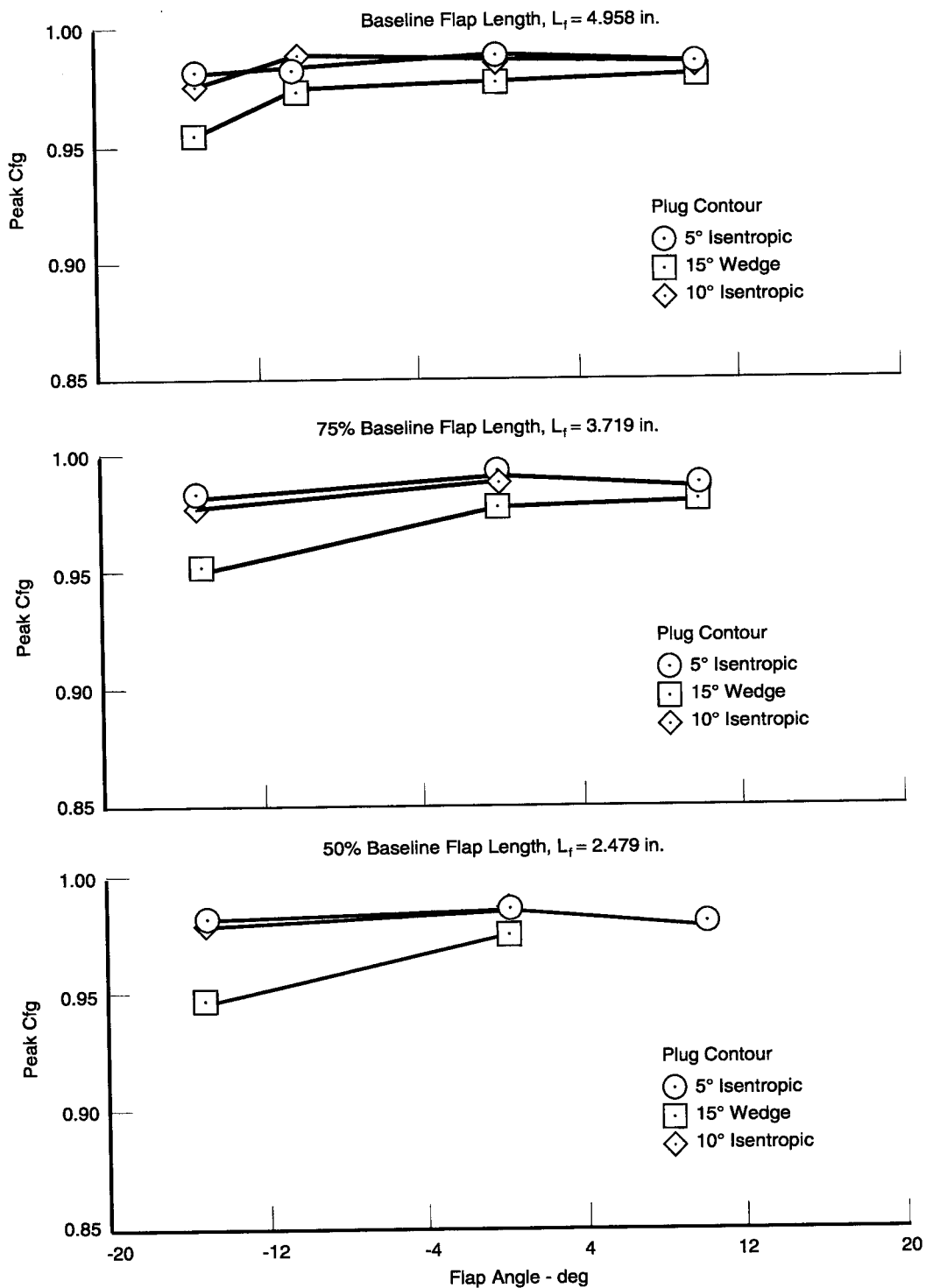


Figure 98. Effect of 2-D/C-D Nozzle Flap Surface Roughness on Peak Performance  
 (Straight Flap,  $L_f = 18$  in.)





74752.cdr

Figure 99. Peak Performance of the 2-D Plug Nozzle

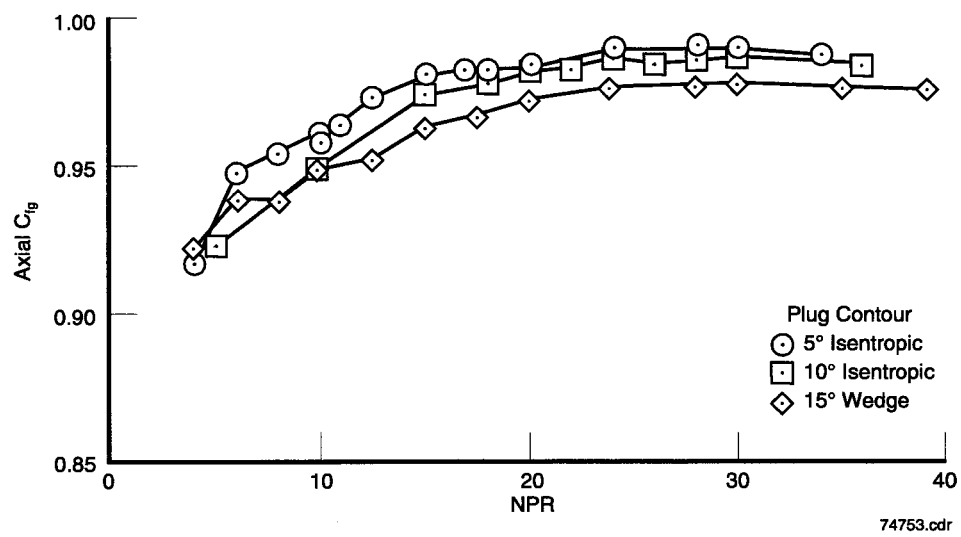


Figure 100. Effect of Plug Contour ( $L_f = 4.958$ , Flap Angle = 0 Degrees)

#### 4.5.1 2-D Plug Nozzle Flap Angle

The effect of cowl angle or internal area ratio (Figure 101) is similar to the effect of area ratio on a 2-D/C-D nozzle. The lower cowl angles perform better at the lower pressure ratios, while angles above 0 degrees perform better at the higher area ratios. The peak performance is at a 0-degree cowl angle for the 5-degree isentropic plug with a flap length of 4.958 in. Even though the performance of the negative cowl angles (into the flow) is better at the lower nozzle pressure ratios (NPRs), the flow tends to be less stable, and often the shock from the cowl separates the flow off the end of the plug creating further instabilities. These observations were made during the test on a video of the Schlieren at the exit of the nozzle.

#### 4.5.2 Plug Nozzle Flap Length

Flap length has little effect on the performance of the isentropic plug and the wedge at a cowl angle of 0 degrees (Figure 102, Figure 103, and Figure 104). For a cowl angle of -15 degrees, the longer flap performs 1 percent higher than the short flap, and 0.4 percent higher than the medium flap at a nozzle pressure ratio of 10. As the NPR increases, the difference in performance of the cowl lengths decreases. This is caused by the performance being driven by the external area ratio and not by the internal area ratio created by the flap. The external area ratio is the same for all the flap lengths, but the internal area ratio is dependent on flap length.

### 4.6 SERN

The peak performance of the isentropic ramps was higher than the flex ramp at all of the area ratios tested (Figure 105).

#### 4.6.1 SERN Ramp Contour Effects

The Isentropic ramp contours perform higher than the flex ramp at a 0-degree flap angle and length (Figure 106). The highest performance at a given flap angle is obtained from the 5-degree isentropic ramp. This contour performs 0.2 percent higher than the 7.5-degree isentropic contour, 0.4 percent higher than the 10-degree isentropic contour, and 0.9 percent higher than the flex contour.

#### 4.6.2 SERN Flap Angle and Length Effects

The flap angle and length control the internal area ratio (Figure 107 and Figure 108). Low area ratios are produced with negative (into the flow) flap angles. Similar to the 2-D/C-D nozzle, the low area ratios perform better at the low nozzle pressure ratios (less than 15). Conversely, the positive (away from flow) flap angles do not perform higher than the 0-degree cowl angle at the higher pressure ratios (greater than 15). This is due to the overexpansion losses caused by the larger flap angles.

### 4.7 CONCLUSIONS

#### 4.7.1 2-D/C-D Nozzle Performance Summary

- The isentropic contours provide the highest performance ( $C_{fg} = 0.992$ ) for a 2.5 area ratio. The two-piece nozzle contour performed about 0.002 lower, and the conventional straight flap was 0.007 lower than isentropic.
- The peak performance for the long flaps at an area ratio of 3.5 and an NPR of 27.5 was 0.988, or 0.8 percent higher than the short flaps due to the higher divergence losses of the shorter flap.
- The additional skin friction drag of the long flaps negates the decrease in divergence losses so that the performance for both the medium and long flaps is within 0.2 percent at an area ratio of 3.5, and a design pressure ratio of 27.5.
- Roughness effects from tests of the knurled long flap showed a 0.002  $C_{fg}$  loss for area ratios between 2.5 and 3.5; but up to 0.0075 loss at 1.1 to 1.3 area ratios.
- The splitter configuration performed lower than the baseline configuration (0.5 percent) at an area ratio of 3.5 and an NPR greater than 15.

#### **4.7.2 2-D Plug Performance Summary**

- The performance of the isentropic plugs was higher than the straight wedge at all of the flap angles and lengths.
- For a 0-degree flap angle and a 4.598 flap length, the isentropic 5-degree plug had a peak  $C_{fg}$  of 0.987, or 1.5 percent higher than the 15-degree wedge, and 0.5 percent higher than the isentropic 10-degree plug.
- The lower cowl angles perform better at the lower pressure ratios, while angles above 0 degrees perform better at the higher area ratios.
- Even though the performance of the negative cowl angles (into the flow) is better at the lower NPRs, the flow tends to be less stable, and often the shock from the flap separates the flow off the end of the plug creating further instabilities.
- At higher NPRs, flap length has little effect on the performance of the isentropic and wedge plugs with a flap angle of 0 degrees.

#### **4.7.3 SERN Performance Summary**

- The isentropic ramps performed higher than the flex ramp.
- The 5-degree isentropic ramp performance ( $C_{fg} = 0.987$ ) was 2 percent higher than that of the 7.5-degree ramp, 0.4 percent higher than that of the 10-degree ramp, and 0.9 percent higher than that of the flex ramp at a flap angle of 0 degrees, and a flap length of 7.379 in.
- The lower flap angles perform better at the lower pressure ratios (NPR less than 15).
- The 0-degree flap angle performs better than the higher angles at pressure ratios above 15. There is no performance benefit seen for flap angles greater than 0 degrees.
- At a 0-degree flap angle and 10-degree isentropic ramp, only the longest flap length showed a slight decrease in peak  $C_{fg}$  from the 0.983 level of the two shorter flaps.
- Flap length had little effect on peak  $C_{fg}$  except for the 15-degree wedge/15-degree flap combination, which showed a 1.5-percent loss for the shortest flap length.

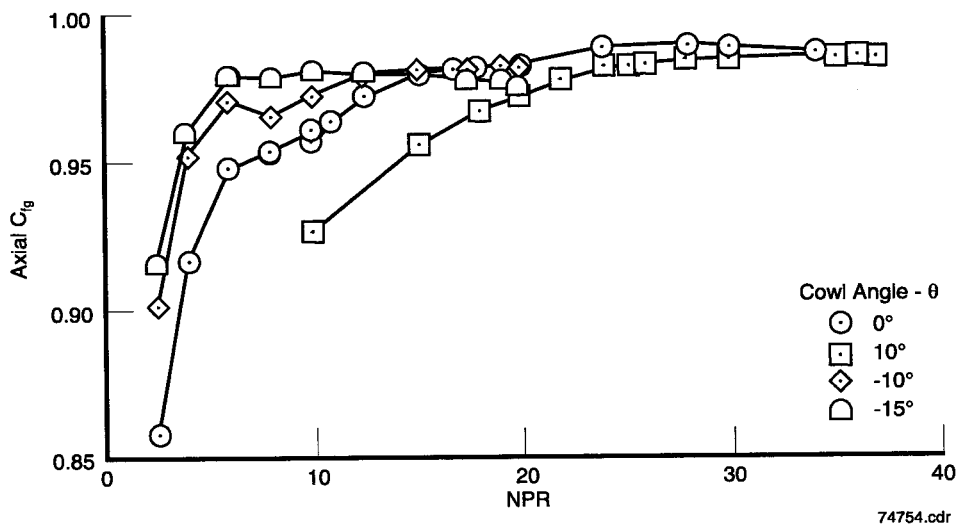


Figure 101. Effect of 2-D Plug Nozzle Cowl Angle Variations on Performance (5-Degree Isentropic Plug Contour,  $L_f = 4.958$  in.)

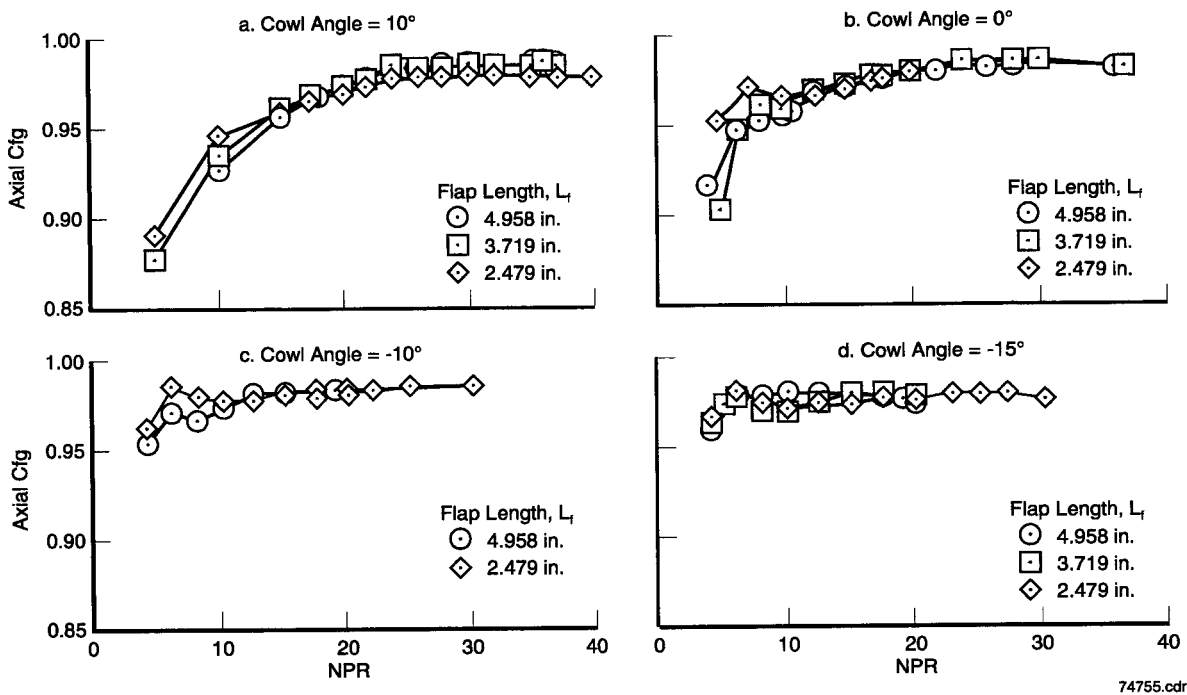


Figure 102. Effect of 2-D Plug Nozzle Flap Length and Cowl Angle Variations on Performance (5-Degree Isentropic Plug)

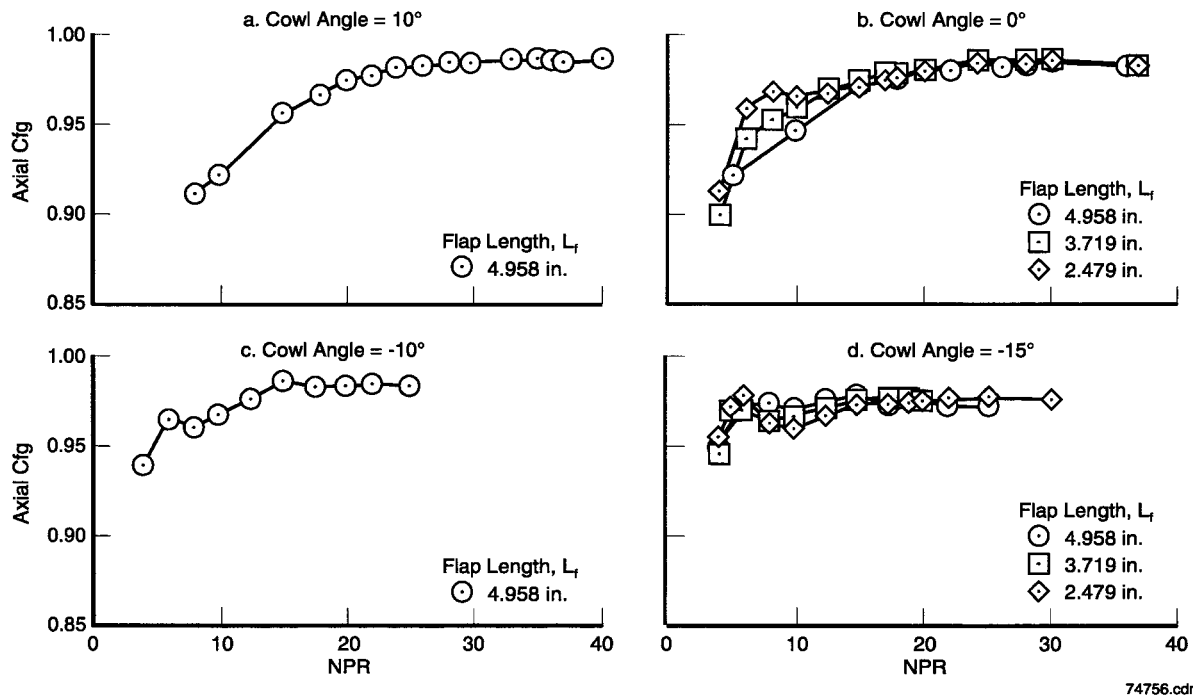


Figure 103. Effect of 2-D Plug Nozzle Flap Length and Cowl Angle Variations on Performance (10-Degree Isentropic Plug)

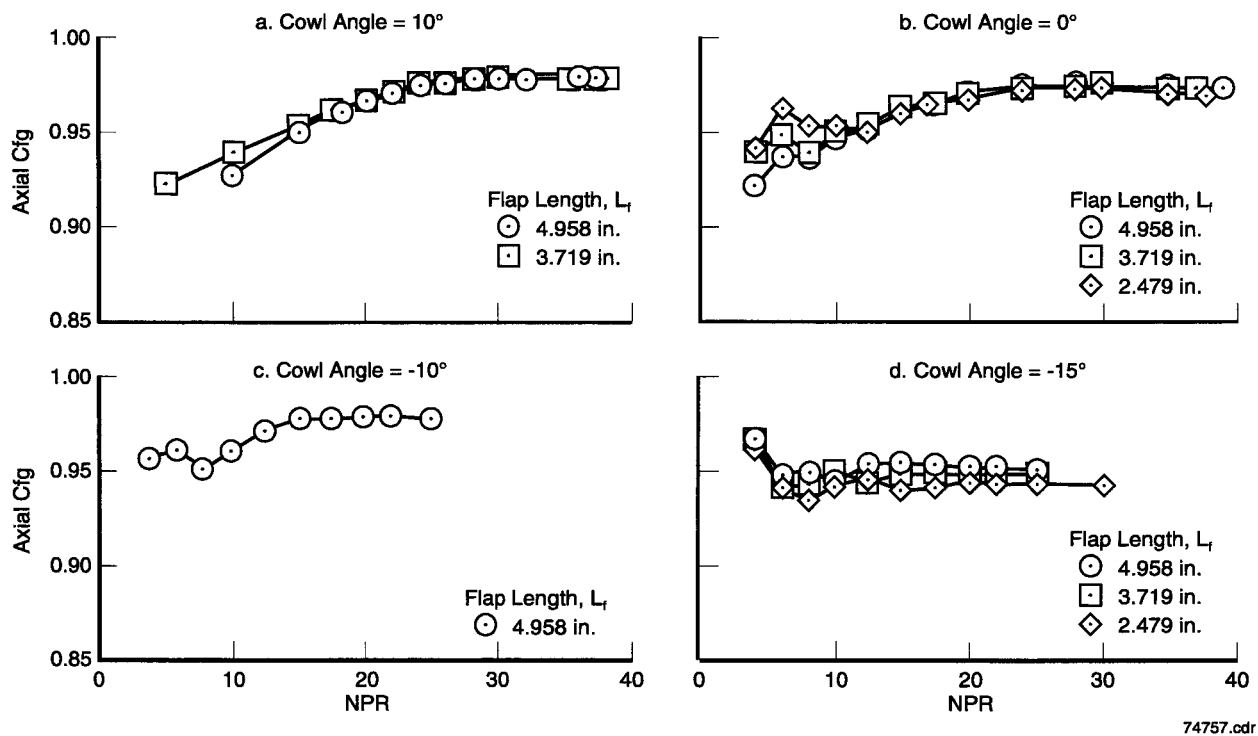


Figure 104. Effect of 2-D Plug Nozzle Flap Length and Cowl Angle Variations on Performance (15-Degree Isentropic Plug)

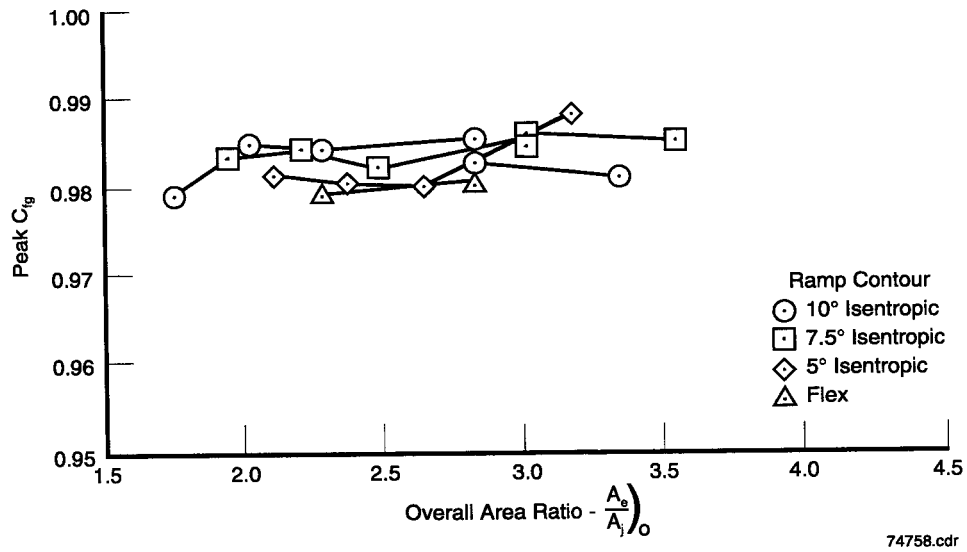


Figure 105. Peak Performance of SERN

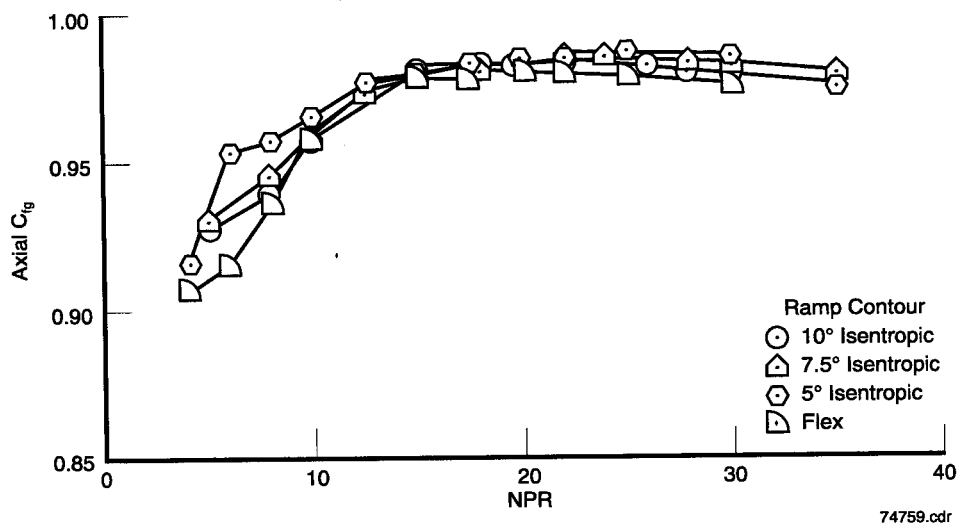


Figure 106. Effect of SERN Ramp Contour on the Performance ( $L_f = 7.379$  in., Flap Angle = 0 Degrees)

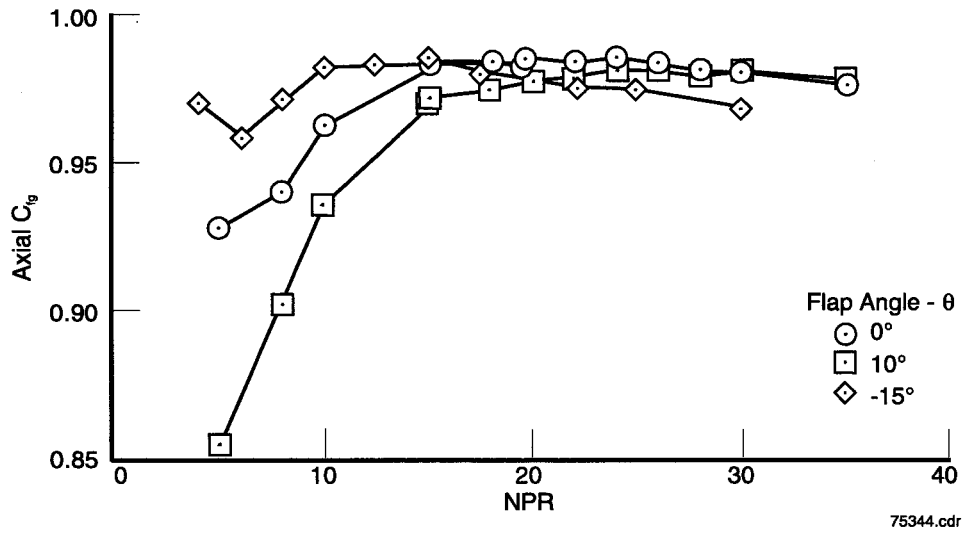


Figure 107. Effect of SERN Flap Angle on the Performance ( $L_f = 7.379$  in., 10-Degree Isentropic Ramp)

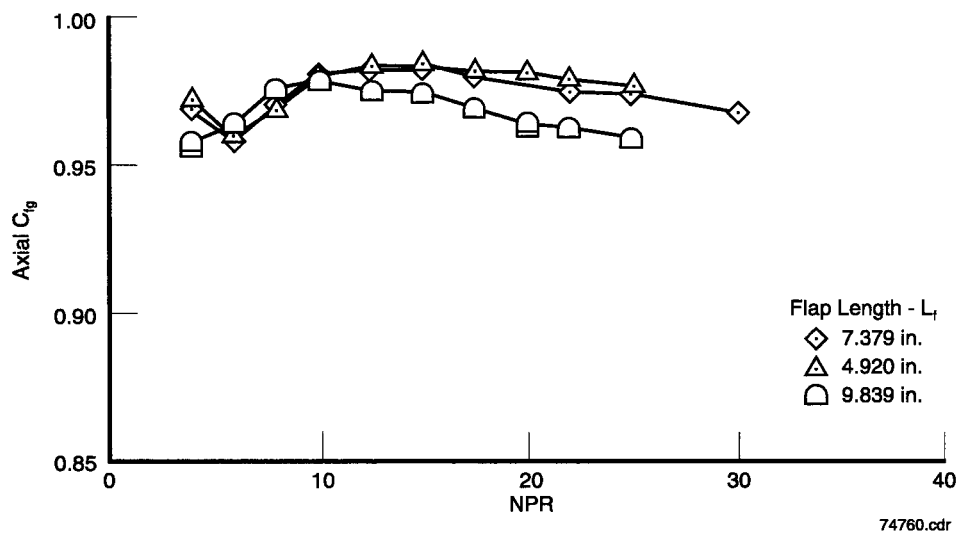


Figure 108. Effect of SERN Flap Length on the Performance (Flap Angle = 0 Degrees, 10-Degree Isentropic Ramp)



## APPENDIX 4-A

### LIST OF SYMBOLS

$A = (S_{fl} \times H_{fl}) - A_e$	Convergent flap flange area, in. <sup>2</sup>
$A_e$	Exit Area of Nozzle, in. <sup>2</sup>
$\frac{A_e}{A_j}$	Area Ratio
$\left(\frac{A_e}{A_j}\right)_I$	Internal Area Ratio
$\left(\frac{A_e}{A_j}\right)_o$	Overall Area Ratio
$A_j$	Geometric Throat Area of Nozzle, in. <sup>2</sup>
$C_d = W/W_{id}$	Mass Flow Coefficient
$C_f$	Skin Friction Coefficient, including roughness effects
$C_{fg}$	Gross Thrust Coefficient, $C_{fg} = F/F_{id}$
$F$	Measured Thrust, lbf
$F_{fl}$	Force on the Flange, $F_{fl} = A(P_{te} - P_{le})$ , lbf
$F_{id}$	Ideal Thrust, lbf
$H_{fl}$	Height of the flange, in.
$L_f$	Internal Surface Flap Length measured from throat to exit, in.
$L$	Flap Length along centerline measured from throat to exit, in.
$K_s$	Roughness, in.
$NPR$	Nozzle Pressure Ratio ( $P_t/P_{amb}$ )
$P_{amb}$	Ambient Pressure, psia
$P_{le}$	Static Pressure at leading edge of convergent flap flange, psia
$P_{sf}$	Static Pressure on the flap, psia
$\frac{P_s}{P_t}$	Static to Total Pressure Ratio
$P_t$	Nozzle Total Pressure, psia
$P_{te}$	Static pressure at trailing edge of convergent flap

	Flange, psia
X	Axial Distance along the centerline from the throat, in.
Y	Vertical distance from centerline, in.
Z	Spanwise distance from centerline, in.
$S_{fl}$	Span or Width of flange, in.
W	Measured Mass Flow, lbm/s
$W_{id}$	Ideal Mass Flow, lbm/s
$\Delta P$	Pressure gradient, $\Delta P = P_{te} - P_{le}$ , psi
$\Delta C_{fg} = F_{fl}/F_{id}$	Thrust Coefficient Difference due to adverse pressure on flange
$\theta$	Flap Angle and Cowl Angle, degrees (positive away from flow, negative into flow)

## REFERENCES

1. Beltran, L.R., Del Roso, R.L., and Del Rosario, R., Advanced Nozzle and Engine Components Test Facility, NASA TM-103684, January 1992.
2. Schlichting, H., Boundary-Layer Theory, McGraw-Hill Book Company, New York, 1968.

## 5. COMPUTATIONAL FLUID DYNAMICS

With the renewed national interest in developing a High Speed Civil Transport (HSCT), there is increasing concern regarding two significant environmental issues that arise from such an aircraft system: airport community noise and engine emissions (ozone depletion). The present effort describes the analysis of a Two-Dimensional (2-D), or planar, mixer-ejector exhaust nozzle in order to achieve the Federal Aviation Regulation (FAR) 36 Stage III noise goals. An ejector is a fluid dynamic pump that provides a means for pumping low energy (velocity or temperature) secondary fluid using the kinetic energy of the primary stream. The fundamental principles of an ejector first suggested by von Karman are based on increasing the thrust of the primary propulsive nozzle and mixing the high-temperature exhaust flow with ambient air to provide lower jet noise. In both cases, the key mechanism for the operation of the ejector is energy transfer from the primary to the secondary fluid stream through viscous mixing. Common ejectors require long mixing ducts to entrain and mix primary and secondary flows. Long mixing ducts result in increased wall friction losses, extra weight, and higher costs. By incorporating a forced mixer, energy can be transmitted from the engine stream to the fan stream in an efficient manner. This means that significant thrust gains can be obtained for many turbofan cycles, and jet exhaust noise reduction benefits may be obtained with minimal engine performance penalties. Forced mixing is dominated by large-scale secondary flows rather than viscous diffusion, and is therefore an efficient mixing process. A key benefit of mixer-ejectors relative to conventional ejectors is that good pumping and effective mixing can be achieved over very short mixing duct lengths. Shortening of the ejector mixing duct is advantageous in aircraft exhaust systems due to savings in weight and fabrication costs. Typical mixer-ejectors show well-mixed shroud exit flows occurring in 1 to 2 mixing duct diameters, as opposed to conventional ejectors which require lengths of 5 to 7 duct diameters.

Significant work has been accomplished in recent years refining and verifying the performance and noise suppression benefits of a mixer-ejector exhaust system. The primary goals of the current program are to assess the impact of propulsion-airframe integration effects on the performance and noise suppression of these nozzles. Of major concern is the effect of the wing flow field and high-lift system on the exhaust nozzle inflow conditions. Similarly, there is a concern as to what effect the exhaust nozzle has on the high-lift performance of the wing. These issues will be addressed in a series of computational and experimental studies of a General Electric Aircraft Engines (GEAE) mixer-ejector exhaust system mounted on the Boeing Reference H wing-body combination. A schematic representation of this assembly is seen in Figure 109 and Figure 110. The experimental studies were performed at the NASA Ames Research Center's (NASA Ames RC's) 40 by 80 ft wind tunnel as part of the Highlift Engine Aeroacoustic Technology (HEAT) program. Aerodynamic data was obtained from coldflow test using a Cold Aerodynamic Model (CAM), while acoustical data was obtained from hot flow test using a Hot Acoustical Model (HAM). During installed testing, the GEAE engine simulator (exhaust nozzle assembly supplied by a heater burner) was mounted on the Reference H wing at the inboard location (approximately 27 percent of wingspan). The assembly is oriented such that the centerline is angled 1-degree out. Definition was provided in the IGES geometry file to integrate the exhaust system to the Boeing Reference H wing. This computation fluid dynamic (CFD) study accurately predicted mixer/ejector pressure distributions and shock locations.

### 5.1 GEOMETRY

The GEAE exhaust system consists of a primary nozzle and a flight-type ejector. The primary nozzles are 2-D and have identical symmetric (opposed) lobes. The chute exit to throat plane area ratio of the nozzles is 1.44. The mixer configuration represents a 20-lobed, 100-percent penetrated chute assembly in an ejector mixing duct having a mixing area ratio (MAR) of 1.0 and a suppressor area ratio (SAR) of 2.8. The lobes of the mixer nozzle have a crest ramp angle of about 14 degrees, a cold-side chute ramp angle of 30 degrees, and a hot-side lobe aspect ratio of 3.14. The ejector duct is 17 in. long (measured from the mixer exit plane to the ejector exit plane). The surface geometry was obtained electronically from NASA Ames RC (B. Smith) in a standardized IGES format. The IGES file was generated from a UNIGRAPHICS file provided by GEAE staff. A cutaway schematic of the nozzle geometry is shown on Figure 111, while cross-sectional slices through the mixer are shown in Figure 112.

During installed testing, the GEAE exhaust nozzle assembly would be mounted on the Reference H wing at the inboard location (approximately 27 percent of wingspan). The assembly is oriented so that the centerline is angled 1 degree outward as viewed from above. A flap fairing definition was provided in the IGES geometry file to integrate the exhaust system to the Boeing Reference H wing.

## 5.2 GRID GENERATION

### 5.2.1 Background

Techniques for generating structured grids include elliptic grid generators, hyperbolic generators, algebraic methods, transfinite interpolation techniques, and conformal mapping. A previous mixer-ejector design was meshed at Pratt & Whitney (P&W) using the conformal mapping technique of Ives and Zacharias (1). An alternative approach is used for the current analysis efforts. Since the production version of the NASTAR Navier-Stokes flow solver code required a structured, single-block grid, it was determined that the full three-dimensional (3-D) grid could be generated by defining 2-D cross-sectional grids at predefined axial stations, and then stacking these together to define the 3-D grid. This approach (called dimension reduction) redefines the grid generation task into two separate efforts. The first stage involves generating cross-sectional cuts of the mixer-ejector geometry. The second stage of the mesh generation process involves stacking the cross-sectional grids to form a 3-D mesh.

### 5.2.2 Grid Generation

A 3-D computational grid was developed using a 2-D gridding technique that uses EXTOP2, a knowledge base expert system multiblock gridding code developed by J.F. Dannenhoffer (2 and 3). The process of generating the 3-D grid consists of a number of separate tasks. First, the CAD nozzle surface geometry files (IGES format) were read into ICEM, a CAD software package. The surface geometry was then y sliced axially using the ICEM cutting plane option. The resulting files, now containing intersections of cutting planes with all the geometric surfaces, were post-processed to give individually cut boundaries. This procedure was effectively used to generate grids for the analysis of P&W's Generation 1 (GEN1) mixer-ejector exhaust nozzles (4 and 5). The P&W GEN1 program assessed the mixing and noise reduction capabilities of vortically-driven (where chute height equals chute width) mixer/ejector nozzles.

The grid generation software based on Dannenhoffer's EXTOP2 program was developed and applied to the given geometry. The power of this structured grid technique is that only boundary definitions are needed; grid smoothing and stretching are functionally controlled by the user instead of only manually controlled by the user; and a knowledge base is maintained that can be used for additional or alternative axial cuts. The generation of the cross-sectional grids from the onset of the mixer geometry to the trailing edge of the ejector flap was accomplished using the functionality of the knowledge base available in EXTOP2. Because of the need for a single-block grid, the grids for the nozzle and chute passages have to be *blended*. This necessarily implies that grid cells will have a wide range of skewness, especially near the trailing edge of the mixer lobe. Viscous stretching to the mixer surface as well as to the lower surface of the shroud were accomplished using the expert system capabilities of EXTOP2. In order to reduce both the number and the effect of the highly skewed cells induced by the severe crest to trough geometry, the EXTOP2 system was used to blend the mixer trailing edge to a benign straight segment at the ejector flap trailing edge. This eliminated the viscous stretching necessary along the mixer surface that is no longer aligned to the nozzle shear layer wake. Consequently, an *unstretching* operation allows a more efficient use of the grid lines. A blending of the grid from the mixer trailing edge to the shroud trailing edge was therefore introduced.

While the NASTAR multi-block Navier-Stokes code was being checked out, the requirement of developing a single-block grid presented new features for the grid generation process. The GEAE geometry represented a combination of features found in the P&W GEN1 vortical and axial mixer nozzles (i.e., the centerline slot resembled the P&W vortical nozzle centerline slot, while the cold flow pinch-off at the shroud resembled the centerline hot flow pinch-off found in the P&W axial nozzle). The current mesh has 300,000 grid points (axial = 113, radial = 88, lateral = 30), with approximately 60 radial points in the mixing duct. The grid is axially stretched and relaxed to produce a Cartesian grid at the exit of the mixing duct. A display of the grid at several cross-sectional cuts is shown

in Figure 113. Figure 114 displays crest (hot) and trough (cold) plane axial grid cuts. Note that a small ramp is used in the crest plane to transition the hot primary flow onto the shroud.

### 5.3 DESIGN POINT

The design point or operating condition to be analyzed is a takeoff condition with forward flight (wind-on) effects. This corresponds to an aircraft operating at an angle of attack of 11 degrees in a freestream Mach number of 0.32. The exhaust system would operate over a range of nozzle pressure ratios (NPR), including an NPR of 3.4 and 4.0. The NPR of 3.4 condition corresponds to a primary flow velocity ( $V_p$ ) of 2400 fps, and a primary flow total temperature ( $T_{op}$ ) of 1590°R.

Flow field boundary conditions for the exhaust system were to be obtained from airframe simulations developed by NASA and the airframe companies. Simulations of various degrees of complexity (potential flow, Euler, and Navier-Stokes [NS]) were to be obtained over wing-body combinations, usually without any modeling of the leading edge high-lift devices. A survey was conducted to determine the best source for the ejector inlet conditions.

- NASA LeRC used the CFL3D (NASA LeRC, Thomas) implicit, multi-block, time-marching Navier-Stokes analysis (Baldwin-Lomax turbulence model) to analyze the clean wing-body configuration for static and forward flight ( $M_\infty = 0.24$ ) with conditions at 11 degrees angle-of-attack. The wing geometry did not model the leading-edge high-lift devices.
- Boeing modeled the wing-body combination using their PANAIR inviscid, incompressible panel method code using Glauert scaling to simulate compressibility effects. An assessment of viscous boundary layer effects was to be obtained using either 2-D strip boundary layer codes or their 3-D boundary layer analysis.
- Brian Smith of NASA Ames RC (6) followed the Boeing approach by modeling the wing-body combination using their lower order (constant strength, quadrilateral doublet panels) potential flow panel code (PMARC) in conjunction with a 2-D strip boundary layer method (Thwaites/Curle: laminar; Nash/Hicks: turbulent). While no modeling of the leading-edge flaps was made, the effect of the ejector was modeled as a specified suction at the appropriate spanwise trailing-edge locations. The output from these calculations were used in our studies cited below.

The flow conditions in the neighborhood of the inboard ejector inlet can be ascertained by post processing of the NASA Ames RC calculations. Streamlines over the upper wing surface were determined, and those key streamlines that would be entrained into the ejector inlet were identified (Figure 115). These streamlines are angled inboard by about 4 degrees while the nacelle has been geometrically aligned 1 degree outboard. Results of 2-D strip boundary layer calculations for these streamlines indicates that the boundary layer thickness at the inlet plane is approximately 2.0 in., the same as the ejector inlet height.

### 5.4 FLOW FIELD SOLVER

In this section, the CFD analysis approach for modeling the mixer-ejector flow field is described. Also included is a brief description of the NASTAR code used, boundary conditions employed in the simulation, and a brief description of some recent analytical studies.

#### 5.4.1 NASTAR Navier-Stokes Analysis

The viscous analysis used was the P&W NASTAR code which solves the Reynolds-averaged form of the governing equations for steady, 3-D flows, including the effects of turbulence and heat release due to chemical reaction. The code was developed at P&W and is based on the method due to Rhie (7). Essentially, NASTAR represents a significant extension of the pressure-correction methodology used in the TEACH family of codes (8). The governing equations are approximated using a finite-volume method. The discretized continuity and momentum equations are used to derive a pressure-correction equation that is used in place of the continuity equation. Rhie's method provides a single-cell, general curvilinear coordinate procedure that is applicable for Mach numbers rang-

ing from incompressible flow to hypersonic flow. The results described in the current study were obtained using the two equation ( $k$ - $\epsilon$ ) model for turbulence (Jones and Launder; 9).

Boundary conditions for the NASTAR analysis entailed specifying the total pressure and total temperature at the entrance to the mixer nozzle (i.e., upstream of the throat) and at the upstream end of the domain for the external flow. A constant value of free-stream static pressure was prescribed along both the upper boundary and downstream end of the domain. The upper boundary was located approximately 60 in. above the centerline of the nozzle to ensure that the near-region flow was not affected by its location. Planes of symmetry defined the lateral extent of the domain and passed through the crest/peak and trough/valley of the mixer. Finally, the lower boundary of the computational domain was also represented as a plane of symmetry. The calculations were initialized using the free-stream velocity everywhere except within the mixer nozzle. Here, the velocity was set to correspond to a Mach number of 0.1 at the entrance stagnation temperature. Within the mixer, the static pressure was varied linearly from the entrance (total) value to the free-stream static pressure at the end of the mixer, thereby avoiding sharp discontinuities in static pressure at the mixer exit. This is the recommended method for initializing the flow field for NASTAR when large pressure differences exist at the boundaries, such as those that occur across a choked, underexpanded nozzle.

The algorithm used in NASTAR provides for a controlled amount of numerical damping to be added to the calculation. The amount of damping is determined from the local cell Reynolds number. For values of local cell Reynolds numbers greater than a user-specified maximum, sufficient dissipation is added to promote numeric stability. Generally (and in the present case), the user-specified maximum cell Reynolds number was increased during the iteration to the recommended upper (minimum added dissipation) limit. Various measures were used to determine whether the computation was converged sufficiently. As with most CFD codes, NASTAR provides the user with periodic reports of the level of residual errors that represent the extent to which the discrete form of the governing equations are in balance. In addition to the residual history, selected integral measures were also monitored as the iteration proceeded. For example, the pumping ratio (the ratio of secondary to primary mass flow rates at the mixer exit) was computed and was seen to approach an asymptotic value indicating that the iteration had essentially converged (see Section 5.5.5). Mass conservation requires that the flow rate within the shroud be constant from one axial position to another. An integral measure of total enthalpy within the shroud was also monitored.

## 5.5 FLOW FIELD ANALYSIS-ISOLATED NACELLE

### 5.5.1 Experimental Data

Figure 116 shows ejector flap pressure distributions for the isolated HAM nozzle for a range of NPRs measured at NASA Ames RC's 40 by 80 ft wind tunnel as part of the HEAT experimental program. The pressure distribution for the 3.6 NPR case shows an abrupt increase at the ejector duct exit plane indicating the presence of a shock wave. Local peaks in the pressure distribution are observed close to the mixer exit plane ( $X = 23.5$  in.) and at a location of 28 in. The axial origin ( $x = 0$ ) is defined as the location of the flange between the transition duct and the upstream circular spool piece. As the NPR is decreased, the shock wave moves from the ejector exit plane into the ejector duct ( $\text{NPR} = 3.6 - 3.3$ ). For NPRs lower than 3.3, the ejector duct recompresses isentropically to freestream pressure and is free of shock waves; from  $X = 25$  in. to the exit plane, the static pressure is close to that of the ejector exit plane. The transition from ejector operation with a shock wave at the exit plane to the shock-free condition has been termed *mode switching*.

### 5.5.2 Isolated Nacelle Analysis

NASTAR Navier-Stokes solutions for the uninstalled mixer-ejector configuration have been obtained for NPRs of 4.0, 3.6, and 3.4. These calculations were done for a takeoff flight Mach number of 0.32. Figure 117 shows the ejector flap pressure distribution for the three numerical computations. The pressure distributions show the same features that are observed in the experimental data. (i.e., a shock wave is present at the exit of the ejector duct for NPRs of 3.6 and higher, whereas the ejector duct is shock free for lower NPR.) The details of the pressure distribu-

tions along the ejector flap are also similar to the experimental data. (i.e., local peaks in pressure are observed at the same locations.) The fluid dynamic features associated with these peaks will be discussed below.

Table 3 summarizes the mixer-ejector (m-e) performance parameters for the nozzle pressure ratios that were analyzed. All three cases show about the same degree of mixedness ( $\eta$  = normalized mass average total temperature), while the lower NPR cases have larger pumping ratios ( $\omega$  = aspiration ratio).

*Table 3. HEAT Test Analysis Matrix*

<i>Case</i>	<i>NPR</i>	<i>T<sub>o</sub> (R)</i>	<i>M<sub>∞</sub></i>	<i>ω</i>	<i>η (%)</i>	<i>Comments</i>
1	4.0	1750	0.32	0.53	80	Isolated m-e
2	3.6	1640	0.32	0.63	79	Isolated m-e
3	3.4	1580	0.32	0.60	79	Isolated m-e

Figure 118 shows the ejector flap surface stagnation temperature as a function of axial distance for two lateral locations; the first aligned with the mixer lobe crest centerline, and the second aligned with the chute centerline. The crest plane solutions start out at the primary flow condition, while the trough plane solution rises from its freestream level as the mixing progresses. The lateral thermal convection process is clearly seen in Figure 119, where cross-sectional  $T_o$  contours are shown in the mixing duct. A closer examination reveals that the lateral movement of the hot flow near the shroud is driven by shock-wave induced pressure gradients. Near the nozzle symmetry axis, the mixing effect induced by the generation of streamwise vorticity is evident. This situation is similar for all of the flow conditions that were computed.

### 5.5.3 Operating Mode 1 — Normal Shock at Ejector Exit Plane

Figure 120 shows a plot of the *shock function* (which is based on the pressure gradient) for the 4.0 NPR case. The figure shows a system of oblique shock waves in the ejector duct which terminates in a normal shock wave at the ejector exit plane. This shock structure is typical of the computed cases for NPRs greater than 3.6.

The oblique shock wave is initiated close to the mixer exit plane where the ramp from the primary nozzle crest merges with the ejector flap. The oblique shock is reflected at the symmetry axis and at the ejector flap several times until it terminates in a normal shock at the ejector exit plane. The local peaks that are observed in the ejector flap pressure distributions correspond to the locations at which the oblique shock waves are initiated and reflected. Figure 121 indicates that the nozzles are operating in an over-expanded mode, with clearly visible sidewall shock waves.

### 5.5.4 Operating Mode 2 — Shock-Free Ejector Duct

Figure 122 shows the shock function for the 3.4 NPR case. From this picture, it is clear that a shock structure is present close to the exit plane of the nozzle, but the oblique shock structure that was present in the 4.0 NPR case is absent for this operating condition. The shock structure that is visible in the figure is generated as a result of the over-expansion of the flow in the nozzle.

### 5.5.5 Convergence History

A check of the numerical accuracy/convergence of these calculations was made in terms of the calculated mass-flow balance and ejector flap pressure distribution. The mass-flow distribution through the ejector duct was monitored as a function of iteration number, and this was used initially as a convergence criterion. Pressure-dominated problems like a transonic fan have required approximately 1,000 iterations to achieve solution convergence. Vortically dominated mixer-ejector configurations (GEN1) typically require approximately 3,000 to 4,000 iterations to converge. Viscous dominated mixer-ejector configurations (GE-type, and GEN1.5) require approximately 8,000 iterations.



An examination of the convergence characteristics of the current cases in terms of the ejector flap pressure distributions has been considered. Even after mass-flow uniformity was reached in the ejector duct, it was observed that the ejector flap pressure loading continued to change. Figure 123 shows the ejector flap pressure distribution for the 4.0 NPR case. Here, mass-flow uniformity was achieved after approximately 9,000 iterations. The abrupt pressure increase that is seen in the duct at 9,750 iterations corresponds to a normal shock wave in the duct. It is apparent from this figure that the shock wave moves toward the ejector exit plane as the computation advances and reaches a steady state at 18,750 iterations (when the shock wave is located at the ejector exit plane).

### 5.5.6 Analysis of Installation Effects

The experiments that have been conducted thus far were for the uninstalled case. Boundary layer profiles at a location 8 in. upstream of the inlet flow guide (approximately 15 in. upstream of the ejector flap leading edge) were provided by NASA. This profile is due to the boundary layer that develops over the nacelle upstream of the ejector inlet. The uninstalled computations that were done included a faring that guides the flow from the wing upper surface into the ejector inlet. In order to model the uninstalled configuration, no inlet profile was specified at the upstream boundary. Figure 124 shows a comparison of the experimental and computed boundary layer profiles at the location where the experimental data were provided. In this plot, velocities for the computed cases are normalized by the velocity at a height 2 in. above the faring surface to eliminate the effect of the profile due to the potential effect of the faring on the inlet flow. The close correspondence between the experimental and theoretical profiles indicates that the computation is a good simulation of the uninstalled experimental condition.

In order to model the wing installation effects on the performance of the nozzle, a boundary layer profile was specified at the inlet boundary. The specified boundary layer profile was based on H wing computations that were performed at NASA Ames RC. These computations indicated that when the wing operates at an angle of attack of 9 degrees, the boundary layer at the trailing edge of the wing has a thickness of approximately 2 in. To model this effect, a 1/7th power law boundary layer profile (a flat-plate profile) with a thickness of 2 in. was specified at the inlet boundary of the secondary stream. This corresponds to the trailing edge of the wing. Because the boundary layer encounters an adverse pressure gradient over the wing, the profile would probably be more severe than the flat-plate (zero pressure gradient) profile that was assumed. To account for this effect, a computation was also done with a more severe 1/4 power law profile. For comparison, the profiles corresponding with the uninstalled case, the 1/7th power law case, and the 1/4th power law cases are shown in Figure 124, along with the experimental uninstalled profile at the location where the experimental data were provided.

Figure 125 shows calculated axial velocity profiles for the flow along the secondary inlet chutes for the uninstalled case. From this figure, it is apparent that the flow accelerates as it flows into the inlet chutes and the mean axial velocity at the exit plane of the nozzle is significantly higher than that at the plane of the ejector flap leading edge. This has a favorable effect on any profile that exists in the flow at the inlet to the chute and there was no tendency for the flow to separate along the chute. Equivalent plots are shown for the 1/7 and 1/4 power law cases in Figure 126. No significant difference exists between profiles at the nozzle exit planes for the three cases, and the ejector performance is not significantly affected. Table 4 shows the mixer performance figures for the three different cases that were analyzed, and Figure 127 shows the ejector flap pressure distributions. Little difference in the performance parameters is noted.

Table 4. Boundary Layer Profile Effect Study

Case	NPR	$T_o$ (R)	$M_\infty$	$\omega$	$\eta$ (%)	Comments
1	4.0	1750	0.32	0.53	80	Isolated m-e
2	4.0	1750	0.32	0.52	79	1/7 B.L. Profile
3	4.0	1750	0.32	0.51	79	1/4 B.L. Profile

## 5.6 CONCLUSIONS — FLOWFIELD OBSERVATIONS

Several calculations of the GEAE mixer-ejector exhaust nozzle assembly for the HEAT test have been accomplished using the NASTAR Navier-Stokes analysis. An examination of the solutions obtained indicates that:

- The calculations predict the experimentally observed flowfield behavior (i.e., that a mode switch behavior, from a shock-free [isentropic] mixing duct to a state with a normal shock near the exit plane occurs around  $\text{NPR} \approx 3.3$ ).
- The chute/flap design drives the hot primary flow onto the flap surface.
- The shock location in the mixing duct is dependent on the flap boundary layer development, resulting in a substantially increased number of iterations required to achieve solution convergence.
- The effect of boundary layer profile ingestion into the ejector is small, and the effect of the *estimated* wing boundary layer profile (no skew) is also small.

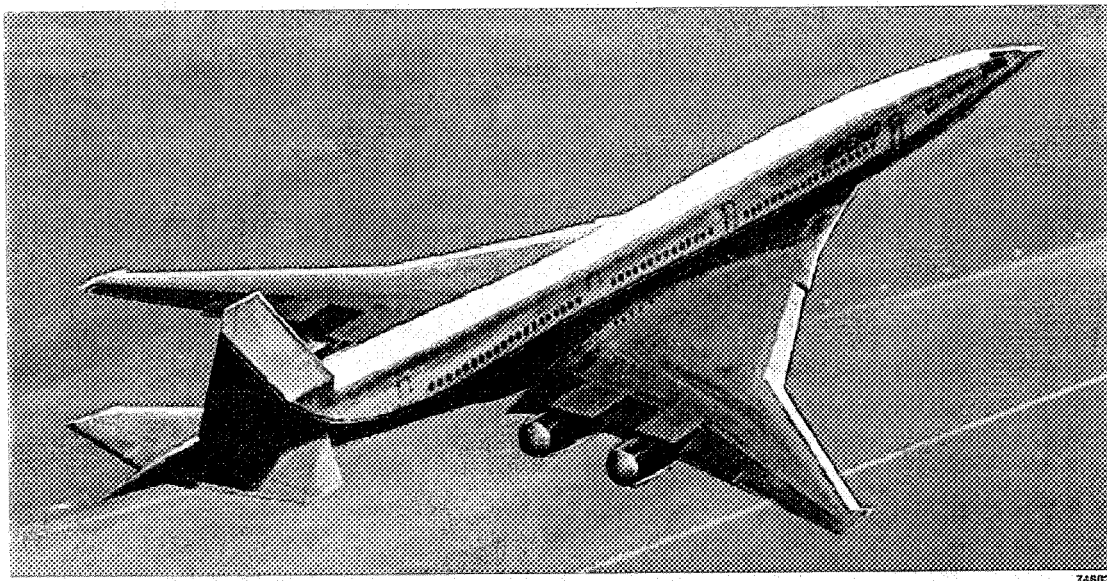
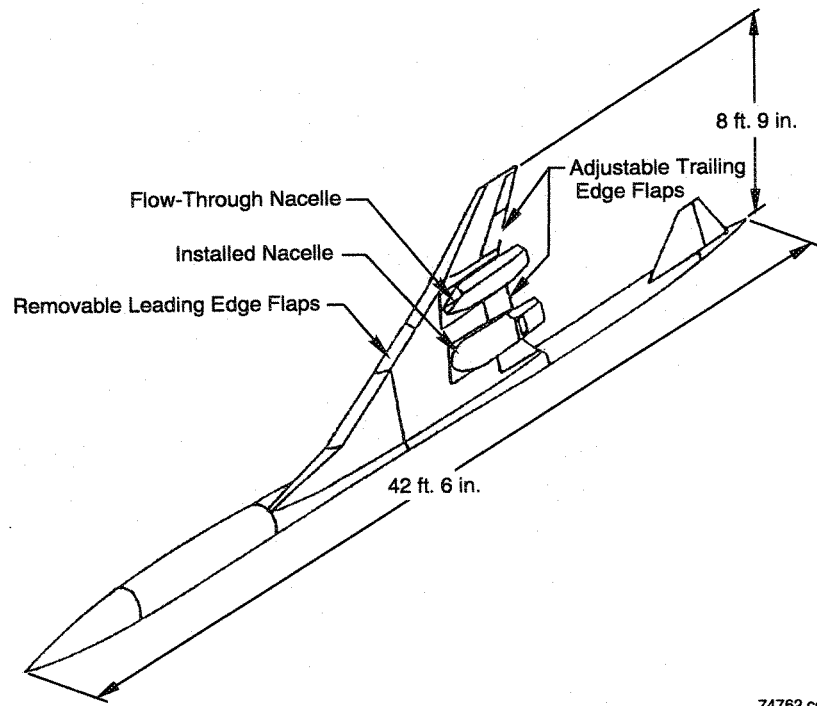
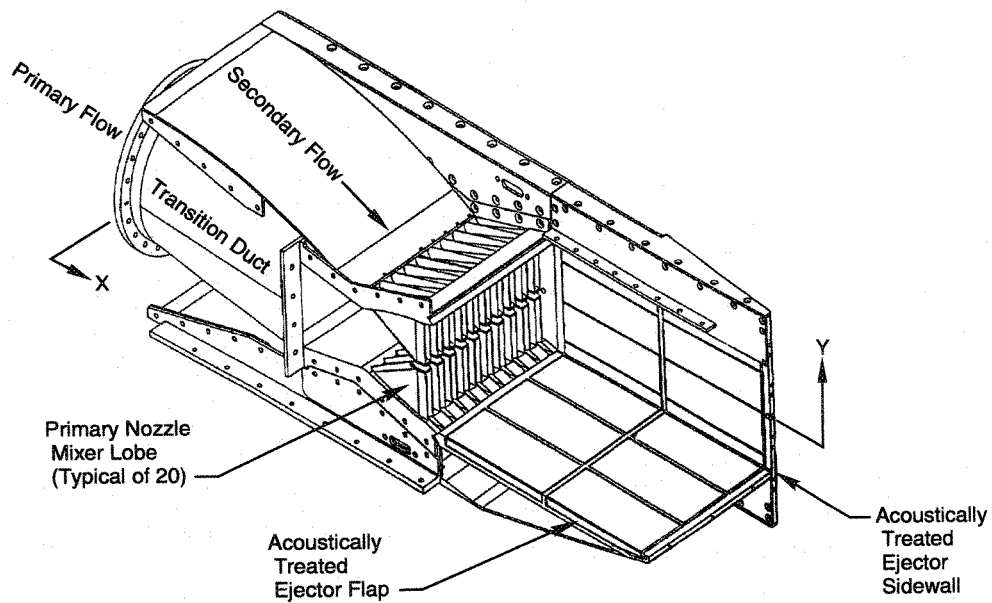


*Figure 109. Schematic of HSCT with Installed Nacelles*



74762.cdr

Figure 110. Schematic of HSCT Heat Test — 13.5 Percent Semispan Model



74761.cdr

Figure 111. Schematic Cutaway of GEAC 2-D Mixer/Ejector Nozzle

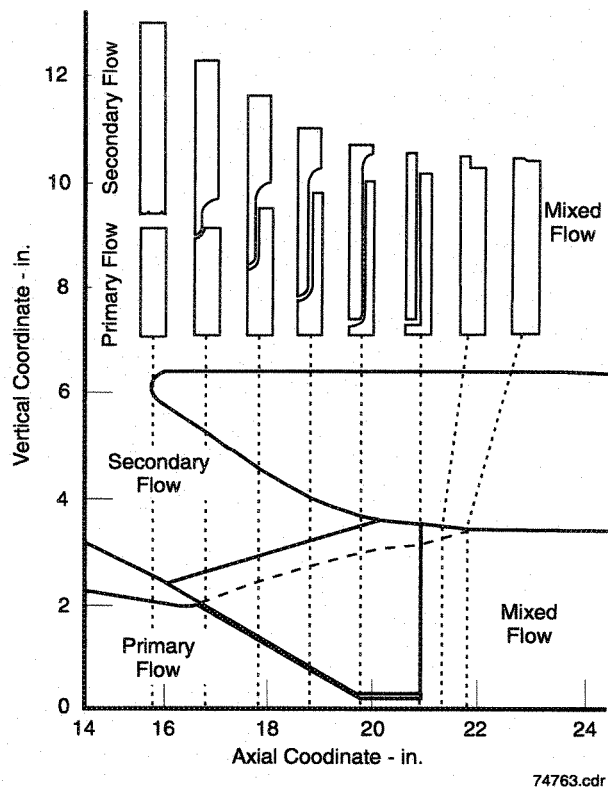


Figure 112. Cross-Sectional Cuts through Mixer Nozzle

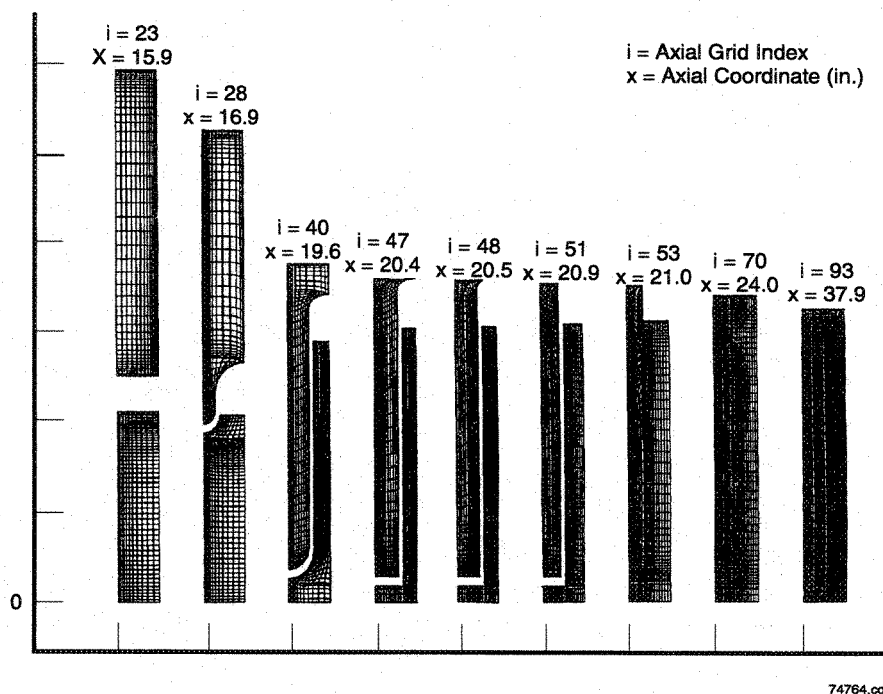


Figure 113. 2-D Cross-Sectional Grids

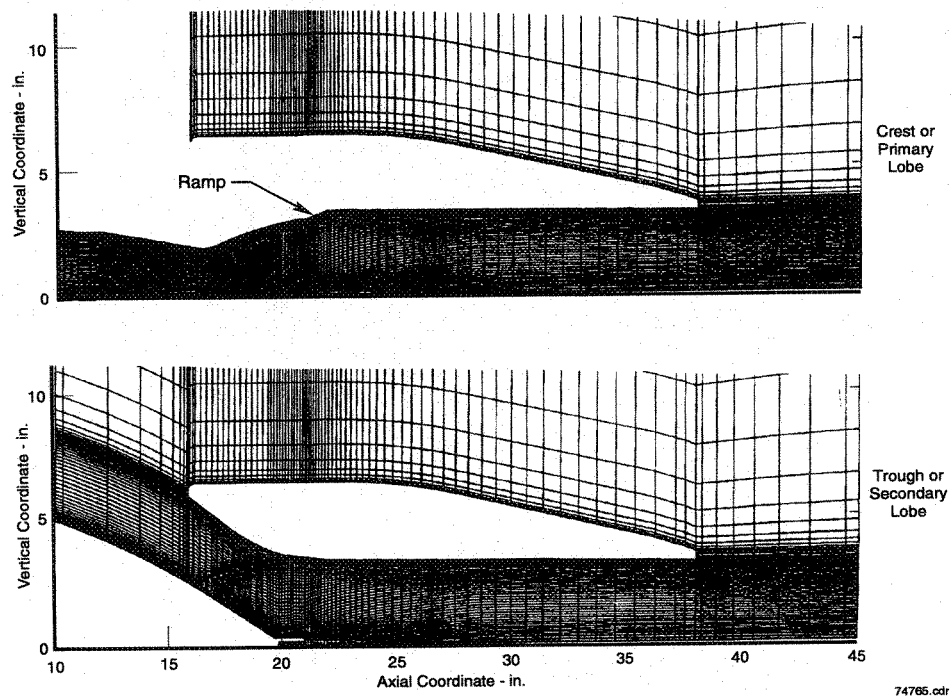


Figure 114. Crest and Trough Plane Axial Grids

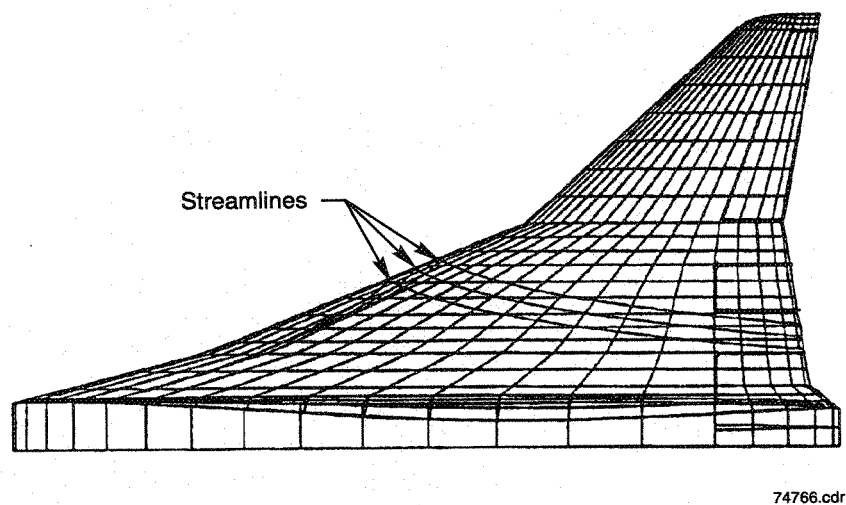
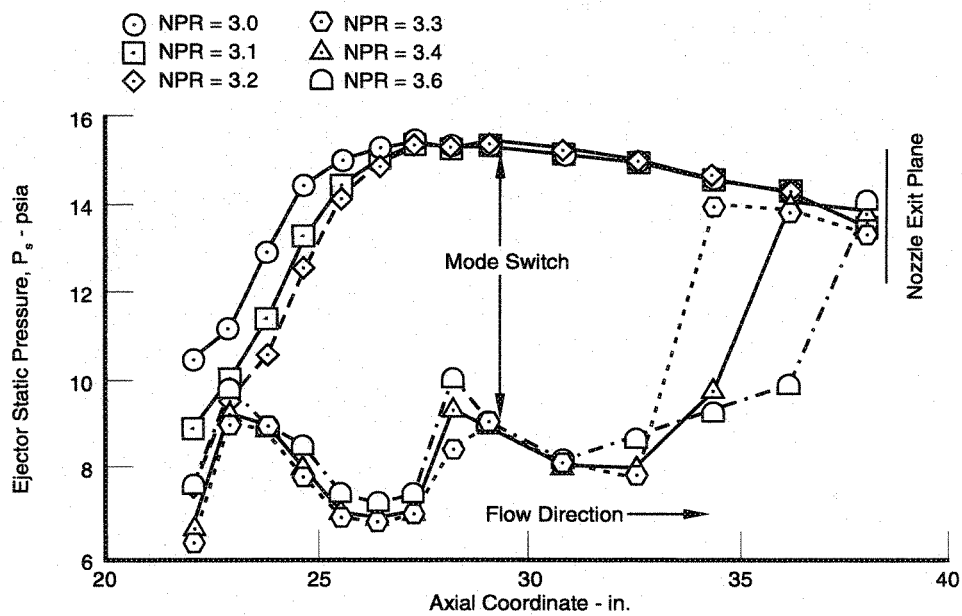
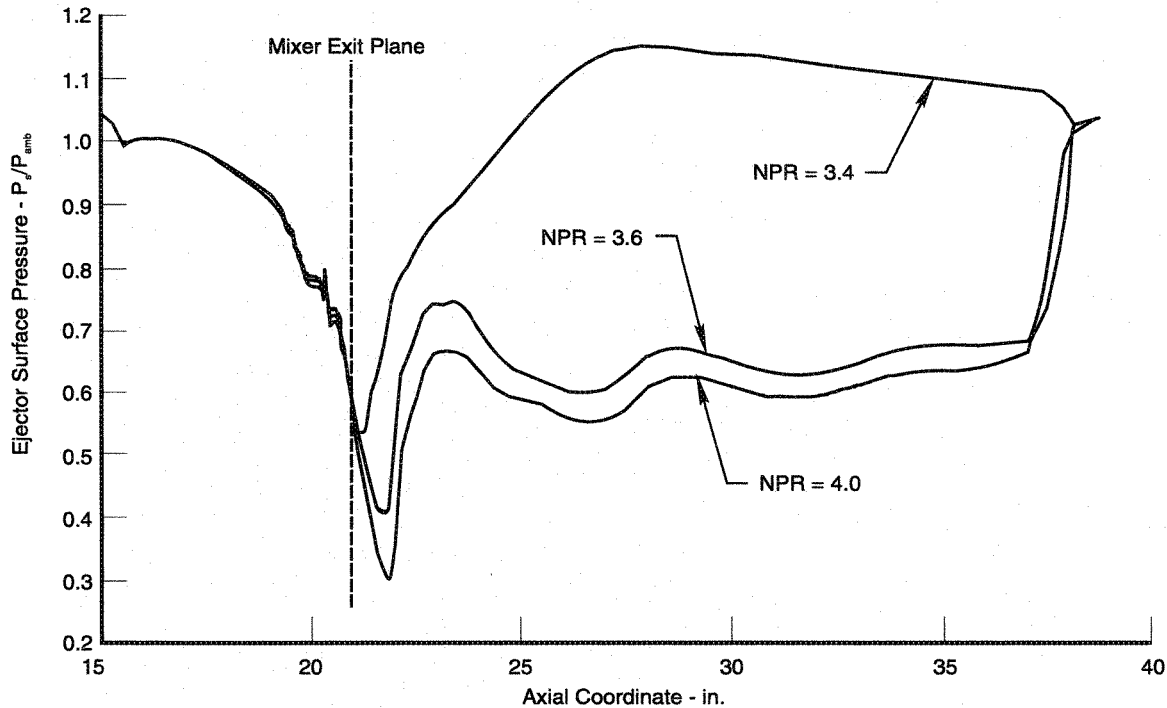


Figure 115. Upper Surface Streamlines on Boeing Reference H Wing



74767.cdr

Figure 116. Ejector Mode Switch as seen in Isolated HAM Ejector Wall Pressures ( $M_\infty = 0.32$ , Simulated LIM Engine Cycle, AMES 40 by 80 Tunnel)



75342.cdr

Figure 117. NASTAR Calculated Mode Switch (As Seen in Ejector Surface Static Pressures) (Isolated Nacelle  $M_\infty = 0.32$ )



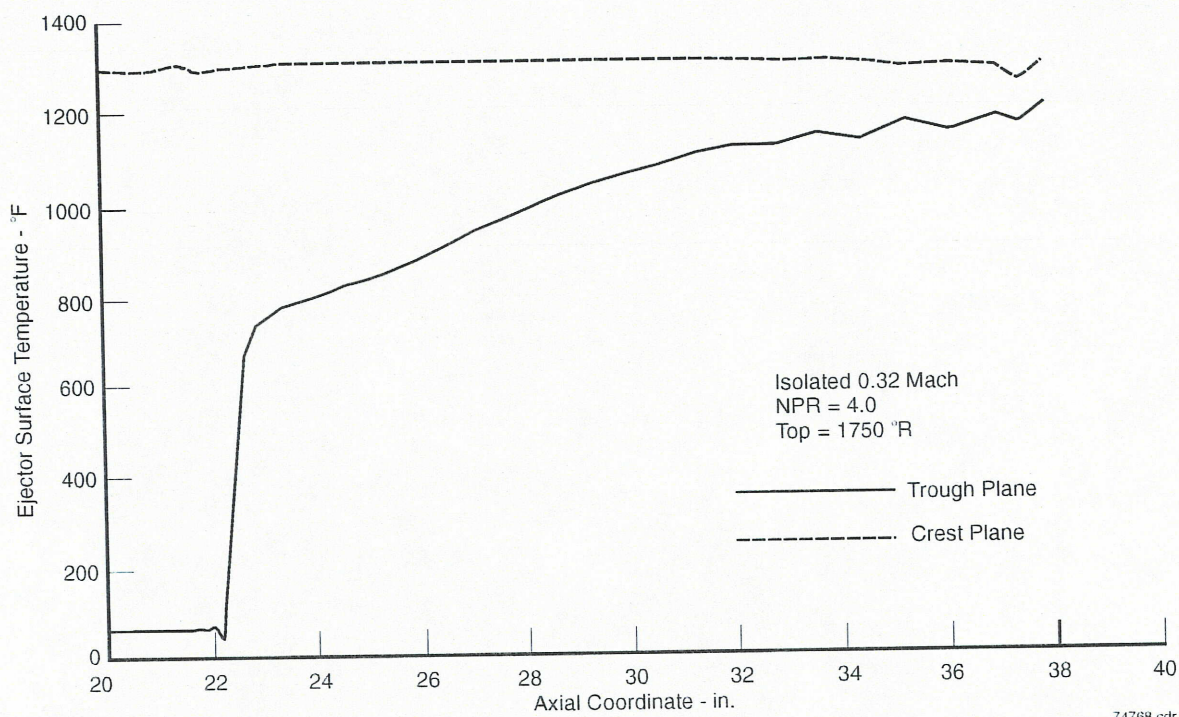


Figure 118. NASTAR Ejector Flap Temperatures

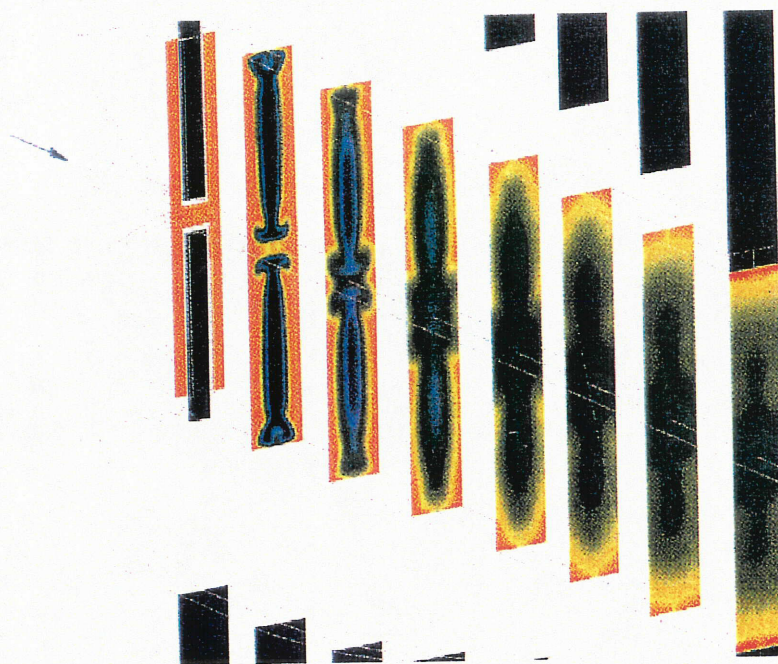


Figure 119. Total Temperature Evolution in Ejector Duct  
(NPR = 4.0, LIM Cycle,  $M_\infty = 0.32$ )



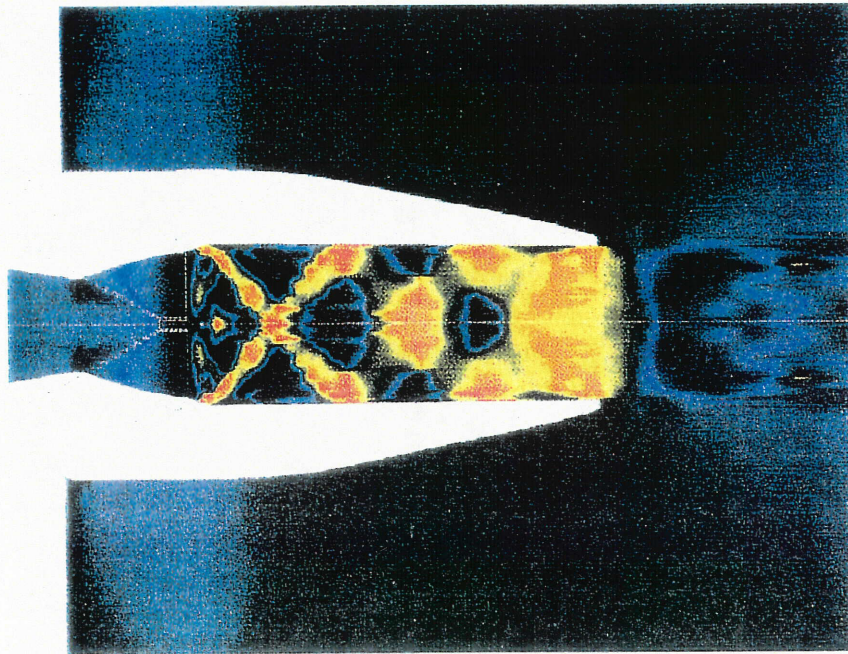


Figure 120. Shock Parameter Contours in Primary Plane  
(NPR = 4.0, LIM Cycle,  $M_\infty = 0.32$ )

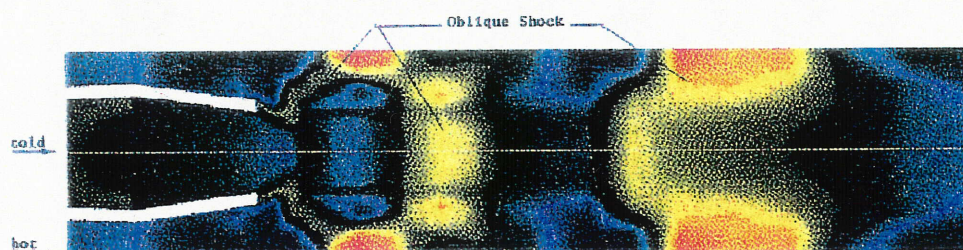


Figure 121. Shock Parameter Illustrates Overexpanded Chute Flow  
(NPR = 4.0, LIM Cycle,  $M_\infty = 0.32$ )



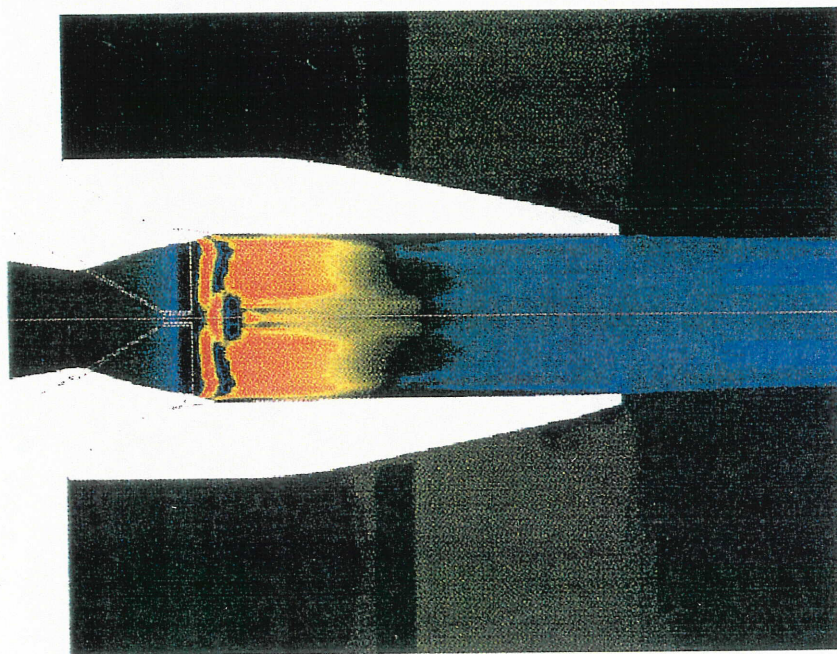


Figure 122. Shock Parameter Contours in Primary Flow Plane  
( $NPR = 3.4$ ,  $T_{op} = 1750^{\circ}R$ ,  $M_{\infty} = 0.32$ )

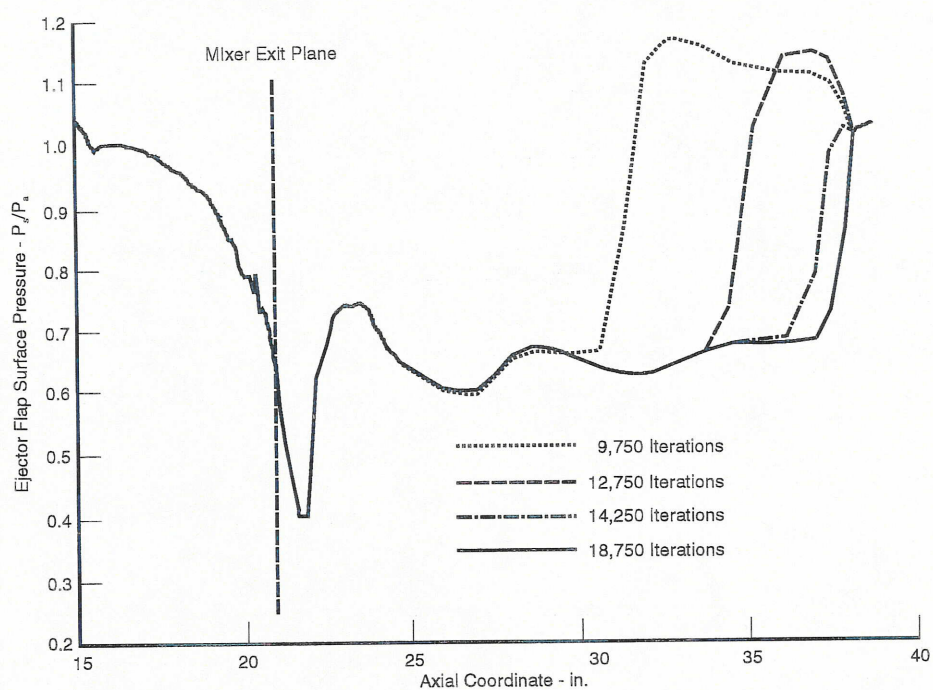
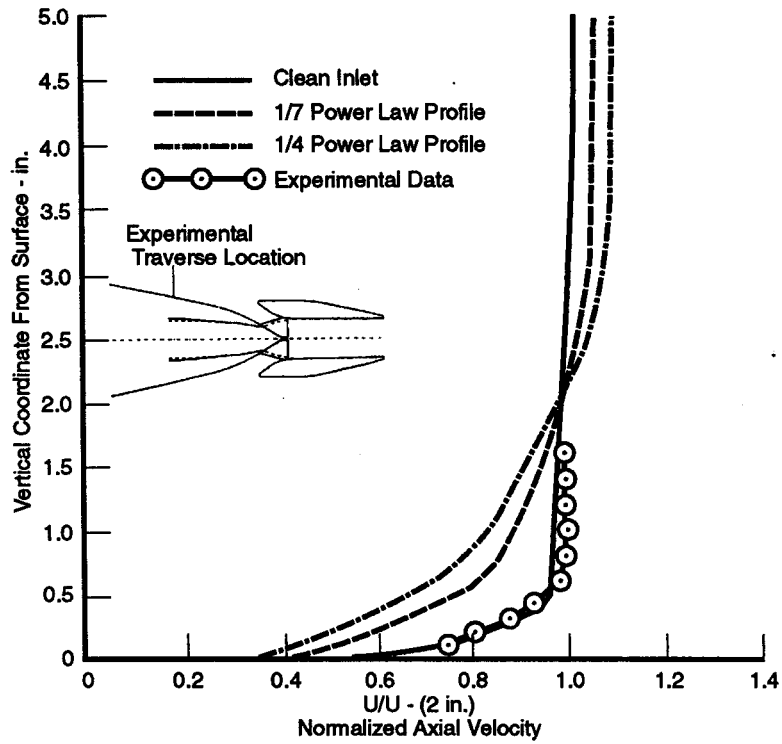
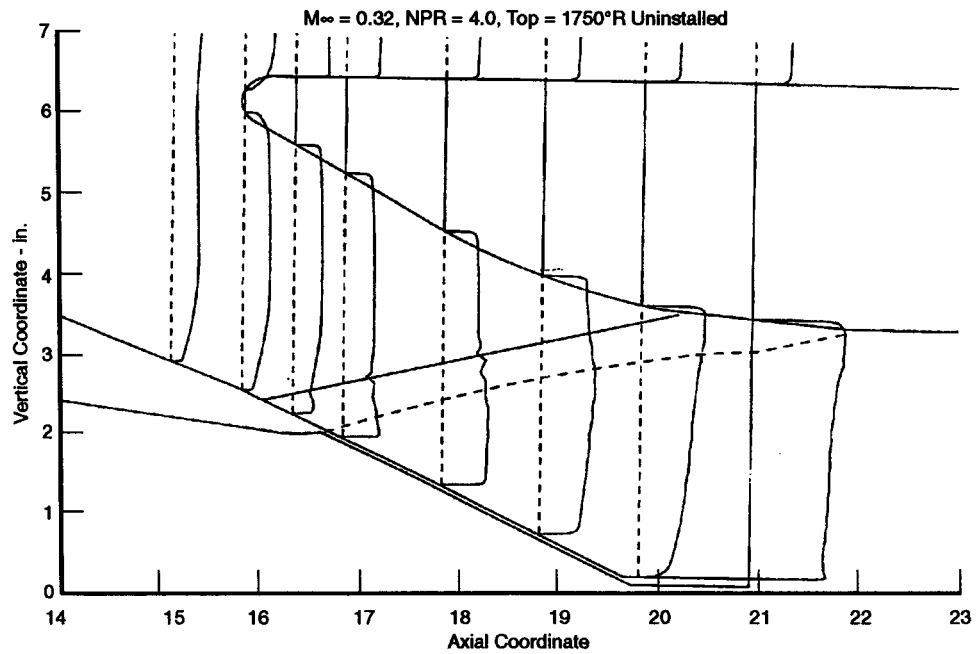


Figure 123. Calculated Ejector Wall Static Pressure Convergence History  
( $NPR = 4.0$ ,  $0.32$  Mach)



74770.odr

Figure 124. Boundary Layer Profile Comparisons  
( $NPR = 4.0$ ,  $M_\infty = 0.32$ )



75343.odr

Figure 125. Profile Development into Ejector Inlet for Uninstalled Case

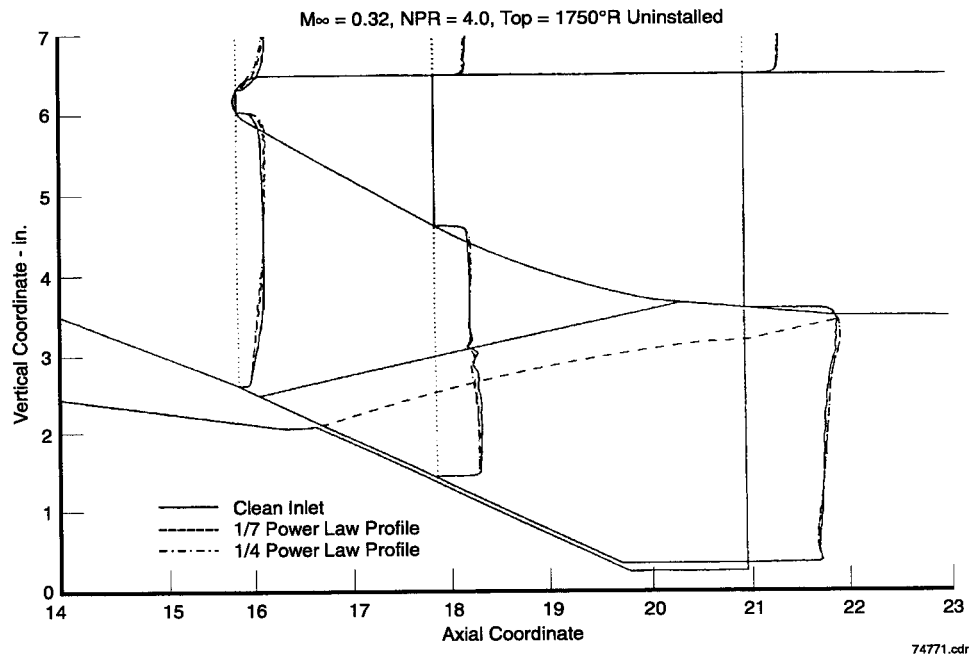


Figure 126. Effect of Inlet Boundary Layer Profile on Flow into Ejector

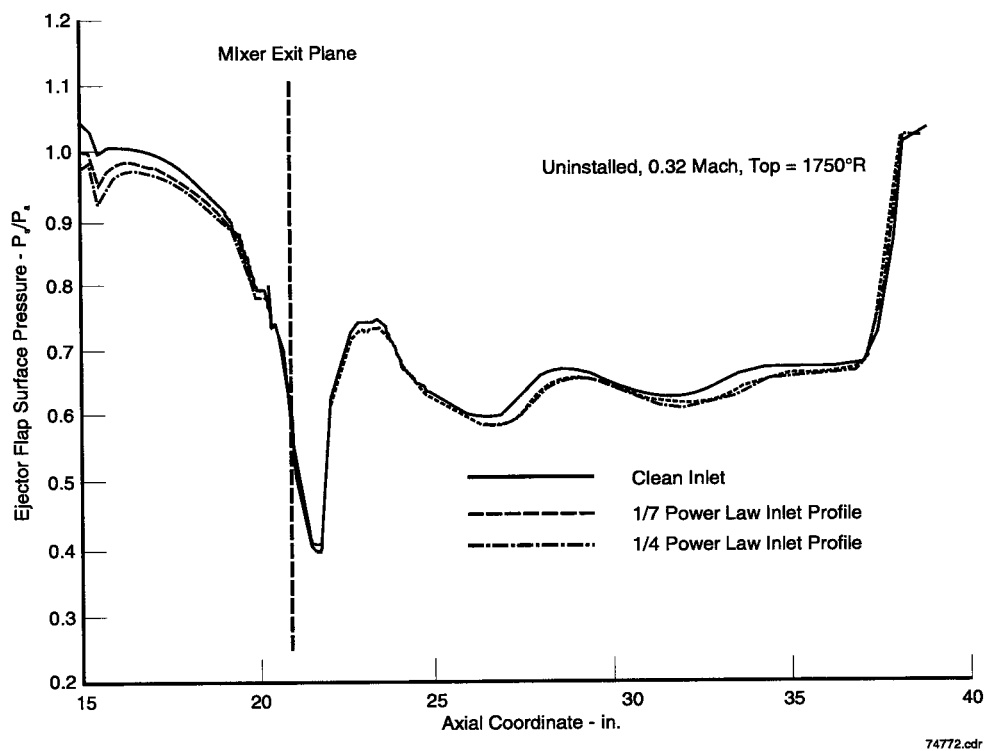


Figure 127. Computed Effect of Inlet Boundary Layer Profile on Ejector Wall Static Pressure Loading ( $NPR = 4.0$ )

## APPENDIX 5-A LIST OF SYMBOLS

A	Area, in. <sup>2</sup>
I	Axial Coordinate Grid Index
M	Mach Number
m	Mass Flow Rate, lbm/sec
MAR	Mixing Duct Area Ratio, $A_e/A_m$
NPR	Nozzle Pressure Ratio
P	Pressure, psia
SAR	Suppressor Area Ratio, $A_m/A_p$
T	Temperature, °R
U	Velocity, ft/sec
X	Axial Coordinate from transition duct inlet flange, in.
Y	Vertical Coordinate from nozzle centerline, in.
$Y_s$	Vertical distance from inlet ramp surface, in.
$\eta$	Thermal Mixedness, $\eta = 100 (1 - [\rho U d A (T_{loc} - T_m) / \rho U d A (T_{in} - T_m)])$
$\omega$	Aspiration Ratio, $M_s/m_p$
$\rho$	Density, lbm/ft <sup>3</sup>
$\nabla p$	Local pressure gradient
$ \nabla p $	Absolute pressure gradient
<b>Subscripts</b>	
a, amb	Ambient conditions
e	Nozzle exit
in	Mixing duct inlet area
loc	Local
m	Mixing plane
o	Stagnation conditions
op	Stagnation conditions in the primary
p	Primary flow
s	Secondary flow
$\infty$	Freestream condition
*	Primary effective throat

## REFERENCES

1. Ives, D.C. and Zacharias, R.M., *Conformal Mapping and Orthogonal Grid Generation*, AIAA 87-2057, AIAA/SAE/ASME/ASEE 23rd Joint Propulsion Conference, San Diego, CA, June 1987.
2. Dannenhoffer, J.F., III, *Computer-Aided Block-Structuring Through the Use of Optimization and Expert System Techniques*, AIAA 91-1585, AIAA 10th Computational Fluid Dynamics Conference, Honolulu, Hawaii, June 1991.
3. Dannenhoffer, J.F., III, *A Block-Structuring Technique for General Geometries*, AIAA 91-0145, AIAA 29th Aerospace Sciences Meeting, Reno, NV, January 1991.
4. Barber, T.J., LaBarre, R.E., and Chiapetta, L.M., *Analysis of Second Generation High Speed Civil Transport Mixer-Ejector Exhaust System*, UTRC 92-6, April 1992.
5. Barber, T.J., Chiapetta, L.C. & LaBarre, R.E., *Computational Studies of P&W Mixer-Ejector Exhaust Nozzle Concepts With Comparisons to GEAE Cell 41 Experimental Data*, UTRC 94-xx, May 31, 1994.
6. Smith, B.E., *PMARC Predictions of Ref H Wing Flowfield*, NASA Ames RC memorandum dated August 24, 1993.
7. Rhie, C.M. & Chow, W.L., *Numerical Study of the Turbulent Flow Past an Airfoil With Trailing Edge Separation*, AIAA J., Vol. 21, No. 11, November 1983, pp. 1525-1532.
8. Patankar, S.V., Numerical Heat Transfer and Fluid Flow, (New York), Hemisphere Publishing, 1980.
9. Jones, W.P. and Launder, B.E., *The Prediction of Laminarization With a Two-Equation Model of Turbulence*, Int. J. Heat and Mass Transfer, Vol. 15, 1972, pp. 301.

## 6. HEAT TRANSFER STUDIES

### 6.1 DESIGN ASSUMPTIONS

This study was undertaken to guide nozzle material selection for a product-size mixer/ejector nozzle. Techniques used for this study include methods for calculating gaspath and coolant thermal boundary conditions. These boundary conditions are for gaspath, fan air cooling (if applicable), nacelle purge, and ambient. Gaspath convective coefficients were obtained assuming a standard flat-plate correlation. Gaspath temperatures for film cooled surfaces were obtained from Pratt & Whitney (P&W) proprietary correlations. Fan air and nacelle purge convective coefficients were obtained assuming a fully developed turbulent flow through a duct. Ambient convective coefficients and temperatures were obtained from correlations for high-speed external flow. The effects of fan air cooling and thermal protection systems on nozzle component temperatures were evaluated in order to match to appropriate materials.

The engine cycle used in the study was a nonaugmented turbofan engine with a bypass ratio of 0.18. The flight point used is the most thermally severe point: Mach = 2.1 at 50,000 ft altitude for full-power transonic accel, where the core gas temperature reaches 1880°F.

Figure 128 and Figure 129 show nozzle locations selected for thermal analysis. These include: transition section, convergent flap, forward divergent flap/mixer, and ejector sidewall near the primary nozzle throat. For each of these nozzle components, temperatures through a cross-section at the worst location were generated. Aft divergent flap temperatures are addressed in 1 and were not examined in this analysis.

Figure 130 shows fan air and nacelle purge distribution assumed for this study. The fan air cooling design for the nozzle is channel convection discharging to film slots. Three film slot locations are indicated in the figure: transition section leading edge (Slot 1), transition section trailing edge (Slot 2), and convergent flap trailing edge (Slot 3). Fan air flow rates of 0.0, 0.5, and 1.0 percent of total engine flow (WAT) were allotted to each film slot. A nacelle purge flow of 3 percent WAT was assumed to be distributed uniformly around the transition section leading-edge perimeter, mixing with 0.5 percent WAT core gas leakage.

Two thermal protection systems (TPS) were used for this study: a 0.02-in. thick magnesium zirconate thermal barrier coating (TBC), and a 0.10-in. thick Nextel 440 fiber insulation. The TPS was applied to the gaspath surface of the hot sheet of all components. Cases where the hot sheet was left unprotected were also examined.

The primary nozzle cross-section model used for the transition section, convergent flap, and ejector sidewall at the primary nozzle throat is shown in Figure 131. A double-wall construction was assumed where the hot sheet may be a detachable liner. A TPS was placed between gaspath and hot sheet for the applicable cases. Fan air convective cooling between hot and cold sheets was assumed for the transition section and convergent flap for the applicable cases. The sidewall by the throat was not convectively cooled. Reverser port walls, guide vanes, and other structures buried in the nozzle cavity were accounted for in the analysis but are not shown in the figure.

The cross-sectional model used for the forward divergent flap/mixer is shown in Figure 132. A single-wall construction using thick sheets was assumed. A TPS was placed between gaspath and hotwall for the applicable cases. This component was not convectively cooled.

These heat transfer studies showed that a combination of insulation and convective cooling was more effective than film cooling for nonafterburning, low-noise nozzles.

### 6.2 ANALYTIC RESULTS

Transition section temperatures using no TPS are shown in Figure 133. These show strong dependence on convective cooling (Slot 2 flow), and moderate dependence on film cooling (Slot 1 flow). The hot sheet runs between 1200 to 1640°F. Hot-to-cold sheet temperature differential averaged 315°F for nonconvectively cooled cases, and 385°F for convectively cooled cases.

Transition section temperatures using a 0.02-in. coating are shown in Figure 134. These show the same dependence on convective and film cooling as the uncoated cases. The hot sheet runs between 1160 to 1580°F; a relatively small decrease from the uncoated cases. Hot-to-cold sheet gradient averages 300°F for nonconvectively cooled cases, and 360°F for convectively cooled cases.

Transition section temperatures using 0.10-in. insulation are shown in Figure 135. These show the same strong dependence on convective cooling, but a reduced dependence on film cooling as with the uninsulated cases. The hot sheet runs between 810 to 1290°F; a substantial decrease from the uninsulated cases. Hot-to-cold sheet gradient averages 265°F for nonconvectively cooled cases, and 195°F for convectively cooled cases.

Convergent flap temperatures using no TPS are shown in Figure 136. These show strong dependence on convective cooling (Slot 3 flow), and little dependence on film cooling (Slot 2 flow). The hot sheet runs between 1285 to 1745°F, the highest of all components. The gradient between hot and cold sheets averages 130°F for nonconvectively cooled cases, and 395°F for convectively cooled cases.

Convergent flap temperatures using the 0.02-in. coating are shown in Figure 137. These show the same dependence on convective and film cooling as for the uncoated cases. The hot sheet runs between 1215 to 1725°F; a relatively small decrease for convectively cooled cases, and almost no decrease for nonconvectively cooled cases compared to an uncoated flap. Hot-to-cold sheet gradient averages 125°F for nonconvectively cooled cases, and 365°F for convectively cooled cases.

Convergent flap temperatures using 0.10-in. insulation are shown in Figure 138. These show the same dependence on convective and film cooling as the uninsulated cases. The hot sheet runs between 800 to 1535°F; a large reduction for convectively cooled cases, and a smaller decrease for nonconvectively cooled cases as compared to an uninsulated flap. Hot and cold sheet gradient averages 115°F for nonconvectively cooled cases, and 150°F for convectively cooled cases.

Forward divergent flap liner temperatures for all three TPS cases are shown in Figure 139. These show moderate dependence on convective cooling from the convergent flap (Slot 3 flow), and little dependence on film cooling from the transition section (Slot 2 flow). Coated and bare liners show almost no difference in temperature, while liners using insulation show a moderate reduction in temperature; running between 1400 to 1685°F for bare and TBC cases, and 1170 to 1335°F for insulated cases.

Stowable mixer temperatures using no TPS are shown in Figure 140. These show moderate dependence on convective cooling from the convergent flap (Slot 3 flow), and little dependence on film cooling from the transition section (Slot 2 flow). The hot-side runs between 1375 to 1655°F, and the hot-to-cold side gradient averages 480°F.

Stowable mixer temperatures using the 0.02-in. coating are shown in Figure 141. These show the same dependence on film cooling as the uncoated cases. The hot-side runs between 1330 to 1600°F; a small decrease from the uncoated cases. The gradient between hot and cold sides averages 460°F.

Stowable mixer temperatures using 0.10-in. insulation are shown in Figure 142. These show the same type of dependence on film cooling as the uninsulated cases. The hot-side runs between 1015 to 1180°F; a substantial decrease from the uninsulated cases. The gradient between hot and cold sides averages 230°F.

Ejector sidewall temperatures using no TPS are shown in Figure 143. These show little dependence on either film cooling from the transition section leading edge (Slot 1 flow), or from the transition section trailing edge (Slot 2 flow). The hot-side runs between 1475 to 1640°F, and the hot-to-cold sheet gradient averages 360°F.

Sidewall temperatures using the 0.02-in. coating are shown in Figure 144. These show little dependence on either film cooling from the transition section leading edge (Slot 1 flow), or from the transition section trailing edge (Slot 2 flow). The hot-side runs between 1455 to 1615°F; a very small decrease from the uncoated cases. The gradient between hot and cold sheets averages 355°F.

Sidewall temperatures using 0.10-in. insulation are shown in Figure 145. These show almost no dependence on film cooling from the transition section leading edge (Slot 1 flow), and little dependence on film cooling from the transition section trailing edge (Slot 2 flow). The hot-side runs between 1175 to 1280°F; a moderate decrease from the uninsulated cases. The gradient between hot and cold sheets averages 295°F.

### 6.3 CONCLUSIONS AND RECOMMENDATIONS

Two tables summarizing temperature ranges and gradients for all components are given below. Nozzle components are broken down between:

- Those using 0.10-in. insulation
- Those using a 0.02-in. thermal barrier coating or left bare
- Those convectively cooled (transition section, convergent flap), or film cooled from the leading edge (forward divergent flap/mixer, sidewall)
- Those not directly cooled by convection or film.

#### *Hot Sheet Temperature Ranges*

<i>Nozzle Component</i>	<i>0.10-in. Insulation — Convection/LE Film (°F)</i>	<i>Bare or TBC — Convection/LE Film (°F)</i>	<i>0.10-in. Insulation — Uncooled (°F)</i>	<i>Bare or TBC — Uncooled (°F)</i>
Transition Section	810-1010	1160-1415	1210-1285	1490-1645
Convergent Flap	800-940	1215-1440	1470-1535	1670-1745
Forward Div Flap	1170-1215	1400-1500	1285-1335	1580-1685
Stowable Mixer	1015-1060	1330-1450	1135-1180	1540-1655
Sidewall at Throat	1175-1230	1455-1585	1210-1280	1525-1640

#### *Hot-to-Cold Sheet Temperature Ranges*

<i>Nozzle Component</i>	<i>0.10-in. Insulation — Convection/LE Film (°F)</i>	<i>Bare or TBC — Convection/LE Film (°F)</i>	<i>0.10-in. Insulation — Uncooled (°F)</i>	<i>Bare or TBC — Uncooled (°F)</i>
Transition Section	150-240	350-400	255-270	290-320
Convergent Flap	120-180	350-415	110-115	125-130
Stowable Mixer	200-215	405-455	255-265	500-535
Sidewall at Throat	285-300	340-365	295-305	355-370

All components show significantly reduced temperatures when insulated from the gaspath using 0.10-in. Nextel fiber insulation. Thermal barrier coating provides a small temperature reduction for convectively cooled components, and almost no impact on nonconvectively cooled components.

The convective cooling of nozzle components is more effective in reducing temperatures than slot film cooling. Film discharged at the leading edge of any component only had a moderate impact on temperature reduction.



Film discharged from the transition section leading edge had a negligible impact on components downstream of the transition section.

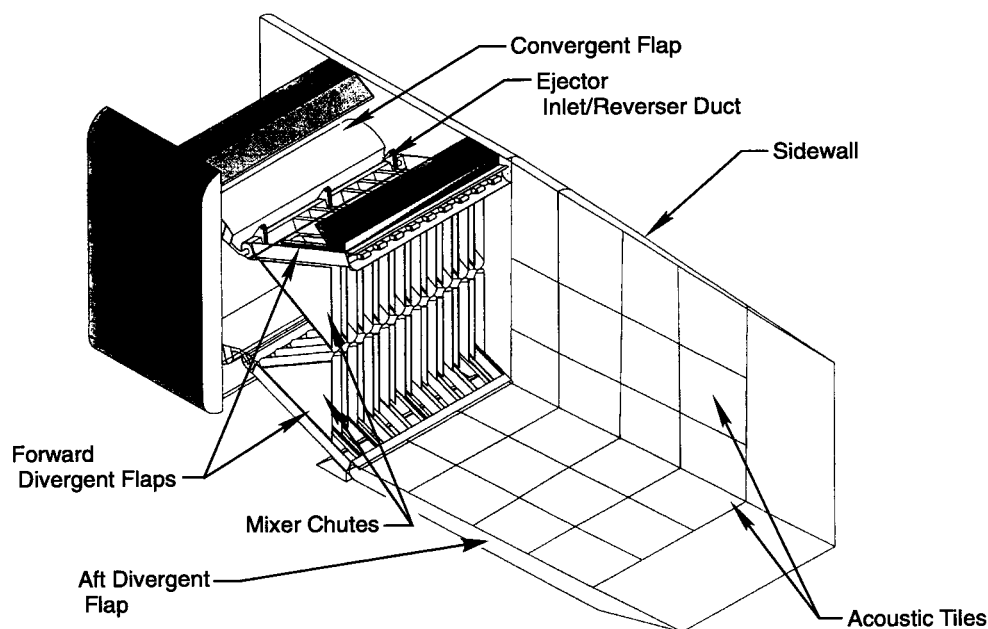
The most effective way to obtain hot-sheet temperatures below 1000°F for any component is a minimum of 0.5 percent total engine flow convective cooling combined with 0.10-in. Nextel fiber insulation. Components using either convective cooling or insulation run between 1000 to 1500°F.

Components using neither convective cooling nor insulation will exceed 1500°F. Components with the most severe thermal gradients are those using convective cooling without insulation (transition section and convergent flap), or those using no convective cooling or insulation (mixer and sidewall).

This study was undertaken to guide nozzle material selection where the effects of fan air cooling and thermal protection systems on material temperature could be evaluated. A comprehensive thermal analysis of a mixer/ejector nozzle was initiated. Nozzle component temperatures for a range of design conditions were generated in order to match to appropriate materials.

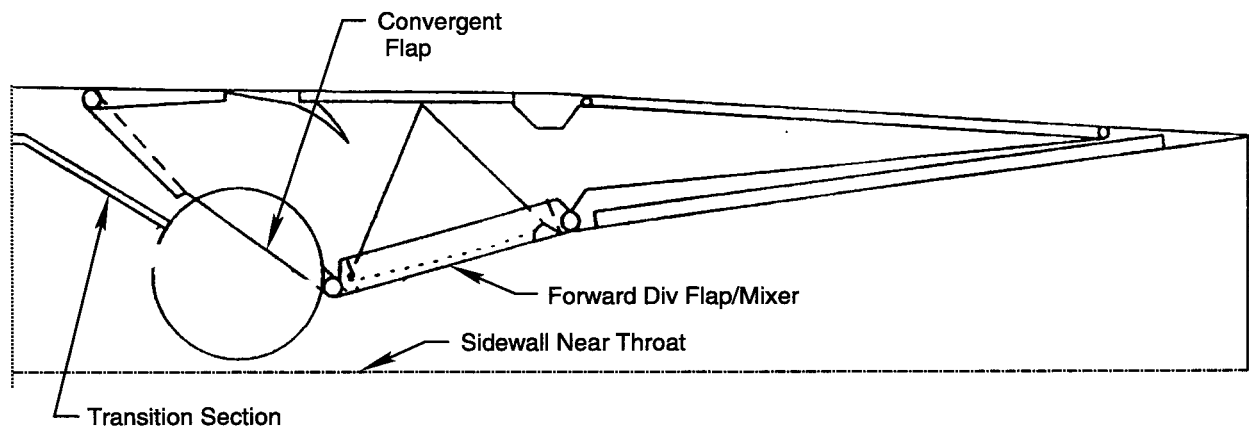
Some key findings of this study are:

- Components show significantly reduced temperatures when insulated from the gaspath (about 20 to 40 percent using 0.10-in. Nextel fiber insulation).
- Convectively cooling nozzle components reduce temperatures more effectively than slot film cooling.
- The most effective way to obtain hot-sheet temperatures below 1000°F for any component is a minimum of 0.5 percent WAT convective cooling combined with 0.10-in. Nextel fiber insulation.
- Components with the most severe thermal gradients are those using convective cooling without insulation (transition section and convergent flap), or those using no convective cooling or insulation (mixer and sidewall).



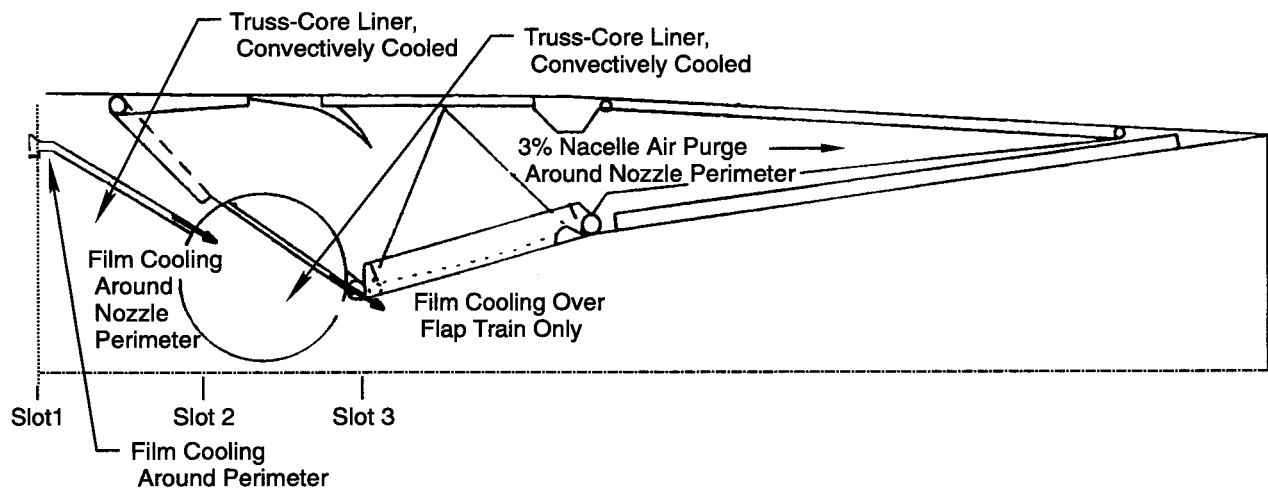
74773.cdr

*Figure 128. Isometric View of Typical Mixer/Ejector Nozzle in Takeoff Mode*



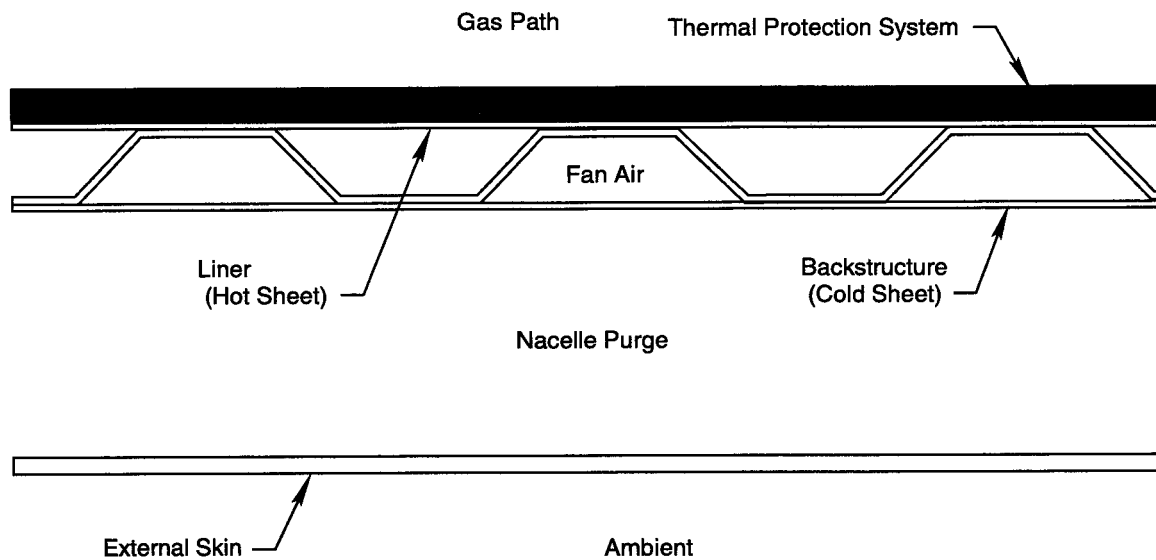
74774.cdr

*Figure 129. Ejector P&W HSR II Mixer/Ejector Nozzle Thermal Analysis Locations — Nozzle Shown in Supercruise Mode*



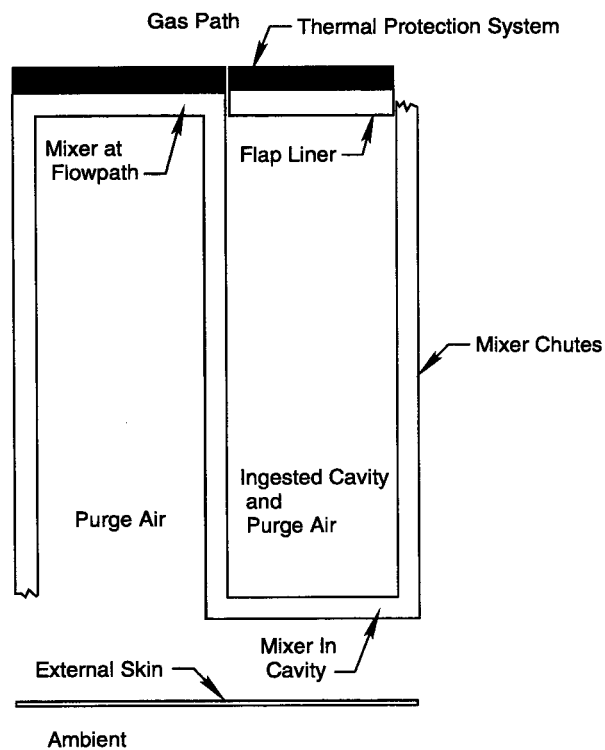
g74775.cdr

*Figure 130. Ejector P&W HSR II Mixer/Ejector Nozzle Thermal Design Features*



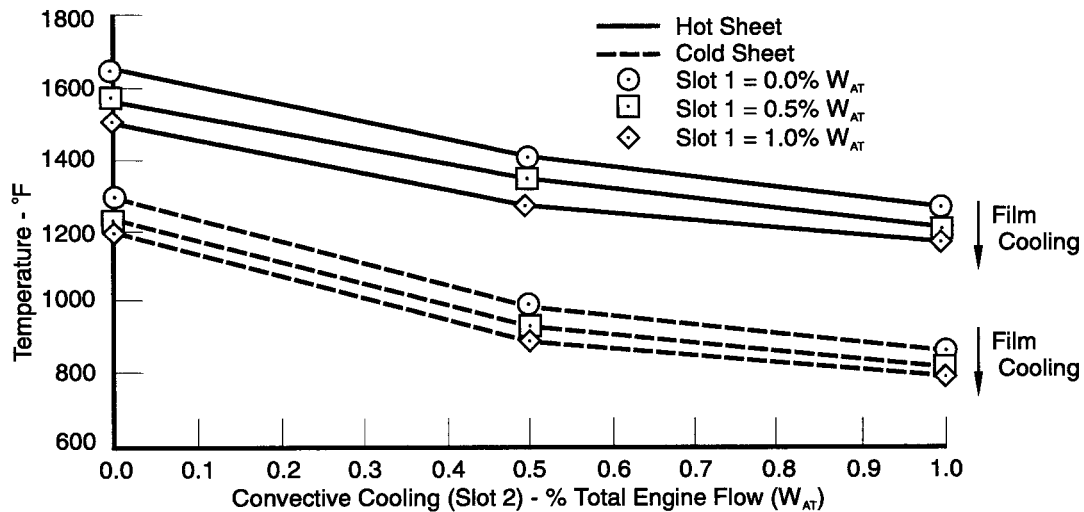
74776.cdr

*Figure 131. Ejector Cross-Section for Transition Section, Convergent Flap and Ejector Sidewall by Primary-Nozzle Throat*



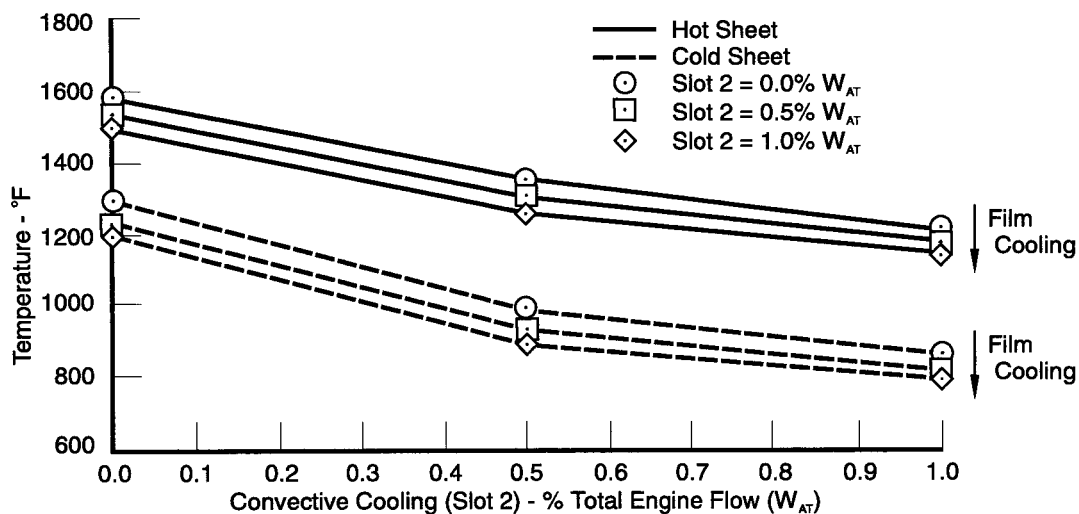
74777.cdr

*Figure 132. Ejector Cross-Section for Forward Divergent Flap/Mixer Chute*



74778.cdr

Figure 133. Ejector Transition Section — Bare Metal



74779.cdr

Figure 134. Ejector Transition Section — 0.02-in. Thick Thermal Barrier Coating

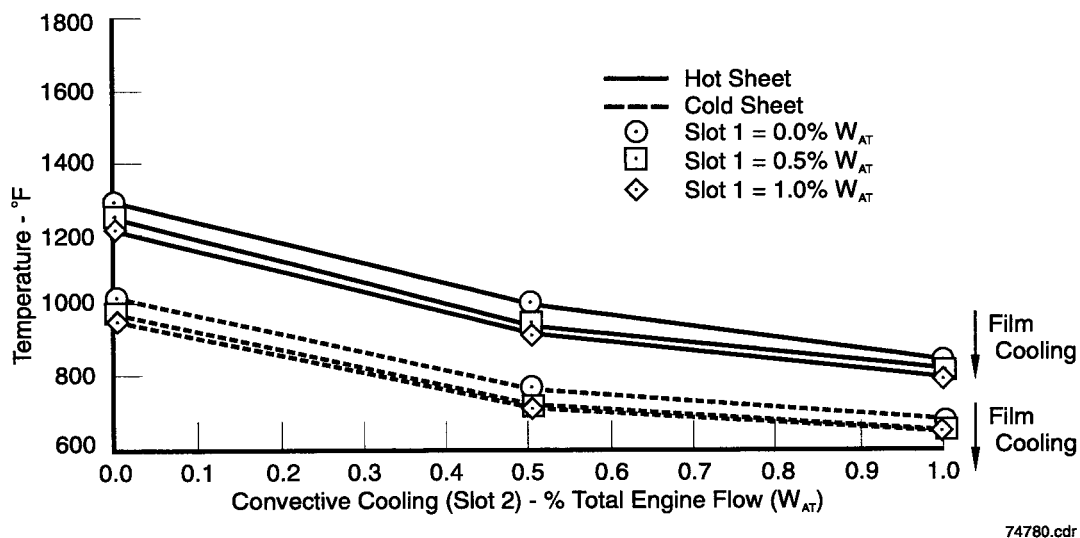


Figure 135. Ejector Transition Section — 0.10-in. Thick Nexel 440 Fiber Insulation

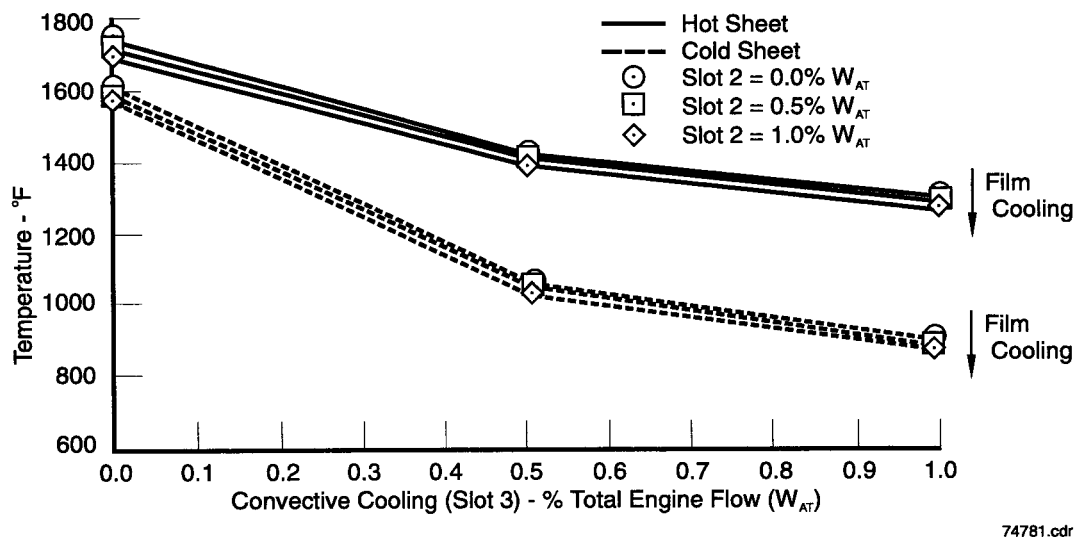
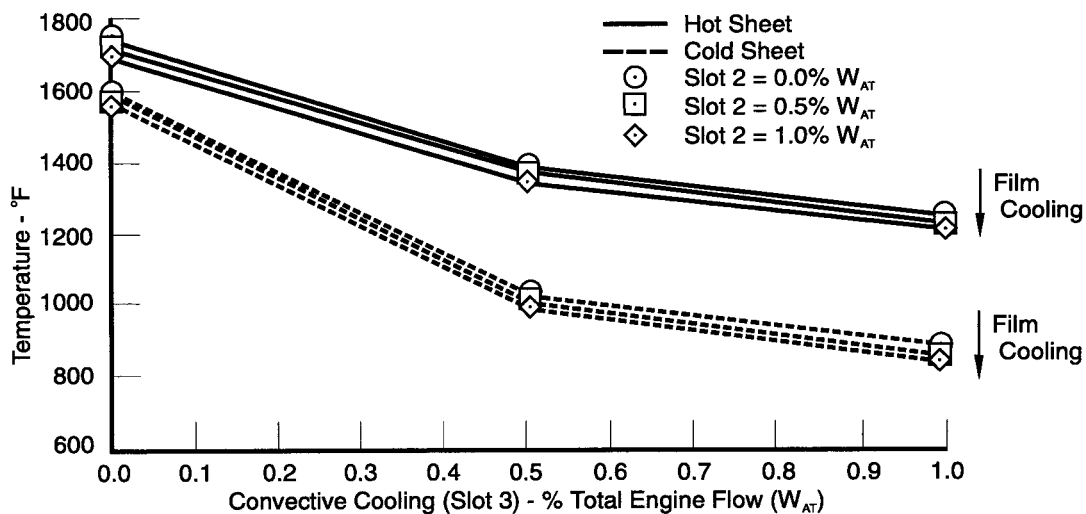
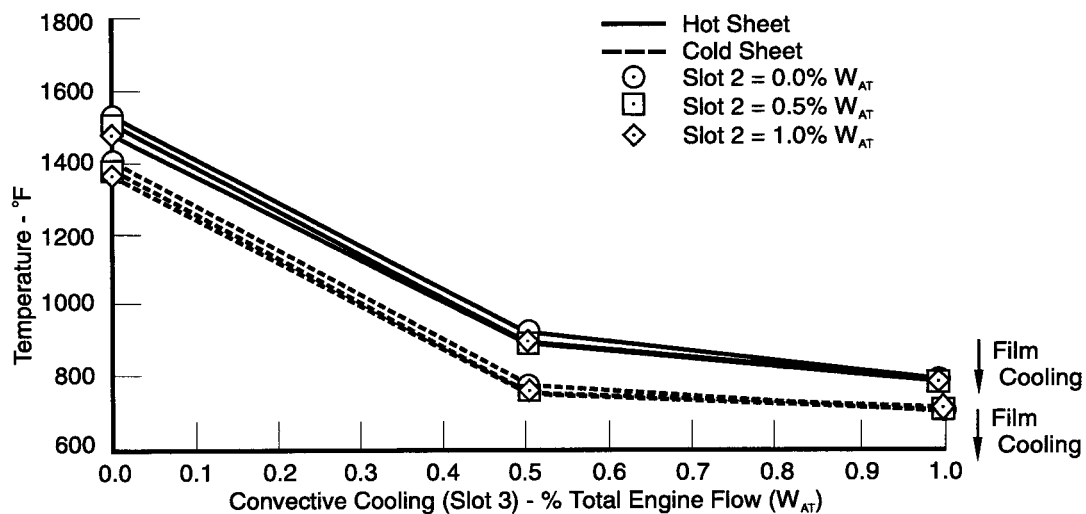


Figure 136. Ejector Convergent Flap — Bare Metal



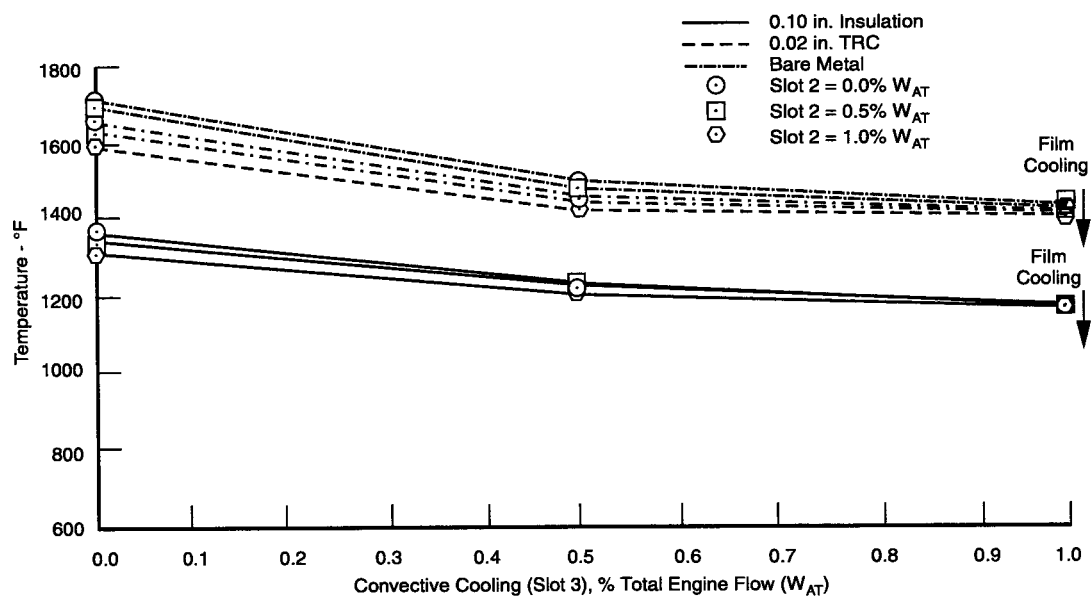
74782.cdr

Figure 137. Ejector Convergent Flap — 0.02-in. Thick Thermal Barrier Coating (TBC)



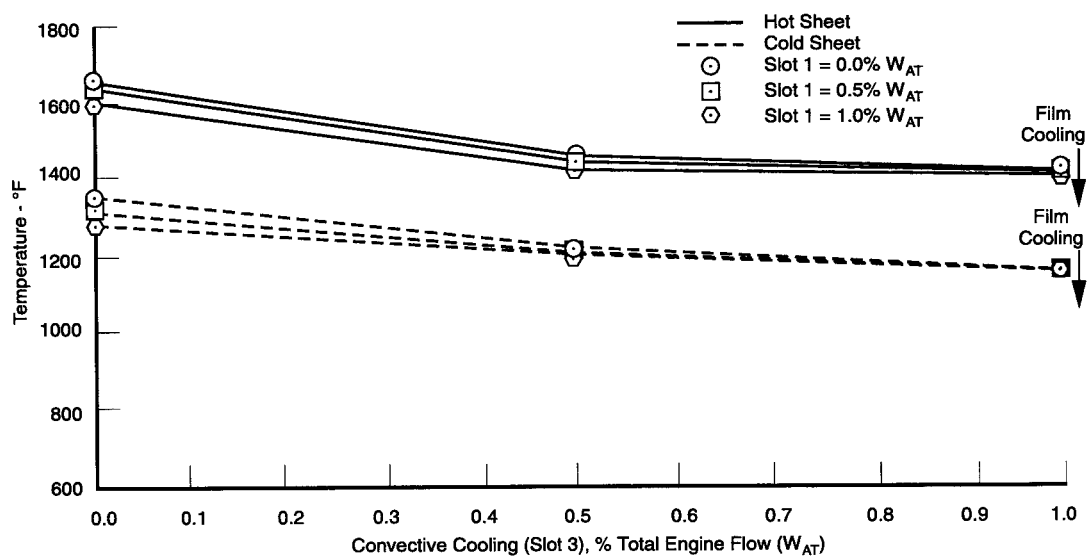
74783.cdr

Figure 138. Ejector Convergent Flap — 0.10-in. Thick Nexel 440 Fiber Insulation



74784.cdr

Figure 139. Ejector Forward Divergent Flap — Metal Liner



74785.cdr

Figure 140. Ejector Stowable Mixer — Bare Metal

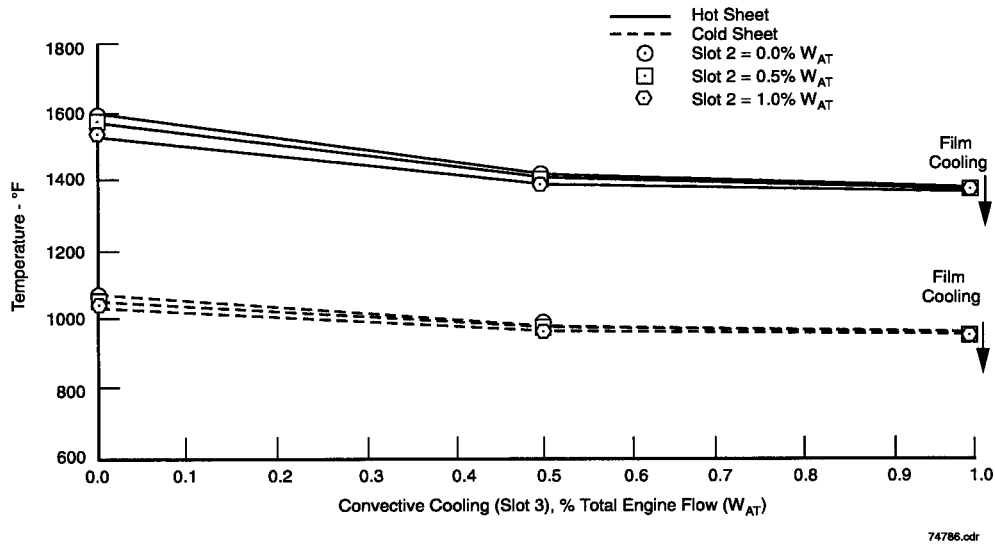


Figure 141. Ejector Stowable Mixer — 0.02-in. Thick Thermal Barrier Coating (TBC)

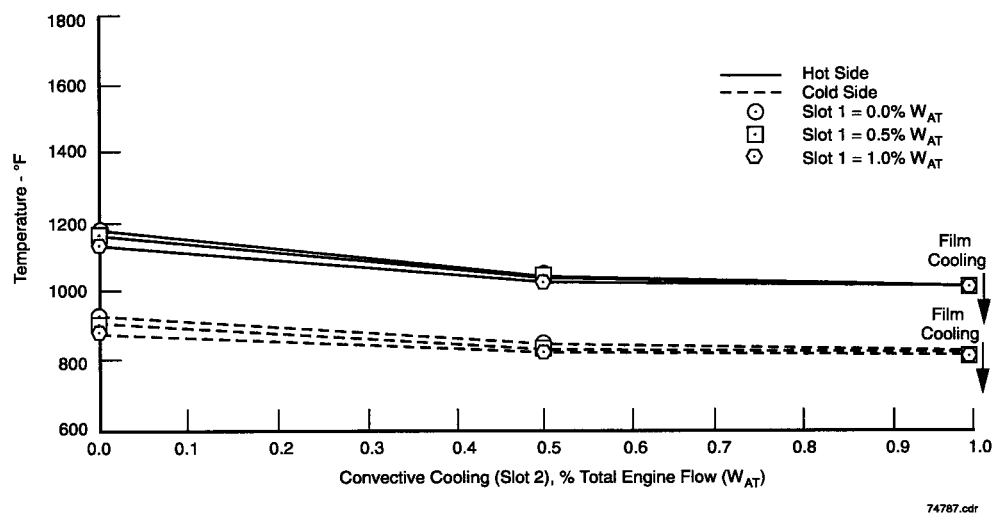


Figure 142. Ejector Stowable Mixer — 0.10-in. Thick Nexel 440 Fiber Insulation



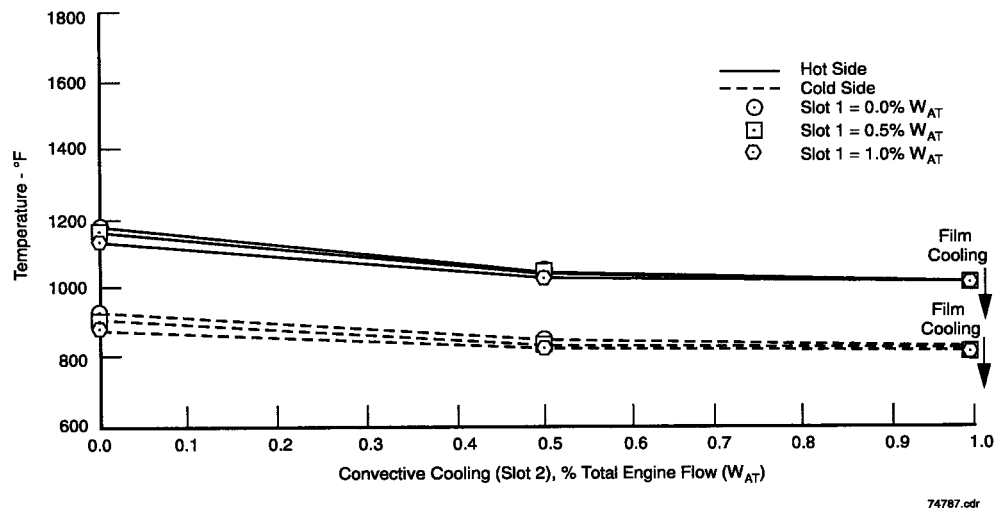


Figure 143. Ejector Sidewall at Primary Nozzle Throat — Bare Metal

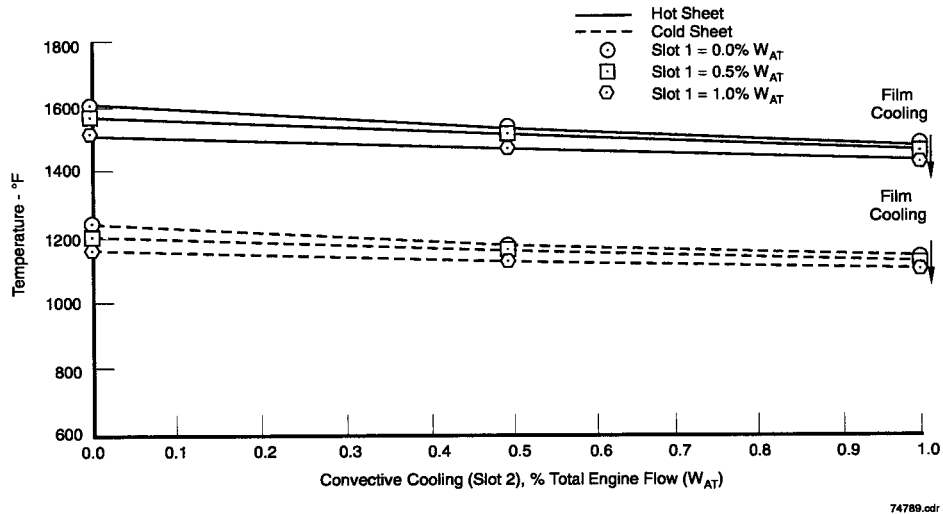


Figure 144. Ejector Sidewall at Primary Nozzle Throat — 0.02-in. Thick Thermal Barrier Coating (TBC)

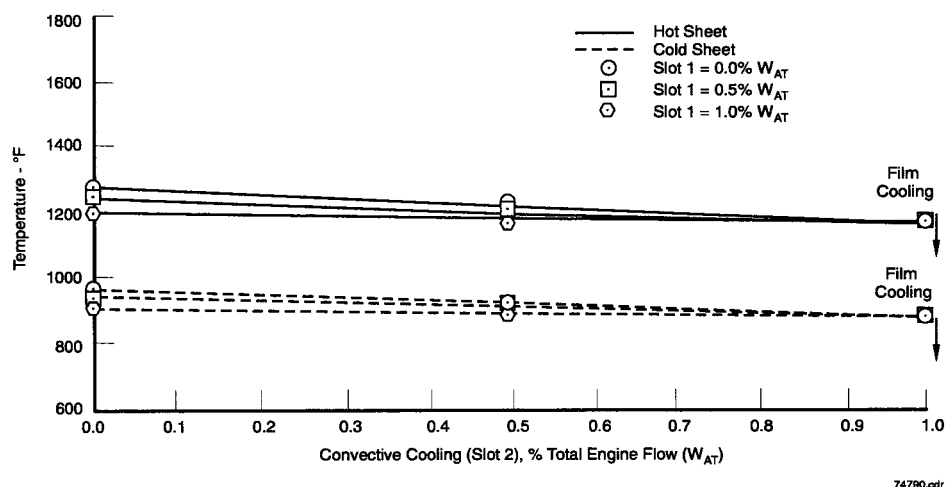


Figure 145. Ejector Sidewall at Primary Nozzle Throat — 0.10-in. Thick Nexel 440 Fiber

## **REFERENCES**

1. Quarterly Report: EPM Quarterly Technical Progress Report 1/94-3/94 Vol. 2 Task B Exhaust Nozzle; 25 April 1994.

## 7. THROAT AUGMENTATION STUDIES

Thrust augmenting ejectors (TAE) are designed for the purpose of obtaining thrust levels significantly above the thrust of the primary jet over a broad range of Mach numbers. Such TAEs make it possible to use ejectors for reducing engine noise, achieving Vertical Short Takeoff and Landing (V/STOL) flight capability, and enhanced aerodynamics and controllability.

Since Theodore von Karman proposed that thrust augmenting ejectors could be designed for achieving V/STOL capability (Reference 1), attempts were made to design practical ejectors for aircraft application. In the 1960s, Dr. Hans von Ohain of the Aerospace Research Laboratories (ARL) conducted several investigations for designing efficient mixers in which the high-energy, low-mass-flow primary gas exchanges momentum and energy with an entrained, low-energy, high-mass-flow secondary gas. A significant result of this work was ARL's hypermixing nozzles that made it possible to design compact ejectors that also provided high values of thrust augmentation. A summary of various ejector projects that were pursued until the early 1980s can be found in Reference 2.

Further work was continued in the Flight Dynamics Laboratory (FDL) of Wright Patterson Air Force Base (WPAFB) in the area of applying ejector integrated wings for V/STOL demonstration aircraft design. A compressible ejector flow analysis was developed (Reference 3) that included empirical ejector losses. The results predicted by the analysis agreed with the results of experiments performed on various ejectors, both at Lockheed and Bell Aerospace (see Reference 3.) The analysis showed that when classical ejectors (i.e., first solution where the mixed flow is subsonic) are used for aircraft flight, the thrust augmentation values decrease with increasing primary gas stagnation temperature and decrease with forward flight speed. However, as the speed increased above around 400 ft/sec, the downward trend of thrust augmentation begins to move upward. Small performance improvements with increasing primary jet stagnation temperature at speeds in excess of 400 ft/sec were also noticed in the results published in Reference 3, but the calculations were terminated at speeds of about 600 ft/sec. Consequently, the conclusion that performance of first solution ejectors degrade with increasing primary jet stagnation temperature and with increasing ejector forward speed remained.

Flight Dynamics Laboratory at WPAFB also undertook a systematic study of ejector designs to determine whether mixed supersonic flow type ejectors (which were not previously recognized as candidates for possible aircraft applications) would provide usable performance levels. Although it was known that two solutions existed for mixed ejector flows in constant area mixing ducts, only the subsonic, first solution ejectors were studied in detail for aircraft integration purposes. The results of the second solution ejector studies provided potential advantages for aircraft application (Reference 3, Reference 5, and Reference 6). The subsonic and supersonic solutions of ejector mixed flows in constant area ejectors are related by the normal shock relations.

A flight-worthy ejector used for thrust augmentation would require many essential elements (such as appropriately selected aerothermodynamic and geometric parameters) including a well-designed diffuser or nozzle after the mixing section. Integration of the entire system is also critical if the desired levels of benefits are to be achieved. An excellent discussion of these requirements is given by Alperin and Wu (Reference 4, Reference 5, and Reference 6). Potential advantages of operating on the supersonic solution branch (second solution) for application to thrust augmentation and for yielding high thrust augmentation values at high speeds were illustrated.

Another significant benefit of using ejectors is the reduction of engine noise. In pioneering work performed in Dornier, Germany, Bernard H. Groethert (Reference 7) showed that ejectors allowing rapid mixing can reduce noise by as much as 20 dB (Reference 7). This was the first published work to show that rapid and efficient mixing not only provides substantial noise reduction, but can also yield useful levels of thrust augmentation.

The High Speed Civil Transport (HSCT) has reopened significant ejector investigations in noise reduction and in achieving desired thrust augmentation. The investigations reported herein explore second solution ejectors, and determine the design aspects of second solution ejectors that will yield high levels of thrust augmentation over a broad range of speeds. This thrust augmentation study indicates the potential benefits of using ejector nozzles in the subsonic cruise mode if the ejector inlet contains a sonic throat plane.

## 7.1 SECONDARY THROAT EJECTOR

Although earlier work showed the potential advantages of operating on the supersonic solution branch, Minardi (Reference 8, Reference 9, and Reference 10) first pointed out that the inlet Mach numbers are subject to the Fabri inlet conditions (Reference 11). This severely limits the performance of the second solution ejectors. Minardi's work was initiated by WPAFB's FDL and showed that ejector efficiencies based on thermodynamic availability are high on the supersonic branch, especially when operating at low subsonic values of the secondary flow inlet Mach numbers ( $M_s$ ). Second solution ejectors operating under these conditions would provide high-thrust augmentation at high speeds. In reality, if the inlet area does not restrict the secondary flow, then the Fabri inlet condition will uniquely determine the single operating point on the mixed flow supersonic branch. The form of the Fabri inlet condition used in this study is presented in Reference 8. The original equations that were used to study ejector performance are developed and presented in Reference 8, Reference 9, and Reference 10. Modifications were developed during this study as discussed below.

Ejector analyses are either carried out by a detailed mixing model using the Navier-Stokes equations, or a control volume approach using integrated forms of conservation equations of mass, momentum, and energy. Based on thermodynamic availability, typical results for ejector efficiency versus secondary inlet Mach number ( $M_s$ ) show the advantage of operating on the supersonic branch, especially at low subsonic values of  $M_s$ . The one-dimensional control-volume approach using compressible ideal gases was chosen for this study because it affords the best approach for doing the parametric studies required to understand the potential of ejectors for thrust augmentation.

As stated above, properly designed diffusers are important in the performance of an ejector. However, the initial study will involve the inlet region of the mixing tube. Fabri and Siestrunk presented the results of an extensive experimental and theoretical study of air-to-air ejectors with high-pressure ratios and a supersonic primary flow in 1958 (Reference 11). If the inlet area does not restrict the mixed flow, then the inlet conditions described by Fabri and Siestrunk (Reference 11) will uniquely determine the single operating point on the supersonic solution branch (referred to as the Fabri inlet condition).

A traditional ejector, similar in principle to the current HSCT nozzle design under study at Pratt & Whitney (P&W) is shown in Figure 146. The main feature is that the secondary flow at the entrance to the ejector must be subsonic or Mach 1 at maximum. The performance of this type of ejector has been under study for many years. The supersonic solution produces very high performance at low subsonic secondary inlet Mach numbers. However, only a single point on the supersonic mixed flow branch can actually be attained. This occurs when the ejector is choked either by the mixed flow or the secondary flow. If the mixed flow is choked, the mixed flow Mach number is 1 at the ejector exit. The secondary flow is choked either at Mach 1 at the inlet, or just after the inlet where the expanding primary flow chokes the secondary flow (i.e., the Fabri inlet condition).

The major features of the traditional ejector are summarized as follows:

- Two solutions are subsonic and supersonic (related by normal shock equations)
- Best performance is supersonic branch at low values of  $M_s$
- Operates at a single point on the supersonic branch when the ejector chokes: Fabri condition or  $M_m = 1$ 
  - Therefore, the low values of  $M_s$  can not be attained, and the best performance can not be achieved.

Because the best performance cannot be achieved with the traditional ejector configuration, Alprin and Wu (Reference 6) suggested putting a throat in the secondary to choke the flow and limit it to lower values of  $M_s$  in order to improve the performance (Figure 147).

The main features of the secondary throat ejector are as follows:

- Alprin and Wu suggest a secondary throat to restrict the bypass ratio ( $\beta$ ) and the mass flow ratio ( $\beta = \dot{m}_s / \dot{m}_p$ ) to achieve high performance.
- Secondary throat ejectors still operate at a single point on the supersonic branch due to choking at the throat ( $\beta < \beta_{\text{Fabri}}$ ) or at exit ( $M_m = 1$ ).
- The highest values of performance can be achieved with this configuration.

We can better understand the operation of a secondary throat ejector if we first discuss the performance of a nozzle using Fanno and Rayleigh lines on a T-s diagram. The Fanno line is based only on the continuity equation and the energy equation for the flow, while the Rayleigh line is based only on the continuity equation and the momentum equation.

## 7.2 NOZZLE PERFORMANCE USING FANNO AND RAYLEIGH LINES

A nozzle with an area ratio that produces an exit Mach number of 1.5 was assumed for the example presented on the T-s diagram of Figure 148. A horizontal line located at the total temperature is indicated, along with the Fanno line based on the exit area for the flow when it is choked. The assumed total conditions are at the point labeled with a 0 (Figure 148).

Two Rayleigh lines are shown for an isentropic flow to the exit area: one subsonic ( $M = 0.61$  for the given area ratio) and the other supersonic ( $M = 1.5$  for the given area ratio). The outer Rayleigh line is for the subsonic flow and intersects the Fanno Line at two points. However, Point 4 on the supersonic branch violates the 2nd Law of Thermodynamics and can not be attained. The inner Rayleigh line is for the supersonic branch, and Points 2 and 3 are possible because they do not violate the 2nd Law of Thermodynamics.

The operation of the nozzle is easily understood when the constant pressure lines shown on the T-s diagram are considered. These lines can represent various values of the back pressure into which the nozzle exhausts. An isentropic line starting at the total temperature and pressure (Point 0) is shown on Figure 148. When the given back pressure line intersects the isentropic line between the Points 0 and 1, the flow is subsonic throughout the nozzle.

When the nozzle chokes, the solutions are found where the given back pressure line intersects the Fanno line. The flow is supersonic, and a shock occurs in the nozzle; the exit flow is subsonic, and the entropy increases in the nozzle. For back pressures less than the one that intersects the Fanno line at Point 2, the nozzle has supersonic flow throughout (after the throat) and operates at Point 3 as soon as the 2nd Law of Thermodynamics permits.

Nozzle performance results are summarized as follows:

### 7.2.1 Unchoked Flow

- Subsonic exit flow:  $P_{\text{exit}} = P_{\text{back}}$  while  $\Delta s = 0$ 
  - Both the Fanno line and Rayleigh line change with back pressure.
  - The mass flow increases as the back pressure decreases.

### 7.2.2 Choked flow (Fixed Fanno Line at Exit)

- Subsonic exit flow:  $P_{\text{exit}} = P_{\text{back}}$  while  $\Delta s = 0$ 
  - Changes are due to differences in the Rayleigh line because of decreases in the impulse function.
  - $\Delta s$  increases as the back pressure decreases.
- Supersonic exit flow ( $P_{\text{exit}} \neq P_{\text{back}}$ )
  - Transition to supersonic flow occurs as soon as the 2nd Law of Thermodynamics permits it: ( $\Delta s = 0$  when  $M > 1$ ).
  - Both the Fanno and Rayleigh lines are independent of the back pressure.

Figure 149 shows a plot of the normalized impulse function versus area ratio ( $A_{\text{exit}}/A^*$ ). The value of the normalized impulse function at the subsonic Mach number (the upper branch) is always larger than the value of the normalized impulse function at the supersonic Mach number (the lower branch) for a given area ratio (Figure 149). Thus, the Rayleigh line for the subsonic Mach number will always be the outer Rayleigh line on the T-s diagram.

We can use a T-s diagram in a similar way to understand the performance of ejectors.

### 7.3 EJECTOR PERFORMANCE USING FANNO AND RAYLEIGH LINES

Figure 150 shows the T-s diagram for a secondary throat ejector that is limited to a very low value of  $M_s$  and therefore, of the bypass ratio ( $\beta$ ). The Fanno line for a choked inlet flow of both the primary and secondary flow is shown. Two Rayleigh lines are shown: one for the subsonic secondary flow, and the other for supersonic secondary flow (the primary is always flowing full and supersonic at the exit). The traditional ejector solution is shown on the diagram (dotted line) along with the reversible mixing line that joins the primary and secondary total conditions. Point 0 on the reversible mixing line is located at the total conditions that would be obtained in reversible mixing and therefore establishes the minimum value of the entropy permitted for the given bypass ratio established by the throat in the secondary.

For high back-pressures, the solution is found at the intersection of the back pressure with the traditional solution. After the secondary flow chokes, the solution is found at the intersection of the back pressure and the Fanno line (Point 1) as it was for the nozzle. The hypothesis is that transition to the supersonic branch takes place as soon as the 2nd Law of Thermodynamics permits. However, the ejector *is not a reversible device*, even ideally. Therefore, some increase in entropy must result from the intrinsic losses in the ejector. Point 4 may not be obtainable because of these losses, and the transition to supersonic flow would then be delayed and occur between Points 1 and 2.

No theory is presently available to determine the intrinsic losses in an ejector. An experimental study will be required to obtain fundamental information on the transition to supersonic flow and the intrinsic losses.

The ejector results are summarized as follows:

#### 7.3.1 Unchoked Flow

- Subsonic exit flow:  $P_{\text{exit}} = P_{\text{back}}$ 
  - Both the Fanno line and Rayleigh line change with back pressure
  - The secondary mass flow and mixed mass flow increase as the back pressure decreases.

#### 7.3.2 Choked flow: Fixed Fanno Line at Exit

- Subsonic exit flow:  $P_{\text{exit}} = P_{\text{back}}$ 
  - Changes are due to changes in the Rayleigh line due to decreases in the impulse function
  - $\Delta s$  increases as the back pressure decreases.
- Supersonic exit flow:  $P_{\text{exit}} \neq P_{\text{back}}$ 
  - Transition to supersonic flow occurs as soon as the 2nd Law of Thermodynamics permits it with intrinsic losses
  - Both the Fanno and Rayleigh lines are fixed and independent of the back pressure.

Figure 151 shows the T-s diagram for the ejector limited to a bypass ratio equal to 0.8. The dimensions of the ejector closely match those of the ejector that P&W will test. It is anticipated that this ejector would transition to the supersonic branch as soon as the secondary flow chokes (i.e., Point 4 on Figure 151). Total conditions for constant kinetic energy (KE) after mixing are indicated in Figure 150 and Figure 151. These conditions are the same as those that would be obtained using an ideal mixing fan with the same bypass ratio as the ejector. It is highly

unlikely that an ejector could outperform an ideal mixing fan. Thus, the supersonic transition at Point 4 is expected to have an entropy greater than that of the constant KE point (for Point 4 in Figure 151, but not for Point 4 in Figure 150).

## 7.4 TYPICAL EJECTOR RESULTS

Figure 152 shows the mixed flow exit static pressure versus  $M_s$  for both subsonic and supersonic values of  $M_s$  and  $M_m$ . The dashed vertical lines indicate the choked conditions for the traditional ejector (Fabri limit) and the two secondary throat ejectors presented on the two previous figures. Both the subsonic and supersonic values of  $M_s$  are indicated for a bypass ratio of 0.8.

The mixed flow would choke the ejector (if not cut off by the Fabri inlet condition) and therefore, a range of  $M_s$  values could not be achieved in the ejector.

The thrust augmentation is shown as a function of  $M_s$  (Figure 153). The limit values of  $M_s$  are again indicated for the traditional ejector and the secondary throat ejector with a bypass ratio of 0.8. The secondary throat ejector can almost obtain a thrust augmentation of 1.2. If the throat was smaller, a thrust augmentation in excess of 1.2 would be likely. This requires verification in an experimental program.

Figure 154 shows the thrust augmentation versus the back pressure for both the traditional injector and the secondary throat injector ( $\beta = 0.8$ ). The performance of the secondary throat ejector is shown in the transition region for both the subsonic and supersonic mixed flow. The ejector will operate only at a single point after transition to the supersonic branch. This configuration would likely transition immediately. An assumed transition is shown at a slightly lower back pressure (from Point 1 to Point 2). The supersonic branch is referred to as plotted versus *transition pressure* since the actual exit stream static pressure is much less (Point 3 on Figure 154). The exit stream static pressure is indicated by the dashed line in Figure 154. Following transition, the conditions at the exit of the ejector are independent of back pressure. A substantial increase in thrust augmentation is possible with the secondary throat ejector that was obtained with the original ejector (Figure 154). However, there is a substantial reduction in performance if the transition is delayed to lower values of back pressure. Thus, determination of the actual transition through the experimental program is critical to understanding the operation of secondary throat ejectors.

A study was also made to show the improvement in performance possible in a traditional ejector by adjusting the secondary exit area. The results of the study are presented in the next section.

## 7.5 SECONDARY EXIT AREA STUDY

When a traditional ejector is controlled by the Fabri inlet condition, the performance can be adjusted by changing the secondary exit area while holding the mixing tube area fixed. This effectively changes the primary nozzle exit area and adjusts the value of the primary Mach number ( $M_p$ ). Therefore, a study of the traditional ejector was made to show the improvement in performance that can be obtained by adjusting the secondary exit area by removing chutes. The results are shown in Figure 155 where the thrust augmentation is plotted versus the primary flow Mach number for both the subsonic and supersonic branch when the flow is choked by the Fabri inlet condition. A modest increase in performance can be achieved if two chutes are removed and the primary throat is set at the nozzle adjustable throat (Figure 155), as opposed to locating the primary throat at the chute exits. The results shown could also be obtained by not completely lowering the chutes into the primary flow. Thus, the concept can be experimentally tested using the current ejector design.

## 7.6 INLET LIP EJECTORS

The point of the secondary throat ejector's transition to the supersonic branch is currently uncertain. Therefore, additional studies of the inlet configuration are planned. The lip shown on Figure 156 can also be used to limit the secondary mass flow at the inlet. This configuration can be solved in closed form since it is reasonable to assume that the pressure on the lip is the same as the pressure in the secondary flow at the inlet. Required adjustments to the new computer program will be made to study this design. Since this configuration has a closed form solution, a



study of its performance over a range of lip sizes will provide information on the lower limits of performance (without friction).

The inlet lip ejector has losses due to the sudden expansion at the entrance to the mixing tube. These losses adjust the value of the impulse function which changes the Rayleigh line and, consequently, the exit Mach number of the mixed flow. The secondary throat ejector makes the adjustments required by the 2nd Law of Thermodynamics through shocks in the exit region of the secondary nozzle. These shocks adjust the impulse function which causes a change in the exit Mach number of the mixed flow.

## **7.7 CONCLUSIONS AND RECOMMENDATIONS**

The results of this study show promise for improving the performance of second solution ejectors by using a throat in the secondary flow. Fanno and Rayleigh lines on a T-s diagram can be used to understand the performance of these ejectors, and to serve as an aid in designing second solution ejectors. A brief summary of the conclusions and recommendations is given below:

### **7.7.1 Conclusions**

- A new approach using Fanno and Rayleigh lines showing ejector and thermodynamic characteristics offers new insight into understanding ejector flows on a T-s diagram.
- A one-dimensional theory for secondary throat ejectors was developed that accounts for an ejector's operation over the complete range of back pressures.
- The performance of the current design can be improved by adjusting the secondary exit area and locating the primary throat at the adjustable main throat.
- The goal of a 1.2 thrust augmentation may be achieved if throats are introduced into the secondary nozzles (i.e., chutes).

### **7.7.2 Recommendations**

- Pratt & Whitney should make provisions in their ejector tests to obtain performance with the chutes not completely lowered, and the primary throat located at the adjustable section.
- Rohini International should:
  - Continue development of the one-dimensional code
  - Add friction effects to the computer program
  - Develop estimates of the effect of incomplete mixing
  - Calculate performance of the P&W ejector at the anticipated test conditions of pressure, temperature, and geometries
- Perform fundamental ejector tests of secondary throat ejectors
  - Determine transition back pressures using flow visualization of ejector tube and exit
  - Measure static pressures and exit total pressures
  - Investigate methods for the acceleration of mixing the hot primary gas and cold secondary gas in order to design more compact ejectors.
- CFD calculations:
  - Develop an understanding of the entropy increase during mixing
  - Study transition to supersonic flow from the entropy study
  - Use geometries and thermodynamic properties consistent with the experimental program
  - Compare results with the flow visualization experiments and pressure data.

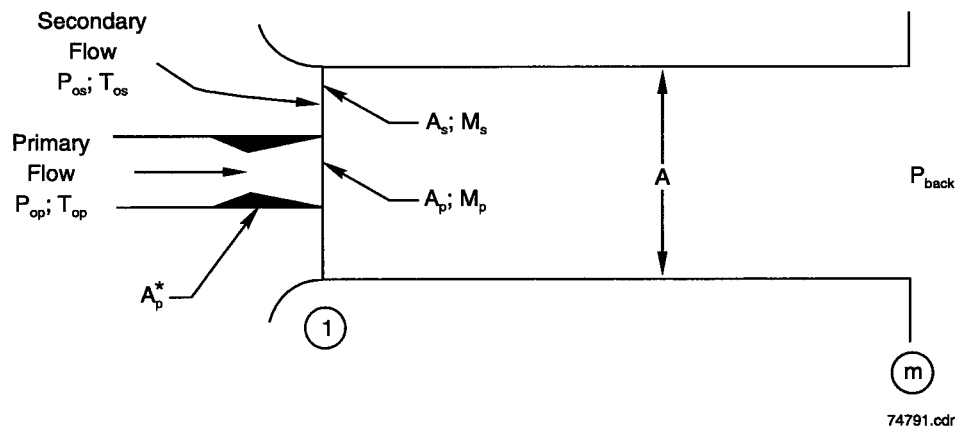


Figure 146. Typical Ejector Design with Converging Secondary Nozzle

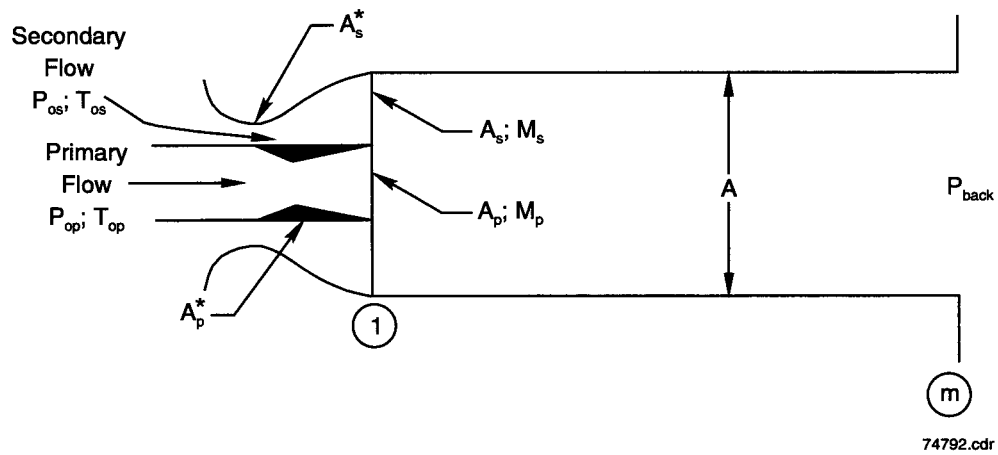


Figure 147. Ejector Design with Converging-Diverging Secondary Nozzle

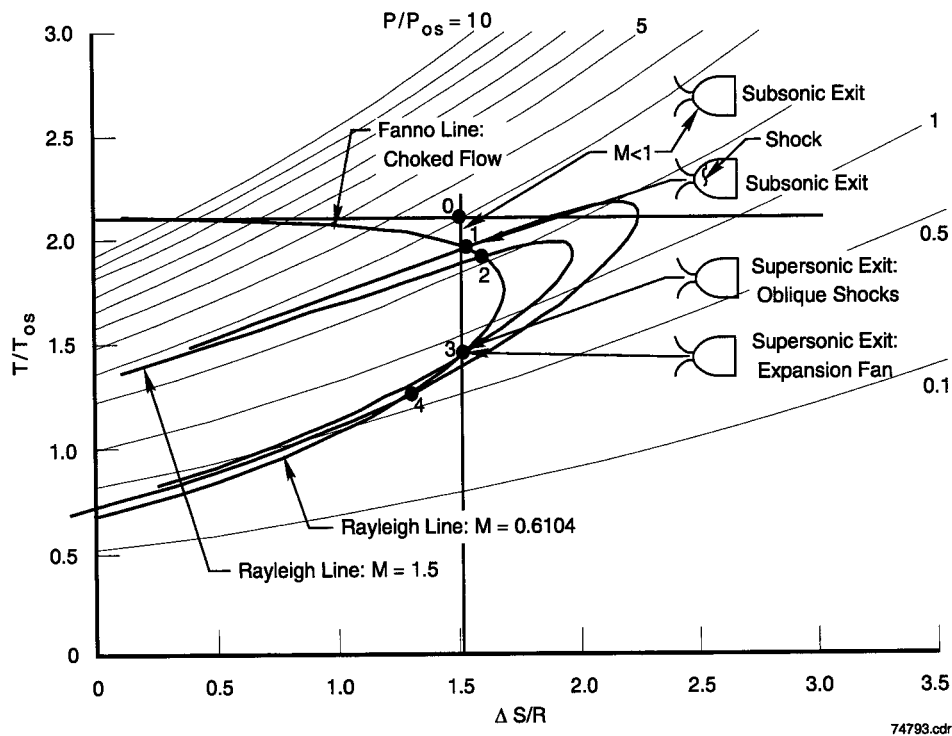


Figure 148. T-s Diagram for Air With Fanno Lines, Rayleigh Lines, and Lines of Constant Pressure for Nozzle Flow with an Exit Mach Number of 1.5

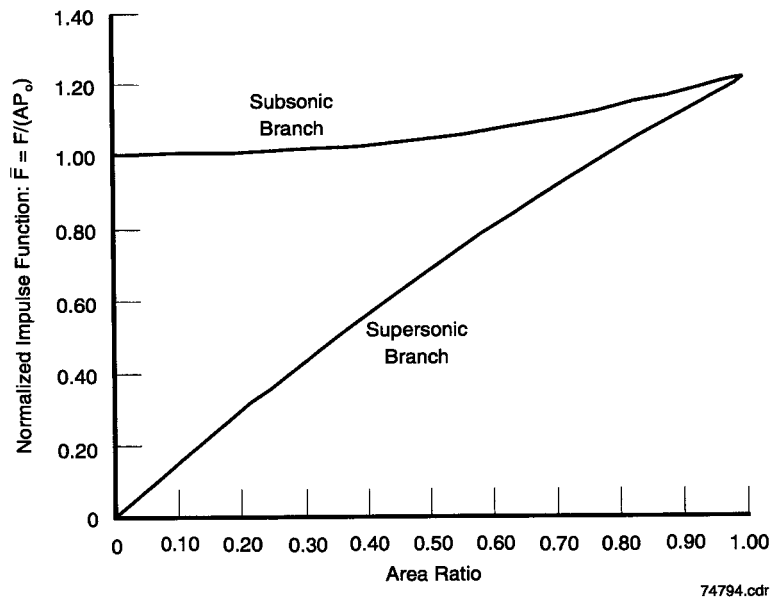


Figure 149. Normalized Impulse Function —  $\Phi$  Versus Area Ratio ( $A_{exit}/A^*$ ) for  $\gamma = 1.4$

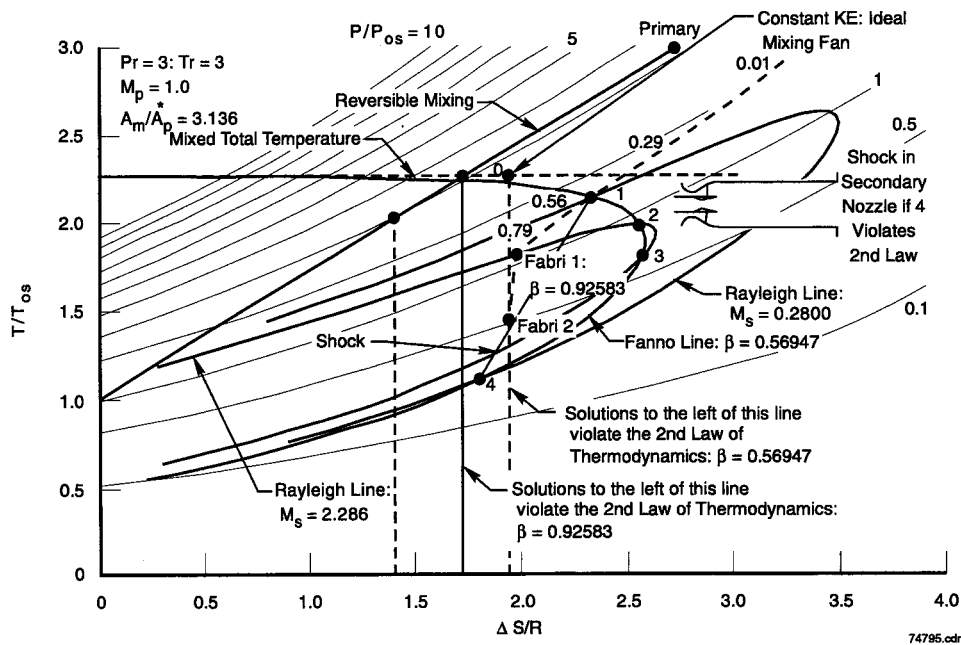


Figure 150. T-s Diagram for Air With Lines of Constant Pressure (a Fanno Line for  $\beta = 0.569$  and Two Associated Rayleigh Lines that can Yield  $\beta = 0.569$ )

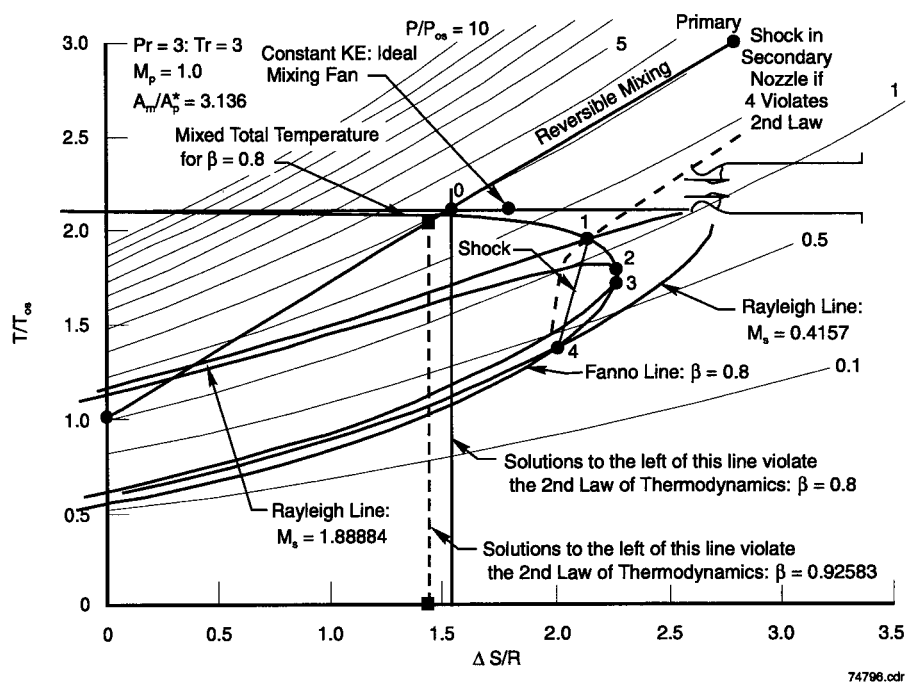


Figure 151. T-s Diagram for Air With Lines of Constant Pressure (a Fanno Line for  $\beta = 0.8$  and Two Associated Rayleigh Lines that can Yield  $\beta = 0.8$ )

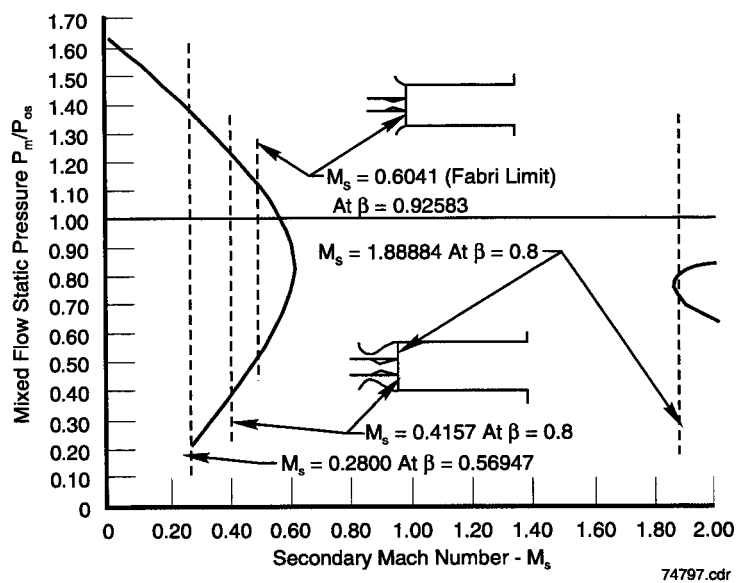


Figure 152.  $P_m/P_{os}$  Versus  $M_s$  —  $Pr = 3$ ;  $Tr = 3$ ;  $M_p = 1.0$ , and  $A_{exit}/A_p^* = 3.136$

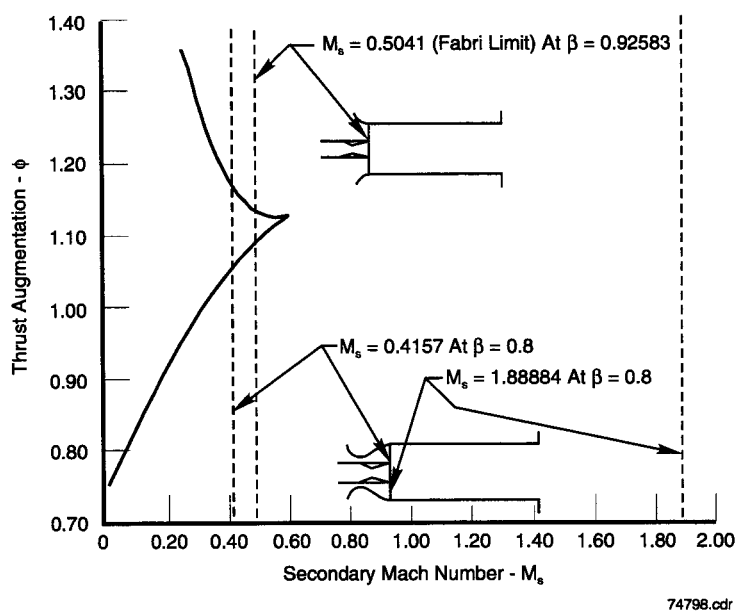


Figure 153.  $\Phi$  Versus  $M_s$  —  $Pr = 3$ ;  $Tr = 3$ ;  $M_p = 1.0$ , and  $A/A_p^* = 3.136$

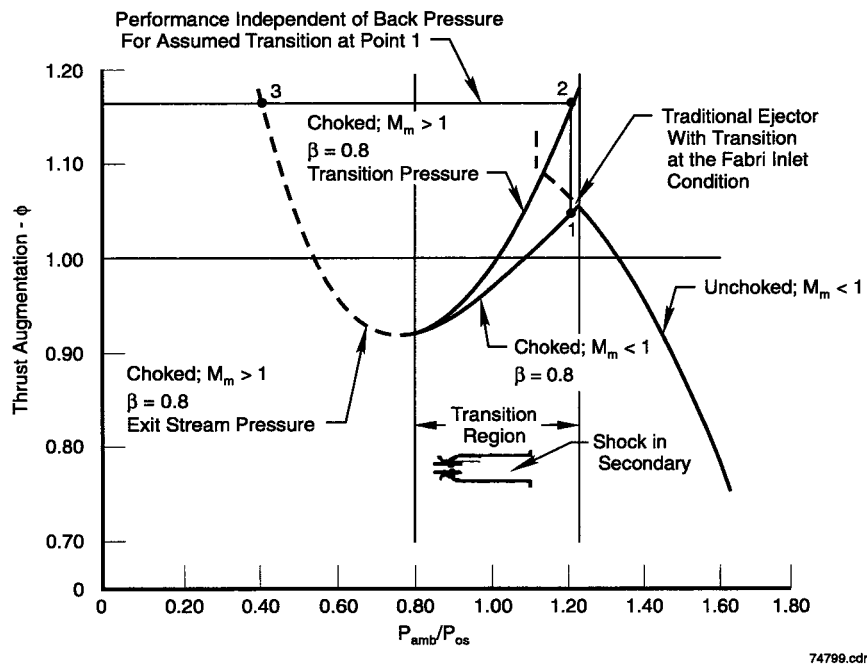


Figure 154. Thrust Augmentation Versus Back Pressure (Subsonic Mixed Flow) or Transition Pressure (Supersonic Mixed Flow)

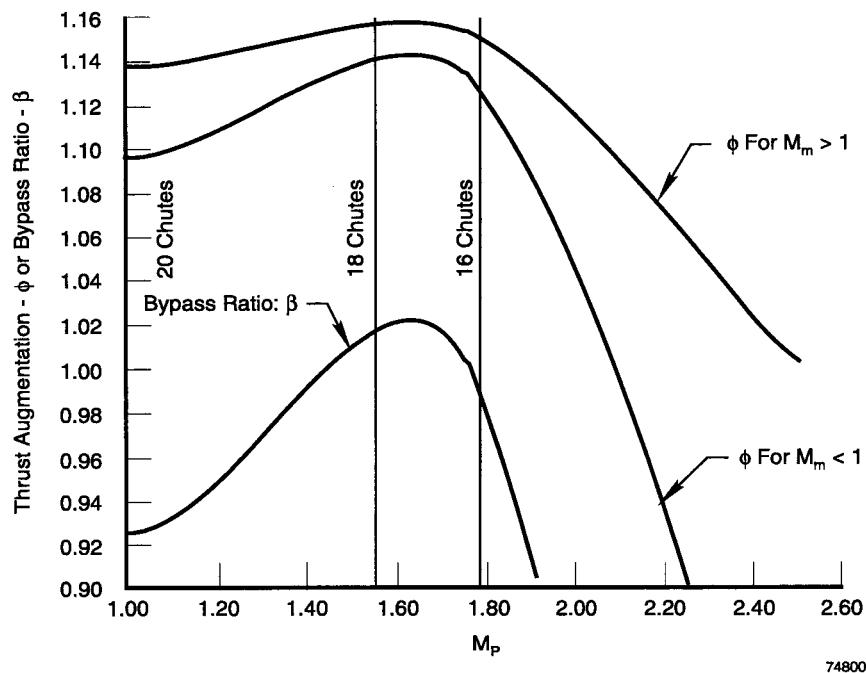
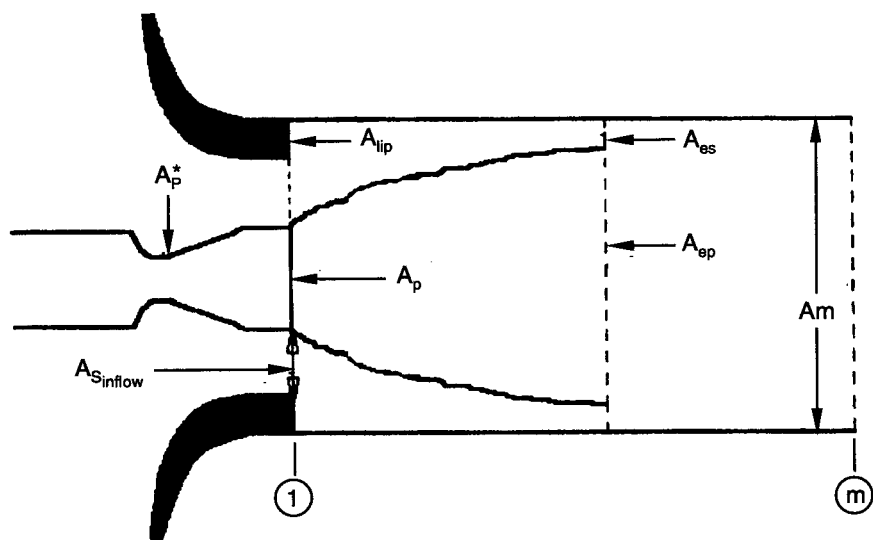


Figure 155. Performance Versus  $M_p$  Showing the Effect of Removing Chutes



74801.cdr

Figure 156. Flow at the Inlet of an Ejector

## APPENDIX 7-A

### LIST OF SYMBOLS

A	Area, in. <sup>2</sup>
F	Thrust, lb <sub>f</sub>
F	Normalized Impulse Function, $F/(AP_o)$
M	Mach Number
m	Mass flow rate, lbm/sec
NPR, or Pr	Nozzle Pressure Ratio
Po	Total, or Stagnation Pressure, psia
p	Static Pressure, psia
R	Gas Constant
s	Entropy
T	Static Temperature, °R
To	Total, or Stagnation Temperature, °R
Tr	Temperature Ratio, $T_{op}/T_{amb}$
$\beta$	Ratio of Secondary to Primary Flowrate
$\gamma$	Ratio of Specific Heats
$\phi$	Thrust Augmentation Ratio, $F_m/F_{ip}$

### Subscripts

back, or amb	Ambient Conditions
exit, or e	Ejector Exit
ep, es	Plane of Equal Static Pressure
lip	Second Throat Restriction
m	Mixed Condition
p	Primary
s	Secondary

### Superscripts

*	Choking Condition, $M = 1.0$
---	------------------------------



## REFERENCES

1. Theodore von Karman, *Theoretical Remarks on Thrust Augmentation*, Reissner Anniversary Volume, Contributions To Applied Mechanics, 1949.
2. R.P. Braden, K.S. Nagaraja, and H.J.P. von Ohain, editors, Proceedings: Ejector Workshop for Aerospace Applications, AFWAL-TR-82-3059, Flight Dynamics Laboratory, Air Force Wright Aeronautical Laboratories, Wright-Patterson Air Force Base, OH, June 1982.
3. K.S. Nagaraja, D.L. Hammond, and J.E. Groetch, One-Dimensional Compressible Ejector Flows, AIAA 73-1184.
4. M. Alprin and J. Wu, High Speed Ejectors, AFFDL-TR-79-3048, May 1979.
5. M. Alprin and J.J. Wu, Thrust Augmenting Ejectors, Part I AIAA Journal, Vol. 21, No. 10, Oct. 1983; Part II AIAA Journal, Vol. 22, No. 12, Dec. 1983.
6. J.J. Wu, Experiments on High Speed Ejectors, NASA Contractor Report 177419, July 1986.
7. B.H. Groethert, *Noise Attenuation and Associated Thrust Increase of Turbojet Engines Through Hyper-Mixing Ejector Shrouds*, presented at the Fifth International Symposium on Air Breathing Engines, Feb. 16-21, 1981, Bangalore, India.
8. J.E. Minardi, Characteristics of High Performance Ejectors, AFWAL-TR-81-3170, January 1982.
9. J.E. Minardi, et al., Ejector Turbine Studies and Experimental Data, DOE/ER/10509-1, November 1982.
10. J.E. Minardi and H.P. von Ohain, Thrust Augmentation Study of High Performance Ejectors, AFWAL-TR-83-3087, November 1983.
11. J. Fabri and R. Siestrunk, *Supersonic Air Ejectors*, Advances in Applied Mechanics, Vol. 5, Academic Press, Inc., New York, NY 1958.

REPORT DOCUMENTATION PAGE			Form Approved OMB No. 0704-0188	
Public reporting burden for this collection of information is estimated to average 1 hour per response, including the time for reviewing instructions, searching existing data sources, gathering and maintaining the data needed, and completing and reviewing the collection of information. Send comments regarding this burden estimate or any other aspect of this collection of information, including suggestions for reducing this burden, to Washington Headquarters Services, Directorate for Information Operations and Reports, 1215 Jefferson Davis Highway, Suite 1204, Arlington, VA 22202-4302, and to the Office of Management and Budget, Paperwork Reduction Project (0704-0188), Washington, DC 20503.				
1. AGENCY USE ONLY (Leave blank)		2. REPORT DATE November 2004		3. REPORT TYPE AND DATES COVERED Final Contractor Report
4. TITLE AND SUBTITLE  Generation 1.5 High Speed Civil Transport (HSCT) Exhaust Nozzle Program			5. FUNDING NUMBERS  WBS-22-7140946 NAS3-26618	
6. AUTHOR(S)  E.B. Thayer, E.J. Gamble, A.R. Guthrie, D.F. Kehret, T.J. Barber, G.J. Hendricks, K.S. Nagaraja, and J.E. Minardi				
7. PERFORMING ORGANIZATION NAME(S) AND ADDRESS(ES)  United Technologies Corporation Pratt & Whitney 400 Main Street East Hartford, Connecticut 06108			8. PERFORMING ORGANIZATION REPORT NUMBER  E-14631	
9. SPONSORING/MONITORING AGENCY NAME(S) AND ADDRESS(ES)  National Aeronautics and Space Administration Washington, DC 20546-0001			10. SPONSORING/MONITORING AGENCY REPORT NUMBER  NASA CR-2004-213131	
11. SUPPLEMENTARY NOTES This research was originally published internally as HSR028 in May 1996. E.B. Thayer, E.J. Gamble, A.R. Guthrie, and D.F. Kehret, United Technologies Corporation, Pratt & Whitney Aircraft, 400 Main Street, East Hartford, Connecticut 06108; T.J. Barber and G.J. Hendricks, United Technologies Research Center, 411 Silver Lane, East Hartford, Connecticut 06108; and K.S. Nagaraja and J.E. Minardi, Rohini International, Cleveland, Ohio. Responsible person, Diane Chapman, Ultra-Efficient Engine Technology Program Office, NASA Glenn Research Center, organization code 2100, 216-433-2309.				
12a. DISTRIBUTION/AVAILABILITY STATEMENT  Unclassified - Unlimited Subject Categories: 01 and 07 Available electronically at <a href="http://gltrs.grc.nasa.gov">http://gltrs.grc.nasa.gov</a> This publication is available from the NASA Center for AeroSpace Information, 301-621-0390.			12b. DISTRIBUTION CODE	
13. ABSTRACT (Maximum 200 words)  The objective of this program was to conduct an experimental and analytical evaluation of low noise exhaust nozzles suitable for future High-Speed Civil Transport (HSCT) aircraft. The experimental portion of the program involved parametric subscale performance model tests of mixer/ejector nozzles in the takeoff mode, and high-speed tests of mixer/ejectors converted to two-dimensional convergent-divergent (2-D/C-D), plug, and single expansion ramp nozzles (SERN) in the cruise mode. Mixer/ejector results show measured static thrust coefficients at secondary flow entrainment levels of 70 percent of primary flow. Results of the high-speed performance tests showed that relatively long, straight-wall, C-D nozzles could meet supersonic cruise thrust coefficient goal of 0.982; but the plug, ramp, and shorter C-D nozzles required isentropic contours to reach the same level of performance. The computational fluid dynamic (CFD) study accurately predicted mixer/ejector pressure distributions and shock locations. Heat transfer studies showed that a combination of insulation and convective cooling was more effective than film cooling for nonafterburning, low-noise nozzles. The thrust augmentation study indicated potential benefits for use of ejector nozzles in the subsonic cruise mode if the ejector inlet contains a sonic throat plane.				
14. SUBJECT TERMS  High-Speed Civil Transport; Low noise exhaust nozzle; Exhaust nozzle; Mixer/ejector nozzles			15. NUMBER OF PAGES 190	
			16. PRICE CODE	
17. SECURITY CLASSIFICATION OF REPORT  Unclassified	18. SECURITY CLASSIFICATION OF THIS PAGE  Unclassified	19. SECURITY CLASSIFICATION OF ABSTRACT  Unclassified	20. LIMITATION OF ABSTRACT	



